UAB
Universitat Autònoma de Barcelona

# Free-standing membranes of Antiferroelectric Lead Zirconate ($PbZrO_3$)

**Umair Saeed**

**Doctoral Thesis**

# Free-standing membranes of Antiferroelectric Lead Zirconate ($PbZrO_3$)

*submitted by*

**Umair Saeed**

*for the degree of* Doctor of Philosophy in Materials Science

*at the* Autonomous University of Barcelona

Advisors:

**Prof. Dr. Gustau Catalán Bernabé**

**Dr. José Santiso**

**Dr. David Pesquera**

Tutor:

**Prof. Dr. Javier Rodríguez- Viejo**

---

**2025**

ICN2 Institut Català de Nanociència i Nanotecnologia

UAB Universitat Autònoma de Barcelona

The research work done during the course of this thesis has been carried out at Institut Català de Nanociència i Nanotecnologia (ICN2) during the period: Dec 2021 and Nov 2025, funded by Spanish Ministry of Science and Innovation under the grant PID2019-108573GB-C21 (FOx-Me) (doi: *10.13039/501100011033*) and European Union's Horizon 2020 research and innovation program under the grant 964931 (TSAR) (doi: *10.3030/964931*). All research at ICN2 is supported by a Severo Ochoa Grant CEX2021-001214-S.

Bellaterra, 20 de Octubre de 2025

El. Prof. Gustau CATALÁN, científico titular y líder del grupo **Oxide Nanophysics**, el Dr. José SANTISO científico titular y líder de unidad **Nanomaterials Growth Unit**, el Dr. David PESQUERA del **Institut Catalá de Nanociéncia I Nanotecnologia (ICN2)**, y el Dr. Javier RODRIGUEZ VIEJO, Catedrático del Departamento de Física de la **Universitat Autónoma de Barcelona (UAB)**, en calidad de tutor de tesis.

**CERTIFICAN**

Que Umair Saeed, ha realizado bajo su dirección y tutoría el trabajo que lleva por título "**Free-standing membranes of Antiferroelectric Lead Zirconate ($PbZrO_3$)**". Dicho trabajo ha sido desarrollado dentro del programa de doctorado de Ciència de Materials y constituye su memoria de tesis doctoral, para optar al grado de Doctor por la Universitat Autónoma de Barcelona.

Prof. Gustau CATALÁN

Group leader, Oxide Nanophysics group

*ICN2 – ICREA*

SANTISO LOPEZ JOSE MANUEL - 38076442B

Firmado digitalmente por SANTISO LOPEZ JOSE MANUEL - 38076442B
Nombre de reconocimiento (DN): c=ES, serialNumber=IDCES-38076442B, givenName=JOSE MANUEL, sn=SANTISO LOPEZ, cn=SANTISO LOPEZ JOSE MANUEL - 38076442B
Fecha: 2025.10.29 13:02:29 +01'00'

Dr. José SANTISO

Unit Leader, Nanomaterials growth unit

*ICN2 CSIC*

Firmado por DAVID PESQUERA HERRERO - DNI ***4076** el día 29/10/2025 con un certificado emitido por EC-Ciutadania

Dr. David PESQUERA

Senior Postdoctoral Researcher

*ICN2*

JAVIER RODRIGUEZ VIEJO - DNI 46620967J

Signat digitalment per JAVIER RODRIGUEZ VIEJO - DNI 46620967J
Data: 2025.10.29 11:33:41 +01'00'

Prof. Javier RODRIGUEZ VIEJO

Full Professor

*UAB*

## Tribunal:

| | | |
|---|---|---|
| Presidente : | **Prof. Marty Gregg**<br>*m.gregg@qub.ac.uk* | School of Mathematics and Physics,<br>Queen´s University,<br>Belfast, Northern Ireland. |
| Vocal : | **Asst. Prof. Mael Guennou**<br>*mael.guennou@uni.lu* | University of Luxembourg.<br>Luxembourg. |
| Secretario : | **Dr. Núria Bagués**<br>*nbagues@cells.es* | ALBA Synchrotron,<br>Barcelona, Spain. |
| Suplente : | **Assoc. Prof. Eric Langenberg**<br>*eric.langenberg@ub.edu* | Universitat de Barcelona,<br>Barcelona, Spain |
| Suplente : | **Dr. Amador Pérez-Tomás**<br>*amador.perez@imb-cnm.csic.es* | Instituto de Microelectrónica de Barcelona (IMB-CNM),<br>Barcelona, Spain. |
| Suplente : | **Dr. Neus Domingo Marimon**<br>*ndomingo@ornl.gov* | Oak Ridge National Laboratory (ORNL),<br>Oak Ridge, USA. |

# Acknowledgments

I left writing the acknowledgements for last, thinking that this would be the easiest. It turns out, I am still as naive (at least in judging the ease of writing this) as when I started my PhD. I will keep this short, I am horrible in these things, but here goes.

Let me start by thanking the members of the jury for putting in the time and effort in reviewing my thesis, I am sure it is a tiring task. I hope you find it as interesting while reading it as much fun I had while doing the experiments (and writing them).

I still remember the day of my first interview with my potential supervisors and my laptop camera decided to not work, and I thought to myself, “wow, that was a good first impression”. Luckily, I got another chance and the camera worked as well. I received the offer, followed by a series of unfortunate events in the visa process, delaying the start of my work by 2 months. When I finally started, it was a huge relief, but I didn’t know what will happen next. There is a certain sense of uncertainty around PhDs, and I was no different. However, my time at ICN2 went more smoothly than I would have imagined; most days it did not feel like I was doing a doctorate but rather just doing some random stuff my head cooked up, not a worry about getting results, just curiosity. All the credit goes to our supervisors, who has given this freedom and work environment, making the workplace feel like home.

Thank you Gustau, for not being just a supervisor but a teacher (and an enabler). It has been nothing short of a privilege working in your group and learning directly from the master. Any words I write here do not amount to the gratitude I have for this opportunity and these last four years that passed in a jiffy. I know it is not easy to supervise generally, and specially me who is very prone to just go on weird side quests. Thank you for the direction and the mentorship. I am hoping that we cross paths again in the academia and if I am lucky, maybe we can even collaborate.

My other supervisor, Santi, the person who made me interested in crystallography and structures and everything epitaxy. It is always refreshing to see you, you have truly showed that you can be an amazing scientist while also enjoying your life, this is such a valuable lesson that I hope I can learn follow as well. It is just amazing to work with you and even sit idly by your side when you do XRD because every moment is a learning moment with you.

My yet another supervisor, David, who I would describe more of as a mentor and trainer. I remember the day Santi introduced us, “this is David, a brilliant scientist”, and boy, do I know this now. I have really learned a lot from you, actually most of what I know comes from you, everything membranes (which is my whole thesis), all the small tricks experimentally and all the tiny details. If you don’t know, we have a little joke among the PhDs: if a manuscript goes through you, the referees will not have much to find faults in. While Gustau gave us ideas, you provided execution. Thank you for everything, from everyday training, discussions, guidance, advice, and helping me settle in the lab. Your discipline and knowledge inspire me.

Dr. Professor Roque, I will miss your voice echoing in the hallways, always making me smile. I am really thankful for all your help, always taking out time for even the smallest things that needed fixing, finding, attaching, breaking and doing all this while keeping the same contagiously enthusiastic demeanour. I can´t begin to tell you how much I have depended on you and how easy everything was because you were there as a safety net. I am very much in gratitude.

Kumara, thank you for teaching me everything about AFM etc. Although, I kind of don't like it (specifically putting the cantilever in the head), you made it interesting and always provided solutions. It is because of you that I have this much PFM in my thesis, otherwise I would have ran the other way. I am very thankful to you for always providing us with a friendly face and letting us take out our daily frustrations.

It was a pleasure meeting and working with you too Wen Xin, especially all things flexoelectric. It was a real treat seeing you work, especially on ICE, who does that? Your work ethics and discipline are really something. Thank you for teaching me some really basic and some really complex ideas as well as just the regular discussions, talks and random conversations.

Felip, you have taught me a lot about crystallography, specially TEM and electron diffraction. It is quite rare for people to be interested in "reciprocal space" as much as you are, and now I am too, thanks to you. I will forever be grateful.

Nona and Saptam, I could not have gone through the four years without you guys, especially all the bureaucratic processes and daily discussions among the "PhD students". The late nights at the synchrotrons are still a very fond memory of mine, maybe not for you Saptam, but what can you do? Science happens.

Also, thank you Liu Ying, my antiferroelectric knowledge started from you, my interest in TEM started from you, and I did my first PFM of antiferroelectrics with you as well.

Yingzhuo, I have learnt a lot from you, especially seeing you try different things with membranes, it was a great experience working with you. Thank you.

Thank you, Jessica for all the hundreds (yes, hundreds) of XRDs you have done for me and always trying to fit in my samples when I needed them urgently.

I have made many friends in the last four years, thank you Sohini, Mani and Marc for welcoming me in Barcelona and introducing me to this wonderful city. You too Kelly and Jesús. All of you have supported me and making these last years that much easier and enjoyable. I appreciate your friendship and all the good times we had. Hopefully, I will visit again soon, or you guys visit me, you are always welcome.

To all my friends back home: Sadan, Nabeel, Wardan, Hurair, Najam, Ahmed Khan, Maaz, Farhan, Ehsan, thank you for always supporting me and believing in me, I miss you guys, and I hope we see each other soon.

To my family: Ami, Abu, Uzair, Shaheer. I love you, I can´t even begin to start thanking you, there are not enough words or pages to contain my gratitude for always being there for me, helping me, raising me, making me better and believing in me.

Finally, my wife Sadeeda, my best friend, you have supported me throughout, have been my safety net, my go to person for anything and everything. Thank you for putting up with my stupidity, even in the dumbest moments of my life. I don’t have the words to describe the influence you had on my life. Thank you.

# Abstract

Antiferroelectric systems are stirring interest in the scientific community due to their potential in applications such as high energy density storage devices, electrocalorics, actuators, negative capacitance and neuromorphic devices. These applications are based on the alignment of antiparallel dipoles by an electric field to a parallel configuration, resulting in a reversible phase transition from an antiferroelectric to a ferroelectric state. Lead zirconate, the first discovered antiferroelectric, is considered to be an archetype that possesses excellent properties for these applications. Despite the extensive research on lead zirconate, its antiferroelectric nature has not been completely understood. This is mainly due to the complex phase coexistence and phase transition properties that it possesses. Moreover, the sensitivity of the system to strain and size perturbations also makes it difficult to tune its properties on demand. Although, thin film technology and epitaxial growth techniques have allowed us to control its properties more precisely by having crystalline, highly oriented films and study the material in more detail, this comes with the baggage of the mechanical clamping onto the growth substrate. This "clamping penalty" is especially important in lead zirconate, where the epitaxial clamping affects the switching behaviour via mechanical boundary conditions, and the phase transition via dislocations and strain fields. It is therefore important to understand the properties of thin film antiferroelectrics in the absence of such mechanical restraints while also having the same film quality and preferential orientations.

In this context, the development of methods to fabricate free standing membranes opens this avenue. Thin films can now be grown on single crystal substrates and, by buffer layer dissolution methods, can be declamped and studied in the absence of the substrate. Due to their flexibility, free-standing membranes or free sheets can also be subjected to different strain conditions to investigate how their properties evolve and understand the underlying physics for these properties. In this thesis, I focus on lead zirconate - $PbZrO_3$ (PZO) free-standing membranes to investigate their properties.

**Chapter 1** starts with an introduction to antiferroelectrics, specifically PZO. I discuss some literature on PZO and the different factors that lead to the properties of PZO. There are multiple competing instabilities such as those that code for polar vs antipolar and in-phase vs out-of-phase octahedral tilts and these instabilities are highly coupled, and changes in one can alter the other. The electric field induced transition to the ferroelectric phase also involves ferroelastic twinning. These couplings and competitions between instabilities render PZO very sensitive to external (or internal) perturbations. Therefore, PZO makes for a complex and interesting case to be studied in thin film form. However, epitaxial growth of PZO comes with mechanical clamping of the film to the substrate. In this context, fabrication of free-standing membranes presents a unique opportunity to separate clamping effects from size effects in such a highly sensitive system as PZO.

The most usual fabrication process of oxide membranes is by dissolution of a buffer layer with water. However, since many perovskites are sensitive to water, the properties of the materials might change. Moreover, the etching process results in formation of ions at the interface of the membrane in a very constricted region. Therefore, there is an additional risk of ion penetration that can change the chemistry of the membranes. In **Chapter 2**, I use lead zirconate and strontium titanate as case examples and find that both of them can get hydrogenated during the sacrificial layer etching process, suggesting a universality of the invasive hydrogenation of perovskite membranes. In our case, both materials display extrinsic (hydrogen-induced) polar phases. The hydrogenation process can be mitigated, however, by suitable annealing processes that result in chemically pure membranes that can then be compared to their epitaxial counterparts.

The switching of PZO from an antiferroelectric to a ferroelectric phase by an electric field induces a volume expansion, and therefore it can be sensitive to the mechanical boundary conditions. The objective of **Chapter 3** is to study how mechanical clamping effects switching behaviour. Our results show that, despite having similar initial strain states, membrane capacitors show faster switching dynamics than their epitaxial counterparts, due to easier accommodation of evolving strains during switching. Conversely, the mechanical clamping due to the substrate hinders the movement of domain walls and phase boundaries, increasing the viscosity within the system. Consequently, membrane capacitors show a higher efficiency for energy storage devices.

In **Chapter 4**, we turn our attention to thickness effects. In epitaxial films, it has been observed that, as the thickness of PZO decreases, it transitions from antiferroelectric to ferroelectric phase. However, this is not a sudden transition but rather a gradual one that involves many intermediate phases and mixing among them. In chapter 4, we investigate the thickness dependence of phases present in the PZO membranes. Although the thickness-induced phase transition has been previously attributed mainly to residual epitaxial strains, our membranes (in the absence of epitaxial clamping) also go through these phase transitions. Moreover, we observe a more complex phase mixing in membranes. Our results suggest that these phase transitions are not (only) caused by epitaxial strains, but rather there is a major contribution from surface effects such as surface tension. The emergence of phases in membranes not observed in epitaxial films is also credited to the inhomogenous strain effects on the suspended membranes that drive the system to other energy minima.

**Chapter 5** deals with the effect of strain. Epitaxially grown PZO films are usually relaxed on the substrates since there are not many lattice matching substrates or buffer layers. Therefore, a systematic study of strain effects on PZO epitaxial films is difficult. Making membranes of PZO allow us to strain them externally, made possible by their flexibility and ease of manipulation. I take advantage of this property of membranes to

study PZO under different strain conditions. The strain conditions range from, on one extreme quasi-homogenous uniaxial strain (induced via large-radius bending of thick membrane capacitors placed on cylindrically-shaped substrate**s**) to, at the other extreme, wrinkles on a single layer PZO where there are significant strain gradients. The results I present show that strains and strain gradients affect not only the energy of the possible phases, but also the energy barriers between them. While homogenously strained membranes exhibit antiferroelectric- type loops under both tensile and compressive strains, the wrinkles show some signs of poling, highlighting the role of flexoelectricity in phase transitions of PZO.

Finally, PZO has potential to be used in neuromorphic memory devices that utilize either the ability to modulate the polarization of PZO or the resistance of the PZO layer. In **Chapter 6**, I demonstrate that the surface polarization can be modulated in PZO by changing the frequency and total magnitude of voltage of the triangular pulses, which in this case is a volatile property. We also explore the resistive switching in PZO associated with the AFE to FE phase transition and use it to tune the dielectric loss (representative of impedance) of PZO capacitors by sub-switching pulses which turns out to be a non-volatile functionality. Furthermore, another characteristic of antiferroelectrics is the possibility of negative capacitance transistors which can be used to drastically reduce the power consumption of a device. I describe briefly the working principles of negative capacitance and some of the strategies I have employed to fabricate such devices. I conclude this chapter and the thesis with an outlook of how the properties and the strategies that have been investigated in this work can be combined to develop devices that exhibit multiple functionalities.

# Resumen

Los sistemas antiferroeléctricos están despertando interés en la comunidad científica debido a su potencial en aplicaciones como dispositivos de almacenamiento de alta densidad energética, electrocalóricos, actuadores, capacitancia negativa y dispositivos neuromórficos. Estas aplicaciones se basan en la alineación de dipolos antiparalelos mediante un campo eléctrico hacia una configuración paralela, lo que resulta en una transición de fase reversible de un estado antiferroeléctrico a un estado ferroeléctrico. El zirconato de plomo, el primer antiferroeléctrico descubierto, se considera un arquetipo que posee excelentes propiedades para estas aplicaciones. A pesar de la extensa investigación sobre el zirconato de plomo, su naturaleza antiferroeléctrica no ha sido completamente comprendida. Esto se debe principalmente a la compleja coexistencia de fases y a las propiedades de transición de fase que posee. Además, la sensibilidad del sistema a perturbaciones de tensión y tamaño también dificulta ajustar sus propiedades a demanda. Aunque la tecnología de películas delgadas y las técnicas de crecimiento epitaxial nos han permitido controlar sus propiedades con mayor precisión mediante películas cristalinas altamente orientadas y estudiar el material en más detalle, esto conlleva la desventaja del acoplamiento mecánico con el sustrato de crecimiento. Esta "penalización por acoplamiento" es especialmente relevante en el zirconato de plomo, donde la sujeción epitaxial afecta el proceso de alineación de dipolos a través de condiciones mecánicas en los límites y la transición de fase mediante dislocaciones y campos de tensión. Por lo tanto, es importante comprender las propiedades de los antiferroeléctricos en películas delgadas en ausencia de tales restricciones mecánicas, manteniendo la misma calidad de película y orientaciones preferenciales.

En este contexto, el desarrollo de métodos para fabricar membranas autoportantes abre nuevas posibilidades. Ahora se pueden crecer películas delgadas sobre sustratos monocristalinos y, mediante la disolución de capas intermedias, se pueden liberar y estudiar en ausencia del sustrato. Gracias a su flexibilidad, las membranas o láminas autoportantes también pueden someterse a diferentes condiciones de tensión para investigar cómo evolucionan sus propiedades y entender la física subyacente. En esta tesis, me concentro en membranas autoportantes de zirconato de plomo – $PbZrO_3$ (PZO) para investigar sus propiedades.

El **Capítulo 1** comienza con una introducción a los antiferroeléctricos, específicamente PZO. Discuto la literatura existente sobre PZO y los diferentes factores que determinan sus propiedades. Existen múltiples inestabilidades en competición, por ejemplo, entre configuraciones polares y antipolares, y entre giros octaédricos en fase y fuera de fase, y estas inestabilidades están fuertemente acopladas; cambios en una pueden alterar la otra. La transición inducida por el campo eléctrico a la fase ferroeléctrica también involucre dominios ferroelásticos. Estos acoplamientos y competencias entre inestabilidades hacen que PZO sea muy sensible a perturbaciones externas (o internas).

Por lo tanto, PZO constituye un caso complejo e interesante para estudiar en forma de película delgada. Sin embargo, el crecimiento epitaxial de PZO viene acompañado de sujeción mecánica de la película al sustrato. En este contexto, la fabricación de membranas autoportantes presenta una oportunidad única para separar los efectos de sujeción de los efectos de tamaño en un sistema tan sensible como PZO.

El proceso de fabricación más habitual de membranas de óxido es mediante la disolución de una capa intermedia con agua. Sin embargo, dado que muchas perovskitas son sensibles al agua, las propiedades del material podrían cambiar. Además, el proceso de disolución provoca la formación de iones en la intercara de la membrana en una región muy restringida. Por lo tanto, existe un riesgo adicional de penetración iónica que puede alterar la química de las membranas. En el **Capítulo 2**, utilizo el zirconato de plomo y el titanio de estroncio como ejemplos de estudio y encuentro que ambos pueden hidrogenarse durante el proceso de disolución de la capa sacrificial, sugiriendo una universalidad de la hidrogenación invasiva de membranas de perovskita. En nuestro caso, ambos materiales muestran fases polares extrínsecas (inducidas por hidrógeno). Sin embargo, el proceso de hidrogenación puede mitigarse mediante procesos de recocido adecuados, obteniendo membranas químicamente puras que luego pueden compararse con sus contrapartes epitaxiales.

La transición del PZO de una fase antiferroeléctrica a una ferroeléctrica mediante un campo eléctrico induce una expansión de volumen, por lo que puede ser sensible a las condiciones mecánicas de contorno. El objetivo del **Capítulo 3** es estudiar cómo la sujeción mecánica afecta el comportamiento de transición. Nuestros resultados muestran que, a pesar de tener estados de tensión iniciales similares, los capacitores de membrana presentan dinámicas de transición más rápidas que sus contrapartes epitaxiales, debido a la mayor facilidad de acomodar las tensiones que evolucionan durante la conmutación. Por el contrario, la sujeción mecánica por el sustrato dificulta el movimiento de las paredes de dominio y las fronteras de fase, aumentando la viscosidad del sistema. En consecuencia, los capacitores de membrana muestran una mayor eficiencia para dispositivos de almacenamiento de energía.

En el **Capítulo 4**, nos centramos en los efectos del grosor. En películas epitaxiales se ha observado que, al disminuir el grosor de PZO, éste pasa de fase antiferroeléctrica a ferroeléctrica. Sin embargo, esta no es una transición repentina, sino gradual, que involucra múltiples fases intermedias y mezclas entre ellas. En este capítulo investigamos la dependencia del grosor de las fases presentes en las membranas de PZO. Aunque la transición inducida por grosor se había atribuido principalmente a tensiones residuales epitaxiales, nuestras membranas (en ausencia de sujeción epitaxial) también experimentan estas transiciones de fase. Además, observamos una mezcla de fases más compleja en las membranas. Nuestros resultados sugieren que estas transiciones de fase no son (solo) causadas por tensiones epitaxiales, sino que

existe una contribución importante de efectos superficiales como la tensión superficial. La aparición de fases en membranas no observadas en películas epitaxiales también se atribuye a los efectos de tensión inhomogénea en las membranas suspendidas, que llevan al sistema a otros mínimos de energía.

El **Capítulo 5** trata sobre el efecto de la tensión mecánica. Las películas epitaxiales de PZO suelen relajarse sobre los sustratos debido a que no existen muchos sustratos o capas intermedias con parámetros de red compatibles. Por lo tanto, un estudio sistemático de los efectos de la tensión en películas epitaxiales de PZO es difícil. La fabricación de membranas de PZO permite aplicarles tensión externa gracias a su flexibilidad y facilidad de manipulación. Aprovecho esta propiedad de las membranas para estudiar PZO bajo diferentes condiciones de tensión mecánica. Las condiciones de tensión varían desde, en un extremo, una tensión uniaxial cuasi-homogénea (inducida mediante flexión de radio grande de capacitores de membrana gruesa colocados sobre sustratos cilíndricos) hasta, en el otro extremo, arrugas en una sola capa de PZO donde existen gradientes de tensión significativos. Los resultados muestran que las tensiones y los gradientes de tensión afectan no solo la energía de las posibles fases, sino también las barreras energéticas entre ellas. Mientras que las membranas homogéneamente tensadas presentan curvas de tipo antiferroeléctrico bajo tensiones tanto de tracción como de compresión, las arrugas muestran signos de polarización, destacando el papel de la flexoelectricidad en las transiciones de fase de PZO.

Finalmente, el PZO tiene potencial para ser utilizado en dispositivos de memoria neuromórfica que aprovechen tanto la capacidad de modular la polarización del PZO como su resistencia. En el **Capítulo 6**, demuestro que la polarización superficial puede modularse en PZO cambiando la frecuencia y la magnitud total del voltaje de los pulsos triangulares, lo cual, en este caso, es una propiedad volátil. También exploramos la resistencia variable en PZO asociada con la transición de fase AFE a FE y la utilizamos para ajustar la pérdida dieléctrica (representativa de la impedancia) de los capacitores de PZO mediante pulsos que no llegan a inducir transición, lo que resulta en una funcionalidad no volátil. Además, otra característica de los antiferroeléctricos es la posibilidad de crear transistores de capacitancia negativa, que pueden utilizarse para reducir drásticamente el consumo de energía de un dispositivo. Describo brevemente los principios de funcionamiento de la capacitancia negativa y algunas de las estrategias que he empleado para fabricar dichos dispositivos. Concluyo este capítulo y la tesis con una perspectiva de cómo las propiedades y estrategias investigadas en este trabajo pueden combinarse para desarrollar dispositivos que exhiban múltiples funcionalidades.

# Resum

Els sistemes antiferroelectrics estan despertant interès en la comunitat científica a causa del seu potencial en aplicacions com ara dispositius d'emmagatzematge d'alta densitat energètica, electrocalòrics, actuadors, capacitança negativa i dispositius neuromòrfics. Aquestes aplicacions es basen en l'alineació de dipols antiparal·lels mitjançant un camp elèctric cap a una configuració paral·lela, resultant en una transició de fase reversible d'un estat antiferroelectric a un estat ferroelèctric. El zirconat de plom, el primer antiferroelectric descobert, es considera un arquetip que posseeix excel·lents propietats per a aquestes aplicacions. Malgrat la extensa recerca sobre el zirconat de plom, la seva naturalesa antiferroelectrica no s'ha entès completament. Això es deu principalment a la complexa coexistència de fases i a les propietats de transició de fase que posseeix. A més, la sensibilitat del sistema a les perturbacions de tensió i de mida també fa difícil ajustar les seves propietats a demanda. Encara que la tecnologia de pel·lícules fines i les tècniques de creixement epitaxial ens han permès controlar les seves propietats amb més precisió mitjançant pel·lícules cristal·lines altament orientades i estudiar el material amb més detall, això ve acompanyat de la limitació del "penal de subjecció mecànica" sobre el substrat de creixement. Aquesta penalització és especialment rellevant en el zirconat de plom, on la subjecció epitaxial afecta el comportament de commutació a través de les condicions mecàniques als límits i la transició de fase mitjançant dislocacions i camps de tensió. Per tant, és important comprendre les propietats dels antiferroelectrics en pel·lícules fines en absència d'aquestes restriccions mecàniques, mantenint la mateixa qualitat de pel·lícula i orientacions preferents.

En aquest context, el desenvolupament de mètodes per fabricar membranes autoportants obre noves possibilitats. Ara es poden créixer pel·lícules fines sobre substrats monocristal·lins i, mitjançant la dissolució de capes intermedies, es poden alliberar i estudiar sense el substrat. Gràcies a la seva flexibilitat, les membranes o làmines autoportants també es poden sotmetre a diferents condicions de tensió per investigar com evolucionen les seves propietats i entendre la física subjacent. En aquesta tesi, em concentro en membranes autoportants de zirconat de plom – $PbZrO_3$ (PZO) per investigar les seves propietats.

El **Capítol 1** comença amb una introducció als antiferroelectrics, específicament PZO. Discuteixo la literatura existent sobre PZO i els diferents factors que determinen les seves propietats. Hi ha múltiples inestabilitats en competència, com ara les que codifiquen polar vs antipolar i inclinacions octaèdriques en fase vs fora de fase, i aquestes inestabilitats estan fortament acoblades; canvis en una poden alterar l'altra. La transició induïda per camp elèctric a la fase ferroelèctrica també implica bessons ferroelàstics. Aquests acoblaments i competències entre inestabilitats fan que PZO sigui molt sensible a perturbacions externes (o internes). Per tant, PZO constitueix un cas complex i interessant per estudiar en forma de pel·lícula fina. Tanmateix, el

creixement epitaxial de PZO ve acompanyat de subjecció mecànica de la pel·lícula al substrat. En aquest context, la fabricació de membranes autoportants presenta una oportunitat única per separar els efectes de subjecció dels efectes de mida en un sistema tan sensible com PZO.

El procés de fabricació més habitual de membranes d'òxid autoportants és mitjançant la dissolució d'una capa intermedia amb aigua. No obstant això, donat que molts perovskites són sensibles a l'aigua, les propietats del material podrien canviar. A més, el procés de gravat provoca la formació d'ions a la interfície de la membrana en una regió molt restringida. Per tant, hi ha un risc addicional de penetració iònica que pot alterar la química de les membranes. Al **Capítol 2**, utilitzo el zirconat de plom i el titanat d'estronci com a exemples d'estudi i trobo que ambdós poden hidrogenar-se durant el procés de gravat de la capa sacrificial, suggerint una universalitat de la hidrogenació invasiva de membranes de perovskita autoportants. En el nostre cas, ambdós materials mostren fases polars extrínseques (induïdes per hidrogen). No obstant això, el procés d'hidrogenació es pot mitigar mitjançant processos de recuit adequats, obtenint membranes químicament pures autoportants que després poden comparar-se amb les seves contrapartides epitaxials.

La commutació de PZO d'una fase antiferroelectrica a ferroelèctrica mitjançant un camp elèctric indueix una expansió de volum, per la qual cosa pot ser sensible a les condicions mecàniques als límits. L'objectiu del **Capítol 3** és estudiar com la subjecció mecànica afecta el comportament de commutació. Els nostres resultats mostren que, malgrat tenir estats de tensió inicials similars, els capacitors de membrana autoportant presenten dinàmiques de commutació més ràpides que les seves contrapartides epitaxials, degut a la major facilitat d'acomodar les tensions que evolucionen durant la commutació. Per contra, la subjecció mecànica pel substrat dificulta el moviment de les parets de domini i de les fronteres de fase, augmentant la viscositat del sistema. En conseqüència, els capacitors de membrana autoportant mostren una major eficiència per a dispositius d'emmagatzematge d'energia.

Al **Capítol 4**, ens centrem en els efectes del gruix. A les pel·lícules epitaxials s'ha observat que, a mesura que disminueix el gruix de PZO, aquest passa de fase antiferroelectrica a ferroelèctrica. No obstant això, aquesta no és una transició brusca, sinó gradual, que implica múltiples fases intermèdies i mescles entre elles. En aquest capítol investiguem la dependència del gruix de les fases presents a les membranes autoportants de PZO. Tot i que la transició induïda pel gruix s'havia atribuït principalment a tensions residuals epitaxials, les nostres membranes autoportants (en absència de subjecció epitaxial) també experimenten aquestes transicions de fase. A més, observem una mescla de fases més complexa a les membranes. Els nostres resultats suggereixen que aquestes transicions de fase no són (només) causades per tensions epitaxials, sinó que hi ha una contribució important dels efectes superficials com la tensió superficial. L'aparició de fases a les membranes autoportants no

observades a les pel·lícules epitaxials també s'atribueix als efectes de tensió inhomogènia a les membranes suspeses, que porten el sistema a altres mínims d'energia.

El **Capítol 5** tracta sobre l'efecte de la tensió. Les pel·lícules epitaxials de PZO solen relaxar-se sobre els substrats degut a que no existeixen molts substrats o capes intermedies amb coincidència de cel·la. Per tant, un estudi sistemàtic dels efectes de tensió a pel·lícules epitaxials de PZO és difícil. La fabricació de membranes autoportants de PZO permet aplicar tensió externa gràcies a la seva flexibilitat i facilitat de manipulació. Aprofito aquesta propietat de les membranes autoportants per estudiar PZO sota diferents condicions de tensió. Les condicions de tensió varien des, en un extrem, d'una tensió uniaxial quasi-homogènia (induint-se mitjançant la flexió de radi gran de capacitors de membrana autoportant gruixuda col·locats sobre substrats cilíndrics) fins, en l'altre extrem, arrugues en una sola capa de PZO on existeixen gradients de tensió significatius. Els resultats mostren que les tensions i els gradients de tensió afecten no només l'energia de les possibles fases, sinó també les barreres energètiques entre elles. Mentre que les membranes autoportants homogèniament tensionades presenten corbes de tipus antiferroelectric sota tensions tant de tracció com de compressió, les arrugues mostren signes de polarització, destacant el paper de la flexoelectricitat en les transicions de fase de PZO.

Finalment, PZO té potencial per ser utilitzat en dispositius de memòria neuromòrfica que aprofitin tant la capacitat de modular la polarització de PZO com la resistència de la capa de PZO. Al **Capítol 6**, demostro que la polarització superficial es pot modular a PZO canviant la freqüència i la magnitud total del voltatge dels polsos triangulars, la qual cosa, en aquest cas, és una propietat volàtil. També explorem la commutació resistiva a PZO associada amb la transició de fase AFE a FE i la utilitzem per ajustar la pèrdua dielèctrica (representativa de la impedància) dels capacitors de membrana autoportant mitjançant polsos sub-comutants, resultant en una funcionalitat no volàtil. A més, una altra característica dels antiferroelectrics és la possibilitat de transistors de capacitança negativa, que poden utilitzar-se per reduir dràsticament el consum d'energia d'un dispositiu. Descric breument els principis de funcionament de la capacitança negativa i algunes de les estratègies que he empleat per fabricar aquests dispositius. Concloc aquest capítol i la tesi amb una perspectiva de com les propietats i estratègies investigades en aquest treball es poden combinar per desenvolupar dispositius que exhibeixin múltiples funcionalitats.

# Table of Contents

# List of Figures

# List of Tables

Chapter 1

# Introduction

## 1.1. Antiferroelectrics

Antiferroelectric systems were a theoretical concept proposed by Kittel in the early 1950s built upon the idea of a correspondence of ferroelectricity (FE) to ferromagnetism, i.e. ferromagnetism and ferroelectricity exist, therefore if antiferromagnetism exists, so should antiferroelectricity (AFE).[1] Analogous to antiferromagnets, antiferroelectrics have an anti-parallel arrangement of dipoles. Unlike antiferromagnets,[a] though, in antiferroelectrics, the antiparallel arrangement of dipoles can be aligned to a parallel one under an electric field, effectively resulting in a field-induced ferroelectric-like state.[b] The first double polarization- electric field hysteresis loop was reported shortly after by Shirane in lead zirconate ($PbZrO_3$_PZO)[2] that has since been regarded as an architype antiferroelectric. Several other materials have been discovered and researched since that show antiferroelectricity, such as $PbHfO_3$, $AgNbO_3$ and $NaNbO_3$[c].[3] However, the research on antiferroelectrics has developed slowly compared to their polar counterparts, ferroelectrics. The reasons were mostly their antipolar nature, and therefore zero macroscopic polarization with concomitant lack of piezoelectricity or memory, and the complexity of the materials (which tend to show competing instabilities, phase coexistence and disorder, as well as high critical fields).[1,4] In spite of all this, antiferroelectrics still have properties (specifically, the ability to abruptly jump in polarization at a critical field) that make them highly useful for some applications such as electrostatic energy storage or electrocaloric cooling, and promising for other even more adventurous concepts such as neuromorphic memories or negative capacitance transistors.

It is, therefore, crucial to understand and tune the properties of antiferroelectrics so they can be best utilized in such applications. One of the key constraints imposed on the use of antiferroelectric thin films for such applications is CMOS compatibility due to the high temperature processing of such materials. In this context, we study free-standing membranes of archetype antiferroelectric PZO, whereby the PZO thin film is detached form the growth substrate and transferred to other substrates (including silicon). The declamping from the initial epitaxial state allows us to investigate the

[a] The switching from an antiferromagnet to ferromagnet requires a very large magnetic field to overcome the exchange interaction between the antiparallel moments and therefore, practically not feasible.

[b] The field induced parallel alignment of dipoles in nominally antiferroelectric materials switch back to an antiparallel configuration upon removal of field, which is in principle, different to a nominally ferroelectric material that has a stable remnant polarization at zero field. However, the field induced phase in AFEs is termed as a ferroelectric phase since this phase is crystallographically indistinguishable from a nominally ferroelectric material. From here on, I call this phase ferroelectric phase in accordance with the convention used in literature.

[c] $NaNbO_3$ is only antiferroelectric in its pristine state. The AFE to FE transition in pure $NaNbO_3$ is irreversible and does not result in a double hysteresis. Therefore, either application of strain or doping is required to obtain clean double hysteresis loops.

effect of external perturbations and dimensionality and separate them out from the effect of epitaxial strain.

## 1.2. Lead Zirconate $PbZrO_3$ (PZO)

The structure of PZO was studied by Hoffman in 1935,[5] even before the discovery of antiferroelectricity. He observed superstructures which he thought originated from a triple lattice. This was followed by works from Megaw[6] and Roberts[7] that assigned tetragonal symmetry to PZO. Later, Shirane observed a double hysteresis loop in PZO confirming the antipolar dipole arrangement.[2] The symmetry of PZO was determined to be orthorhombic by Shirane and Sawaguchi[8] with lattice parameters : a = 5.87 Å, b = 11.74 Å and c = 8.20 Å at room temperature, resulting in a ground state of Pbam space group. The unit cell of this structure relates to the parent cubic cell as $a_O = \sqrt{2}\, a_{PC}$, $b_O = 2\sqrt{2}\, a_{PC}$ and $c = 2\, a_{PC}$ with $a_{PC} \,||| [120]_O$ and $c_{pc} \,||| [001]_O$, where $a_{PC}$ and $b_{PC}$ are symmetrically equivalent (PC stands for pseudocubic).

This Pbam antiferroelectric phase is characterized by ↑↑↓↓ modulation of Pb atoms with the direction of antipolar displacement being $<100>_O \,||\, <110>_{PC}$ and an antiferrodistortive order (oxygen octahedral tilts) of $a^-a^-c^0$ in Glazer´s notations.[9] The crystal structure of the PZO Pbam phase is shown in **Figure 1.1a-b**.

As we heat the system, PZO undergoes a phase transition from the AFE phase to the cubic paraelectric phase at 503K.[8] However, upon cooling, it first undergoes a transition to a rhombohedral (R3c) ferroelectric phase and then finally to the AFE one.[10–12] The temperature range at which this ferroelectric phase is present is very small (5 – 10 K). The ferroelectric phase has parallel dipoles in $<111>_{PC}$ directions with $a^-a^-a^-$ tilts, crystal structure shown in **Figure 1.1c**.[13] The presence of this phase suggests that the energy associated with the AFE (Pbam) and FE (R3c) phases are very similar.[10]

Due to the similar energies of the AFE and FE phases, an electric field can be applied causing PZO to undergo an AFE to FE transition. The field-induced ferroelectric phase adopts the R3c structure,[2,14] which reverts to the AFE one on the removal of field, giving rise to the characteristic double hysteresis loop. This phase transition is also accompanied by an increase in the volume of the unit cell (**Figure 1.1d**). Experimentally, it has been reported since very early on that there is some remnant polarization (an opening in the pinched loop)[15] as well as triple (or even more) loops during the electric field cycling. This has been attributed to the coexistence of FE phase (or a slow relaxing FE phase).[16]

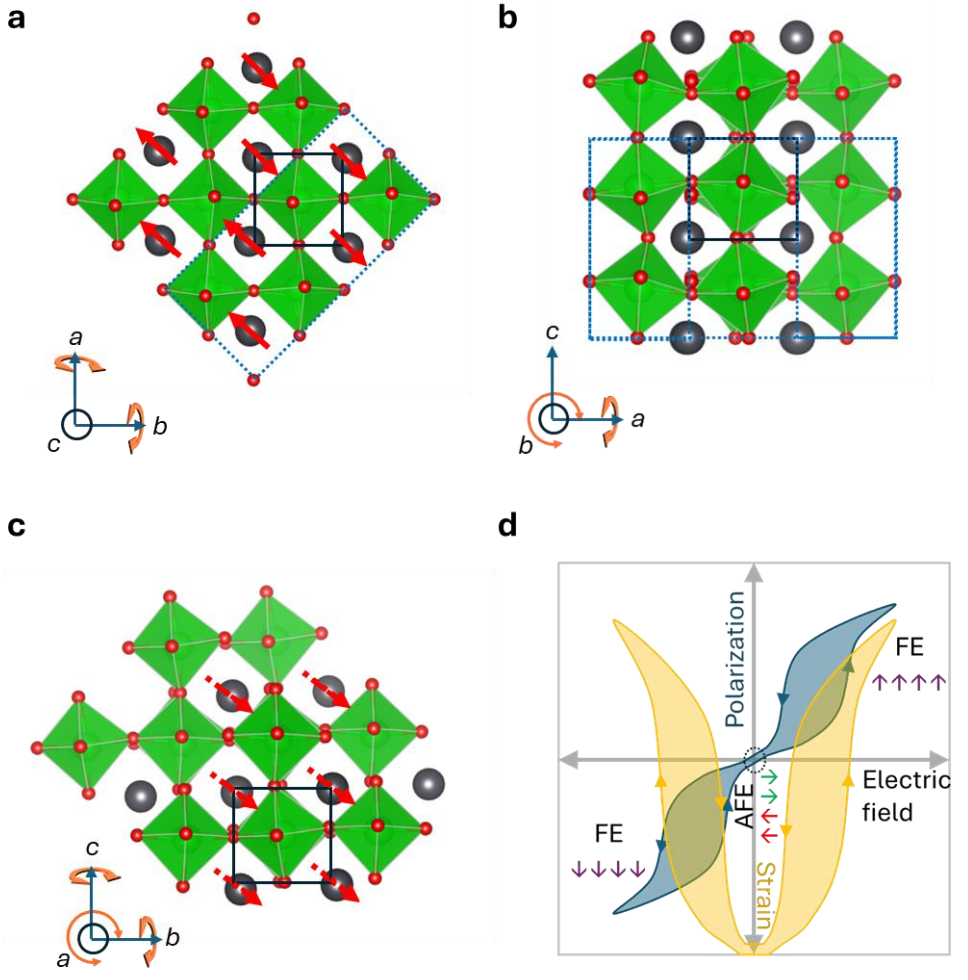


***Figure 1.1.*** *Crystal structure of Pbam phase of PZO from* ***(a)*** $c_{PC}$ *zone axis showing the two up two down modulation, the blue dotted rectangles show the orthorhombic unit cell, solid black squares represent the pseudocubic unit cell, double sided orange arrows in the compass show axis of rotations of octahedral tilts,* ***(b)*** $a_{PC}$/ $b_{PC}$ *zone axis,* ***(c)*** *Crystal structure of ferroelectric R3c phase of PZO, dotted red arrows show displacement with an out-of-plane component, black atoms represent Pb, red represent oxygen, green represent Zr (that are hidden inside the octahedra)* ***(d)*** *Schematic of Polarization and Strain as a function of electric field representing the double hysteresis loop.*

### 1.2.1. PZO, why is it Antiferroelectric (and is it)?

So far, I have described a very simple picture of PZO that has been extensively verified experimentally. However, there are many open questions that go along the lines of (i) why PZO adopts its antiferroelectric nature (how the structural instabilities contribute and so on) and (ii) what the actual ground state of this material is –including the question of whether its true ground state is really antiferroelectric. The theoretical modelling and calculations that are used to answer these questions point towards a very

complex energy landscape and are not in agreement about all the details. In any case, I will summarize some important findings relating to different factors that contribute to the antiferroelectric and antiferrodistortive nature.

### *1.2.1.1. Goldschmidt tolerance factor (t):*

The Goldschmidt tolerance factor is a geometric estimation of the stability of a perovskite lattice to form a cubic structure or conversely, the expected lattice distortion. It is based on the ionic radii, hence bond lengths and can be calculated as:

$$t = \frac{R_A + R_O}{\sqrt{2}(R_B + R_O)} \qquad (1.1)$$

Where $R_A$, $R_B$ and $R_O$ are radius of A, B and O atoms respectively in the perovskite $ABO_3$ structure.

For t =1, the structure can accommodate all the ions without any distortion and results in an ideal cubic structure. For t >1, the oxygen octahedral expands resulting in a tetragonal like distortion, whereas for t <1, the lattice is too small to accommodate the oxygen octahedrals, resulting in a tilt in the octahedrals. In case of PZO, the tolerance factor equals 0.96 causing antiferrodistortive tilts. In PZO, these are in anti-phase in two pseudocubic directions and zero in third, or $a^-a^-c^0$ tilt pattern (Glazer´s notation). Moreover, this distortion is accompanied by antipolar displacements of lead atoms in $[110]_{PC} \parallel [100]_O$ directions. This antipolar Pb displacement is not explained by the factor, since there are many perovskites that have octahaderal tilts but are not antiferroelectric or ferroelectric. The tolerance factor, therefore, tells us about a lattice distortion expected based on geometry;[17] however, there are other factors such as stabilizing forces and atomic coordination that also contribute to the final structure of the compound.[18] In this scenario, one must go to the material specific case to understand the structural instabilities that are present in PZO.

### *1.2.1.2. Phonon modes:*

Phonon modes and their instabilities can provide valuable insights into why PZO adopts the specific tilt of $a^-a^-c^0$ as well as the antiferroelectric order. Numerous first-principle studies and experiments on the phonon modes of PZO show that, in its cubic structure, it has multiple instabilities[19–25] as shown in **Figure 1.2a**. These instabilities are:

I. Ferroelectric mode (Γ) with wave vector $q_\Gamma = 2\pi/a$ (0, 0, 0)
II. Antipolar mode (Σ) with wave vector $q_\Sigma = 2\pi/a$ (¼, ¼, 0)
III. Antiferrodistortive (AFD) mode:

i. Anti-phase oxygen octahedral tilts (R) with wave vector $q_R = 2\pi/a$ (½ , ½ , ½).
ii. In-phase oxygen octahedral tilts (M) with wave vector $q_M = 2\pi/a$ (½ , ½ , 0).

All these instabilities are dominated by either the A-type (Pb) or O atoms contributions.[22] However, the two main instabilities are the antipolar mode (Σ) and the anti-phase tilt mode (R), that allow the condensation of this Pbam structure.

Whereas some other theoretical works suggest that the phonon mode that drives the transition is actually the ferroelectric instability (Γ) but later is suppressed by the anti-polar one (Σ),[21] which is consistent with the emergence of rhombohedral R3c phase upon cooling. Another remarkable feature of the band is its flatness between the M and R points, signifying that the energy gain for the system to move between these points in minimal. In fact, the flatness of this phonon band may allow for the incommensuration to exist in PZO,[26] specifically stabilized under stress.[27]

Due to the complex land scape of the instabilities, the energies of different phases are very close to each other[19] (**Figure 1.2b**) and hence, PZO can exist in different polymorphs. There are many local energy minima that correspond to different phases and some of these phases are even predicted to be the true ground state of PZO. One such predicted ground state is the Ima2 phase with ↓↓↑ Pb displacement pattern (ferrielectric phase: FiE).[28] Furthermore, due to an additional instability in the Pbam phase of PZO at the Z point of the reciprocal space, a structure that includes a complex Pb displacement pattern and super tilting of oxygen octahedrals with space group Pnam (antiferroelectric in nature) is also predicted to be the lowest energy phase.[26]

Finally, other than the instabilities, flexoelectric coupling has also been attributed to the stabilization of the antiferroelectric phase in PZO that does not allow an incommensurate phase to condense.[21] Contrarily, experimental evidence suggests that the flexocoupling (ratio of flexoelectric coefficient to the permittivity) in antiferroelectric PZO is similar to other dielectric perovskites such as $SrTiO_3$ (STO) making it unlikely to be the sole cause of this transition. At the Curie temperature, however, the flexocoupling of PZO shows an intense peak, making it non-trivial, nonetheless.[29]

Despite conflicting reports, one thing is clear: there are strong structural instabilities that are highly coupled. Any extrinsic (or intrinsic) stimulus affecting one instability would influence the others, tipping the balance in favour of another phase. Crucially, these phases are non-trivial, and they have different polarization vectors; hence, the functional properties can be tuned. To this end, it is necessary to understand how different conditions can affect this energy landscape.

This brings us to the elaboration of thin films. Advances in epitaxial growth techniques have allowed us to precisely control crystal orientation, film thickness (down to the monolayer level), and strain via substrate choice. These methods have been successfully applied to PZO, enabling the fabrication of high-quality single-crystal films and the exploration of novel phase behaviour and functionality under engineered boundary conditions. The behaviour of these epitaxial films, particularly in relation to strain and orientation, will be discussed later in the thesis. However, while epitaxial films offer significant control, the same epitaxy that favours the growth of well-oriented films also imposes mechanical clamping that can constrain or mask the intrinsic behaviour of PZO. To study the material in an unconstrained state, one promising approach is to remove the substrate altogether, while also maintaining the initial film qualities that are imparted by the epitaxial growth. From this perspective, the fabrication of free-standing membranes has opened a new horizon.

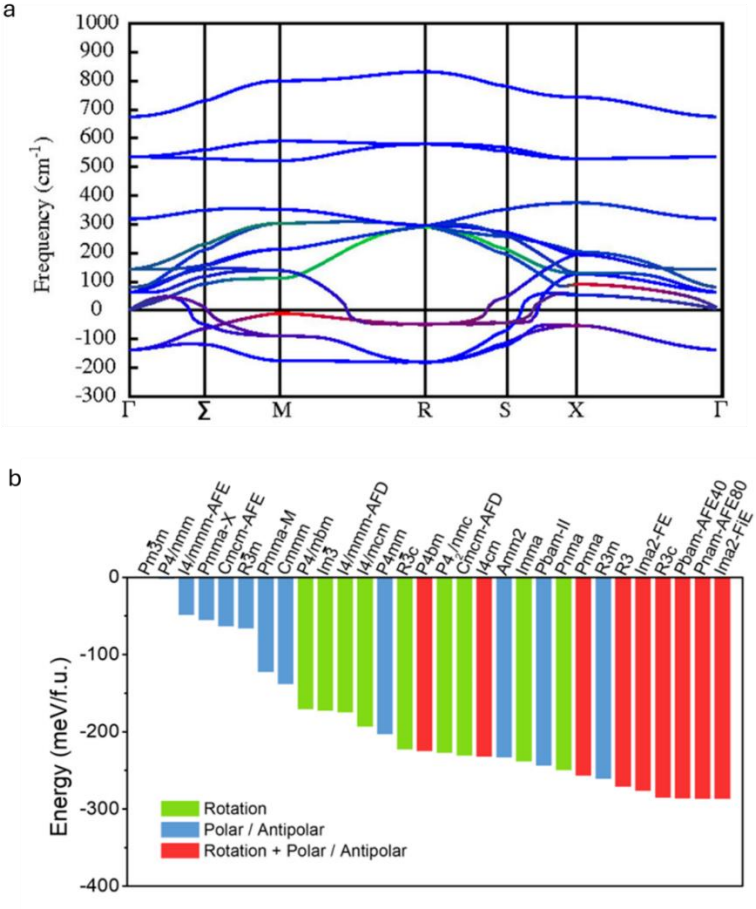


***Figure 1.2.*** ***(a)*** *Phonon dispersion curves of PZO in its cubic phase showing multiple instabilities (reproduced with permission from Springer Nature (ref. 25)),* ***(b)*** *Energy of different phases in PZO with respect to the parent cubic phase, where AFE: Antiferroelectric, FE: Ferroelectric, FiE: Ferrielectric and AFD: Antiferrodistortive (Reprinted figure with permission from H. Zhang, H.-C. Thong, L. Bastogne, C. Gui, X. He, and P. Ghosez, Phys. Rev. B 110, 054109 (2024) (ref 19)).*

## 1.3. Sacrificial layers to fabricate free-standing membranes

The possibility of declamping thin films from their growth substrates presents an exciting opportunity to study not only the intrinsic properties of materials in the low-dimensional regime, free from epitaxial strain, but also to subject these layers to extrinsic stimuli and modulate their functionalities. Several strategies have been developed to achieve this, including stress-mediated delamination (or spalling),[30] mechanical exfoliation enabled by remote epitaxy,[31–33] and more recently, the wet etching of sacrificial buffer layers.[34,35] This sacrificial layer method has taken over the field of membranes due to the relatively simple process and ease of implementation.

The choice of buffer layer is limited by several factors, particularly for epitaxial growth, where the functional films must be highly crystalline and exhibit specific crystal orientations. Consequently, the buffer layers themselves must also be coherently grown on the substrate with high crystalline quality, while remaining amenable to selective etching for film release.

Within the perovskite family, several materials exhibit these necessary traits. Some common examples include $La_xSr_{1-x}MnO_3$ (LSMO)[36] and $SrRuO_3$.[37] However, etching these materials typically requires aggressive chemical treatments, such as hydrochloric acid for LSMO, which can potentially damage the functional films. The introduction of $Sr_3Al_2O_6$ (SAO)[35] marked a significant advancement, as it can be coherently grown on most perovskite oxide substrates and easily etched using water. Since then, related materials (formed by replacing Sr with either Ca or Ba)[38] have also emerged as promising candidates for use as water-soluble sacrificial layers.

### 1.3.1. Fabrication of free-standing membranes

#### *1.3.1.1. $(Ca, Sr, Ba)_3Al_2O_6$ (CSB-AO)*

The fabrication of free-standing membranes or free sheets using SAO was first implemented by the group of Prof. Hwang.[35] They demonstrated that free-standing membranes of STO can be made by using SAO as buffer layers, and that these membranes can retain their crystalline quality even after being declamped and transferred to other substrates. This breakthrough opened new possibilities for investigating oxide perovskites under various conditions. Since then, membranes of other functional oxides such as ferroelectric and multiferroics have been fabricated and studied extensively.

CSB-AO materials have a very large lattice parameter, but their higher order interplanar distances closely match the commonly used perovskite substrates, e.g. interplanar distance of SAO (004) is 3.96 Å,[35] closely matching $SrTiO_3$ (001) (STO), with a lattice parameter of 3.905 Å, and $GdScO_3$ $(001)_{PC}$ (GSO)_ lattice parameter of 3.96 Å. The lattice parameters of the soluble layer can also be tuned by having different ratios of Ca, Sr or Ba between 3.85 Å at the lowest extreme for CAO[39] and 4.13 Å for

BAO[40] at the other. Moreover, this compositional tuning can also be used to control their solubilities and etching rates.[38] The enhanced solubility of these materials arises from their open crystal structures; rather than forming a continuous Al–O framework, they contain $Al_6O_{18}^{18-}$ rings,[35] which readily hydrolyse in water, enabling efficient dissolution (crystal structure of SAO is shown in **Figure 1.3a-b**).

*1.3.1.2. Transfer of declamped thin films to secondary substrates*

The fabrication of free-standing membranes typically begins with the epitaxial growth of a sacrificial layer, followed by deposition of the functional layer. From this heterostructure, several methods can be employed to retrieve and transfer the functional film onto a secondary substrate. The most common method, also used in this work, involves attaching the heterostructure to a support polymer and immersing the assembly in water.[34,35] As the sacrificial layer dissolves, the functional film remains adhered to the polymer, allowing the original substrate to be removed. The polymer–membrane stack is then brought into contact with a preheated secondary substrate, after which the polymer is carefully peeled away, leaving the membrane transferred (**Figure 1.3c**). Another widely used approach is the scooping (or "fishing") method,[41] where the heterostructure is immersed in water and, once the sacrificial layer is etched, the released membrane floats to the surface. A secondary substrate is then used to scoop the membrane out of the water as shown in **Figure 1.3d**.

Owing to the development of reliable methods for growing and transferring high-quality membranes, research has increasingly focused on uncovering the fundamental properties of materials free from epitaxial constraints, as well as on leveraging this newfound freedom to enable innovative applications. Ferroelectric and antiferroelectric materials are well-suited to this approach, as their functional properties such as their switchable polarization and field-induced phase transitions are sensitive to strain and thus, conversely, also to strain release.

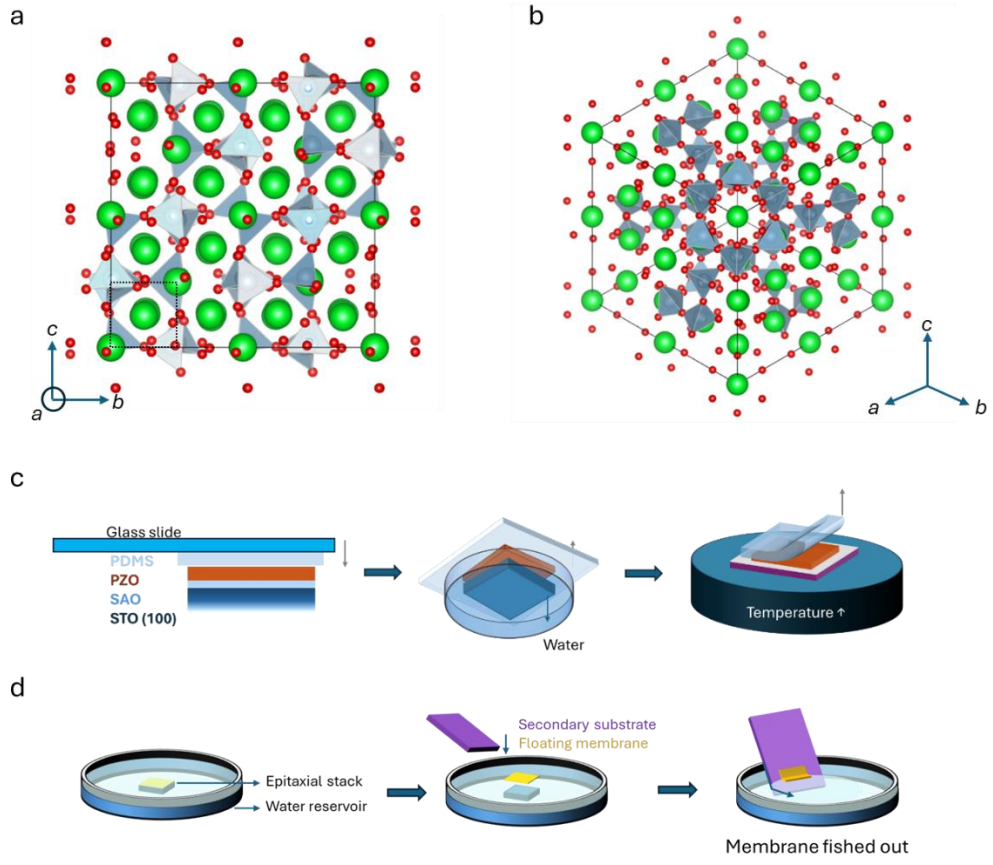


***Figure 1.3***. *Crystal structure of $Sr_3Al_2O_6$ projected along* ***(a)*** *[100] direction,* ***(b)*** *[111] direction, where green atoms are Sr, grey are Al and red represent O atoms, the small square box in (a) marks quarter of the unit cell of SAO that matches one unit cell of STO (001) substrate; transfer process of membranes using* ***(c)*** *support polymer PDMS (PZO as an example),* ***(d)*** *fishing method.*

## 1.3.2. Ferroelectric and antiferroelectric membranes

Ferroelectric and antiferroelectrics materials are essential for wide range of applications, for example energy storage,[42] memory devices[43,44] and tunnel junctions.[45] However, their integration on CMOS technology was limited by their high growth temperatures, or if the temperature was lowered, their poor crystalline quality. The advent of membrane fabrication and transferring techniques offer a solution in this context: they can be grown on lattice-matched substrates at high temperatures to ensure their crystallinity and subsequently transferred to relevant substrates. It is, therefore, important to understand their properties in free-standing form. Many works have been done in this context, and it has been found that the free-standing membranes may have some advantages over their epitaxial counterparts in some respects. Ferroelectric capacitors made from epitaxial heterostructures, for example, exhibit faster switching dynamics when released from the growth substrate.[36] Moreover, free-standing

membranes can be subjected to different strain conditions by various methods. One such example is the application of uniaxial strain on STO membranes to induce ferroelectricity.[46] Another degree of freedom comes from tuning electrode lattice parameter and thickness, allowing the tuning of curie temperature and saturation polarization,[36] or self-rolling of multi-layered membranes due to differential strains.[47] These straining strategies can be taken to extreme cases by having wrinkles on the membranes, to study effects of varying strains and strain gradients to tune domain structures in ferroelectrics.[36,48–50]

Other than the fundamental studies of membrane properties, membranes have been demonstrated to be highly suitable for applications, such as photostrictive actuation of $BaTiO_3$ membranes that exceeds the actuation produced in clamped ferroelectric films.[51] Recently, the field of "twistronics" [52] is also gaining traction where we can stack multiple layers of perovskite oxides on top of each other with some twist angles, similar to what researchers have been doing in 2D materials, and some very exotic phenomena have been observed such as "apparent polarization" in ideally non-polar, conducting oxides,[53] polar vortices in ferroelectric[54] and paraelectric materials[55] or theoretically, change in the electronic band structure.[56]

At the time of starting my project, there were no studies of antiferroelectric membranes. Even now, antiferroelectric membranes have not been explored nearly as much as the ferroelectric systems, and the few studies that exist point to the impact of both thickness and strain effects on the delicate balance between antiferroelectricity and ferroelectricity, resulting in phase coexistence and even full phase transition from AFE to FE depending on the membrane characteristics.

The goal of this thesis is to address this gap by investigating free standing membranes of antiferroelectrics under different extrinsic conditions. For this purpose, PZO is an ideal case study to understand how the declamping affects its intrinsic properties due to the richness of its phase diagram and the interdependency of its competing instabilities. Here, we will investigate the effects of declamping of PZO films in terms of their switching dynamics, the dimensionality induced phase coexistence and transitions, and the influence of different strain conditions on the intrinsic and functional behaviour of the membranes. Finally, we will explore functional device concepts and how the distinct functional features of PZO can be integrated into them.

Chapter 2

# Fabrication of chemically pure free-standing membranes: hidden hydrogenation due to sacrificial layer etching

## 2.1. Introduction

I briefly discussed earlier the growing interest on membranes and the properties they exhibit. These membranes offer new and novel ways to tune the properties of perovskites over the epitaxial films and study intrinsic effects in the absence of clamping. While the benefits of removing the mechanical boundary conditions from the thin films are becoming known, one thing that has not been investigated as thoroughly is the chemical consequences of the fabrication process of the membranes, specifically their exposure to water in the etching step.

Many materials are known to be very susceptible to hydrogen and water penetration that can result in the degradation or change of their required properties.[57] Ferroelectric perovskite oxides such as $BaTiO_3$ can form oxyhydrites[58–60] when hydrogen occupies the oxygen vacancies, completely killing the ferroelectricity. Similar theoretical works have also been done on $PbZr_xTi_{1-x}O_3$ that predict loss of ferroelectric polarization in the presence of hydrogen[61] and an increase in the leakage current.[62] $SrRuO_3$, which is a ferromagnetic metal at low temperatures, undergo an orthorhombic to tetragonal phase transition due to hydrogenation and shows a reversal of the sign of Anomalous Hall effect.[63] Many perovskites such as $SrCoO_{2.5}$,[64,65] $NdNiO_3$[66] and $CaRuO_3$[67] consistently show an increase in their lattice volume once the hydrogen is incorporated into their crystal structure. In these cases, the hydrogen was deliberately introduced in the materials using different techniques such as electrical bias and annealing in hydrogen rich environments. However, to the best of my knowledge, there are no studies on the effect of protonation in membranes. These studies are relevant because, during their fabrication sacrificial layers dissolve due to the hydrolysis of the $Al_6O_{18}^{18-}$ rings, and during this etching process, there is a formation of ions such as $H^+$ and $OH^-$, so there is an obvious risk that hydrogen incorporates into the lattice due to the high concentration of $H^+$ ions[68] at the interface, which would affect the properties of the membranes.

In the context of this thesis, this hydrogen incorporation is specifically important since properties of PZO are linked to the strain state as well as the dipolar interactions, both of which can be affected by the intercalation of charged hydrogen ions. It is therefore important to ensure that the PZO membranes are free of hydrogen defects so any results we obtain can be accurately attributed to the clamping state of the film and not effected by chemical impurities.

In this chapter, I report an investigation of hydrogenation of PZO membranes that happen during the fabrication process. I will demonstrate that hydrogen ions diffuse into the PZO membranes during the etching of the sacrificial layer and induce strain. Although this strain does not directly drive any phase transition, it causes a metastability in the field induced ferroelectric phase. Another question that I answer is if this hydrogenation process in unique to PZO or can happen in other materials, and

as we will discuss later, it also effects membranes of STO and induces ferroelectric-type behaviour. On the plus side, this hydrogen effect can be mitigated by annealing the membranes under suitable conditions.

## 2.2. Lead Zirconate (PZO) membranes

I grew three PZO films of thicknesses 75, 36 and 17 nm using PLD (growth optimizations and conditions are given in **Appendix A**). The transfer process is the same as I discussed earlier (and **Appendix B1**), and the membranes are transferred to Pt-coated Si substrates. The evidence of hydrogenation of PZO membranes is provided by Raman spectroscopy and the hydrogenation- induced strain by X-Ray diffraction. I also used Piezoresponse force microscopy to investigate the ferroelectric properties of the 75 and 36 nm membranes. The membranes were subsequently annealed and investigated again with the same characterization techniques.

### 2.2.1. Raman Spectroscopy: Evidence of hydrogenation and effect of annealing

Hydrogen defects in perovskite oxides can form bonds with the oxygen atoms. These O-H bonds can be detected using Raman spectroscopy and give a characteristic peak at 3730 $cm^{-1}$ for O-H stretching.[62,69] We can probe this peak during the annealing process to obtain qualitative information of the deprotonation process. I annealed the 75 nm membrane at 260°C in 0.5 mbar pressure of air and collected the Raman spectra as the annealing continues (**Figure 2.1a**). The peak at 3730 $cm^{-1}$ becomes less intense and finally disappears marking the removal of hydrogen in the lattice. To make sure that this peak did not simply originate from adsorbates, I placed the membrane again in water for 18 hours, and the peak did not reappear (top spectrum in **Figure 2.1a**).

I also measured the Raman spectra of the PZO membrane at room temperature before and after annealing, referred to as as-transferred and annealed membrane respectively, shown in **Figure 2.1b**. The PZO membrane, in both cases, shows peaks that closely correspond to the antiferroelectric Pbam phase.[70–72] However, there is a systematic red shift in the spectra after annealing. Since the Raman spectra (number of peaks) does not show any evidence of a phase change, we attribute this shift to the strain state of the membranes.

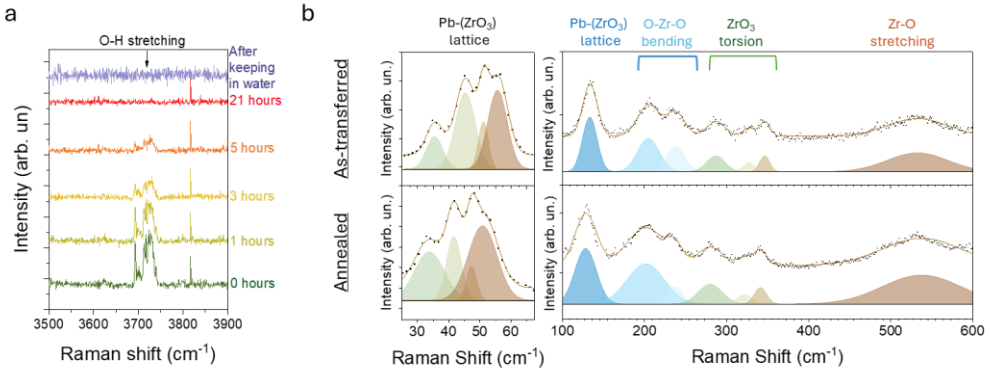


***Figure 2.1. (a)*** *In-situ monitoring of O-H stretching Raman peak while vacuum annealing at 260°C and later immersing in DI water,* ***(b)*** *Room temperature Raman spectra for as-transferred (**top**) and annealed (**bottom**) PZO membrane with the assigned modes labelled at top (the scatter dots are data points, the brown line shows the total fitting curve).*

## 2.2.2. X-Ray diffraction: Strain states of PZO membranes

We used XRD (θ-2θ-scans, rocking curve and Reciprocal space maps (RSMs)) to characterize the epitaxial film (before etching), as-transferred and annealed membrane as shown in **Figure 2.2**. The epitaxial film shows high crystalline growth (FWHM of rocking curve = 0.06º and Laue fringes) as well as in-plane lattice parameter a = 4.13 Å, whereas the bulk value is 4.16 Å, as seen from the reciprocal space map around $(-103)_{PC}$ peaks (**Appendix C1**). The in-plane lattice parameter measured for PZO in the epitaxial stack is the average of the parameters of two ferroelastic domains rather than a compressively strained film. After transferring the membrane, the in-plane lattice parameter increases to 4.19 Å and the rocking curve broadens (FWHM = 0.5º), indicating an average tensile strain of 0.7% and loss of texture respectively. Surprisingly, the out-of-plane lattice parameter shows no change in strain; combined with the in-plane expansion, the implication is a volume expansion of the lattice during the etching process. The results for the 36 nm and 17 nm PZO membrane also show the same behaviour (**Appendix C3** and **C5**). In fact, the in-plane lattice parameter in these thinner membranes is 4.21 Å (compared to the bulk value of 4.16 Å) resulting in a strain of 1.2% (compared to the bulk value), implying an even bigger relative volume expansion than in the thicker film. These differences point to a change in concentration of the hydrogen defects that is higher in the thinner membranes than the thicker one. Moreover, the broadening of the rocking curves in the as-transferred membranes is also more pronounced for the thinner membranes, as the thinner membranes can conform more closely to the underlying surface topography due to their flexibilty. Meanwhile, after annealing,[a] all the membranes relax to their bulk like, strain free state with lattice

[a] 36 nm membrane in this case was annealed in partial oxygen pressure of 133 mbar at 260°C for 4 hours, whereas the 17 nm membrane was annealed in 0.5 mbar pressure of air at 260°C.

parameters of 4.16 Å in both in-plane and out-of-plane directions (**Figure 2c**, bottom panel). This removal of strain is in accordance with the Raman data shown above and suggests that hydrogen is responsible for the volume expansion in the membranes.

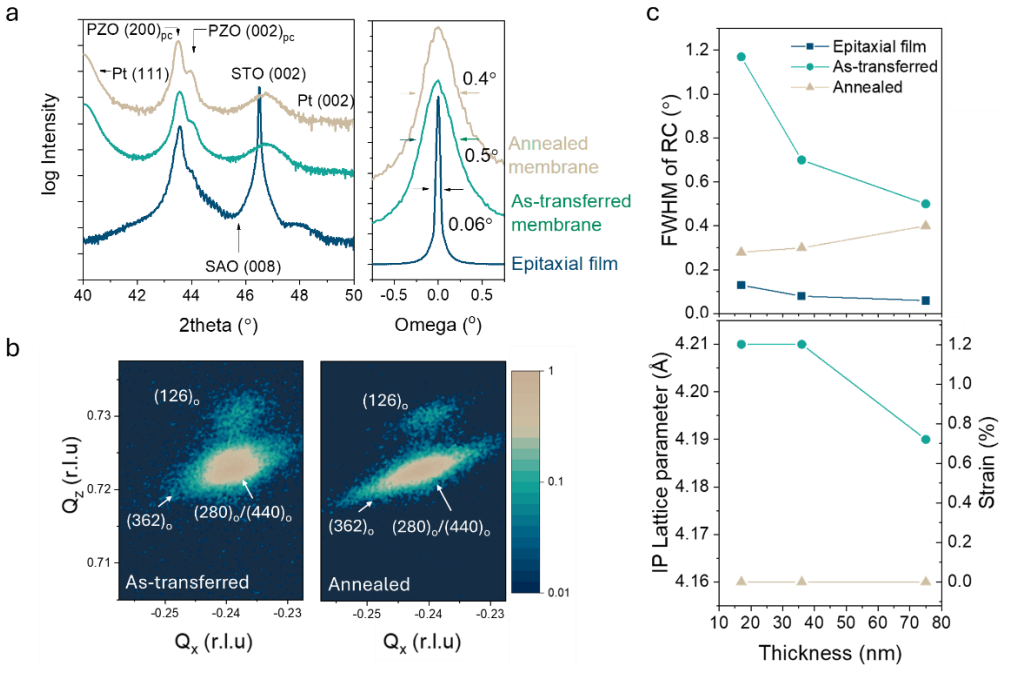


***Figure 2.2.*** *XRD for the PZO membranes at different stages,* ***(a)*** *θ-2θ XRD scans (left) and rocking curves around (002) reflection (right) for the 75 nm PZO epitaxial film, as-transferred and annealed membrane,* ***(b)*** *RSM around (-103)$_{PC}$ peak of PZO for the as-transferred (left) and annealed membrane (right),* ***(c)*** *Evolution of FWHM of RCs of membranes after each stage of processing and thickness dependence of in-plane lattice parameter and calculated strain evolution for the as- transferred and annealed PZO membranes (for the peak originating from (100)$_{PC}$/ (120)$_{O}$ domains).*

Although hydrogen is not known to act as a (A, B or O site) dopant for PZO, it can be interstitial, causing chemical strain. At the same time, the material is very sensitive to strains due to its complex energy landscape, specifically due to the contribution of the antiferrodistortive order (anti-phase oxygen octahedral tilts) to the condensation of the Pbam phase. These tilts can get reduced due to tensile strain and the volume expansion (increase in *effective* Goldschmidt´s tolerance factor) and hence can drive phase transitions in the material. Moreover, hydrogen ions may bond to adjacent oxygens forming defect dipoles that favour polarization. Although Raman spectroscopy shows no evidence of a phase transition during annealing (removal of hydrogen), the functional properties can still be affected. The antiferroelectric nature of as-transferred and annealed PZO membranes of 75 nm membrane was therefore characterized using Piezoresponse force microscopy in Dual AC resonant tracking mode (DART- PFM)[73] and switching spectroscopy (SS-PFM).[74]

### 2.2.3. Piezoresponse force microscopy

I attempted to write domains on the as-transferred and annealed 75 nm membrane by applying +10 V to the AFM tip and scanning an area of 3 x 3 $\mu m^2$, and then an area of 1 x 1 $\mu m^2$ with -10 V within the previous square for both samples (**Figure 2.3**). The as-transferred membrane shows a clear phase contrast of 180º between the up and down poled regions, along with higher amplitudes separated by a low amplitude domain wall. This is the characteristic response of up and down polarized ferroelectric materials. However, these contrasts decrease and finally disappear with subsequent scans, showing a time-dependant relaxation. On the other hand, the up and down poled regions in the annealed membrane show no contrast. In fact, this response is what we expect from an antiferroelectric: the regions switch to a ferroelectric phase only in the presence of an electric field but reverts to its non-polar state as the tip moves away. The behaviour of the as-transferred membrane can be explained by pinning of the induced ferroelectric phase by hydrogen defects, and the ferroelectric phase then relaxes back to non-polar state over time.

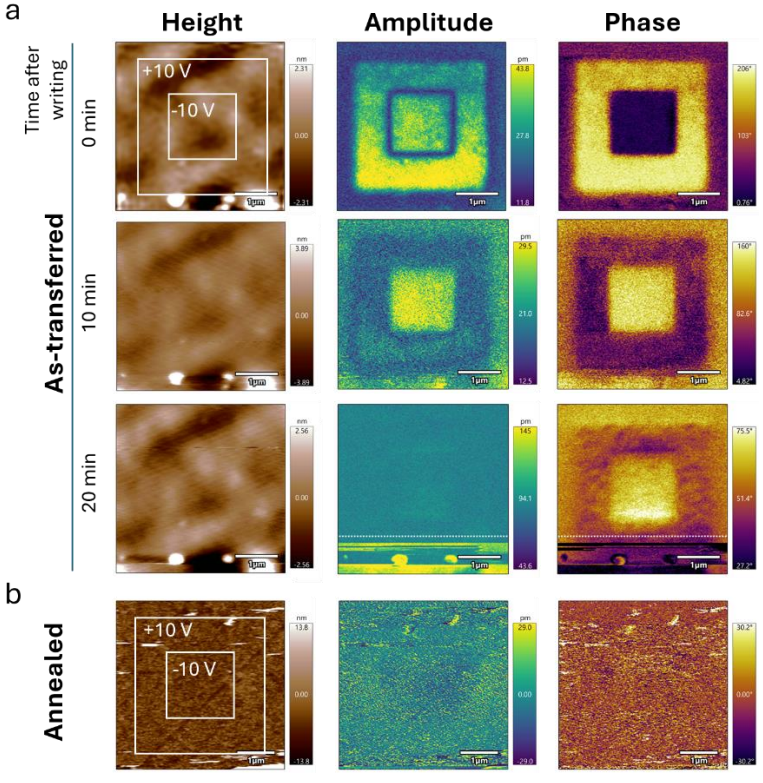


***Figure 2.3**. AFM topography, PFM amplitude and phase after writing square patterns indicated for the **(a)** as-transferred 75 nm PZO membrane and their time evolution (Data below dashed line in the bottom panels is unreliable due to strong crosstalk with topography), **(b)** annealed PZO membrane showing no polarization switching.*

We further explored the idea of pinning of phases by defects using SS-PFM. SS-PFM loops are obtained by applying a pulsed triangular wave, and values for phase and amplitude are recorded during bias application as well as after the bias has been removed, called on- and off- loops respectively. While the off-loops are used in ferroelectrics to study the switching behaviour and stability of the domains, avoiding the electrostatic contributions, in antiferroelectrics, the phase transition only happens in the presence of the bias, hence, both loops are important.[75] In these measurements, the frequency of the loops was 0.1 Hz with each on- and off-cycle of 0.14 seconds (for the loop shape, please see **Appendix H**).

The SS-PFM loops (shown in **Figure 2.4**) for the as-transferred 75 nm membrane show a typical ferroelectric- like behaviour, with the on-loops showing higher amplitudes due to piezoelectric contributions as compared to off- loops. However, from Raman, we know that the as-transferred membrane is antiferroelectric. These results are consistent with the fact that hydrogen can act as pinning centres for the field- induced FE phase making it metastable. By contrast, the annealed membrane shows a distinct behaviour in the on- loop, where the amplitude increases suddenly at around 6 V accompanied by a drop in phase as well. This sudden increase happens at the AFE to FE transition where the piezoelectricity of the ferroelectric phase kicks in,[75–77] Meanwhile, the off- loop resembles FE type loop, suggesting the existence of coexisting or slow relaxing ferroelectric domains.[78–80]

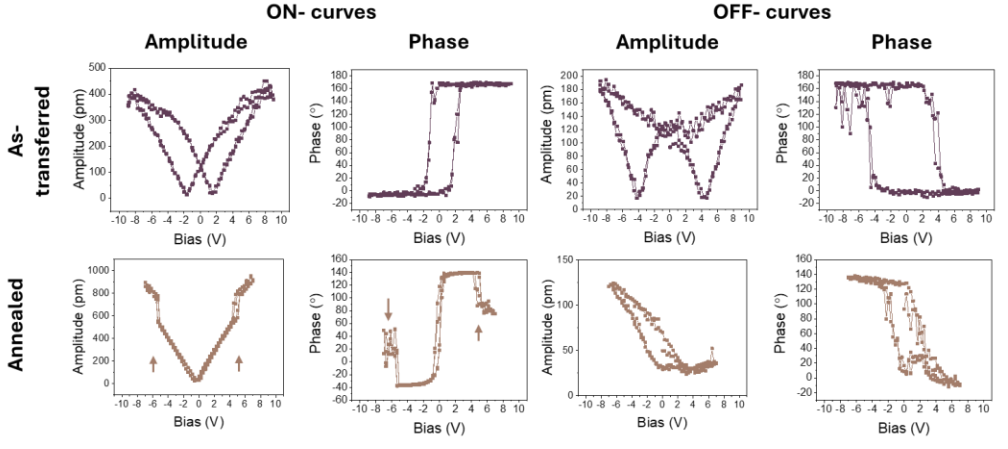


***Figure 2.4.*** *SS-PFM of a 75 nm PZO membrane (top panels: as-transferred, bottom panels: annealed), showing (from left to right) amplitude and phase loops in on- and off- stage.*

All in all, the results indicate that the PZO membranes can get hydrogenated by the etching process and cause strain in the membranes. Although, the strain does not seem to lead to any phase transition, the functional properties are affected by the defects; specifically, the field-induced ferroelectric phase gets pinned, becoming metastable rather than unstable. Conversely, annealing removes these hydrogen defects recovering the expected "clean" antiferroelectric properties of PZO.

## 2.3. Strontium Titanate (STO) membranes

To determine if etching-induced hydrogenation is unique to PZO or a more general phenomena of oxide membranes, I next investigated $SrTiO_3$ (STO). STO is a very common perovskite that is often used as substrate material. It is cubic at room temperature and tetragonal at low temperatures, and it is a quantum paraelectric, i.e. it stays in its paraelectric phase due to quantum fluctuations but is famous for transitioning into a ferroelectric state under small perturbations of strain or lattice distortion and hence is also very sensitive.

I grew a 16 nm STO film on SAO-buffered STO (001) substrate and repeated the process that I did for PZO (**Figure 2.4**). In this case, I used a very high annealing temperature (1000°C for 20 minutes in 50 sccm $O_2$ flow), based on previous works that demonstrate that the enthalpy of formation of O-H bonds is much higher in STO than PZO.[81,82]

The XRD investigation of STO membranes (as-transferred and annealed) does not show a significant difference in the strain state before and after annealing. The as-transferred membrane shows in-plane and out-of-plane lattice parameters of 3.898 Å and 3.907 Å respectively, whereas the annealed membrane lattice parameter is 3.903 Å in-plane and 3.906 Å out-of-plane. Similar to PZO, annealing process is effective in de-hydrogenation of the STO membrane as evident from the removal of the Raman peak associated to O-H stretching mode. Surprisingly, as-transferred STO membrane shows a very intense peak at ~800 $cm^{-1}$ (LO4 mode) which is related to the displacement of Oxygen atoms with respect to Ti atom and is one of the polar modes of STO.[83,84] Although, the first order scattering modes are prohibited in cubic STO due to symmetry considerations, presence of LO4 mode means that the symmetry (at least locally) is not cubic. In contrast, the annealed membrane does not show these modes but only second-order scattering modes consistent with its cubic symmetry. Finally, since LO4 mode is considered a polar mode in STO, we perform SS-PFM measurements to check the possible ferroelectric nature of the as-transferred membrane and compare it to the annealed membrane. The results (**Figure 2.4e**), indeed show that the as-transferred membrane gives a ferroelectric- or electret- type loop (clear butterfly hysteresis loop), while the annealed membrane does not.

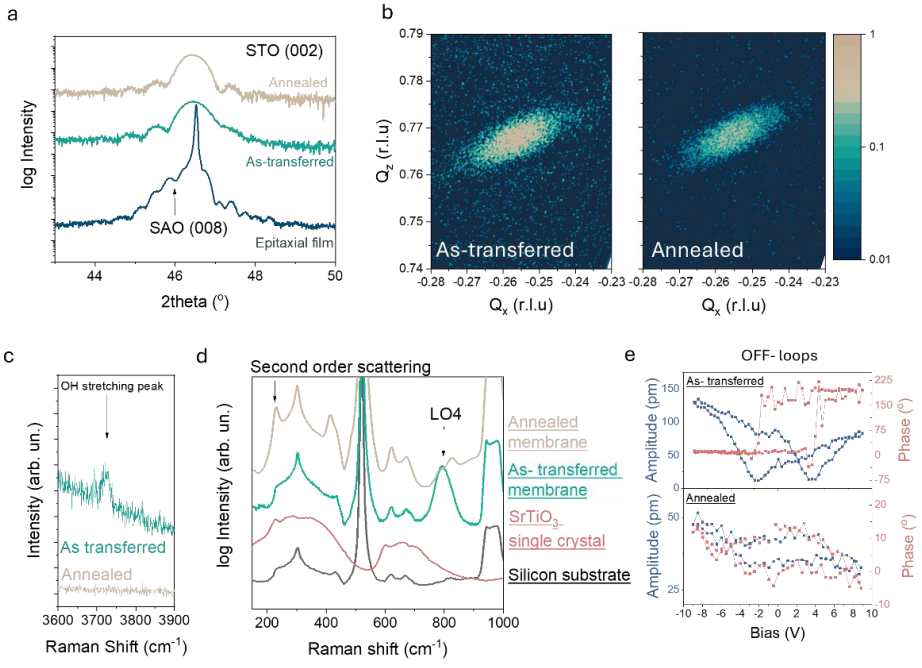


***Figure 2.4.*** *Characterization of STO membrane,* ***(a)*** *θ-2θ scans of the as-grown, as-transferred and annealed STO film,* ***(b)*** *RSMs around the (-103) peak of STO for the as-transferred (left) and annealed (right) membrane,* ***(c)*** *O-H stretching Raman peak for the as-transferred STO membrane (top) not present in the annealed membrane (bottom),* ***(d)*** *Raman spectra of as- transferred and annealed STO membrane with Silicon and STO single crystal spectra as references,* ***(e)*** *SS-PFM loops in OFF- stage for the as-transferred (top) and annealed (bottom) membrane.*

## 2.4. Discussion and conclusions

The intercalation of hydrogen in the lattice of perovskite oxides has been actively pursued and studied in the past to bring about different properties. As discussed in the introduction, there are various processes to achieve this intercalation, such as annealing, bias, and acidic media. In our case, this intercalation is not intentional but appears as a seemingly inevitable byproduct of the fabrication process. The formation of $H^+$ ions during the sacrificial layer etching, in combination with the enhanced activity of the chemical reactions (either due to the reactivity of the species, or else due to the interfacial geometry) can bring about this hydrogenation process.

While there are similarities between PZO and STO (both get hydrogenated), there are also non-trivial differences. One obvious question is why PZO shows such a high strain due to the hydrogenation compared to STO. There are different factors that may account for this difference.

1. PZO has a much larger lattice parameter than STO, hence the larger interstitial space can accommodate the hydrogen more readily.

2. Our films are grown on STO (001) substrate, therefore the STO films can grow dislocation-free, whereas PZO relaxes on the substrate at very low thickness due to higher mismatch. These dislocations can act as reservoirs for hydrogen and provide a pathway for their diffusion into the lattice.[85,86]
3. Lastly, one of the factors affecting the ability of a material to uptake hydrogen is the electronegativity of the elements involved. Particularly in perovskites, the difference between electronegativities of A and B cations play a role. This difference is larger in PZO (2.33 for Pb and 1.33 for Zr on the Pauling scale) as compared to STO (0.95 for Sr and 1.54 for Ti).[87,88]

Moreover, we see that hydrogen atoms or ions can distort the lattice in two ways. First is volume expansion, which in the case of PZO lattice may affect the octahedral tilts. Although octahedral tilts are strongly coupled to the antiferroelectric order and therefore, the condensation of the Pbam phase, we do not see any evidence of hydrogen induced phase change. On the other hand, we still see a higher propensity of the membrane for metastable ferroelectricity, but we speculate that this metastability comes from the pinning of phase boundaries rather than a phase change itself. In contrast, the STO membrane does not exhibit any hydrogen-indued strain. According to McCluskey,[81] hydrogen in STO can take a more "invisible" role replacing Sr vacancies, which might explain why we do not observe a lattice expansion.[86] Nevertheless, the presence of first order scattering modes in as-transferred membrane points towards a lattice distortion away from the cubic symmetry, which may result from local distortions in the octahedra either from interstitial defects or from H in Sr vacancies.[69,89–91] This result seems in contradiction with the XRD, which (within our resolution) suggests cubic symmetry for the STO membranes both before and after annealing. We have no clear answer for how these two seemingly contradicting results can coexist, but perhaps they can be reconciled if the polar regions are smaller than the correlation length of the XRD -as happens also in relaxor ferroelectrics. Another question that arises is, given the popularity of membranes made by water-based etching, why has the hydrogenation of the membranes evaded detection for so long? First, presence of light atoms such as hydrogen is difficult to detect using common characterization techniques such as EDX or XPS. Moreover, as demonstrated, not all materials show high strains or, if strained, it can be attributed to the incomplete relaxation of epitaxial strains. Hydrogen is detectable only if its detection is specifically targeted, and even then, there are a few techniques to do so such as Raman, EELS and in some cases, TOF-SIMS. The Raman peak we observe is at 3730 $cm^{-1}$, which is a very high frequency mode and an uninteresting region for perovskite oxides. Moreover, coincidentally, researchers have been mitigating this effect unknowingly. One of the most important things while working with membranes is the optimization of the interface between the membrane and the recipient substrate, or between multiple membranes in case of twistronics; this interface optimization often involves high-temperature annealing.[55,92–94] Moreover, interfaces as well as top surfaces usually

contain other contaminants from the transfer process, either due to exposure with water, or the contact with support polymers. The solution to this problem is also annealing or heating the samples in oxygen environments by using $CO_2$ lasers to burn off contaminants or for surface reconstruction.[34,52,94] During this optimization process, the hydrogen defects can be removed.

While hydrogenation is a pervasive problem, we have shown that this hydrogenation can be mitigated by suitable annealing process. Such a step is necessary for making meaningful comparisons between epitaxial films and membranes. On the other hand, hydrogenation might itself present an approach to tune the properties of the materials for different applications, such as stabilizing surface polarizations for electronics (we will discuss this more in **Chapter 6**) or as hydrogen storage. The fabrication process of membranes might be used to hydrogenate the membranes without annealing in reducing environments, applying bias or using acidic solutions. The control of the hydrogenation process is an important step in this direction which might be possible by tuning the etching rate of the sacrificial layer or by its thickness, playing off on the time it takes for the membrane to be completely detached against the time required for diffusion. At any rate, now that we know how to fabricate chemically pure (in the sense of hydrogen-free) membranes of PZO by thermal annealing, we can move on to investigating their functional properties and how they compare to their epitaxial counterparts in **Chapter 3**.

Chapter 3

# Switching dynamics of antiferroelectric capacitors: Effect of mechanical clamping to the substrate

Parts of this chapter have been published in Adv. Electron. Mater. 2024, 10, 2400102

## 3.1. Introduction

Epitaxial growth has enabled growth of highly crystalline thin films with a complete control of orientation, hence allowing us to study directional properties of materials, apply a range of strains for strain engineering, and tune properties such as piezoresponse of piezoelectrics, Curie temperatures and maximum attainable polarization in ferroelectrics or induce novel phases.[95–98] These advantages of epitaxial films have been used in many technological advancements such as transistors,[99] memristors,[100,101] tunnelling devices[102–104] etc. On the other hand, since the films grown on substrates via epitaxy are mechanically clamped to them, it is sometimes difficult to isolate the effects of clamping from size effects. The mechanical clamping can also affect negatively on some of the functional properties of the films, such as degradation of electromechanical properties of FEs due to restriction in the field-induced deformation or reduction of dielectric permittivity in relaxor ferroelectric such as ($BaZr_{0.5}Ti_{0.5}O_3$) due to substrate induced orientations.[105,106]

Antiferroelectric materials such as PZO can also be impacted by the growth substrate. The properties of PZO thin films are anisotropic, e.g. there is higher polarization in $(111)_{PC}$ oriented films, as that is the polar axis of the field-induced rhombohedral phase.[16] The electromechanical properties of PZO thin films are also highly dependent on not only the crystallographic orientation but also on the domain variants they possess. Since the AFE-FE transition is accompanied by a volume expansion, the mechanical clamping induced by the substrate can restrain it or direct it in the out-of-plane direction resulting in anisotropic stress and strains.[107] Accordingly, this clamping will alter how the switching from the AFE to the FE phase proceeds.

These previous investigations showcase how the epitaxial films of PZO differ from the bulk form, due to the film being clamped to the substrate. Therefore, the comparison between bulk and epitaxial films of PZO becomes convoluted both by size effects and also by the substrate clamping, and we need to separate out these two contributions to understand how PZO responds to electric fields in the thin film regime. Such investigation would also have practical repercussions, since the final goal is to integrate them in CMOS technology such as transistors and capacitors, where the epitaxial growth has not been achieved .

In this chapter, we study the switching dynamics of PZO capacitors after being removed from the substrate via sacrificial layer etching and compare them to capacitors nominally grown directly on substrates.

## 3.2. Synthesis and experimental methods

Tri-layer epitaxial heterostructures consisting of 300 nm PZO thin films with top and bottom 35 nm SRO electrodes were grown on (110)-oriented $GdScO_3$ (GSO) single crystal substrates via pulsed laser deposition (PLD) (growth details provided in

**Appendix A**, note: the PZO layers in these capacitors were grown at 550°C). Tri-layers that were deposited directly on the GSO substrate are from now on referred to as "on GSO". We also grew similar capacitor structures on SAO-buffered substrates. The SAO layer was subsequently etched in water, releasing the capacitor structure that was transferred to a metal-coated silicon substrate. These membranes adhere to the silicon supports by virtue of van der Waals forces. The membrane capacitors released from GSO are henceforth referred to as ¨off GSO".

To perform electrical measurements in the on GSO epitaxial capacitors, the top SRO electrodes were patterned as circular discs (10-400 µm diameter) by wet etching method using $NaIO_4$ (**Figure 3.1a**). For the off GSO membrane capacitors, electrode patterning was not required, because during the transfer the membranes crack, readily providing rectangular-shaped small capacitors with dimensions varying between 10 and 100 um lateral size (**Figure 3.1b**).

The frequency dependant displacement current- voltage loops were measured using aixACCT TF analyzer 2000,[a] where the contact to the bottom and top electrodes was made using manual micrometre probe station; the polarization was then calculated by integrating the current with respect to time.

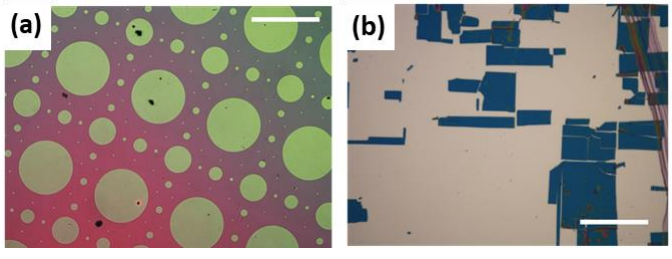


***Figure 3.1. (a)*** *Patterned SRO top electrodes on epitaxial heterostructure under a light microscope (scale bar: 500 µm),* ***(b)*** *Free-standing capacitors on Au coated Silicon substrate under a light microscope (scale bar: 100 µm).*

## 3.3. Structure

### 3.3.1. Transmission Electron microscopy

We examined cross sections of both On GSO and Off GSO capacitors under scanning transmission electron microscopy (STEM)[b] where the cross-section was done in the $<100>_{PC}$ pseudocubic direction. The images (**Figure 3.2)** show that the 300 nm PZO

[a] The frequency dependent and resistor-capacitor measurements were done at ICMAB, Barcelona, Spain, special thanks to Dr. Ignasi Fina for assisting in these measurements.

[b] Special thanks to Dr. Liu Ying (School of Aerospace, Mechanical & Mechatronic Engineering, The University of Sydney, Australia) for STEM imaging and analyses.

grew via columnar growth mode in both cases (HRTEM image of the boundary of the columns is shown in **Appendix D1.1**). Using high angle annular dark field (HAADF) images, mappings for lead atom displacements with respect to zirconium atoms and geometric phase analysis (GPA) were calculated. We choose to do this in selected areas with $(120)_O$ orientation with anti-polar direction oriented 45° out of (surface) plane. We observe the typical two up - two down dipole arrangement consistent with the Pbam phase. Additionally, we also observe ferrielectric modulations of the dipole magnitudes (red circle) and translational boundaries (white lines) with uncompensated dipole sublattices. These observations are very similar to those in single crystals and ceramics as well as thin films.[80,108] The two samples (epitaxial film and released membrane) thus show similar room-temperature antiferroelectric structure.

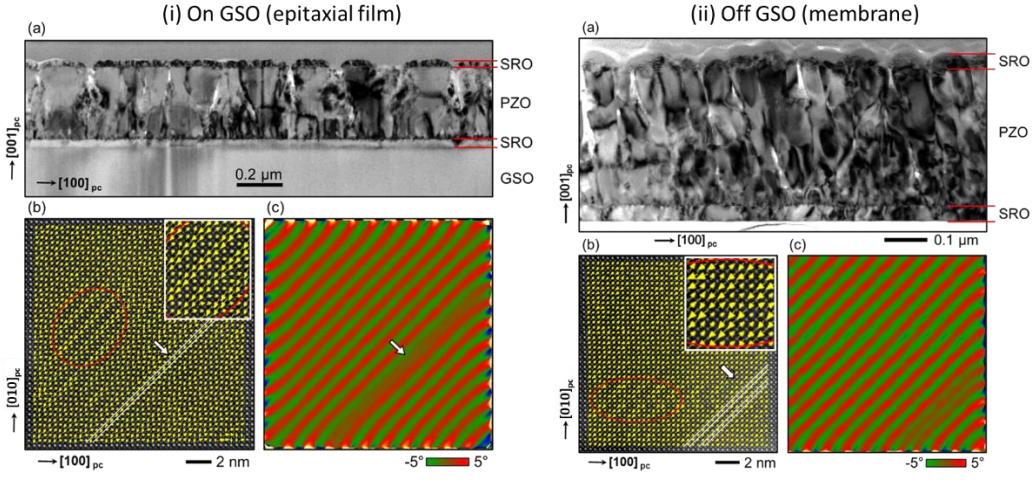


***Figure 3.2.*** *STEM of* ***(i)*** *On GSO (epitaxial film) and* ***(ii)*** *Off GSO (membrane), where* ***(a)*** *Low resolution TEM image,* ***(b)*** *Lead atom displacement mapping superimposed on HAADF TEM image and inset showing zoom in of the red circle,* ***(c)*** *GPA rotation maps.*

## 3.3.2. X-Ray Diffraction

We also used high resolution X-ray diffraction (HRXRD) to gain macroscopic quantitative insight into the strain states of the PZO layers in both cases, shown in **Figure 3.3a**. Both samples show a mixture of the two orientations expected from growth on a $(100)_{PC}$ substrate (**Appendix A3**). The epitaxial film capacitor On GSO shows a predominant $(001)_{PC} = (001)_O$ orientation (black diffractogram) with a relatively lower contribution of $(100)_{PC} = (120)_O$ oriented domains. Similar behaviour is found in the Off GSO capacitor before release (red diffractogram), whereas after release, the predominant orientation is $(100)_{PC} = (120)_O$ .

We can use HRXRD to then calculate the out-of-plane lattice parameters for each orientation by Bragg´s law and hence the average strain using:

$$\varepsilon_{(hkl)} = \frac{a_{(hkl)_{sample}} - a_{(hkl)_{bulk}}}{a_{(hkl)_{bulk}}} * 100 \qquad (3.1)$$

In addition, we calculate inhomogeneous strains in On GSO and Off GSO after release using Williamson-Hall plots (**Figure 3.3b**).[109,110] This method is based on the broadness of the XRD peaks (FWHM: $\beta_{\text{sample}}$) as a function of the peak angle ($\Theta$) for each orientation: $(h00)_{\text{pc}}$ and $(00l)_{\text{pc}}$, and fitted to the equation:

$$(\beta_{sample}\cos(\theta))^2 = (\frac{K\lambda}{D})^2 + (4\varepsilon_i \sin(\theta))^2 \quad (3.2)$$

Where the first term on the right is related to size effects ($D$ is the coherence length in the out-of-plane direction, and the smaller this coherent length the bigger the broadening), while the second term is related to the inhomogeneous strain $\varepsilon_i$., $\lambda$ is the XRD wavelength, $K$ is a geometric constant depending on the shape of the crystal and equals 0.94 for spherical crystals with cubic symmetry.[110] The broadening due to sample ($\beta_{\text{sample}}$) is calculated by subtracting the broadening due to instrument ($\beta_{\text{instrument}}$) from the FWHM of the peak we obtain from XRD ($\beta_{\text{experimental}}$). The calculated average strains and inhomogeneous strains (as percentages) are summarized in **Table 3.1**.

Although we see somewhat lower strains in the released Off GSO capacitor (0.1 - 0.15% vs 0.2 - 0.3% in On GSO), the difference between the two samples is marginal (detailed RSMs around different peaks are shown in **Appendix D1.2**). This is expected as the lattice mismatch between PZO and the SRO (strained on STO) is more than 4% and PZO in each case grows relaxed. The inhomogeneous strains are also very comparable. Since the strain states are very similar, we have confidence that any eventual differences between the functional properties of On GSO and Off GSO cannot be attributed to strain itself, but to the mechanical clamping state.

**Table 3.1:** Calculated Lattice parameters and strains for film and membrane capacitors.

| | Peak | Volume fraction | Lattice parameter (Å) | Bulk Lattice Parameter (Å)[111] | Strain (%) | Inhomogeneous strain (%) |
|---|---|---|---|---|---|---|
| **On GSO** | $(002)_{\text{pc}} = (004)_{\text{o}}$ | 0.79 | 4.118 | 4.126 | -0.199 | 0.13 |
| | $(200)_{\text{pc}} = (240)_{\text{o}}$ | 0.21 | 4.156 | 4.168 | -0.288 | 0.12 |
| **Off GSO** | $(002)_{\text{pc}} = (004)_{\text{o}}$ | 0.29 | 4.122 | 4.126 | -0.102 | 0.11 |
| | $(200)_{\text{pc}} = (240)_{\text{o}}$ | 0.71 | 4.162 | 4.168 | -0.144 | 0.11 |

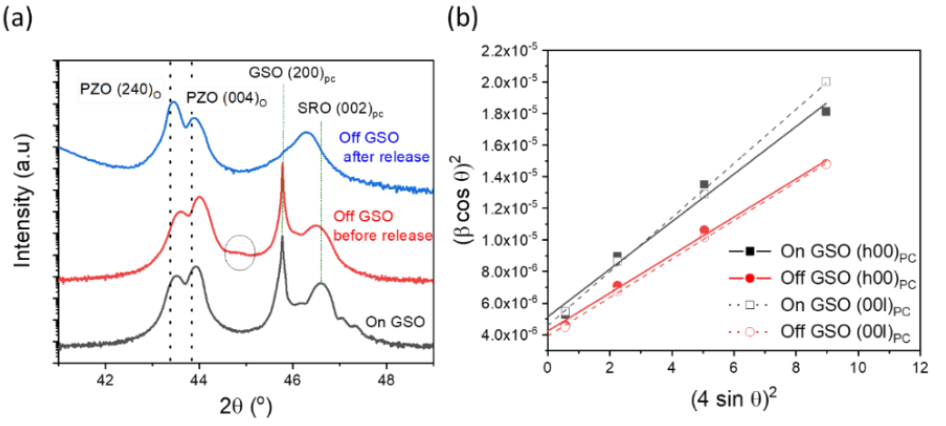


***Figure 3.3.*** *HRXRD of heterostructures grown on* ***(a)*** *GSO substrates, black lines for "On GSO" films, red for heterostructure with SAO before release, and blue for "Off GSO" membranes after release, the black dotted lines on the PZO peaks represent the bulk 2-theta value for each orientation, circle in the red curve shows the SAO peak,* ***(b)*** *Williamson-Hall type plot for "On GSO" films and "Off GSO" membranes. The slope of these fits reflects the inhomogeneous strain (lattice parameter variance), which is very slightly higher in the epitaxial film than in the released membrane.*

## 3.4. Functional properties

### 3.4.1. Polarization-Voltage loops

We measured current- voltage loops for epitaxial (On GSO) and membrane (Off GSO) capacitors at 10 kHz as shown in **Figure 3.4a.** The results show four switching peaks corresponding to AFE to down polarized (up polarized) FE and down polarized (up polarized) FE to AFE transition on the positive (negative) voltages, typical of AFE behaviour. But there are differences between the samples: while the On GSO capacitor shows broader current peaks and a higher baseline, Off GSO capacitors shows a higher voltage for the AFE-FE transition, sharper current peaks and lower baseline. Consequently, Polarization- Voltage (calculated from the integration of current density with respect to time) for the On GSO capacitor shows a broader transition (due to broader current peaks) and higher remnant polarization (due to higher baseline and broader peaks), whereas the Off GSO capacitor shows a much clearer double hysteresis loop with sharper transitions and low remnant polarization. These features of the loops can be used to interpret the nature of the systems as follows:

1. Broader current peaks, and hence the gradual transition in P-V loops can result from higher disorder within the On GSO capacitor that results in a distribution of activation energies between the non-polar ground state, and the field induced polar phase. This is also reflected in the lower coercive field of the On GSO capacitor.[112,113]

2. Since phase transitions are governed by both the height -and the slope of the energy barriers (both of which the disorder distributes into multiple steps), the higher disorder in On GSO enables the onset of the AFE to FE transition at a lower Voltage.
3. However, our structural investigations (STEM and XRDs) do not show a substantial difference in crystal symmetry, in concentration of ferrielectric phases, or disorder resulting from homogenous or inhomogeneous strain. Therefore, we do not think that the disorder is resulting from either the strain state or the coexisting polar phases.
4. Instead, the disorder here seems to develop during the application of the electric field itself, due to the evolving strains in the capacitors during the transition (volume expansion during the AFE to FE transition) and how the On GSO capacitor is mechanically clamped to the substrate.
5. This evolving disorder should result in a more frictional landscape for the switching in On GSO as compared to Off GSO.

This friction should also affect the response of the capacitor to the applied electric field and impact its switching dynamics. To substantiate this claim, we examine the switching hysteresis loops as a function of loop frequency (10 kHz to 80 kHz).

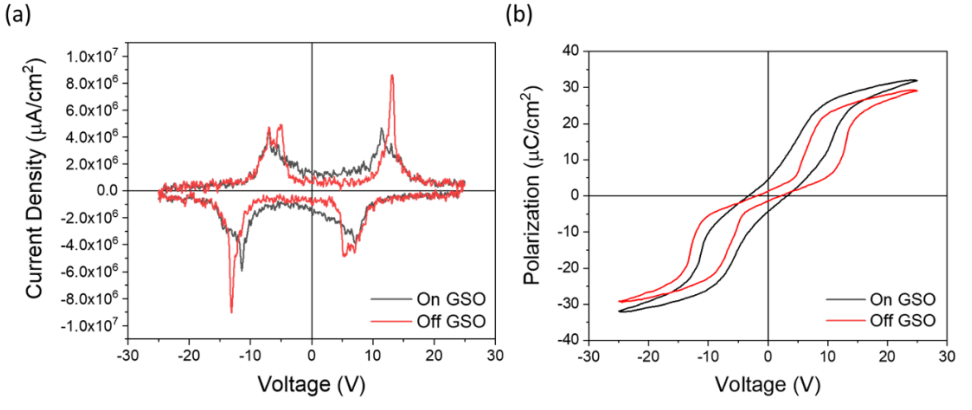


***Figure 3.4.*** *Comparison of* ***(a)*** *I-V curves and* ***(b)*** *Polarization loops of epitaxial film "on GSO" vs membrane "off GSO" at 10 kHz. The released film shows a sharper, more antiferroelectric-like double hysteresis with lower remnant polarization at 0 V.*

### 3.4.2. Switching dynamics

We perform the I-V loop measurements in a high frequency range (10 kHz to 80 kHz) and calculated the P-E loops, and we choose this frequency range due to several reasons:

1. Higher frequencies allow for the minimization of leakage currents.
2. At higher frequencies, the differences between the dynamics of the systems tend to become more obvious.
3. The amplification level of the signal in the equipment can be kept the same in this frequency range (the amplification level affects the Resistance- capacitance (RC) time constants.)

The current density vs electric field curves are shown in **Figure 3.5a-b.** We see that the current peaks shift as a function of frequency. Additionally, at higher frequencies, the current density increases , and we see that most of the current peaks in both cases are asymmetric with wide shoulders on one side (more obvious for On GSO), whereas Off GSO shows two distinct switching events for the FE-AFE transition. The asymmetric peaks in On GSO themselves can be a convolution of two peaks. The presence of two peaks suggests the existence of an intermediate stage or bridging phase, for example ferrielectric *Ima2* phase with ↓↑↑ modulation.[16,28] Alternatively, another possibility is that the double peaks might also arise from the switching of domains with different orientations in our samples. The splitting of the peak in Off GSO capacitor is made visible due to each peak being sharper, which as we discussed before, is attributed to lower disorder.

From the current-electric field loops, we extract the switching fields for the AFE to FE and FE to AFE transitions as a function of hysteresis loop frequency, and fitted with equations based on the Kolmogorov-Avrami-Ishibashi (KAI) model:[114–117]

$$E_{AFE-FE} = A + K_A * f^{\beta} \tag{3.3}$$

$$E_{FE-AFE} = F - K_F * f^{\beta} \tag{3.4}$$

where $A$ and $F$ are the quasistatic electric fields for AFE to FE and FE to AFE switching, which are related to the energy barrier for the transition, and $K_A$, $K_F$ and $\beta$ are dynamic parameters related to the mobility of domain walls or phase boundaries. We ruled out contact resistance differences (**Appendix D1.4**),[118] which is important because the apparent exponents in these fittings can otherwise be influenced by electronic time constants (RC) of the capacitors.[118] As mentioned, the FE-AFE switching of the membranes has two steps. We focused on the most intense of the two switching peaks; the smaller one was also fitted and showed a similar trend with a slightly slower relaxation time (**Appendix D1.5** and **1.6**), so the conclusions of the

present analysis apply equally to both. The results of the fitting are summarized in **Table 3.2**.[a]

**Table 3.2:** Values of fitted parameters from **Equation 3.3 and 3.4**.

| FITTING PARAMETERS | | ON GSO | OFF GSO |
|---|---|---|---|
| $E_{AFE-FE} = A + K_A * f^{\beta}$ | $A$ | 330 | 404 |
| | $K_A$ | 3.80 | 5.17 |
| | $\beta$ | 0.88 | 0.80 |
| $E_{FE-AFE} = F - K_F * f^{\beta}$ | $F$ | 253 | 222 |
| | $K_F$ | 2.90 | 10.3 |
| | $\beta$ | 0.96 | 0.62 |

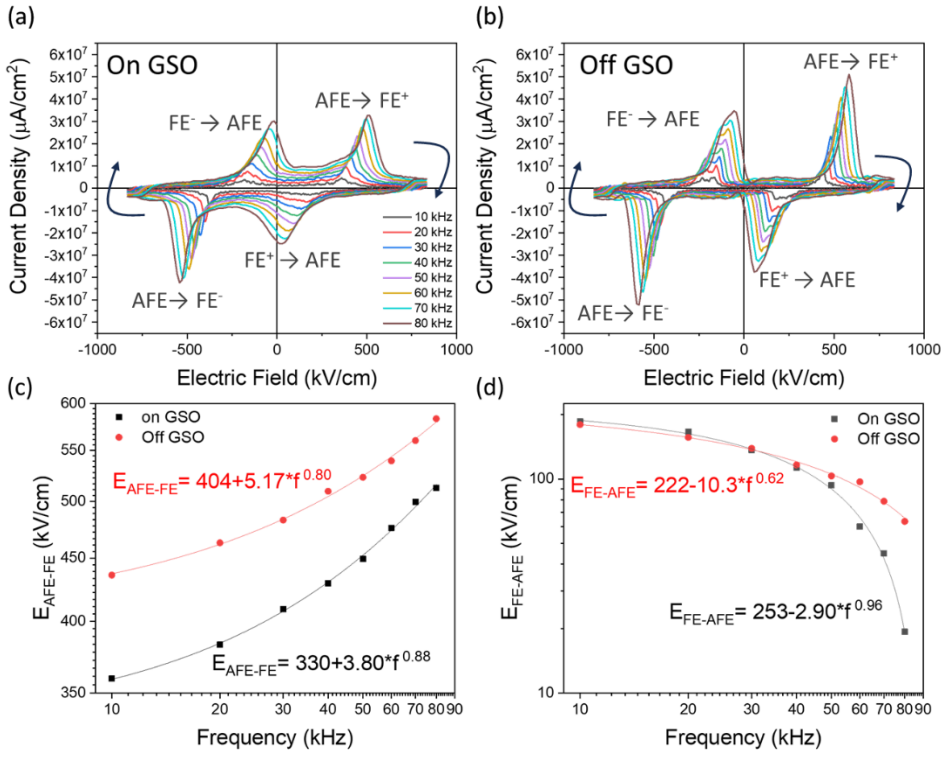


***Figure 3.5.*** *Current density – Electric field curves of,* ***(a)*** *"on GSO" film,* ***(b)*** *"off GSO" membrane, and KAI model fittings for* ***(c)*** *AFE- FE switching fields and,* ***(d)*** *FE- AFE switching fields, arrows in* ***a*** *and* ***b*** *represent the direction of electric field cycling, with all the transitions labelled.*

[a] Similar analysis was done for capacitors grown and declamped from STO (001) substrates and is shown in **Appendix D2**.

The parameters $A$ and $F$ represent the critical fields in the static limit ($f = 0$). We observe a higher value of $A$ in membranes compared to epitaxial films. This goes in line with the previous discussion on how the disorder in the epitaxial film On GSO can cause an earlier onset of the transition and give a lower apparent value of the energy barrier.

The frequency dependence of hysteresis behaviour is captured by the coefficients $K$ and principally the exponent $\beta$, whose impact of critical field increases exponentially with frequency. Lower values of $\beta$ means a lower dispersion of the switching fields, and hence a lower dependence on the frequency, indicating the ability of the system to respond faster to the varying electric field. Therefore, the Off GSO capacitor shows a more agile response compared to the On GSO capacitor. The dispersion captures the metastability of the field-induced ferroelectric phase, so that at higher frequencies the ferroelectric phase does not have time to fully revert back to the antiferroelectric ground state. With this in mind, we can define two meaningful frequencies:

1. With increasing frequency, the FE-AFE field decreases (more rapidly for the On GSO than the Off GSO) and at a critical frequency $f_c$, this field becomes 0, therefore $f_c = \left(\frac{F}{K_F}\right)^{1/\beta}$. The values for $f_c$ for On GSO and Off GSO are 90 kHz and 144 kHz respectively. At any frequency higher than this, most of the polarization will remain dynamically trapped in the ferroelectric state at 0 V, hence an increase in "remnant" polarization will be measured.
2. Another critical frequency can be calculated in the case where the dispersion of $E_{FE\text{-}AFE}$ is higher than the $E_{AFE\text{-}FE}$. If that happens, at a finite frequency, $f_F$, the positive FE to AFE switching field (when polarization goes from $+P_{ferro}$ to 0) catches up with the negative AFE to FE (when polarization goes from 0 to $-P_{ferro}$). Beyond that frequency, the capacitor will switch directly between up and down polarized states without having time to go through the non-polar phase. This can be calculated using $E_{FE-AFE}(f_F) = -E_{AFE-FE}(f_F)$. For the On GSO film, this frequency is $f_F \sim 1$ MHz, and the "ferroelectric-like" coercive field ($E_{FE\text{-}AFE}(f_F)$) is 2.5 MV/cm. Whereas, the membrane does not exhibit this frequency because of a higher dispersion of $E_{AFE\text{-}FE}$ than the $E_{FE\text{-}AFE}$.

The KAI model equations in the case of AFEs can be understood in terms of the elastic ($A$ and $F$) and plastic ($K_{A,F} * f^{\beta}$) response.[115] For the forward switching process, the electric field induces the transition, i.e. the lead atoms get aligned in the direction of the field and there is a volume expansion associated with this alignment. This is a quasi-static response of the material to the electric field and is termed as elastic since these changes are recovered once the field is removed. The electric field also derives the motion of the domain walls and phase boundaries which is not necessarily recovered, hence termed as the plastic response. Therefore, for the AFE to FE switching, the electric field has to overcome both the elastic and plastic barriers and

hence, $E_{AFE-FE} = A + K_A * f^{\beta}$ . Meanwhile, in the FE to AFE switching, the elastic return force (F) has to overcome the electric field and the plastic pinning , $E_{FE-AFE} + K_F * f^{\beta} = F$.

The dynamic term $K_{A,F} * f^{\beta}$ represents the viscous motion of the phase boundaries and domain walls. This viscosity is mainly represented by the exponent *β,* that depends on many factors:

1. The AFE to FE transition that leads to hysteresis involves ferroelastic twinning and volume expansion and hence an evolution of internal strains. This leads to higher $\beta$ values as compared to ferroelectric systems,[36] where the spontaneous strain for oppositely-oriented domains is theoretically identical.
2. The scaling behaviour of switching fields as a function of frequency can have different regimes depending on the dominant mechanism of domain wall motion, namely, thermally activated (at lower frequencies) or viscous processes (at higher frequencies).[119] Since, we are working at higher frequency ranges and probing mainly the viscous processes, the values of $\beta$ we observe in our measurements for both epitaxial film and membrane capacitors are higher than the previous reports on AFEs.[114]
3. The difference in $\beta$ values between the On GSO and Off GSO capacitors arises from additional friction likely caused by interfacial strain, defect pinning and mechanical clamping in On GSO film, (clamping) which is absent in Off GSO.
4. Unlike ferroelectrics where $\beta$ factor represents the domain growth dimensionality, in antiferroelectrics, it is also affected by evolving strains and dynamics of the structural transition.

### 3.4.3. Domain growth dimensionality

The authors of the original KAI model[117] used the scaling of hysteresis with respect to frequency to determine the dimensionality of domain growth from the $\beta$ exponent by using the formula $\boldsymbol{d = \beta * \alpha}$, where *d* is the dimensionality of the domain growth and $\alpha$ is a value based on the applied wave form (where $\boldsymbol{\alpha}$ **= 5.7** for triangular pulses), and has been widely used in ferroelectric systems.[36,117,120,121] However, in our case, this $\boldsymbol{\alpha}$ leads to values of *d* greater than 3. To understand this anomaly, we will revisit briefly the method used by the authors.

The original KAI model was used to determine the dimensionality (*d*) of growth in thin films of *ferroelectrics*, as stated below:

$$q(E) = 1 - \exp\left[-f^{-d}\varphi(E)\right] \qquad (3.5)$$

Where *q(E)* is the volume fraction of the switched domains, *f* is the frequency of the applied electric field, and *φ(E)* is a function of applied field and depends on the wave form. The value of $q$ can be determined using:

$$q = \frac{P_t - P_{min}}{P_s - P_{min}} \tag{3.6}$$

Where $P_{min}$ is the polarization at zero electric field (negative remnant polarization), $P_t$ is the polarization at time $t$ and $P_s$ is the saturation polarization

Rewriting Equation 3.5,

$$\ln \ln (1-q)^{-1} = -d \ln f + \ln \varphi(E) \tag{3.7}$$

Hence, the negative gradient of the plot of *ln ln (1-q)*$^{-1}$ vs *ln f* gives the dimensionality of growth of the emerging domains.

Equation 3.5 can also be rearranged to

$$f^d \ln (1 - q(E))^{-1} = \varphi(E) \tag{3.8}$$

Combining this model with Avrami formula for step field where the polarization is evolving with time at a constant applied field:

$$q(t) = 1 - \exp[-t^d \Psi(E)] \tag{3.9}$$

Where *t* is time, and *Ψ(E)* is a function of the step field; and the *d* in both cases is ideally the same.

To further simplify, we can take q = ½ that occurs at coercive field ($E_c$), leading to the relation: $E_c \propto f^{\frac{d}{\alpha}}$, and this relation has been widely used since then.

The authors also plotted *φ(E)* against $E^{\alpha}$ and the value of $\alpha$ they obtained from their fitting was 5.7 (for each frequency they investigated), hence obtained the power law $\varphi(E) \propto E^{\alpha}$.[117] The function *φ(E)* should, therefore, be independent of frequency and dependent on only the field. The power law: $\varphi(E) \propto E^{\alpha}$ obtained here, in the words of the authors, ¨is not the one to be derived from our model but the one which present experimental result implies¨. It is nonetheless important to note that the value of 5.7 cannot be considered a universal value and hence, cannot be used to determine the dimensionality of growth when using the scaling of hysteresis behaviour as a function of frequency.

Therefore, for this work, instead of using the power law directly, we modify some parameters to determine the dimensionality of the growth of the emerging ferroelectric phase.

We focus on one of the double hysteresis loops (positive electric field) and we take the value for $P_{min}$ as the polarization at $E(t = t_0) = \frac{A+F}{2}$, since the hysteresis is symmetrical around this value of electric field. $P_s$ is the saturation polarization. $P_t$ is taken at $E\left(t = t_0 + \frac{1}{8}T\right)$, where T is the time-period of the wave, as done by the original authors. However, the time, $t$ can be chosen differently as long as it meets certain criteria:

i. There should be some switching (or phase transition in our case) for each frequency for the time, t, hence we should be in the current peak region.
ii. The sample should not reach saturation polarization in every frequency for the value of time, t.

We use equation 3.7 and plot $\boldsymbol{ln\ ln\ (1\text{-}q)^{-1}}$ against $\boldsymbol{ln\ f}$, where the gradient then equals "effective" dimensionality of phase growth. The results for our analysis are shown in **Figure 3.6a.** We observe two distinct frequency ranges: a plateau region at lower frequencies and a higher gradient region at higher frequencies. The two regions originate from the choice of time at which the value of $P_t$ is taken. For lower frequencies, the value of $P_t$ (at time $t$) is close to that of $P_s$ i.e. the phase transition has completed, and we lie in the region beyond that of the hysteresis loop. For higher frequencies, the transition is not complete, and the $P_t$ lies in the region of the hysteresis loop and hence represents the growth phase. Therefore, the gradient in this region reflects the ¨effective growth dimensionality¨. The dimensionality of growth is 1.01 in "On GSO" and therefore 1-dimensional growth, e.g. stripe domains growing laterally or needle domains growing vertically, and 1.71 in "Off GSO". 2-dimensional growth is associated with broadening of cylindrical domains, however, this non-integer value of 1.71 can mean a mixed growth mode or presence of fractal domain walls and phase boundaries.

These results signify how clamping can restrict the dimensional growth of the ferroelectric phase at high frequencies, since the mechanical clamping limits the accommodation of the strains due to ferroelastic twinning at the phase boundaries, which in turn restricts the sideways propagation of phase boundaries. On the other hand, free-standing membranes can accommodate these strains better and hence, the emerging ferroelectric phase can grow more freely and in 2-dimensions. Generally, 3-dimensional growth in ferroelectric and antiferroelectric thin films is unusual since the initial nucleation (that is deterministic) occurs at the electrode interface and this nucleus grows rapidly in the out-of-plane direction towards the opposite electrode, which is rarely the limiting factor of the domain switching or phase transition.

Similarly, we also plot the $\ln\left(\frac{E}{E_0}\right)$ vs $\ln \varphi$ for On GSO as an example, where $E_0$ is the maximum electric field applied, as shown in **Figure 3.6b**. The dotted box shows where

the AFE to FE transition occurs and the gradient of the graph in this region equals α. Our plots at different frequencies do not fall on a universal curve and the gradient changes from 9.44 to 2.15 with an increase in frequency (i.e. $\varphi(E)$ is not a function of the applied field only), and therefore, cannot be directly used to determine the dimensionality of growth using $\boldsymbol{d = \beta * \alpha}$. This variation can be caused by the characteristics of the system and how it behaves under electric field. One main difference in our case would be our system is an AFE, where phase boundary motion is subject to not only pinning by defects but also strain fields. These varying values of $\alpha$ might also be the case in other systems and considered before using the KAI model directly.

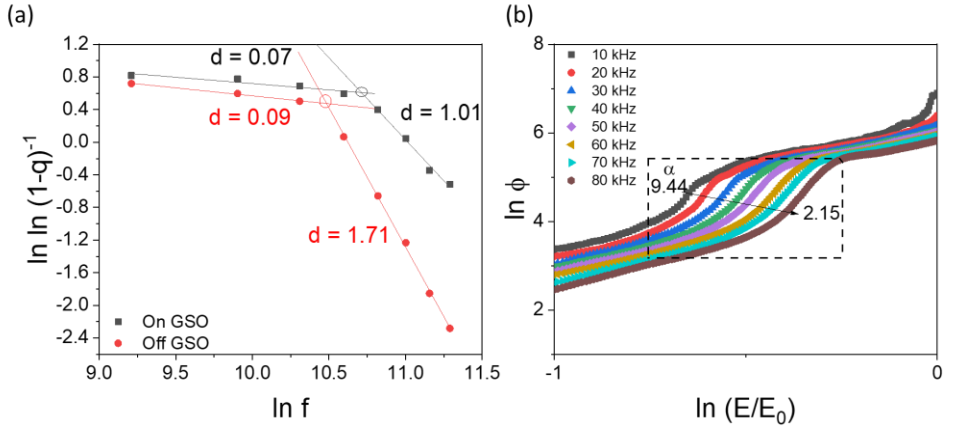


***Figure 3.6.*** *(a) Plot of fraction of phase switched as a function of frequency, the gradients of the plot represent the domain growth dimensionality, (b) determination of coefficient α for different frequencies for On GSO membrane.*

## 3.5. Dielectric response

The structural and functional analysis indicates that (i) there is not much difference in strain between epitaxial films and free-standing ones, in spite of which (ii) the epitaxial films have a higher "viscosity" in their switching dynamics, with a bigger frequency dispersion and slower response than the membranes. These observations are reflected by the behaviour of the dielectric constant as a function of temperature (**Figure 3.7a**) and amplitude of the AC electric field (**Figure 3.7b**).[a]

The temperature-permittivity measurements show:

[a] P-E loops at different temperatures and fitting of dielectric permittivity with modified Curie- Weiss law are shown in **Appendix D1.7**.

i. Both epitaxial film and membrane capacitors show a Curie temperature of 510 K, very close to bulk value,[122] consistent with the near-zero strain within our PZO layer.
ii. Epitaxial film also shows a more diffuse transition due to the higher disorder as compared to the membrane capacitor.
iii. Both capacitors show low losses consistent with a high quality of the capacitors; however, the membrane shows lower losses due to lower domain wall friction and pinning, consistent with the results from switching dynamics analysis.

To quantify the viscosity of epitaxial film and membrane capacitors, we measured the relative permittivity of the capacitors as a function of AC field amplitude and fit the measurements to the hyperbolic law (a modified Rayleigh law):[123,124]

$$\varepsilon_r(E_0) = \varepsilon_{\mathrm{rl}} + \sqrt{{\varepsilon_{r-rev}}^2 + (\alpha_r * E_0)^2} \tag{3.10}$$

Where $E_o$ is the oscillating electric field, $\varepsilon_{rl}$ is the intrinsic lattice contribution, $\varepsilon_{r\text{-}rev}$ is the reversible contribution from domain wall vibrations, and $\alpha_r$ is Rayleigh´s-like coefficient, signifying the extent of domain wall friction against the irregular energy landscape due to internal defects and disorder. The value of $\alpha_r$ for the On GSO film and Off GSO membrane capacitors are 0.57 cm kV$^{-1}$ and 0.22 cm kV$^{-1}$ respectively. Moreover, we can describe a threshold Electric field ($E_{th}$) that represents the extent of wall pinning using:[125]

$$E_{th} = \frac{\varepsilon_{r-rev}}{\alpha_r} \tag{3.11}$$

$E_{th}$ values are calculated to be 18.2 kV cm$^{-1}$ and 8.13 kV cm$^{-1}$ for the film and membrane respectively, showing explicitly that the pinning field is lower in the membrane capacitor.

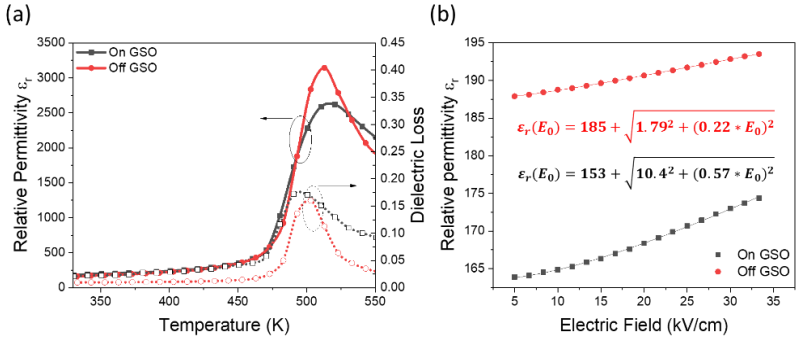


***Figure 3.7. (a)*** *Relative permittivity and dielectric loss measurements, "On GSO" film and "Off GSO" membrane,* ***(b)*** *Fitting of relative permittivity as a function of AC electric field using eq. 3.10, from which the Rayleigh coefficients were obtained. The free-standing membrane not only shows higher permittivity, but also lower electric field dependence, consistent with lower domain wall friction.*

## 3.6. Relaxation mechanism of the capacitors after DC poling

The mechanism behind the hinderance to motion of domain walls, either in the AFE phase or the FE phase as described above is an interesting aspect, considering that the dynamics of switching are different in the two capacitors. Instead of studying the motion while applying the electric field, we can also study it in the relaxation stage after poling the capacitors to investigate the time scales of relaxations and the physical phenomena behind it. To do this, we applied a DC bias of 15 V for 40 seconds to both capacitors and measure subsequent PE loops at 2 kHz to capture the relaxation of remnant polarization as shown in **Figure 3.8**, and fitted the results to the equation:[126–129]

$$P_r(t) = P_0\, e^{\left(\left(-\frac{t}{\tau}\right)^{\gamma}\right)} + c \qquad (3.12)$$

Where $P_r(t)$ is the remnant Polarization, $P_0$ is a pre-exponential constant signifying the starting polarization (post-poling) at t = 0, $\tau$ is a characteristic relaxation time, $\gamma$ is the exponential constant, and $c$ is another constant representing the remnant polarization after complete relaxation. The relaxation dynamics are therefore regulated by $\tau$ and $\gamma$ . There are some interesting points to note here:

1. The PE loops themselves can affect the intrinsic relaxation behaviour of the capacitors. We try to minimize this by using a minimum voltage to cause a phase transition in both capacitors, as well as doing the loops at same delays for each. The shape of the PE loop after poling and the relaxation behaviour does not correspond to simply the relaxation of FE phase to AFE phase, but rather to the effect of movement of defects and strong pinning centres in our capacitors.
2. The relaxation of the remnant polarization in On GSO capacitor is very slow compared to the Off GSO capacitor, as seen by the difference in $\tau$ values (9000 s vs 390 s).
3. Despite all these differences, the value of the exponent $\gamma$ is approximately the same (~0.4), signifying that the relaxation mechanism in these capacitors is the same.

This kind of stretched exponential functions have been used to describe relaxations in disordered electronic and molecular systems, where the relaxations can be dominated by either short range forces ( $\gamma$ = 0.6) or by long range Coulombic interactions ( $\gamma$ = 0.42).[126] Interestingly, the value of the power factor 0.4 is very close to the value found in simulations for the distribution of jerk (avalanche- type movement) energy in systems where there is strong ferroelastic twinning, as well as in ferroelectrics with high density of domain walls.[126,128] The value of 0.42 for the exponent also represents a motion of domain walls via a pinning- depinning mechanism (that introduces viscosity in the system) rather than creep motion, which seems to be the case for both of these capacitors.[127]

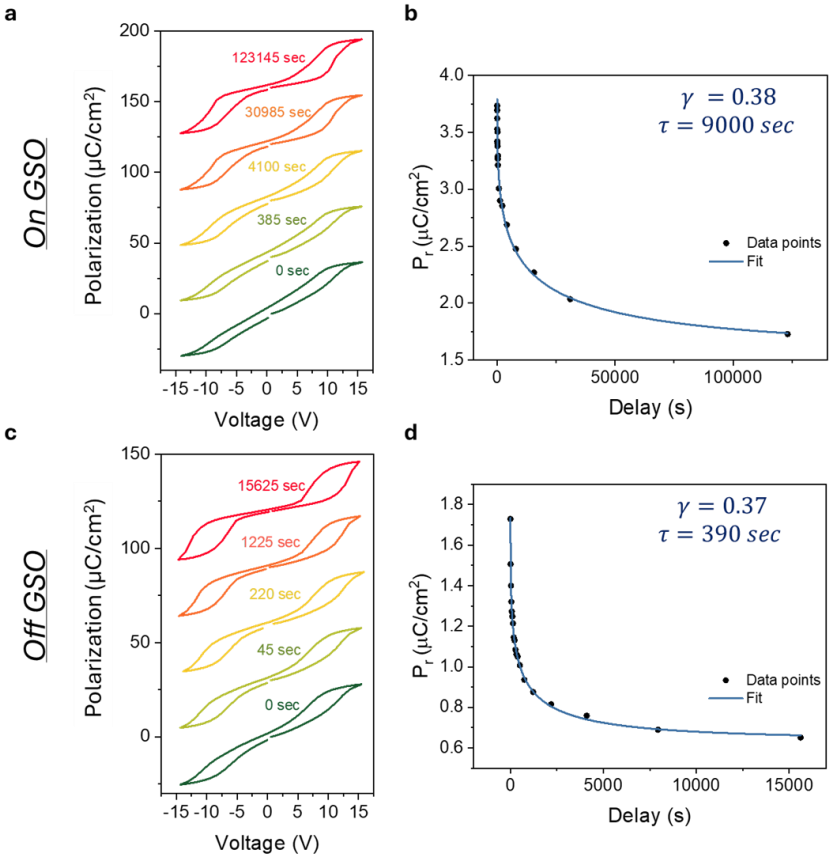


***Figure 3.8.*** *P-V loops* ***(a, c)*** *taken at specified delay times after DC poling and fitting of the remnant polarization with stretched exponential function* ***(b, d)****: for On GSO capacitor* ***(a, b)****, and Off GSO capacitor* ***(c, d)****, the loops are manually off-set for better visualization.*

## 3.7. Energy Storage characteristics

The dynamic change in the shape of the hysteresis loop also influences the energy storage behaviour of the capacitors. The recoverable energy is maximized when the remnant polarization is lower, saturation polarization is higher, and the difference between switching fields (AFE-FE vs FE-AFE) is lower (as illustrated in the **Figure 3.9a**).

In **Figure 3.9b,** we compare the energy storage density and the efficiency of the on-GSO and off-GSO capacitors, calculated using **Equations 3.13(a-c)** below:

$$U_{recoverable} = \int_{P(E=0)}^{P(E=E_{max})} E_{return} dP \qquad (3.13a)$$

$$U_{loss} = \int_{P(E=0)}^{P(E=E_{max})} (E_{forward} - E_{return})\, dP \qquad (3.13b)$$

$$Efficiency\ (\%) = \frac{U_{recoverable}}{U_{recoverable}+U_{loss}} * 100 \qquad (3.13c)$$

where $U_{recoverable}$ is the recoverable energy, $U_{loss}$ is the energy loss, and $E_{max}$ is the maximum applied electric field.

As expected, the efficiency of both capacitors decreases as a function of loop frequency due to the higher hysteresis and domain wall friction. However, even though the membrane capacitor has a slightly higher coercive field and a slightly lower saturation polarization, the main difference stems from the difference in the remnant polarization. Moreover, the membrane shows higher efficiencies throughout the frequency regime due to faster dynamics and switching speed, which facilitate the return to the P=0 state. This difference is amplified at higher frequencies, specifically the two critical frequencies (described in the **section 3.4.2**):

i. $f_c$: at this frequency, the remnant polarization will increase, and since this frequency is lower for the epitaxial film capacitor (90 kHz vs 144 kHz for the membrane), the efficiency difference in this frequency range will be dramatically higher.

*ii.* $f_F$: this frequency exists only for the epitaxial film capacitor, above which it shows pseudo-ferroelectric behaviour, and therefore, the recoverable energy will be minimized and the loss maximized, whereas the membrane capacitor will still behave as antiferroelectric. While, the ferroelectric behaviour may be of interest for high frequency operation, the coercive field for the switching is excessively high.

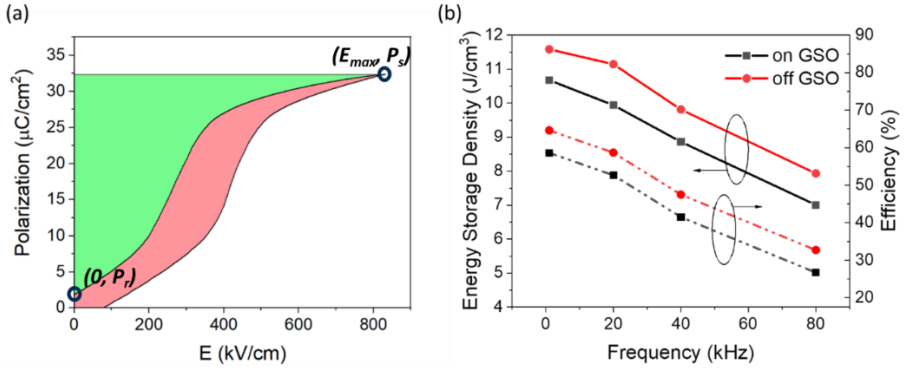


***Figure 3.9. (a)*** *Positive voltage loop (centred) of SRO/PZO/SRO membrane capacitor (off GSO) measured at 1 kHz. The green area represents the recoverable energy, pink area represents the energy loss,* ***(b)*** *Energy Storage density and efficiency of epitaxial film and membrane capacitors. Both properties decrease as a function of increasing frequency reflecting the frictional dynamics of the AFE-FE boundaries. In membranes, smaller pinning results in enhanced efficiency and storage density.*

## 3.8. Conclusions

In this chapter, I demonstrated that membrane capacitors switch faster than epitaxial ones due to a decrease in the viscosity of motion of domain walls and phase boundaries

enabled by the removal of the substrate. Moreover, the higher dynamic disorder in the epitaxial film capacitors due to evolving mechanical stress during the field-induced transition also imposes a hindrance to the switching dynamics. On the other hand, the mechanisms underlying the motion of the domain walls/phase boundaries is similar, i.e. pinning- depinning.

While declamping leads to an increase in the energy storage efficiency of the membrane capacitors, clamping induced effects may still provide some benefits for epitaxial films over the membrane capacitors; for example, epitaxial films can show higher out-of-plane electromechanical strains due to in-plane clamping.[107] Moreover, the slower switching dynamics in epitaxial films might be useful for non-volatile memory devices while the faster dynamics of membranes in volatile memory elements. Manipulating the dynamics of switching are also important in other electronics such as neuromorphic memories and negative capacitance transistors. We will explore the possible applications of AFEs in electronics further in **Chapter 6**.

While in this chapter we compared epitaxial vs membrane capacitors and tried to isolate the effects of mechanical clamping by ensuring that other factors (thickness, strain) remain the same, PZO can be affected by these factors as well. We will explore how each of these factors can change the functional properties and/or coexisting phases of the PZO layers in the following chapters.

Chapter 4

# Dimensionality-driven phase transitions in PZO membranes

## 4.1. Introduction

The coexistence of FE and AFE phases in PZO has been long speculated due to the opening of the hysteresis loop at zero field.[15,16] With advanced electron microscopic techniques, the ferroelectric FE phase was indeed observed directly to coexist with the AFE one in thin films.[108,129] Studies have shown that the R3c phase exists near the PZO-substrate interface, and this coexistence has been attributed to the residual strains and the strain field around dislocations.[129] Moreover, the coexisting phases are quite often not the common AFE and ferroelectric R3c. There have been observations of many other different phases in PZO (pure or doped) thin films such as:

I. Ferrielectric Ima2 phase, both as translational boundaries within the Pbam matrix or as high-volume phase.[80,130]
II. Ferrielectric phase with uncompensated dipoles (↑↑..).[131,132]
III. Incommensurate phases with uncompensated dipoles.[130]
IV. Tetragonal-like antiferroelectric phase with (↑↑→→) modulations with displacement in <100> pseudocubic directions.[133]
V. Ferroelectric phase with $<110>_{PC}$ polar direction and $a^-a^-c^+$ tilts.[79,131]
VI. Ferroelectric phase (Monoclinic) with $[uuv^*]_{PC}$ displacement[a]. The tilt system in this monoclinic phase is under dispute, but the possibilities include $a^0a^0c^+$ and $a^-a^-c^+$.
VII. *Theoretical prediction* of a tetragonal ferroelectric phase with $<001>_{PC}$ polar direction and $a^0a^0c^-$ tilts (I4cm phase).[134]

Crystal structures of the monoclinic and the tetragonal phases are drawn in **Appendix E1**.

All these phases appear at different thicknesses of PZO. Moreover, there appears to be a well-defined phase transition sequence from R3c to Pbam as the thickness of films grown on STO (001) increases:

Rhombohedral R3c (FE: $[111]_{PC}$, $a^-a^-a^-$) → Monoclinic Pc (FE: $[uuv^*]_{PC}$, $a^0a^0c^+$) → Orthorhombic Ima2 (Ferrielectric (FiE): $[110]_{PC}$, $a^-a^-c^0$) → Orthorhombic Pbam (AFE, $[110]_{PC}$, $a^-a^-c^0$).[108]

The brackets show the functionality, Pb displacement direction and tilt system sequentially. The thickness at which the next phase appears also depends on the substrate, e.g. when grown on $KTaO_3$, which has a larger lattice parameter, the

[a] $[uuv^*]$ displacement vector means that the Pb dipoles are displaced in a direction intermediate to $[111]_{PC}$ and $[001]_{PC}$ directions. This direction can be understood as the addition of two vectors: $v_{[uuv^*]}=|v_{[111]}|\ \hat{v}_{[111]}+|v_{[00\text{-}1]}|\ \hat{v}_{[00\text{-}1]}$, where $|v_{[111]}| > |v_{[00\text{-}1]}|$. In addition to this displacement, there is a small antiferroelectric modulation in Pb displacement along the $[110]_{PC}$ direction.

subsequent phases appear at lower thicknesses, implying the effect of residual strains from the misfit.[108]

However, theoretical studies show that these phase transitions may also occur not because of the strain effects but due to surface effects.[134] At very small thicknesses, dimensionality, surface tension and electrical boundary conditions can all upend the delicate energy balance between AFE and FE, tilting the scales in favour of the latter.[134] Likewise, ferroelectric materials such as BTO are also predicted to go through phase transitions due to surface tension effects (i.e. compressive strains on the surface) and the electrodes are needed only to screen the depolarizing fields.[135] This prediction is consistent with the observation of ferrielectric phases near the surface of PZO single crystals.[131]

These observations showcase how sensitive the system of PZO is, especially as thin films, and how different factors may contribute to the same effect. This makes it difficult to isolate the causes of the observations made when the films are grown on substrates, where there are combined effects from residual strains, mechanical constraints and surfaces.

Therefore, in this chapter, I will discuss our investigation into phase coexistence in substrate-free PZO membranes of different thicknesses: 36 nm, 17 nm and 5 nm, to try to isolate pure size effects.

## 4.2. Experimental Techniques

PZO membranes were fabricated using the sacrificial layer etching method. The PZO membranes of different thicknesses were directly transferred to either Pt-coated Silicon substrates for XRD or to planar view TEM grids, schematic shown in **Figure 4.1a**. The TEM grids used for the following observations are made of Silicon with suspended Silicon nitride ($SiN_x$) membranes containing holes of 1 μm diameter. Optical images of 36 nm PZO membrane transferred to the grid are shown in **Figure 4.1b** and **c** where the blue background is the silicon chip, square marked with black square is the $SiN_x$ membrane, PZO appears yellow on Silicon and pink on $SiN_x$. All the membranes were then annealed after transfer in oxygen partial pressure of 133 mbar at 260°C for 4 hours as done in **Chapter 2**.

The analyses of HR-TEM images were done using hyperspy[136] and atomap[137] python libraries, wherein the atomic positions are refined by 2D-Gaussians. The displacements of Pb atoms were calculated by the offset from the geometric centres of nearest four Zr atoms, and with respect to the surrounding four cations for O displacements.

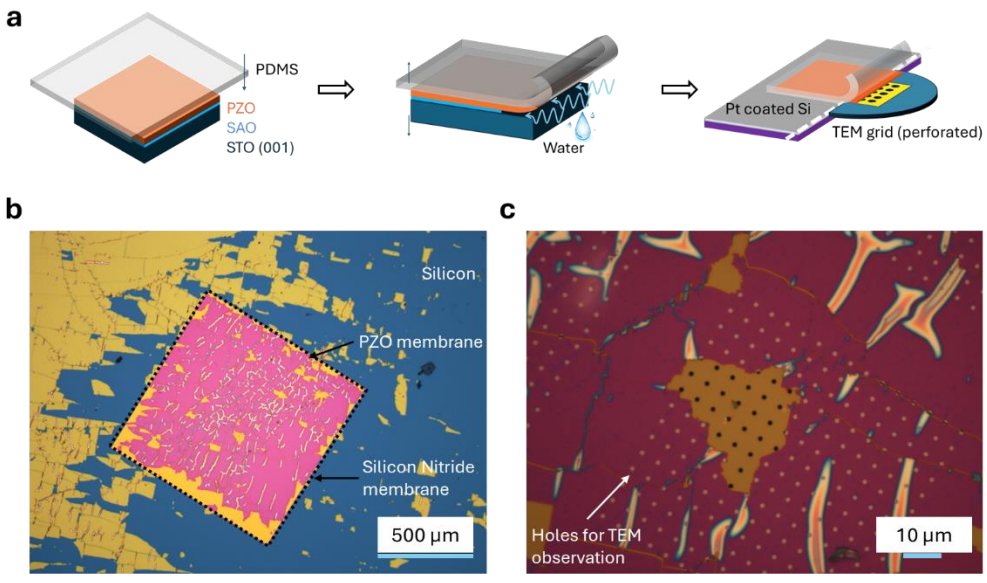


***Figure 4.1. (a)*** *Schematic of the transfer method for membranes on Pt coated Silicon and TEM grids,* ***(b, c)*** *Optical images of 36 nm PZO membrane on the TEM grid.*

## 4.3. X-Ray diffraction of membranes

X-Ray diffractions were carried out on the epitaxial stacks of PZO/SAO//STO (001) where the thickness of PZO was 36 nm, 17 nm and 5 nm, and PZO membranes of 36 nm and 17 nm transferred to Pt coated Silicon substrates as shown in **Figure 4.2**. We were not able to carry out XRD on the 5 nm membrane because the signal was too low to be detected. The epitaxial stacks show high crystalline quality of PZO. While the 36 nm and 17 nm PZO shows singe domain orientation ($(100)_{PC}$= $(120)_{O}$), the 5 nm film shows a small peak at lower 2theta value corresponding to a strained layer. After release, we observe a slight relaxation of the PZO membrane towards a higher 2theta value signifying the release of residual misfit strains.

RSM measurements were then conducted to obtain information about the in-plane and out-of-plane lattice parameters as shown in **Figure 4.2b** and **c**. RSMs of the 36 nm membrane shows majority $(100)_{PC}$ domain orientation and minority $(001)_{PC}$ domains, meaning that there was some reorientation during the release process. The 17 nm membrane, on the other hand shows a broad peak due to lower thickness and the two domains are not distinguishable. The lattice parameters obtained for the $(100)_{PC}$ domains for both membranes are 4.15 Å in-plane and 4.16 Å out-of-plane for the $(280)_{O}$/$(440)_{O}$ peak.

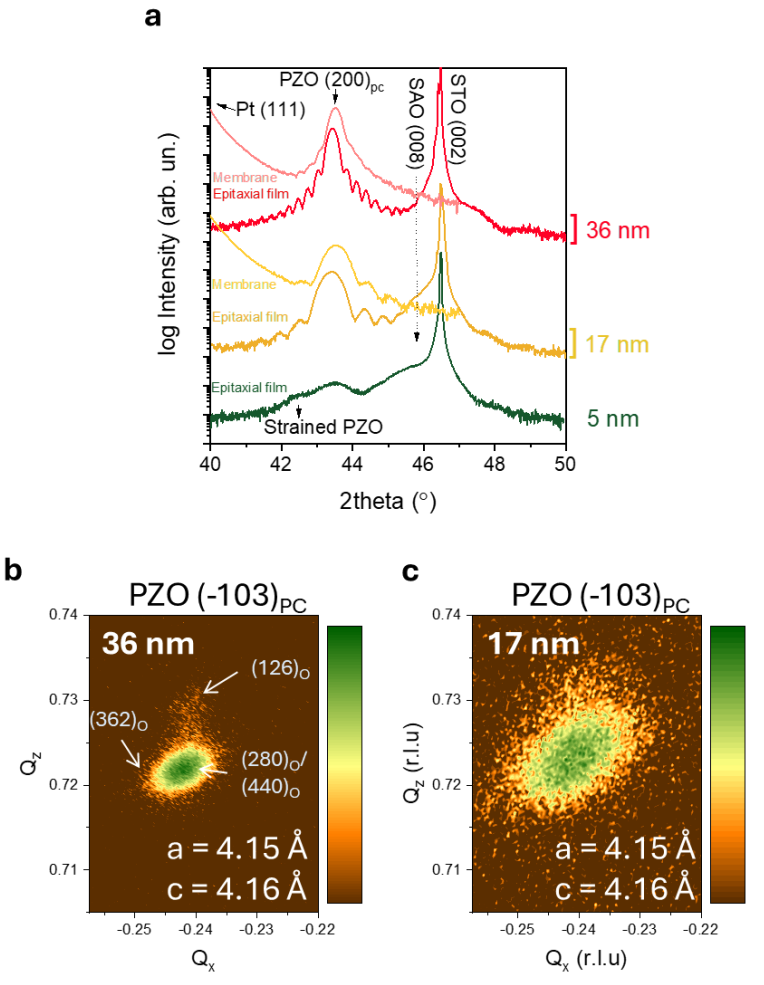


***Figure 4.2.*** *XRD measurements for the epitaxial stacks and membranes,* ***(a)*** *theta-2theta scans of epitaxial films and membranes transferred to Pt- coated Silicon, RSMs around (-103)PC peaks of PZO membranes transferred to Pt-coated Silicon of* ***(b)****36 nm and* ***(c)*** *17nm.*

## 4.4. Transmission Electron Microscopy

To get a complete picture of the coexistence of phases, we used transmission electron microscopy (TEM) methods, namely Selected Area Electron Diffraction (SAED) to

determine the phases in the membranes and Annular Bright Field (ABF) to visualize Pb displacement and oxygen columns at the surface.[a]

### 4.4.1. 36 nm PZO membrane

**Figure 4.3a** shows the electron diffraction pattern (EDP) of 36 nm membrane from $[001]_{PC}$ zone axis. Superlattice reflections at ¼ $(110)_{PC}$ positions are clearly seen, consistent with the $(001)_{PC}$-oriented 90º domains of AFE Pbam phase. However, these spots are elongated suggesting an absence of a well-defined long range order -or at least a finite size along the elongation axis of the spots. By comparing this pattern with the theoretical EDP in **Figure 4.3b**, there is a discrepancy between the relative intensities of the satellites and the main reflections (marked as a rectangular box), in fact, the relative intensities are inversed. This observation indicates that the $(001)_{PC}$ domains coexist with other regions that contribute to the main spot but not the superlattice spots. Since, the superlattice spots ½ $(001)_{PC}$ originating from $(100)_{PC}$ domains (due to unit cell doubling in the c-axis) are absent, this domain orientation can be ruled out.

Moreover, we see a very weak superlattice spot corresponding to ½ (110) peak that is not present in the simulated Pbam structure. This spot can have different origins. First is the double diffraction of the electron beam, where the peak appears due to $\left(\frac{1}{2}\frac{1}{2}0\right) = \left(\frac{3}{2}\frac{1}{2}0\right) + (-1\ 0\ 0)$. The second origin can be the presence of a monoclinic Pc phase,[108,131] which is ferroelectric in nature, as observed in PZO thin films as well as PZO based materials that acts as a bridging phase between the AFE Pbam phase and FE R3c phase. Pc phase has a ferroelectric modulation in $[uuv^*]_{PC}$ directions with small antiferroelectric modulation in $[-110]_{PC}$ direction. The oxygen octahedral tilt in this phase has been under debate, but the tilts previously assigned are either $a^-a^-c^-$, $a^-a^-c^+$ or $a^0a^0c^+$.[108,131,138] We will discuss the nature of this phase in more detail in the **Discussion** section.

We then conducted a tilting experiment to obtain EDP from $[011]_{PC}$ zone axis (**Figure 4.3c**). The spots from this zone axis are elongated. Since the beam path through the sample in this orientation is increased by a factor of √2, this elongation can be attributed to internal strains caused by bending of the film and coherency strain due to phase coexistence, otherwise minimal along the normal direction. We can see two types

[a] I would like to acknowledge the contributions from numerous collaborators in this work. Special thanks to Felip Sandiumenge and Judith Oró (ICMAB-CSIC, Barcelona, Spain) for carrying out the diffraction experiments as well as: Belen Ballestros, Kapil Gupta and Bernat Mundet Bolos from ICN2 Electron Microscopy unit, Barcelona, Spain and Cesar Magen from INMA, Zaragoza, Spain for the High resolution imaging.

of superlattice spots in this case: ½ (h k l), where $h = k = l$ called R1 spots, and where $h \neq k \neq l$ called R2 spots (**Figure 4.3e**). Both of these spots are present in the EDP of the Pbam phase. R1 spots arise due to the antiparallel arrangement of the lead atoms, whereas R2 spots arise from the $a^-a^-c^0$ tilt system. However, we see a weak spot in the red square (not present in the simulated EDP) that can arise from 90 degree domains, since, in this orientation, there are no multiple scattering paths yielding diffracted intensity in these positions. Also note that EDP from this zone axis cannot distinguish between antiferroelectric Pbam and ferroelectric R3c phase, since the R3c structure is a slightly distorted building block of the Pbam phase and the EDP of R3c is completely contained within that of the Pbam.

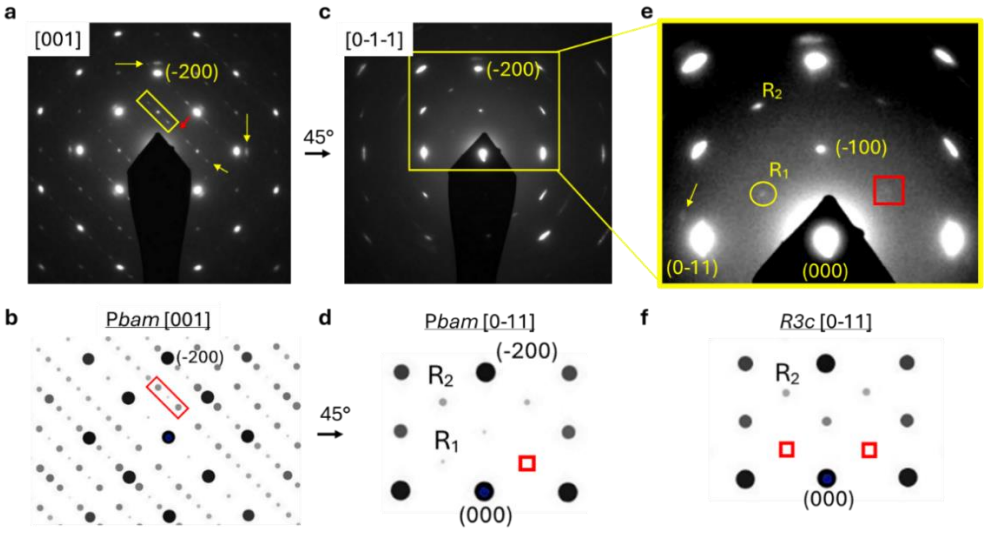


***Figure 4.3.*** *Electron diffraction experiment for the 36 nm membrane,* ***(a)*** *EDP from* $[001]_{PC}$ *zone axis, showing weak ¼ order reflection in* $<110>_{PC}$ *directions,* ***(b)*** *Simulated EDP of the Pbam phase from [001] zone axis,* ***(c)*** *EDP from* $[0\text{-}1\text{-}1]_{PC}$ *zone axis after tilting the sample 45°,* ***(d)*** *Simulated EDP of the Pbam phase from* $[0\text{-}1\text{-}1]_{PC}$ *zone axis,* ***(e)*** *Magnified image of the square box in* ***b****,* ***(f)*** *simulated EDP of the R3c phase from* $[0\text{-}1\text{-}1]_{PC}$ *zone axis*

We further used annular bright field (ABF) imaging to obtain atomic positions of lead and zirconium as well as oxygen atoms (**Figure 4.4,** additional figures in **Appendix E5**). We observe a continuous variation of Pb atom displacements , where the majority of the displacements are seen in $<110>_{PC}$ directions as well as regions of $<100>_{PC}$ displacements and regions of no apparent displacements. Oxygen displacement mapping of the same region shows that there is a continuous variation of oxygen atom displacement as well. We see regions of different combinations of Pb displacements and oxygen chain linearity, that can be used to infer the phases present (note on interpretation of phases is presented in **Appendix E3**):

1. Pb displacement in $[110]_{PC}$ direction with oxygen chains zigzagging in two orthogonal directions: ferroelectric rhombohedral phase (R3c) (yellow box), which is the majority ferroelectric phase.
2. Pb displacements in $[-110]_{PC}$ direction with oxygen chain zigzagging in one direction and linear in the orthogonal direction: ferroelectric monoclinic phase (Pc) (red box) (we will discuss the Pc phase in more detail in the D**iscussion** section, see also **Appendix E1** and **E3**).
3. Pb displacements in $[100]_{PC}$ direction with almost no oxygen displacements (linear chains in two orthogonal direction): possibly a tetragonal ferroelectric (I4cm) phase (orange box).
4. Regions of no Pb displacements or oxygen displacements (colinear chains): possible cubic phase, or Pb displacement out of plane. In the latter case, these kinds of modulations are also consistent with I4cm phase.

Other than the regions consisting of well-defined phases, we also see disordered regions. These regions are defined as where the Pb displacement modulation and the corresponding oxygen chains do not match any phase, rather the two distortion types seem to be decoupled. Examples of such regions are shown in **Figures 4.4b** and **d** as purple arrows, along which, although the Pb displacement changes in magnitude and direction, the oxygen chains (representing the octahedral tilt) seem to maintain their pattern, or vice versa. As discussed previously, these disordered regions act as low energy pathways of transformation between different phases. However, the spatial distribution is difficult to pin down. One example would be the speculated tetragonal like phase as discussed above, whether these regions are disordered simply connecting two well defined phases or they adopt a well-defined phase themselves. The bottom line, at any rate, is that already in membranes as thick as 36 nm there is a departure away from the pure antiferroelectric Pbam phase, manifested as a co-existence of nano-domains of different symmetry.

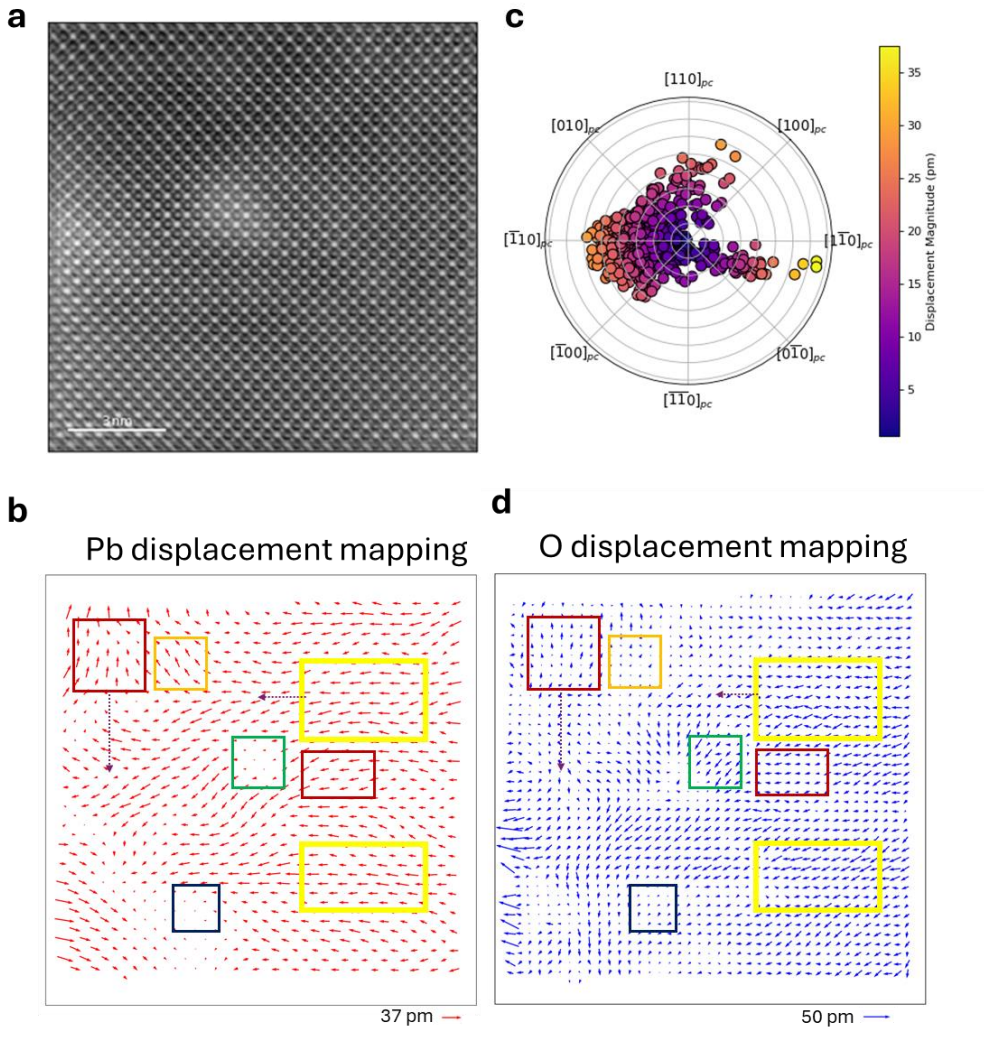


***Figure 4.4.*** *STEM of 36 nm membrane* ***(a)*** *ABF image (contrast inversed),* ***(b)*** *Pb displacement mapping,* ***(c)*** *Polar map of Pb displacements (the directions in the map correspond to the directions in the ABF image),* ***(d)*** *O displacement mapping.*

## 4.4.2. 17 nm PZO membrane

In 17 nm membrane, we observe a strong dependence of the phase composition on the relaxation state of the suspended sheet, where we see two kinds of drumheads, one without a star-shaped pattern and one with.

Here, we discuss the drum without the pattern (the drumhead with star- shaped pattern is analysed in **Appendix E4**). We perform a similar rotation experiment to obtain EDP from different zone axes. The $[001]_{PC}$ pattern (**Figure 4.5a**) features ¼ $\{110\}_{PC}$

reflections along two mutually orthogonal directions indicating 90 degree domains of $[001]_{PC}$-oriented Pbam domains.

Looking in detail (enlarged image in the right panel of **Figure 4.5a**), we also observe ¼ $(100)_{PC}$ superlattice reflections. To our knowledge, this modulation has not been observed before in PZO but is characteristic of other perovskites with Pnam space group. In fact, this space group has been proposed to be the ground phase of PZO from first- principle calculations (crystal structure of the Pnam phase of PZO is shown in **Appendix E2**). The lack of experimental evidence of this phase was attributed to the suppression of the phonon modes by quantum fluctuations.[26] Moreover, it has been observed that the 90-degree domain walls of antiferroelectric Pbam phase in PZO, with head-to-head and tail-to-tail configuration can form an ordered array of topological vortices and antivortices,[139] and the lead displacement pattern in these regions is very similar to the one predicted for the Pnam phase. It is therefore possible that the 90° domain walls of Pbam phase themselves adopt the Pnam structure, or act as nucleating points for this phase to grow. However, such head-to-head and tail-to-tail domain walls are energetically unfavourable, and they are annihilated under electron beam exposure by the movement of the domain walls resulting in a head-to-tail arrangement and a translation boundary. It therefore seems more likely that the Pnam structure only exists as a bridging phase between Pbam domains, suggesting a high corelation between the Pbam and Pnam phases.

After tilting the sample by about 16° to the $[103]_{PC}$ zone axis (**Figure 4.5b)** , the pattern obtained still contains strong contributions from the $[001]_{PC}$ zone axis due to the bending of the suspended regions. The reflections corresponding to $[103]_{PC}$ zone axis are marked in circles. From this zone axis, the $(0\ 0\ ¼)_{PC}$ reflections are more pronounced in two orthogonal directions.

Tilts about the $<112>_{PC}$ zone axis are also shown in the **Figure 4.5c**. EDP from $<112>_{PC}$ zone axis at about 35° from the film normal, can be explained entirely by a combination of the diffraction patterns of the $[1\text{-}12]_{PC}$ and $[112]_{PC}$ Pbam zone axis. Meanwhile, superlattice reflections at ¼ $(hkl)_{PC}$ positions can be explained by combining $[211]_{PC}$ and $[2\text{-}11]_{PC}$ Pnam structure. The $[101]_{PC}$ zone axis EDP (**Figure 4.5d**) exhibits R-type spots common to both Pbam and Pnam structure. Moreover, satellites with modulation wave vector approximately aligned with the $<111>_{PC}$ directions are attributed to the AFE modulations brought into diffraction by the coexistence of $\{110\}_{PC}$ twin domains and bending. Finally, the EDP from $[111]_{PC}$ zone axis (**Figure 4.5e**) shows no superlattice reflections, which can be due to the increased length of the beam path through the membrane.

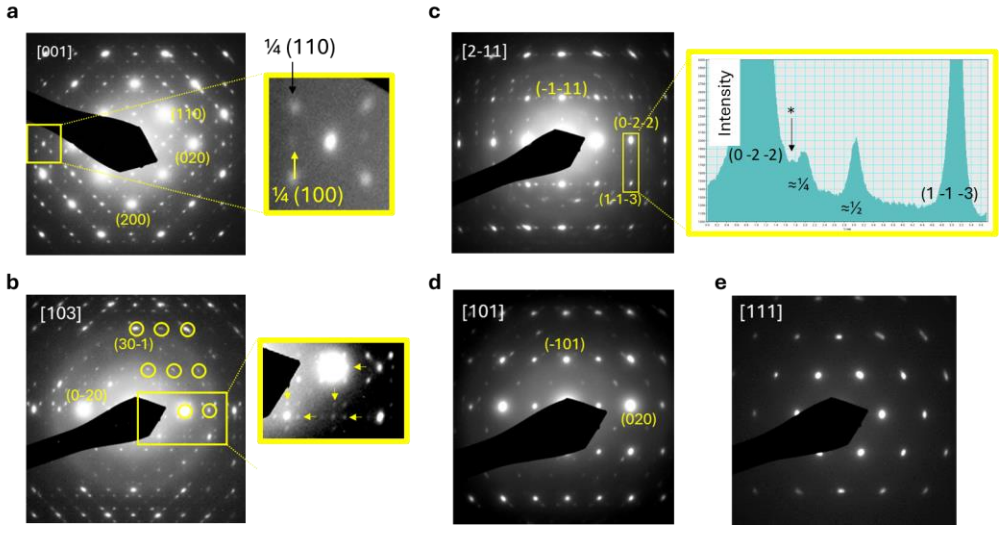


***Figure 4.5.*** *Tilting + Electron diffraction experiment of 17 nm PZO membrane, EDP from different zone axis:* ***(a)*** *$[001]_{PC}$, right panel shows the zoom in region of the yellow square* ***(b)*** *$[103]_{PC}$,* ***(c)*** *$[2\text{-}11]_{PC}$,* ***(d)*** *$[101]_{PC}$,* ***(e)*** *diffraction pattern from $[111]_{PC}$ zone axis.*

### 4.4.3. 5 nm PZO membrane

Electron diffraction patterns for the 5 nm PZO membrane from three zone axis, $[001]_{PC}$, $[110]_{PC}$ and $[111]_{PC}$, are shown in **Figure 4.6a-c**. The primary reflections are marked as yellow circles. Additional spots marked as yellow arrows will be discussed later. There are many superlattice reflections that appear in the electron diffraction patterns. From $[001]_{PC}$ zone axis (**Figure 4.6a**), superlattice reflections at ½(hk0) can be observed. These reflections can arise from both $a^0a^0c^+$ and $a^-a^-c^0$ tilt systems, where the difference is that the $a^0a^0c^+$ tilt system does not give reflections for $h = \pm k$ rows, while $a^-a^-c^0$ does not give for $h = k$ row only. From this diffraction pattern, it is difficult to discern between these two tilts since the common reflections might be more visible, while the other spots with the certain extinction rules might be too weak. On the other hand, diffraction done from $[110]_{PC}$ zone axis (**Figure 4.6b**) does not give any spots for the $a^0a^0c^+$ tilt system. Here, however, we can observe superlattice reflections at ½(*ooo*) spots originating for anti-phase tilting. While $a^-a^-a^-$ tilts give superlattice reflections at $h \neq k \neq l$ i.e. R2 (marked as red squares), other superlattice reflections in orange circles (R1 spots) can appear due to $a^-a^-c^0$ systems, hence the two systems cannot be distinguished. We can also observe ½(-*hh*0) spots, although very weak that generally appear due to antiparallel modulation of Pb in both the AFE Pbam and the FE Pc phase (green boxes). Finally moving to $[111]_{PC}$ zone axis, the diffraction experiment reveals ½(-*hh*0) (red arrows) spots that are consistent with $a^0a^0c^+$ as well as $a^-a^-c^0$ tilting. The $a^0a^0c^+$ tilting can result in these spots in all $<111>_{PC}$ zone axes, while $a^-a^-c^0$ can cause the reflections only in some of the $<111>_{PC}$ zone axes. However,

access to all $<111>_{PC}$ zone axes is not possible in our planar view membrane samples, rendering the distinction between the tilts impossible.

We also observe strong diffused scattering in our membranes throughout the diffraction experiments. In the $[001]_{PC}$ zone axis, the diffused streaks run along the $<110>_{PC}$ directions, suggesting a continuum of dipole-line arrangements consistent with IC phases. The diffused streaks in $[110]_{PC}$ zone axis, however, are along the $<112>_{PC}$ directions, which might be related to the diffused scattering observed in the previous diffraction pattern. Such diffused streaks have been previously observed from $[531]_{PC}$ zone axis in PZT systems in the R3c region of the phase diagram.[140] Experiments and simulations suggest that this kind of disorder comes from the Pb atoms being only highly coherent along the individual chains, while the chains lack correlation among them.[141] The phase transition in PZT hence is a diffused one where the range of order changes continuously. Since we are working with pure PZO membranes, we can safely ignore the ordering of the B-cations as in case of PZT as the cause of this disorder.

To understand the diffraction patterns, we consider two possibilities. One is that there are two phases that give rise to the diffraction patterns: one with $a^-a^-c^0$ tilt and one with $a^0a^0c^+$. The former tilt system can exist within the IC phases, suggested by the diffused streaks while the $a^0a^0c^+$ tilt system corresponds to the monoclinic phase . The other possibility is the presence of $a^-a^-c^+$ tilt corresponding to the monoclinic phase. Since it is difficult to distinguish between these two cases, we must consider both as probable. We will discuss this in more detail in the **Discussion.**

To investigate the origin of the additional spots (marked as yellow arrows), we obtain a low magnification HAADF image in one of the regions **(Figure 4.6d**). The image shows regions of two different contrasts and taking the FFT of this image (**(Figure 4.6e)**, we can observe the same spots as the electron diffraction. Marking these additional spots and taking the inverse FFT (i-FFT in **Figure 4.6f)** indicates that these additional spots come from the darker region of the HAADF. We speculate that these regions are highly strained regions of PZO that did not completely relax during the etching process and are frozen due to misfit dislocations. The GPA rotation of the same region shows high strains in these regions (**Appendix E7**).

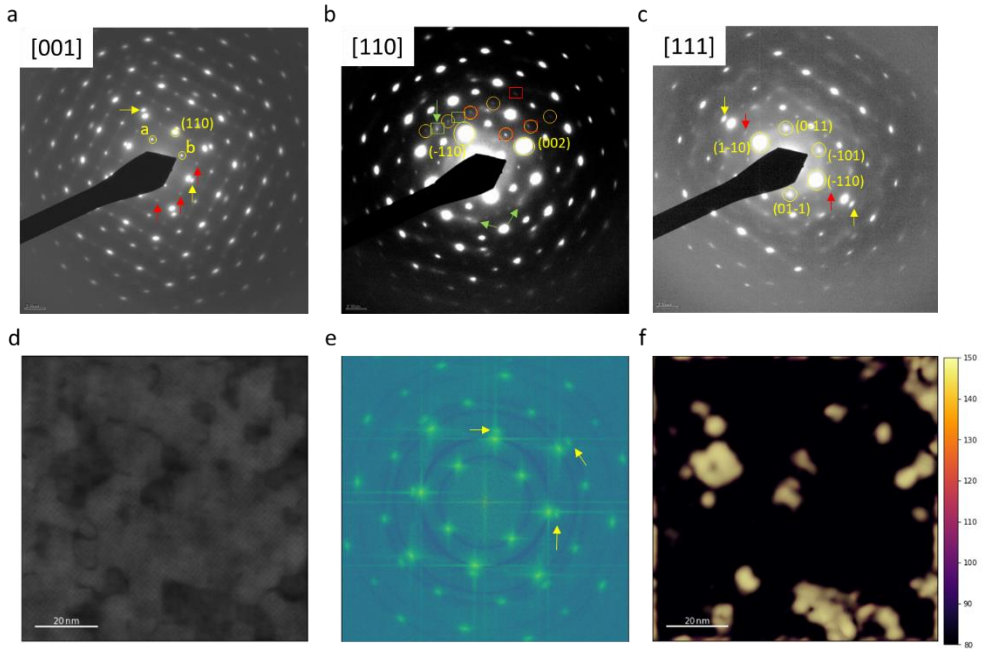


***Figure 4.6**. Electron diffraction patterns for 5 nm PZO membrane from **(a)** [001]$_{PC}$ zone axis, **(b)** [110]$_{PC}$ zone axis **(c)** [111]$_{PC}$ zone axis **(d)** Low magnification HAADF image of 5 nm PZO membrane, **(e)** FFT of the image in (d), **(f)** i-FFT of the spots marked as yellow arrows in (e).*

Then we move to ABF imaging of the areas that are not affected by these strained regions and high dislocations; two such regions are shown in **Figure 4.7** (and **Appendix E6**). The Pb displacement and O displacement shows a very similar picture as that of the 36 nm membrane, exhibiting regions of R3c, Pc and tetragonal phases.

However, as we discussed before, the diffraction patterns (that probe the whole volume) for the 36 nm and 5 nm membranes are drastically different. The different results from the high-resolution imaging and electron diffraction suggests that the phases that condense on the surfaces of the membranes are the same irrespective of the thickness, while the main phase transitions occur in the bulk.

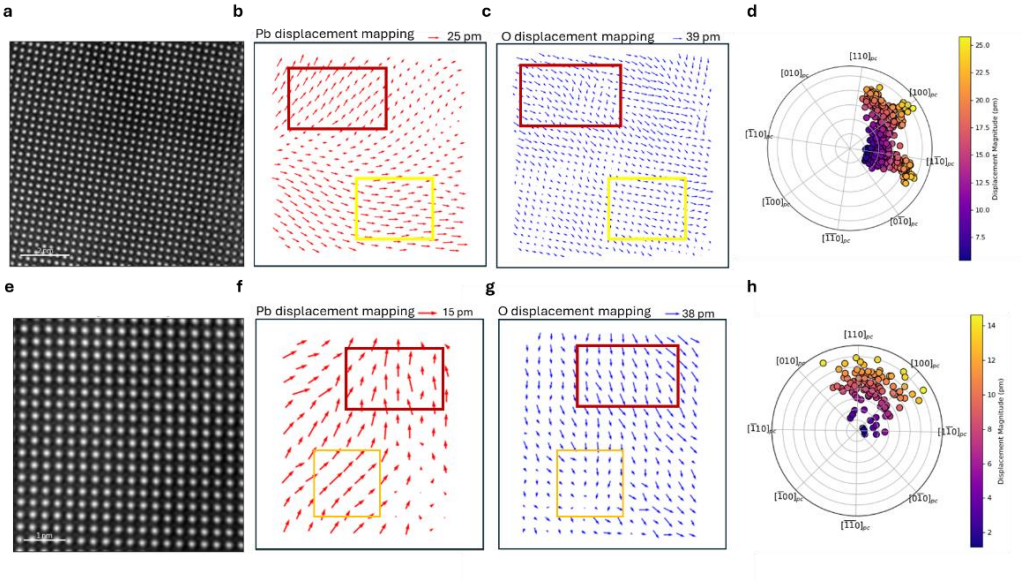


***Figure 4.7.*** *ABF imaging of two regions of 5 nm PZO membrane where* ***(a, e)*** *ABF image,* ***(b, f)*** *Pb displacement mapping,* ***(c, g)*** *O displacement mapping,* ***(d, h)*** *Polar maps. Yellow rectangles mark the R3c phase, orange rectangle marks the tetragonal- like phase and red rectangles mark the Pc phase. The directions in the polar maps also act as the compass for the ABF images.*

The phase mixing in the three membranes that we have investigated is very intricate and rich. The presence of the phases interpreted by EDP or ABF imaging is summarized in **Table 4.1** for the different thicknesses. However, the overall pattern that appears is as the thickness of the membranes decreases, they tend to become more ferroelectric, and the antiferroelectric phases are suppressed.

**Table 4.1**: Summary of the phases present in different thicknesses of PZO

| **Thickness of the membrane** | **Phases interpreted** | |
|---|---|---|
| | ***from* EDP** | ***from* ABF** |
| 36 nm | • AFE: *Pbam*<br>• FE: *Pc*<br>• IC | • FE: *R3c*<br>• FE: *Pc*<br>• FE: *I4cm* (Speculated) |
| 17 nm | • AFE: *Pbam*<br>• AFE: *Pnam*<br>• IC<br>• FE: *Pc* | ---------- |
| 5 nm | • FE: *Pc*<br>• IC phase and/or disordered *R3c* phase | • FE: *R3c*<br>• FE: *Pc*<br>• FE: *I4cm* (speculated) |

## 4.5. Discussion

### 4.5.1. Monoclinic phase in PZO

The existence of a monoclinic phases in PZT has been under extensive discussion in the literature. In the PZO-PZT phase diagram, monoclinic phases appear as bridging phases between the AFE Pbam and FE R3c phase as well as between FE R3c and P4mm phases. The tilt system that has been assigned to the latter case is $a^0a^0c^+$ and is suggested to be an intermediate tilt system between $a^-a^-a^-$ in R3c and no tilting in P4mm, and Pb displacement along $[uuv^*]_{PC}$. The resulting phase with these tilts and displacements is Cm.[142,143] The other monoclinic phase, Pc that appears between Pbam and R3c phases was also assigned the same tilt system.[144,145] The symmetry is lower in the Pc phase because Pb atoms also have a small AFE modulation. Recently, this Pc phase was also observed in pure PZO and associated to the same Pb displacement vectors and tilt. It is still unclear, however, which tilt system the monoclinic phase of PZO possesses, $a^0a^0c^+$ or $a^-a^-c^+$. I will discuss both cases briefly.

The tilt system in the monoclinic phase in PZT was found to be $a^0a^0c^+$ based on neutron diffraction done by Fu. et. al.[145] They further performed Rietveld refinements which surprisingly, does show some small antiphase tilts in the octahedrals (structure drawn in **Appendix E1**). Liu et. al also excluded $a^-a^-c^+$ tilt system because of the absence of diffused streaks in FFT corresponding to ½ {001}PC reflections in PZT thin films.[144] However, these streaks do not originate from $a^-a^-c^+$ tilt system but rather from the coexistence of orthorhombic and rhombohedral phases as in the case of $BiFeO_3/NdGaO_3$ epitaxial stacks.[146] It is, however, important to note that all these investigations were performed on PZT, rather than pure PZO and there might be subtle differences in the lattices. On the other hand, the phase transitions in PZO are very similar to the transitions in PZO- PTO phase diagram, and hence $a^0a^0c^+$ is also possible.

In pure PZO, the signatures of the "non-rhombohedral" ferroelectric phase were first observed by Liu et. al.[131] in thin films grown on SRO buffered STO (001) substrate. The authors here noted that the tilt system had a $c^+$ component rather than $c^0$ (as in the case of Pbam_ $a^-a^-c^0$) or $c^-$ (as in R3c) in the ferroelectric phase. Moreover, in PZO, the tilt axes rotate along with the displacement vectors, i.e. Pbam has both vectors in $<110>_{PC}$, and R3c in $<111>_{PC}$. Additionally, the theoretically predicted tetragonal phase in PZO with symmetry I4cm with [001] polar direction has the tilt system $a^0a^0c^-$. Therefore, the same trend might also exist in Pc. This pattern would suggest that the tilt system is indeed $a^-a^-c^+$ in the monoclinic Pc phase that acts as a bridge between Pbam and R3c phases.

Our diffraction studies on specifically 5 nm PZO membrane can be explained by both the presence of two phases with different tilt systems ($a^-a^-c^0$ and $a^0a^0c^+$) or the presence of the tilt system $a^-a^-c^+$. In the former case, if the diffused streaks that we observe in the SAED patterns come from the incommensurate phases (that have been assigned the tilt system similar to Pbam), the monoclinic phase would have the tilt system $a^0a^0c^+$.On the other hand, the diffused streaks might also arise from disorder in the rhombohedral

phase. In this case, the diffraction pattern will be consistent with the monoclinic phase having the $a^-a^-c^+$ tilts. The presence of $a^-a^-c^+$ has also been predicted in PZO from theoretical calculations in Pnam phase (both 80 and 40 atoms unit cell phases),[26,147] although the phases studied in these calculations were antiferroelectric.

Therefore, to make a case for either of the tilt system in our studies, we need to first observe the origin of the diffused streaks. For this purpose, STEM investigations on cross-section of 5 nm PZO membranes (from $[010]_{PC}$ and $[110]_{PC}$ zone axes) are under progress. Regardless, one thing that is agreed upon is that the monoclinic phase is ferroelectric and therefore, the transition from AFE to FE phases as the thickness decreases is clear.

### 4.5.2. Origin of the size-dependent phase transition and phase mixing

To summarize our observations, we find that membranes of PZO across all thicknesses exhibit an intricate mixture of different antiferroelectric, IC and ferroelectric phases. The general trend of the transition from an antiferroelectric nature to a ferroelectric nature, as seen in PZO epitaxial films[108] and $NaNbO_3$ membranes[148] also persist in PZO membranes but, crucially (and surprisingly, given the lack of epitaxial strain), at much higher critical thicknesses; our membranes already show a high concentration of ferroelectric phases at 36 nm, whereas in epitaxial films grown on STO (compressive residual strain) the ferroelectric phase appears around 15 nm.[131]

In PZO epitaxial films, structural transitions and presence of a ferroelectric phase have previously been attributed to epitaxial and misfit strains.[108,149] However, our observations here show that, despite the absence of epitaxial clamping, antiferroelectric membranes still have a similar tendency towards ferroelectricity. This observation is consistent with studies on $NaNbO_3$ membranes as well as theoretical predictions on PZO.[134,148] Additionally, the phase mixing seems to get more complex in membranes of PZO compared with epitaxial films, with the phase coexistence spanning much higher thickness ranges, as well as including novel and non-trivial phases. We attribute this to different extrinsic effects that are enhanced in the absence of epitaxial clamping, which include surface effects, micro bending and localized strains. There are two major points to note here:

1. The contribution from surface effects in the AFE to FE transition in PZO have been reported to induce FiE near the surfaces of a single crystal.[131] In PZO, surface tension can modify the tilting pattern and destabilize antiferroelectricity in favour of ferroelectricity. Moreover, theoretical calculations show that charge-compensating surfaces can help stabilize the FE phase.[134] Surfaces under short-circuit boundary conditions reduce energy-costly depolarization fields, allowing ferroelectric polarization to emerge. From our results, despite the absence of any electrodes, when we remove the film from the substrate, thereby increasing the

free surfaces, the membrane becomes ferroelectric. First, this signifies that free surfaces, alone can induce phase transitions in the absence of epitaxial clamping. Second, the presence of electrodes at the surfaces to provide charges is not a necessary ingredient for such phase transitions but can come about by either surface tension effects (compressive stresses)[135] or by adsorbates;[150] and third, the phases condensing on the surfaces of the membranes of the different thicknesses seem to be very similar. We speculate that the surface-induced ferroelectric phases may have a finite penetration depth. Our planar view observations can be explained by considering that in thicker membranes, there is an AFE region sandwiched between the two FE regions, whereas, as the membranes get thinner, this AFE region decreases until it is completely suppressed completing the phase transition. TEM in cross-sectional cuts should help us confirm this thickness evolution.

2. The phase transition sequence from AFE to FE occurs in the PZO-PTO (or with some other dopants like La) phase diagram.[108,151] As PZO is doped with Ti, the material goes from Antiferroelectric Pbam to ferroelectric R3c and finally to tetragonal ferroelectric P4mm. These phase transitions involve rotation of dipoles from being antiparallel in $<110>_{PC}$ (Pbam) to parallel in $<111>_{PC}$ (R3c) and finally, parallel in $<001>_{PC}$ (P4mm).[143,145,151] This sequence is enabled by the simultaneous change in the AFD order i.e. the axis of octahedral tilt rotates as well and matches the polarization vector. Between these phases, monoclinic phases emerge of symmetries Pc (between Pbam and R3c)[108,151] and Cm (between R3c and P4mm).[142] The extreme point of this phase diagram, PTO, hence, shows ferroelectricity with [001] polar direction and no oxygen octahedral tilts. In pure PZO, a similar phase transition was observed as a function of thickness,[108] apart from the appearance of FiE Ima2 phase that does not occur in PZT. In our case, we do not observe the Ima2 phase and neither a clear sequential transition, rather a mixture of phases. However, the common trend of suppression of the AFE order is maintained. The complex phase mixture and lack of a defined sequence may arise from the declamping of thin films and transferring to perforated substrates where localized bending and inhomogenous strains may derive the system towards different energy minima and disorder.

In our case, it is difficult to say which of the factors: suppression of Σ (anti-polar) mode or the M and R modes (structural instabilities driving tilts) is the leading mechanism for the AFE-FE phase transition. Since our membranes are single layers suspended on perforated substrates, we can attribute compressive forces due to surface tension to cause the transition via the tilts.[135] Theory suggests that the phase transition is brought on about the suppression of the Σ (anti-polar) mode by charge compensating surfaces,[134] the stabilization of ferroelectricity is further helped by depolarization field screening, either by adsorbates or (and) by the propensity of PZO to break down into

smaller domains having different phases with different polarization directions that may allow it to reduce the depolarizing fields.

Although, the AFD and AFE/FE orders are coupled strongly, in the case of PZO (as with PZT), the two degrees of freedom decouple during transitions between two local minima and thus new symmetries can emerge. These are generally termed as intermediate or bridging phases and are often disordered structures. Their disorder is also linked to the flatness of the phonon branch between the M and the R points. The best evidence for this disorder comes from diffused scattering studies that show that even the parent phase has a lower symmetry than the cubic one.[27,152] This disorder is retained even below Curie temperature as seen in our diffraction study resulting in elliptical spots and diffused streaks.

A question then arises: why are the surfaces of the membranes overwhelmingly polar as compared to cross-sections of epitaxial films even though, in the latter, the FIB exposes the surface being observed? One possible explanation is that, unlike epitaxial films, the membranes undergo annealing after transfer to mitigate the pervasive hydrogenation. This annealing is done above the Curie temperature, effectively removing any energy barriers between the different phases. Hence, this allows the membranes to transition into the stable ferroelectric phase near the surface during cooling. Moreover, as we saw in **Chapter 2** (and we will again in **Chapter 5**), the PFM measurements do not identify presence of ferroelectric domains on the surface of membranes, which is seemingly inconsistent with our TEM observations. A possible explanation for this is the surface confinement of ferroelectricity, which will them be strongly affected by depolarizing fields that will tend to break the FE polar order into small up and down domains. Given the expected small size and random distribution of these domains. PFM resolution may not be good enough to observe this polydomain configuration. This polydomain state might also contribute to the disorder seen in PZO.

## 4.6. Implications and conclusions

Phase coexistence has interesting implications for electronics, specifically memory devices. The presence of different phases due to the flat energy landscape, enhanced by local strains and surface tensions, means that small external perturbations can drive the system (at least locally and/or transiently) to a different energy minimum, corresponding to different non-polar or polar states. This multi-state polarization can in turn be effectively used to control the macro-scale polarization of the material, thus providing an opportunity for antiferroelectric membranes to be used in neuromorphic elements,[44] both as artificial neurons, where volatility is needed, and synapses, where non-volatile memory retention is required, we will explore these possibilities further in **Chapter 6**.

Moreover, the disorder seen in the membranes across all thicknesses is interesting in itself. Order-disorder phase transitions were predicted in PZO and PZO-based

materials as low energy pathways between different phases as discussed above. However, the spatial existence of such disordered regions between different phases has not been thoroughly discussed. Recently, a lot of interest has grown where non-ergodic relaxor ferroelectric behaviour is induced in materials that are typically ferroelectric or antiferroelectric.[153–156] This relaxor-like behaviour is usually brought about by doping the materials that can frustrate the long-range order to create nano-polar regions inducing disorder. Disorder in such materials in turn allows us to manipulate the electrical switching behaviour by reducing the hysteresis (hence, energy loss) as well as making the switching more diffused. The result is an increase in the efficiency, energy storage and breakdown strengths of such materials. Meanwhile, here we show that membranes based on pure PZO display this behaviour inherently. This opens a new pathway for designing electronics alternative to compositional tuning, based on nominally antiferroelectric materials. However, in order to follow that pathway, further understanding on phase coexistence and phase stabilization mechanisms requires microstructural studies such as the one initiated in this thesis.

Chapter 5

# Strain effects in PZO membranes

## 5.1. Introduction

As discussed in the introduction of **Chapter 3**, one of the advantages of epitaxial growth is strain engineering, whereby a suitable substrate or a buffer layer can be used to epitaxially strain the functional film. By choices of different substrates, we can change the strain in the film from a compressive to a tensile regime. This has proven to be a very successful strategy to tune properties of perovskites, for example, ferroelectricity in $SrTiO_3$ films[157] as well as controlling the polarization and curie temperatures in $BaTiO_3$.[158]

In the case of PZO, there are not many choices of substrates or buffer layers to strain it due to its large lattice parameter (**Figure 5.1)**.[159] Conventionally, PZO is grown on commonly used substrates such as $SrTiO_3$, $DyScO_3$, $GdScO_3$ or $NdScO_3$ that have misfits of 2.75-4% in the best case of $NdScO_3$, resulting in misfit dislocations that rapidly relax the strain. Recently, a buffer layer of $LaLuO_3$ has been successfully utilized to stabilize antiferroelectricity down to 9 nm by tensile strain, leading to almost zero remnant polarization.[160] Despite this, we still do not have many options to study PZO in different regimes of strains. PZO, however, remains an interesting material for strain engineering due to the rich landscape of coexisting phases (as we have seen in the previous chapter) and their dependence on the strain state. Moreover, the volume expansion of the lattice due to the electric field-induced phase transition also causes a direct correlation of functional properties with strain conditions.

Membranes again serve as a special platform for strain engineering. Although PZO and other perovskites tend to be brittle as bulk, in the low thickness regimes, their mechanical properties change, and they become very flexible.[46,161,162] Moreover, the presence of domain walls also provide elasticity to the PZO systems.[163] Hence, membranes may be used to study the properties of materials under extreme strain conditions, beyond what epitaxial growth can enable. Uniaxial stretching has been a successful methodology to induce ferroelectricity in STO membranes, and study the effect of strains and strain gradients on the domain structures of ferroelectrics such as BTO and PTO.[162,164,165] Recent works on PZO also showcase the flexibility of membranes and the effect of strains on the switching behaviour of PZO capacitors.[161] Here, we study the effect of strain states on PZO , ranging from homogenous strain induced by substrate curvature to extreme strain gradients induced by membrane wrinkling.

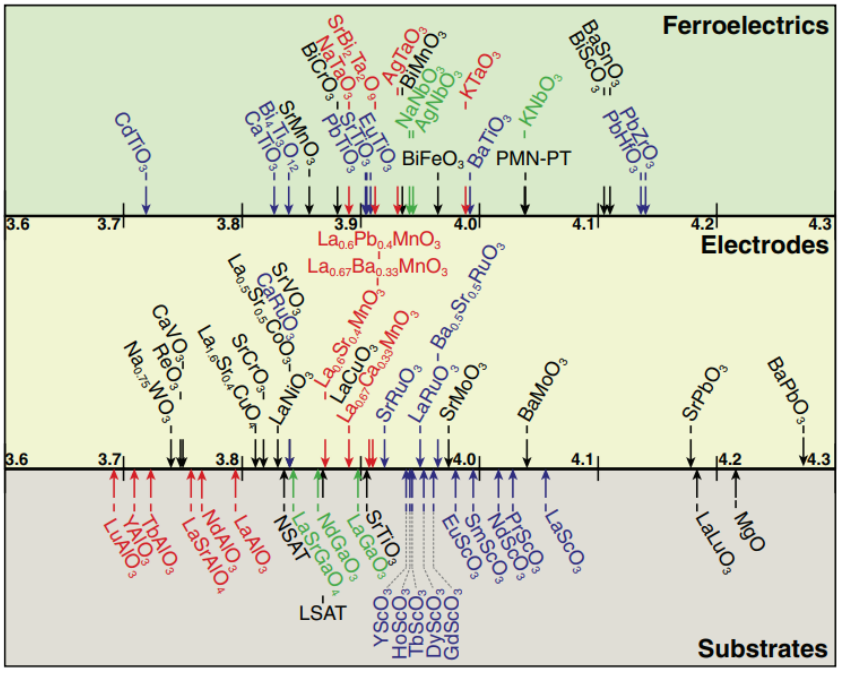


***Figure 5.1.*** *Lattice parameters of different materials that can be used as substrates (bottom section), electrodes (middle section) and functional materials (top section), representing the isolation of PZO in terms of lattice matching materials (used with permission of IOP Publishing Ltd., from "New modalities of strain-control of ferroelectric thin films", A. R. Damodaran, J. C. Agar, S. Pandya, Z. Chen, L. Dedon, R. Xu, B. Apgar, S. Saremi & L. W. Martin, J. Phys.: Condens. Matter* ***28****, 263001 (2016) (ref 159)).*

## 5.2. Macroscopic strain via bending

PZO capacitors can be transferred to a flexible substrate and strained via bending; as long as the mechanical neutral plane is outside of the film, there will be a net strain in addition to the strain gradient (due to the curvature). However, there is a limit to how much a substrate can be bent, imposed both by the mechanical properties of the substrate and the deposited electrode as well as the possibility of PZO to slip and relax over the bent substrates due to insufficient adhesion. In this context, I present a way of transferring the membrane to polymeric substrates by gold bonding and bending the structures via cylindrical moulds.

### 5.2.1. Gold bonding for membrane transfer and straining stage

The transfer of membrane capacitors onto flexible substrates is an effective method of applying strain. However, the conventional method of transferring the membrane involves the membrane adhering to the secondary substrate via Van der Waal´s forces, and, in presence of high strains, the membrane can relax by sliding on the substrate. Therefore, it is important to have a good adhesion between the substrate and the membrane to ensure a proper transfer of strain. To achieve this, we employ

thermocompression of gold,[166,167] a commonly-used method in the semiconductor industry, schematic shown in **Figure 5.2a**. We start by depositing gold films of 5 nm on top of both our epitaxial stack (35 nm SRO/300 nm PZO/ 35 nm SRO/SAO//STO (001)) and the substrate, Kapton tape in this case. This deposition is done via sputtering which allows strong bonding between the gold and the film/Kapton. We then bring the two gold layers in contact, clamp them together using a house-made clamping system and anneal the system (still clamped) in vacuum at 250ºC for 4 hours. This causes the two gold layers to bond via interdiffusion, and hence the membrane capacitor is firmly attached to the Kapton. The whole assembly (epitaxial stack + Kapton in the clamping system) is placed in water for the SAO to etch, after which the substrate is removed.

We applied strain on our membranes via bending onto a copper stage with protrusions of different radii of curvature, ranging from 5 mm to 0.5 mm in the positive (convex) curvature case and 3.6 mm in the negative (concave) curvature case. By applying opposite curvatures, we can deliver both tensile and compressive strains. However, we are limited to lower values of compressive strain due to geometry restrictions for contacting the probes to the top electrodes.

While applying strains by bending the samples, one side effect is, of course, the existence of strain gradients in the functional layer. This cannot be avoided, but the ratio of strain to strain gradient can be maximized by choosing a thick enough secondary substrate, so that the neutral bending plane is far away from the film. In our case, the thickness of the Kapton tape is 120 μm compared to the 370 nm capacitor thickness. The neutral plane, hence, lies 54 μm away from the membrane- Kapton interface, inside the Kapton substrate. The neutral plane is not in the dead center of the substrate because the higher Young's modulus of the film does skew the location of the neutral plane towards it; the equation used to determine the location of the neutral plane from the top surface is:[161,168]

$$y = \frac{\frac{\gamma_K t_K^2}{2}+\gamma_G t_G\left(t_K+\frac{t_G}{2}\right)+\gamma_{SRO} t_{SRO}\left(t_K+t_G+\frac{t_{SRO}}{2}\right)+ \gamma_{PZO} t_{PZO}\left(t_K+t_G+t_{SRO}+\frac{t_{PZO}}{2}\right) + \gamma_{SRO} t_{SRO}\left(t_K+t_G+t_{SRO}+ t_{PZO}+\frac{t_{SRO}}{2}\right)}{\gamma_K t_K+\gamma_G t_G+\gamma_{SRO} t_{SRO}+\gamma_{PZO} t_{PZO}+\gamma_{SRO} t_{PZO}} \quad (5.1)$$

Where $\gamma$ are the Young´s modulus and t is the thickness of each layer, K in subscripts stand for Kapton, G for gold. The values for Young´s modulus are 217 GPa for PZO,[169] 161 GPa for SRO,[170] 2.76 GPa for Kapton tape and 75 GPa for Gold.[171]

Strain on the top surface can then be calculated as

$$\varepsilon = y/R \quad (5.2)$$

Where R is the bending radius.

In our case of highest curvature of 1.767 $mm^{-1}$ , the calculated strain gradient comes out to be ~1767 $m^{-1}$. This corresponds to a flexoelectric field of 0.052 kV $cm^{-1}$ (flexocoupling of PZO ~ 3 V)[29] or flexoelectric polarization of 6.9 x $10^{-4}$ μC $cm^{-2}$ (flexoelectric coefficient = 3.9 nC $m^{-1}$)[29] and therefore strain gradient effects can be safely neglected (**Figure 5.2b**).

To verify the transfer of strain to the membrane capacitor via this method, we attach the stack to the copper stage with a bending radius of 5 mm. This corresponds to an in-plane strain of 1.07 % (tensile) on the capacitor (the strain value of 1.07% is the *geometric* strain calculated from the curvature).

We compare the diffractograms of the flat stack vs the bent stack **(Figure 5.2c)**. Since the diffractogram of the bent PZO membrane (orange curve) also includes the peaks from the bending stage, we include the diffractogram of the stage as well for reference (red curve). In both strain states (flat and curved with 5 mm radius of curvature), the PZO membrane shows two domain orientations: $(120)_O||(100)_{PC}$ and $(001)_O||(001)_{PC}$. While the flat membrane shows the PZO and SRO peaks very close to the bulk values: 0.416 nm for PZO $(120)_O$, 0.411 nm for PZO $(001)_O$ and 0.393 nm for SRO $(002)_{PC}$, there is a shift of all peaks to higher 2theta angles (and therefore smaller out-of-plane lattice parameters) under in-plane tensile strain; this out-of-plane compression is determined by the Poisson's ratio of the material. The calculated out-of-plane strains for the bent membrane are -0.4% for PZO $(120)_O$, -0.38% for PZO $(001)_O$, and -0.6% for SRO $(002)_{PC}$. Using the measured out-of-plane strain and bulk Poisson´s ratio for PZO (0.34)[172] and SRO (0.33),[173] the *expected* in-plane tensile strains calculated are 1.11% for PZO and 1.15% for the SRO layer, which are higher than the geometric strain, giving an efficiency of strain transfer higher than 100%. This discrepancy may be caused by the lower thicknesses of the layers, inducing a change in the mechanical properties of the thin films (i.e. Poisson´s ratio might be higher in membranes) or anisotropy of the strain. In any case, the method to induce strain via bending seems to be an effective strategy. Moreover, we also see a change in the relative domain population of the PZO membrane: as interpreted from the intensity of the XRD peaks, the $(001)_{PC}$ domains increase (the fittings are shown in **Appendix F1**). This is due to the compressive strain in the out-of-plane direction, which favours the domains with shorter lattice parameter in that direction.

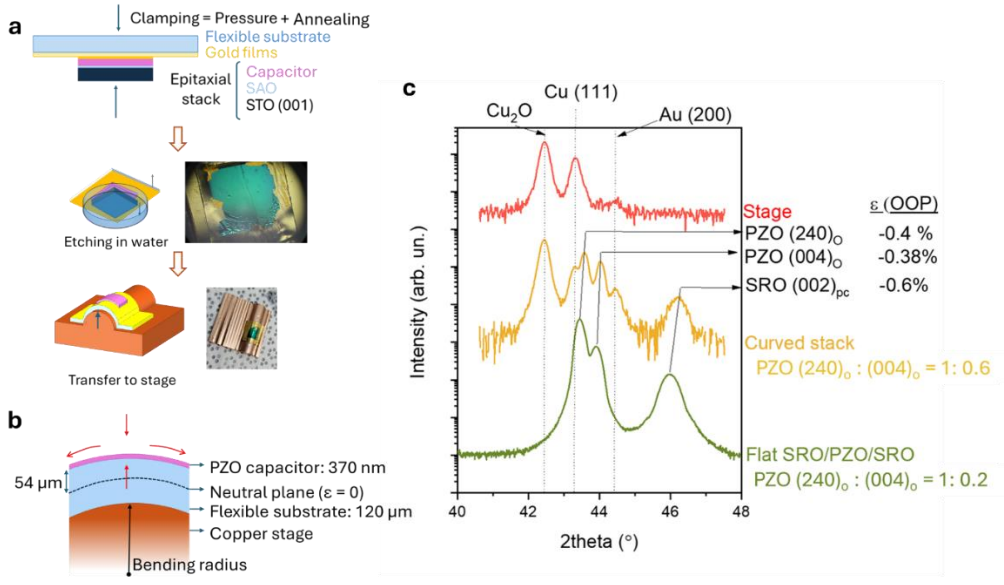


***Figure 5.2. (a)*** *Schematic and optical images of gold bonding method to transfer large area membranes on to flexible substrates (Kapton tape in this case),* ***(b)*** *Cross section schematic of the stack on the copper stage, showing the neutral plane and different strains: tensile strain in direction parallel to curvature and compressive strains in the out-of-plane direction (marked as red arrows) and into the plane of the paper (not shown),* ***(c)*** *XRD for flat capacitor, bended capacitor to a radius of curvature of 5 mm, and the Copper stage as reference, showing a shift of PZO peaks to higher 2theta angles (compressive strain) and reorientation of some (120)o domains to (001)o domains.*

## 5.2.2. Functional properties as a function of strain

We then measure the Switching current - Electric field (I-E) curves and calculate the corresponding Polarization – Electric field (P-E) loops for the SRO/PZO/SRO stack at different bending radii. **Figure 5.3a** shows the radius of curvature (ROC) and the corresponding curvature (= 1/ROC), the mathematically calculated in-plane and out-of-plane strain for each measurement. By measuring the I-E (**Figure 5.3b**) and calculating the P-E loops (**Figure 5.3c**), we can obtain the switching electric fields, saturation polarizations and remnant polarizations (**Figure 5.3d-e)**. Finally, these can be used to calculate energy storage and efficiency (**Figure 5.3f**). It is important to note, however, that as we go to higher curvature stages, the efficiency of strain transfer might diminish (via slippage or shear) and the strain values in the figure are nominal strain (calculated from curvature) rather than measured.

At all strain conditions, we see four switching peaks and double hysteresis loops characteristic of antiferroelectrics. As the in-plane strain changes from compressive to tensile, the forward switching field (AFE to FE) moves to higher values while the backward switching (FE to AFE) moves to lower fields, hence increasing the hysteresis. Moreover, the saturation polarization decreases, while the remnant polarization remains very similar until the FE-AFE current peak moves to below zero

field in the case of the highest tensile strain. We can calculate the ratio of returning polarization to total switching polarization as $\frac{P_s - P_r}{P_s}$, where $P_s$ is the saturation polarization, and $P_r$ is the remnant polarization; this ratio is representative of the functionality where a value of 1 represents ideal AFE and 0 represents ideal FE. For the highest tensile strain, the value of this ratio drops from 0.87 to 0.42, marking a significant increase in functional ferroelectric behaviour. Conversely, the dependence of P-E loops on the strain conditions is the increase of energy storage density and efficiency of the capacitors under compressive strains, which reduce the hysteresis and increase the saturation polarization. .

Previous results on antiferroelectrics show that biaxial compressive strains applied via epitaxy favour ferroelectricity,[108,149] while antiferroelectric phase is preferred under biaxial tensile strains.[160] In our case, we see a somewhat opposite tendency: tensile strain applied via bending (which is uniaxial) favours antiferroelectricity. An increase in the stability of the ferroelectric phase would be expected to cause the switching fields to move towards zero field, while higher stability of the AFE phase would cause the switching fields to move to higher values, which is not what we see; tensile strain does decrease the return field from FE to AFE, but it also increases the forward field from AFE to FE. Therefore, there is a clear discrepancy considering that the tensile strain via bending should induce compressive strains in the other two directions (stabilizing the FE phase). We believe the difference is related to the uniaxial nature of the bending strain delivered in our experiment that can lead to anisotropic strains as opposed to the biaxial nature of epitaxial strain which is isotropic. Although, anisotropy may indeed change the energy balance between the FE and AFE phases, our results cannot be explained purely by the stability of phases alone, but rather by the energy barriers that have to be overcome to jump between the phases.

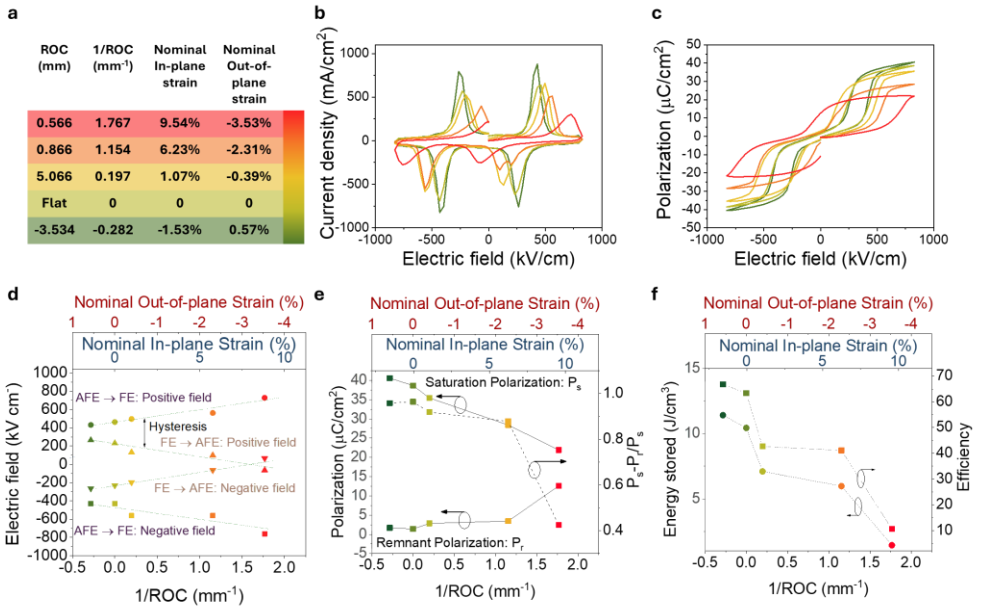


***Figure 5.3. (a)*** *Table showing different radius of curvatures (ROC) and the mathematically calculated in-plane and out-of-plane strains, the colour scheme is also the key for other figures,* ***(b)*** *Switching currents under different strains,* ***(c)*** *P-E loops under different strains; variation of* ***(d)*** *Switching electric fields (lines are guides for the eye),* ***(e)*** *Saturation polarization, remnant polarization and* $(P_s\text{-}P_r)/P_s$ *and* ***(f)*** *Energy storage density and efficiency as a function of curvature. Top axes also show calculated strains.*

The electromechanical coupling in PZO also means that the mechanical boundary conditions will affect the switching behaviour. Uniaxial in-plane tensile strain results in a compressive strain in the other two directions. An out-of-plane compressive strain disfavours polarization in that direction due to electrostrictive coupling. This is seen in our loops as a decrease in the saturation polarization in the tensile strain regime. In terms of the free energy, this means that the two energy minima corresponding to the ferroelectric state move closer to zero polarization. Normally, though, reduced polarization should be expected to result in reduced energy barrier between the polar and non-polar (antiferroelectric) state, our observation that this is not the case suggests that the anisotropy of the uniaxial strain hinders the polarization switching path, thus increasing the height of the barrier.

Another factor that may influence the difference with respect to the biaxial strain case[161] are the domain populations. There are three cases in PZO under the application of both strain (ε) and electric field (E):

1. $\varepsilon \parallel [001]_{PC}$, $E \parallel [100]_{PC}$
2. $\varepsilon \parallel [010]_{PC}$, $E \parallel [100]_{PC}$
3. $\varepsilon \parallel [100]_{PC}$, $E \parallel [001]_{PC}$

The combined effect of the strain and electric field will be different for all three cases since these domains are ferroelastic and anisotropic, and the phase transition involves

volume expansion. There can, therefore, be reorientation of domains under strain and field, as we observed. In our samples, we have a majority of $(100)_{PC}$ domains (at zero strain) which would fall under cases 1 and 2. On the other hand, Guo *et. al*[161] investigated the effects of curvature on PZO membranes as well, with majority $(001)_{PC}$ domains hence, the case 3 is applicable. They observed an increase of the hysteresis with no change in saturation polarization under compressive strain, and a decrease in saturation polarization with no change in hysteresis under tensile strain. The relation between the strain direction and the electric field direction might explain the differences observed, and theoretical studies are underway which might provide us with a quantifiable model. Building upon that, since the domain orientation can be controlled by using buffer layers,[107,160] we surmise that similar straining conditions can be used to achieve completely different effects in PZO membranes.

## 5.3. PZO rolls

The previous section focuses on the case of having strain with minimal strain gradient and the conclusion is that, though the switching barrier is modified, the antiferroelectric ground state of PZO at zero field seems to be unchanged. In the following section we want to look at the complementary situation of combining strain with strain gradient. We can achieve this scenario by making rolls of PZO.

### 5.3.1. Fabrication of PZO rolls

For functional measurements, we need a bottom electrode. To obtain a geometry of PZO roll with a bottom SRO electrode, I grew an SRO (10 nm)/ PZO (80 nm) stack on SAO buffered STO (001) substrate and immersed it partially in the water in the vertical direction (**Figure 5.4a**). As the SAO etches, the SRO/PZO starts rolling due to the lattice mismatch between the two layers. We can stop the etching process when SAO is partially etched, keeping the roll attached to the rest of the film. Hence, the PZO surface is exposed while the top SRO can now be used as bottom electrode for PFM measurements as shown in **Figure 5.4a** and **b**.

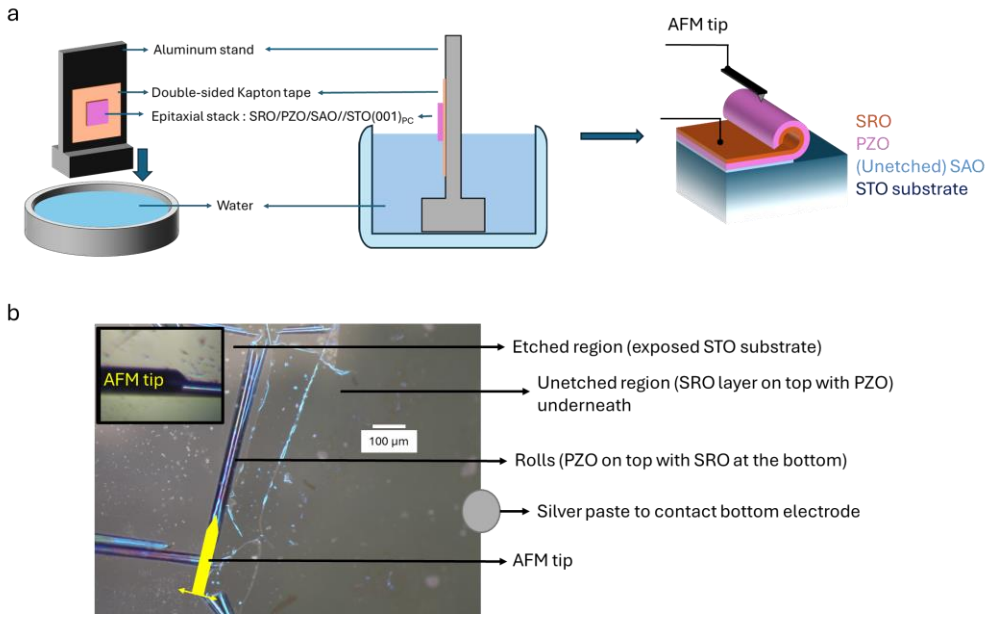


***Figure 5.4. (a)*** *Fabrication method for PZO/SRO rolls,* ***(b)*** *Optical image of roll partially etched on STO (001) substrate and how the PFM measurements are done, inset shows the optical image from the integrated optical microscope in the AFM showing the AFM tip and the roll.*

## 5.3.2. PFM of PZO/SRO rolls

We then study the functional property of the rolls by PFM. From the AFM of the rolled membrane, we can get topography (**Figure 5.5a-b**). Even though, the radius of curvature in a roll should not change (hence fitted with an equation for the circle), in this case, the surface texture was best fitted with a parabolic function. The divergence from a perfect circular fitting might be due to an artifact from the AFM measurement at the edges. The radius of curvature ($r$) was then calculated using:

$$r = \frac{(1+(\frac{dy}{dx})^2)^{\frac{3}{2}}}{\frac{d^2y}{dx^2}} \qquad (5.1)$$

$r$ can be then used to calculate strain at the surface using $\varepsilon = y/r$, where $y$ is the distance between neutral plane and the surface and assumed to be equal to half of the thickness ($t/2$) of the membrane. The maximum strain is calculated to be 0.156 %, which is relatively small. Meanwhile, the strain gradient in the out-of-plane direction will be $2\varepsilon/t$, and it amounts to $3.9\times10^{-4}$ $m^{-1}$. Multiplying the strain gradient by the known flexoelectric coefficient of PZO, we can calculate the out-of-plane flexoelectric field, which equals 1.35 kV/cm. Although this flexoelectric field is 22 times larger than in the previous section, it is still well below the critical field for switching from AFE to FE, and therefore a phase change is not expected.

We then did PFM on the rolls that were obtained. We attempt to write three rectangles of +12/-12/+12V on the roll and read the written domains (**Figure 5.5d-l**). After writing, we see a contrast in both the vertical and lateral PFM. However, this does not correspond to ferroelectric domains but rather charge injection mechanisms, where there is amplitude contrast between the down and up poled regions (rather than the same amplitude with a dark contrast at the domain wall as in ferroelectrics). The rolls, therefore, do not show evidence of ferroelectricity, consistent with their expected antiferroelectric ground state (additional albeit inconclusive evidence of this AFE ground state can be found in the **Appendix F2**).

We then measured Switching-Spectroscopy Piezoresponse Force Microscopy (SS-PFM) loops on the rolls. SS-PFM loops were done at two different frequencies: a slower one (0.1 Hz with On/Off cycle of 0.18 sec), and a faster one (1.0 Hz with On/Off cycle of 0.014 sec), to look for possible differences in the polarization relaxation dynamics. The loops are shown in **Figure 5.6.** At higher frequency, the loops look ferroelectric, while the rolls behave as antiferroelectric at lower frequencies, signifying that, at high frequencies, the PZO layer does not have quite enough time to relax back.

The antiferroelectricity in the PZO/SRO rolls is consistent with the low strain and strain gradients that might not be enough to induce a phase change. Next, we move on to the extreme case of large strain gradients induced by wrinkles that are formed when membranes are transferred via viscoelastic support layers.

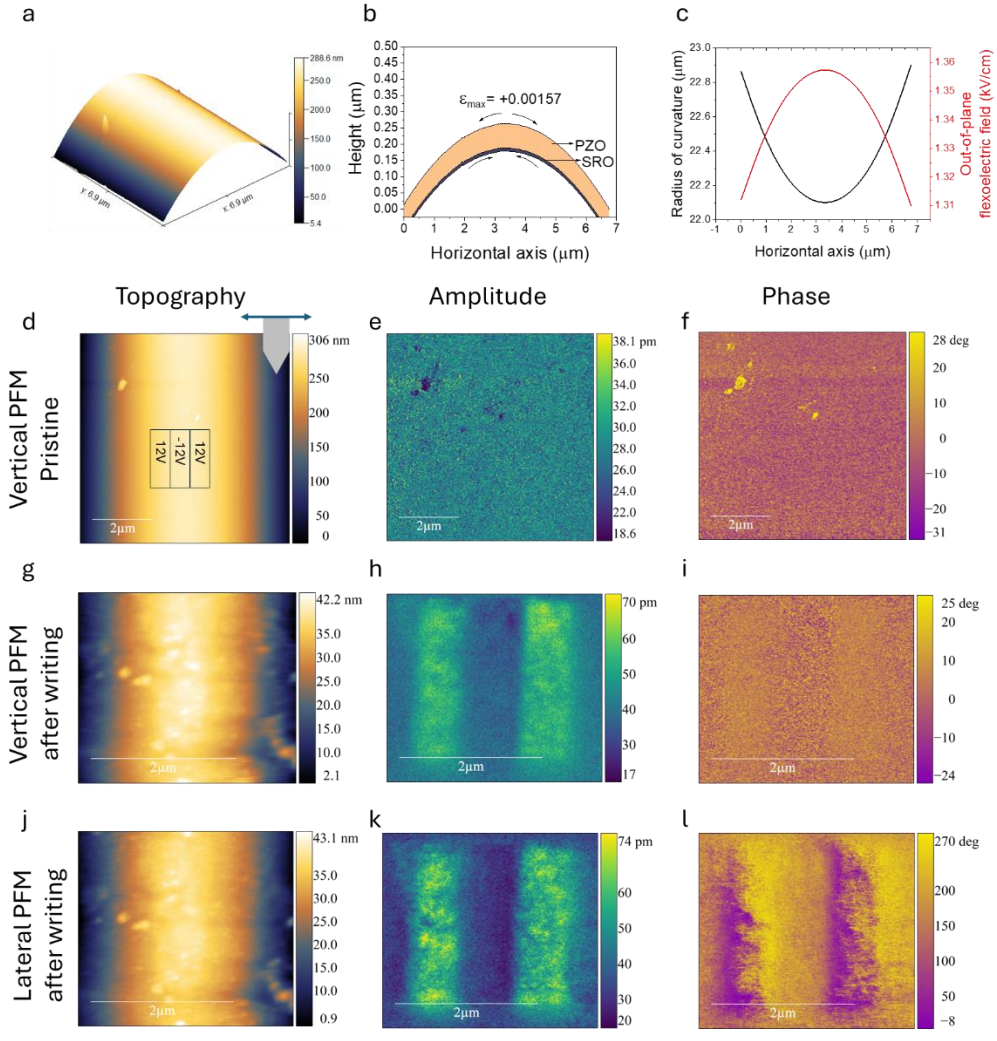


***Figure 5.5.*** *AFM/ PFM measurements on PZO/SRO rolls attached to STO (001) substrate* ***(a)*** *3D rendering of a roll,* ***(b)*** *Topography of the roll showing PZO and SRO layers (bottom surface is a graphical addition),* ***(c)*** *Calculated radius of curvature and out-of-plane flexoelectric field for the roll,* ***(d)*** *Topography,* ***(e)*** *PFM Amplitude* ***(f)*** *PFM phase of the rolls before writing* ***(g-i)*** *topography, amplitude and phase in vertical PFM after writing and* ***(j-l)*** *same in lateral mode PFM.*

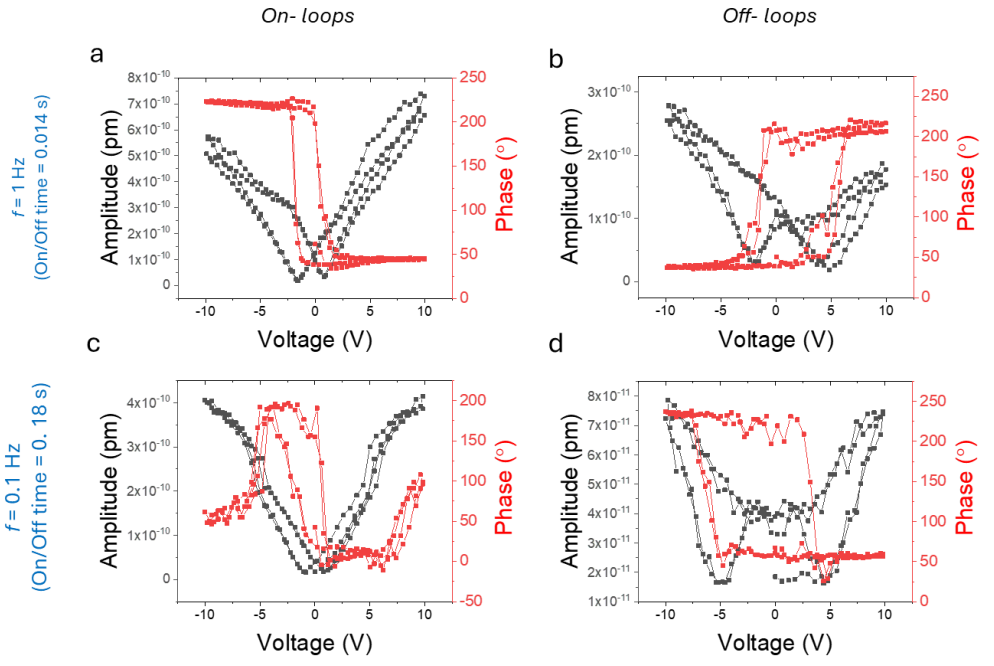


***Figure 5.6.*** *SS-PFM loops on PZO/SRO rolls,* ***(a-b)*** *loops at 1 Hz with On/Off time of 0.014 sec,* ***(c-d)*** *loops at 0.1 Hz with On /Off time of 0.18 sec, where* ***(a, c)*** *are On-loops,* ***(b, d)*** *are Off-loops.*

## 5.4. Wrinkles on PZO membranes

The extreme case for the strain state in PZO membranes can be achieved in wrinkles. When the membranes are transferred to an elastic substrate, they can form wrinkles due to strain relaxations. Even on a rigid substrate, residual wrinkles may remain from the intermediate transfer stage to the polymeric PDMS stamp, optical images for such wrinkles on 36 nm PZO membrane are shown in **Figure 5.7**. Wrinkles have a high curvature and, since the membrane is a single layer, the neutral plane lies within the membrane, leading to tensile strains on the top surface and compressive on the bottom, resulting in very high strain gradients. The combined effects from surface strains and flexoelectricity might result in phase transitions in these wrinkles. To probe these possible phase transitions, we use PFM to look at the wrinkles in PZO.

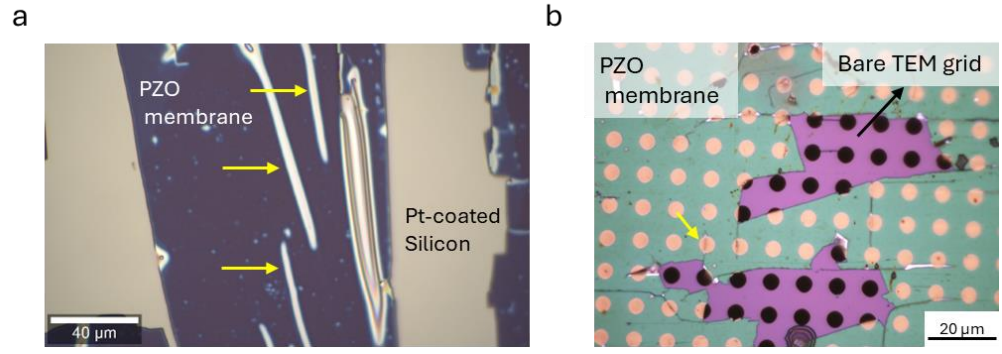


***Figure 5.7****. Wrinkles on 36 nm PZO membrane after being transferred to* ***(a)*** *Pt- coated Silicon substrate,* ***(b)*** *TEM grid with 5 µm holes, wrinkles are marked as yellow arrows.*

### 5.4.1. PFM on stand-alone PZO wrinkles

AFM and PFM are first done on a 36 nm wrinkled PZO membrane transferred to a Pt coated Silicon substrate, results shown in **Figure 5.8**. The topography of the wrinkle shows that its shape is different from those found in ferroelectric membranes of BTO or PTO,[164,174] instead of a classic wrinkle with a smooth change in curvature across the profile, the shape resembles that of a fold where most of the strain gradients are concentrated at the apex. This means that most of the membrane has a low curvature (albeit suspended) and the strains and strain gradients are highly localized. The shape of the wrinkle, shown in **Figure 5.8a-b**, can then be used to calculate the radius of curvature ($r$) at each point, similar to what was done PZO/SRO rolls. The corresponding flexoelectric field can be calculated by multiplying the strain gradient by the flexocoupling of PZO (= 3V).[29] The calculated radius of curvature and resulting flexoelectric field are shown in **Figure 5.8c**. The maximum field in the out-of-plane direction comes out to be around 200 kV/cm, which is close to the switching field for PZO. It is nevertheless important to remember that the top surface is under extreme tensile strain (~0.09) which from our bending experiments show an increase in the switching field, whereas the bottom surface which is under compressive strain might have a lower switching field. I further performed vertical (**Figure 5.8d-f)** and lateral (**g-i)** PFM measurements on this fold. In both cases, we do not see convincing evidence of a ferroelectric phase: although the lateral PFM- phase does show some contrast, the amplitude does not show contrast expected from two domains with a domain wall in between.

If we look closely, we also observe some randomly oriented line features in topography, and corresponding contrasts in phase and amplitude. These features can be seen to even run over the wrinkle, therefore the origin of these is not from the substrate. However, these features are too small to be resolved by AFM. Therefore, we cannot confidently attribute any properties to them or even if they come from the PZO membrane itself.

The lack of detection of a clear ferroelectric phase in this case can be due to multiple factors. One of course is that the film may not be ferroelectric at all. If it is ferroelectric, perhaps the domains might be too small for the resolution of PFM or, conversely, they are all pointing in the same direction (which would be consistent with the unidirectional nature of the flexoelectric field) and thus there is no contrast between domains of opposite polarization –because they all have the same polarization. This hypothesis, however, would not explain the lack of vertical PFM contrast between the wrinkle (presumed FE) and the flat (presumed AFE). Yet another hypothesis is that the ferroelectric phase, if present, is buried at the bottom of the wrinkle, where the compressive strain (which we know favours ferroelectricity) is maximal. If the top of the wrinkle, which is under tensile strain, remains AFE, it might mask or muffle the PFM response from the ferroelectric region underneath. To seek further clarity, it would be advantageous to perform the PFM measurements on wrinkles that have a bottom electrode, as that would ensure a through-sample penetration of the probing field.

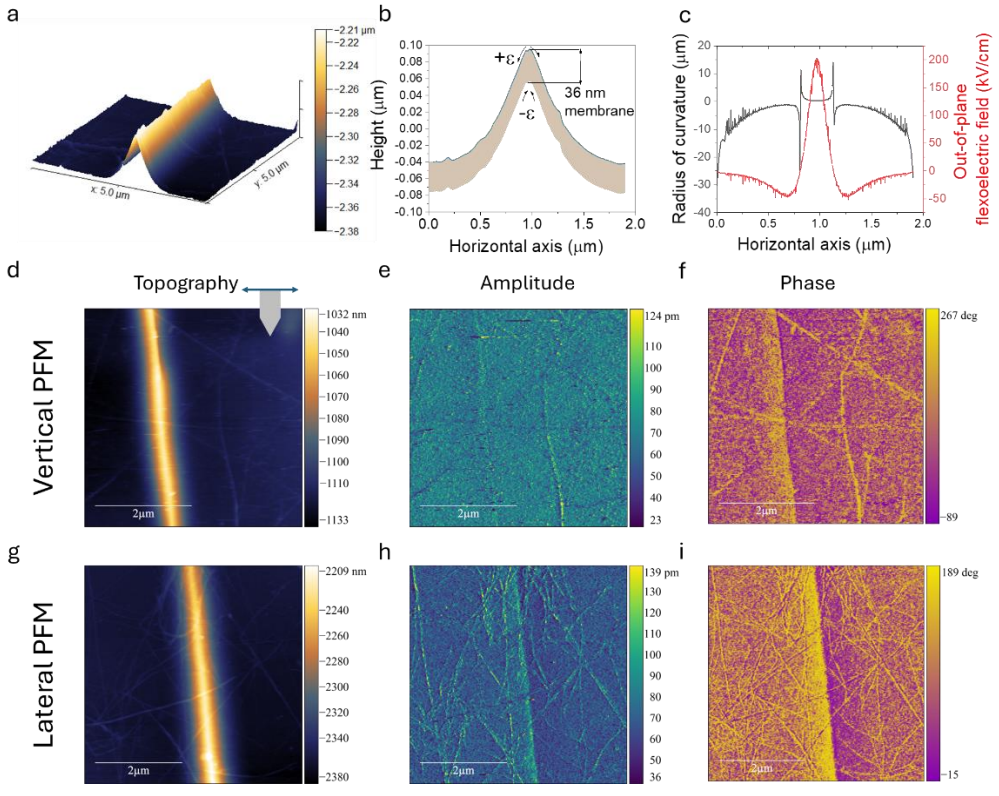


***Figure 5.8.*** *AFM/ PFM measurements on PZO wrinkle,* ***(a)*** *3D rendering of a wrinkles,* ***(b)*** *Topography of the wrinkles (bottom surface is a graphical addition),* ***(c)*** *Calculated radius of curvature and out-of-plane flexoelectric field for the wrinkle,* ***(d, g)*** *Topography,* ***(e, h)*** *Amplitude,* ***(f, i)*** *phase of the wrinkles in vertical mode* ***(d-f)*** *and lateral mode* ***(g-i)****, the tip scanning direction is shown in d.*

### 5.4.2. PFM on PZO wrinkles with Pt back electrode

The strategy used to measure the PFM in presence of a bottom electrode is to transfer the membrane on a perforated substrate, in this case a TEM grid with 5 μm holes (**Figure 5.7b**). The TEM grid is then inverted and Pt back electrode is deposited via sputtering. The TEM grid is then attached to a metal disk using conducting silver paste, followed by AFM and PFM measurements. We obtained some wrinkles on top of the holes, but the wrinkle profile is different, showing a wavy shape (**Figure 5.9**). The calculated radius of curvature and resulting flexoelectric fields approach the switching fields in this case as well similar to the previous one.

Vertical and lateral PFM measurements show some contrast, but the clearer contrast is again in the lateral PFM, suggesting either that the polar domains have a major in-plane component, or that the out-of-plane component is the same –which, to remind, would be fully consistent with the radial orientation of the flexoelectric field, but inconsistent with the lack of amplitude contrast between the flat and the curved part of the film. In addition, in the top part of the wrinkle, the piezoresponse seems to have a stripy pattern in the direction orthogonal to the wrinkle axis, suggesting the existence of stripe domains –although it is unclear whether they are just ferroelastic or ferroelastic and ferroelectric.

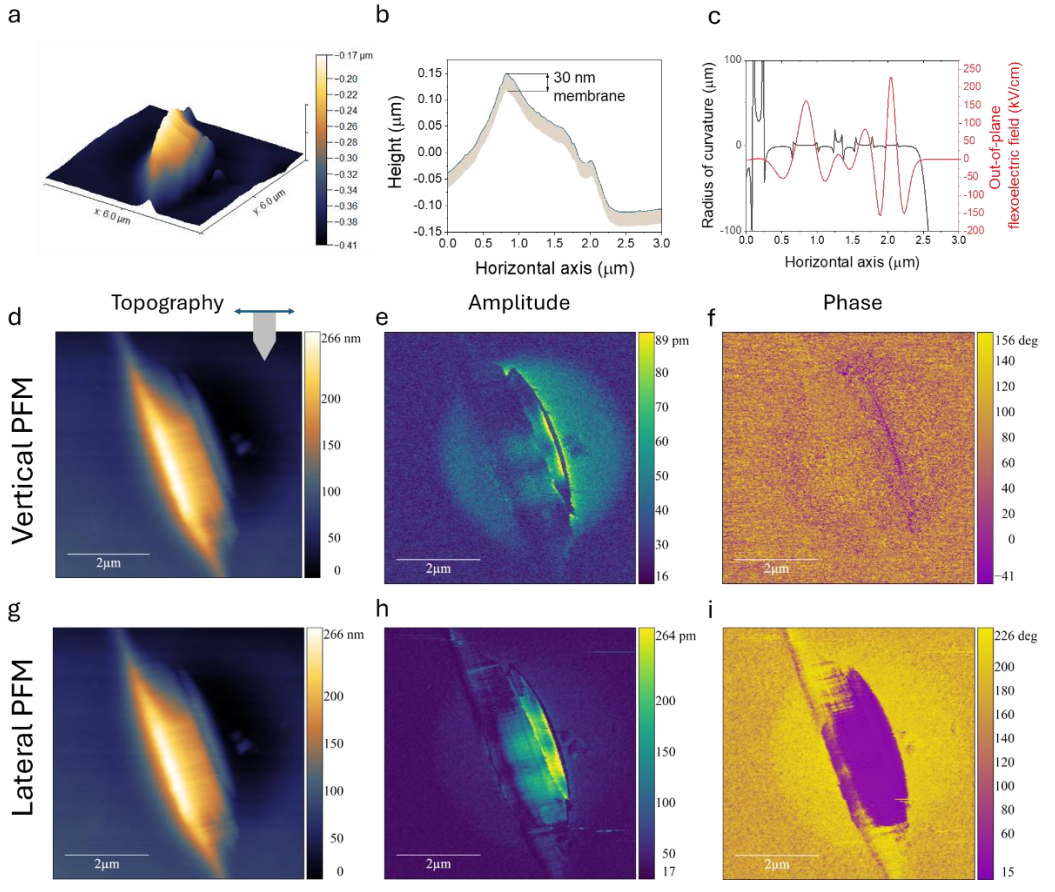


***Figure 5.9.*** *AFM/ PFM measurements on PZO wrinkle,* ***(a)*** *3D rendering of a wrinkle on a hole,* ***(b)*** *Topography of the wrinkles (bottom surface is a graphical addition),* ***(c)*** *Calculated radius of curvature and out-of-plane flexoelectric field for the wrinkles,* ***(d, g)*** *Topography,* ***(e, h)*** *Amplitude,* ***(f, i)*** *phase of the wrinkles in vertical mode* ***(d-f)*** *and lateral mode* ***(g-i).***

Thanks to the back electrode, we can now do a writing experiment as shown in **Figure 5.10,** where I wrote two regions with +10V and -10V. After writing, the contrast pattern changes significantly, specifically in the lateral PFM, while the topography does not seem to change. The results here also give us some confidence that the contrast we see is not simply due to the cross-talk with topography. After writing, the stripy domain pattern gets more obvious, and stripes of low amplitude are also now visible marking the domain walls. However, it is still inconclusive whether the domains are at the top, bottom or through the thickness of the wrinkle.

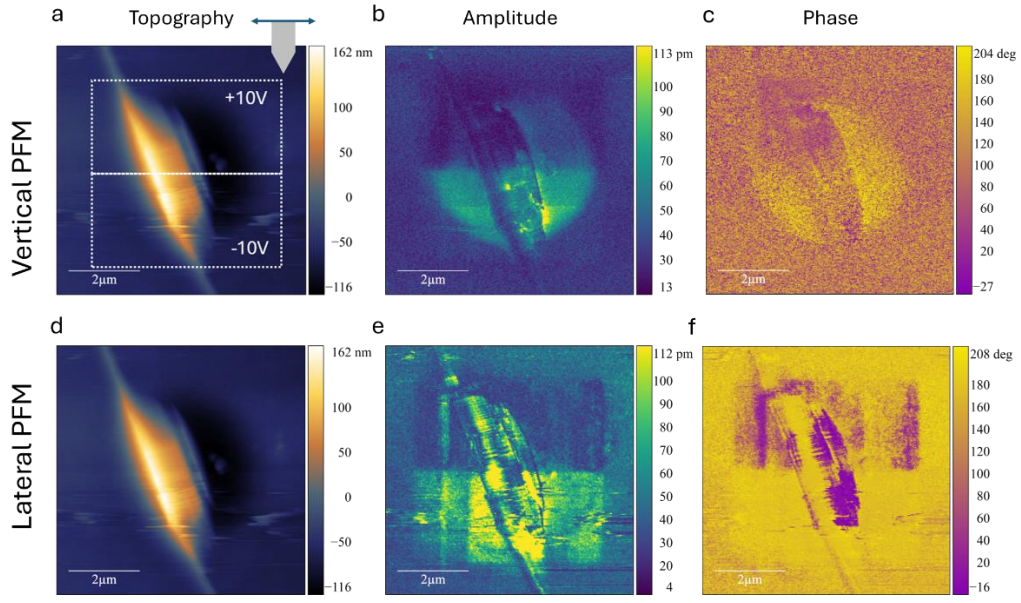


***Figure 5.10.*** *AFM/ PFM measurements on PZO wrinkle after writing,* ***(a, d)*** *Topography,* ***(b, e)*** *Amplitude,* ***(c, f)*** *phase of the wrinkles in vertical mode* ***(a-c)*** *and lateral mode* ***(d-f).***

(Finally, we also conducted SHG measurements[a] on 17 nm PZO membrane showing an increase in the polarization in the wrinkles, the mapping is included in **Appendix F3**.)

## 5.5. Conclusions and outlook

In this chapter, I report how the strain and strain gradients affect the properties of PZO. When bending the PZO capacitors, the PE loops change their shape, and this change is consistent with a change in energy barrier heights between the AFE and FE phases.

We also fabricated rolls of PZO/SRO ,where the self-rolling of partially etched samples is caused by the mechanical mismatch between the two layers. The PZO layer in these rolls exhibited AFE behaviour because of insufficient strain and strain gradients to cause a phase transition. In contrast, wrinkles of PZO, which have much larger curvatures, showed polarization both in SHG and in PFM measurements. The latter also suggested that at least part of this polarization is switchable and therefore ferroelectric, suggesting that the combination of strain and strain gradients can induce ferroelectricity and align the ferroelectric domains in the wrinkle to the extent that they become readable in PFM. Nonetheless, how the domains and phases evolve across the

[a] The SHG measurements were done at the Institute of Science (Tokyo, Japan) in collaboration with Prof. Hiroko Yokota.

thickness under varying strains is missing. In the future, it will be interesting to observe cross-section of PZO wrinkles under transmission electron microscopy to visualize how the local strain and strain gradient affect the microstructure and polar displacements of PZO at a local level.

Finally, the presence of ferroelectric domains on the wrinkle suggests that adding a flexoelectric field (due to strain gradients) may allow the system to overcome the energy barrier that is otherwise hard to surmount with pure strain. Strain gradients thus provide another degree of freedom that has to be considered when discussing phase transitions in thin films of PZO.

Chapter 6

# Electronics based on antiferroelectric PZO

## 6.1. Memory devices

### 6.1.1. Introduction

The modern world is built upon foundations of rapid technological growth and connectivity. These are accompanied by an ever-increasing demand for energy to derive the unprecedented development we have seen in the last few centuries. Although energy production is the cornerstone of this progress, energy storage is no less essential. In this case, AFEs, like PZO are a good candidate for high power density capacitors, as I discussed in **Chapter 3**. While the potential of AFEs as capacitors is well known, they may also help solve another problem related to energy consumption: the high demand of energy in computations.

Modern computing systems are dominantly based on von Neumann architecture,[175,176] whereby the data storage and processing happen in two different physical units (memory and transistor). During the computation process, the data have to be transferred back and forth between these units, which not only consumes more power but also limits the speed at which these computations can be done. This problem has grown to be an important challenge with the surge in computationally-thirsty Artificial Intelligence.[177] A possible solution to this problem is in-memory computing[178,179] whereby computations are performed in the memory unit itself. Such processing units utilize the physical properties of the memory systems and work on the same principle as the human brain, which uses neurons and synapses both for memory and for logic. Because such systems are inspired by the working of the brain, they are termed "neuromorphic memory".[180] Neuromorphic memories have two main components: neurons that are the nodes where computation happens, and synapses that connect these neurons and whose weight acts as memory. The weight of the synapses, in contexts of real circuits, usually define the conductance of the synapses. This weight determines the current that goes through synapse reaching the neurons. Neurons integrate the charges coming from all the synapses connected to it and depending on whether the current reaches a threshold, can fire a pulse into other synapses termed as spike. This process is called Integrate-and-fire. After firing, the neuron relaxes and is not able to fire again for a certain amount of time called the refractory time.[181,182] We can already see that there are two behaviours that are important, a non-volatile one in the memory (synapse) and a volatile one in the processing unit (neuron).

Moreover, the synapses have different kinds of "plasticity", that is, their weights can change. This tuning can be done via electrical pulses, and the response to these pulses can be determined by the properties of the material or the system; for example, a train of pulses can habituate the synapse such that the response to each subsequent pulse has a lower effect on the property such as conductance.

Conversely, a repeated event might increase the sensitivity, priming the neural response called sensitization. If the conduction gets higher, it is called potentiation; decrease in conduction is termed as depression.[181]

To summarize, from an application point of view, we need to design synapses and/or neurons. For synapses, the material must have a non-volatile property such as resistance or polarization (to electrostatically control resistance in a channel layer as in a field effect transistor) that can be changed with electrical pulses with a predictable behaviour. For neurons, we require a volatile logic element that spikes if a threshold current is reached and relaxes back for the next spiking event.

Memory devices, and neuromorphic applications in particular, make use of two tuneable properties: polarization of the dielectric layer (such as $BaTiO_3$ and $Hf_xZr_{1-x}O_2$) to tune the resistance in a semiconducting channel layer, or else directly the resistance of the material i.e. memristors.[183–185]

In this context, AFEs provide an alternative to explore neuromorphic functionalities, and they have recently gained some traction. AFEs based on Hafnia-Zirconia ($Hf_xZr_{1-x}O_2$_ HZO)[a] are the most commonly used since they are CMOS-compatible. The conductance of these layers is polarization-dependent and can be changed by using voltage pulses, usually greater than the voltage needed to switch the AFE to FE phase, Moreover, while the AFE to FE transition is a volatile property, the functionalities can be non-volatile by charge trapping that modifies the conductance.[186] While these studies have been largely limited to HZO, the fabrication of membranes demonstrated in this thesis allows us to use a large family of perovskite antiferroelectrics such as PZO that can then be transferred to Silicon substrates, thus making them CMOS-friendly.

PZO is additionally interesting for neuromorphic memories because it possesses specific functional properties that are traditionally associated with neuromorphic devices: multi-state polarization (enabled by phase coexistence) and time-dependent properties (enabled by the metastability of the field-induced transitions). These properties have been discussed in previous chapters and are applicable as both neurons as well as synapses. In this chapter, I will present some preliminary results that we obtained in the pursuit of proof-of-concept devices that showcase the potential of AFEs in general and PZO in particular, as well as how these measurements can be built upon.

[a] Although the fluorite-like HZO materials do not have an antipolar ground state and therefore are not, strictu senso, antiferroelectric, some of them do display the key functionality of antiferroelectrics, namely their field-induced transition from a non-polar to a polar state, accompanied by double hysteresis.

### 6.1.2. Polarization modulation of PZO capacitors for charge- based electronics

Charge-based electronics work on the same principle as a field-effect transistor. A dielectric material is connected to a gate. The channel layer is then deposited on the dielectric, which is usually a semiconductor, of which the conductance is dependent on the depletion region determined by polarization of the dielectric. Therefore, a precise control on the polarization of the dielectric is necessary. AFEs provide an interesting option where volatile properties are needed, since the polarization resulting from the field- induced ferroelectric phase is only metastable. Moreover, the phase transition from AFE to FE involves displacement current that is well defined and determined by the material and hence can be used as current pulses for other devices. Additionally, the phase coexistence explored in **Chapter 4** provides us with opportunities in non-volatile functionalities as well, since the presence of different phases are locally stable. Therefore, we will examine how these functionalities can be tuned and used in the following sections.

#### *6.1.2.1. Remnant Polarization as a function of Electric field cycle parameters*

PZO capacitors (from **Chapter 3**), On GSO and Off GSO were studied by varying the applied voltage and frequency, as shown in **Figure 6.1**. While the On GSO capacitors show a high dependence of remnant polarization on both the applied voltage and frequency, Off GSO membrane capacitors have very low remnant polarization, independent of the voltage cycle parameters.

This stark difference is due to the difference in the switching dynamics of the two capacitors as discussed in **Chapter 3**. From these measurements, we can obtain two different properties.

1. The switching current peak, which is analogous to a current pulse. These displacement current pulses are an intrinsic property of antiferroelectric materials. Through proper electrical circuits, they can be fed into a memristor or a ferroelectric device to control its polarization that in turn controls (gates) the conductivity of a semiconductor channel for synapse functionality. Our results into switching dynamics indicate that it is possible to control the amplitude as well as pulse width of these pulses since the peak is sharper in the membranes due to its faster switching and broader in the epitaxial film capacitor.
2. Short-term memory: the remnant polarization is higher in film capacitors than the membrane capacitors. This polarization is in fact a dynamical consequence of pinning and will relax over time. Hence, the polarization is a volatile property that can be used in combination with semiconductor channel layers to mimic a neuron where the activation needs to decay over time and a certain refractory period is

required. Moreover, since epitaxial and membrane capacitors have different dynamics, the time-domain of this volatility also varies.

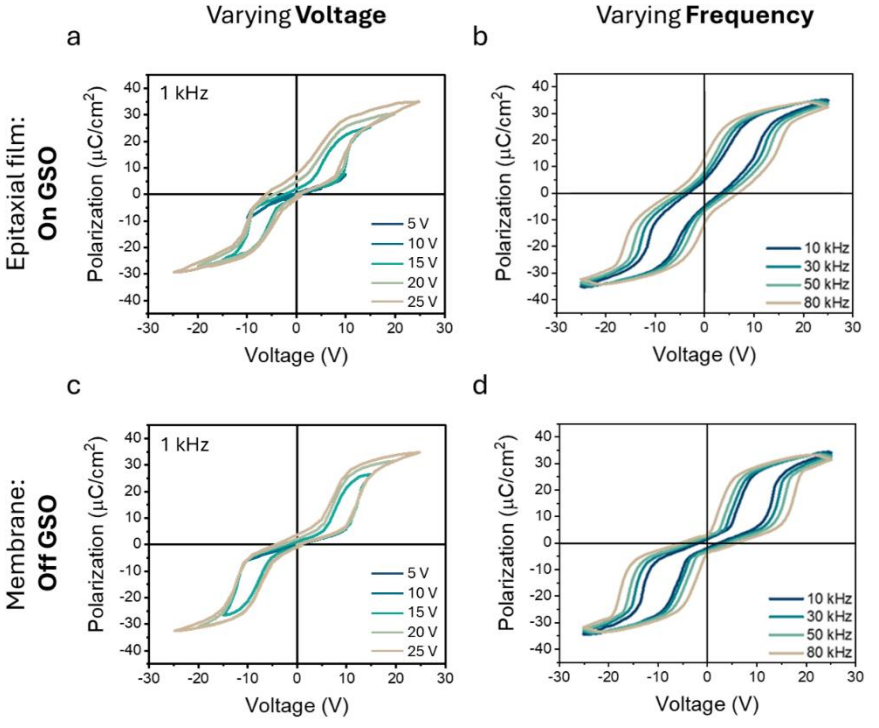


***Figure 6.1.*** *P-V loops of Epitaxial film* ***(a, b)*** *and membrane* ***(c, d)*** *capacitors as a function of applied Voltage* ***(a, c)*** *and loop frequency* ***(b, d)****.*

### *6.1.2.2. Remnant Polarization as a function of number of cycles*

Another way to modulate remnant polarization is by subjecting the capacitor to repeated pulses. We can do this by applying PUND (Positive Up Negative Down) measurements repeatedly and measure the switching and non-switching polarization in PZO capacitor. PUND measurements involve a first negative pulse to reset the capacitor, followed by two positive pulses. In case for FEs, the first pulse switches the capacitor and the maximum polarization change (P*) includes both remnant and non-remnant contributions, the second pulse switches the capacitor again, the polarization change (P^) only includes the non-remnant contribution. The difference in the two polarizations equals the remnant polarization.

In AFEs, PUND measures the switching AFE phase and the coexisting FE phase. After the reset pulse, the first pulse causes a transition from the AFE to FE phase as well as poling the coexisting FE phase. The second pulse only causes the AFE to FE phase transition. Therefore, the difference between the P* and P^ gives us the polarization

contribution from the coexisting and/or slow-relaxing FE phases and is termed as remnant polarization.

The behaviour of On GSO capacitor under repeated cycles (15 V pulses with 10 ms pulse difference) is shown in **Figure 6.2**. The results show that the coexisting FE phases that contribute to the remnant polarization increase as a function of number of PUND cycles until the capacitor breaks down. The polarization can thus be changed by applying a train of pulses that mimics potentiation in charge-based devices. The change in polarization as a function of number of pulses is also linear for the first 1000 cycles, which is a desirable property to predictably tune memory devices. However, one major drawback of the "antifatigue" mechanism (in the sense that it represents an increase rather than decrease of polarization with repeated switching) is that the capacitor cannot be reset to its initial state.

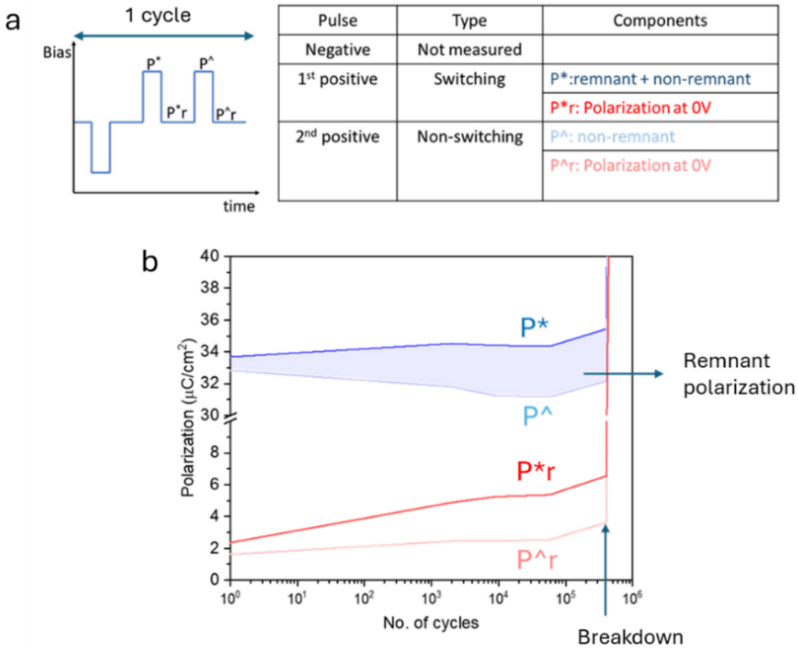


| Pulse | Type | Components |
|---|---|---|
| Negative | Not measured | |
| 1st positive | Switching | P*:remnant + non-remnant |
| | | P*r: Polarization at 0V |
| 2nd positive | Non-switching | P^: non-remnant |
| | | P^r: Polarization at 0V |

***Figure 6.2. (a)*** *Schematic of PUND loop measurement showing the negative pulse followed by two positive pulses and the corresponding measured polarization and what they represent in the table on the right,* ***(b)*** *Different polarizations measured as a function of no. of cycles.*

## 6.1.3. Resistance modulation of PZO capacitors

### *6.1.3.1. Resistive switching in PZO*

The resistance of the PZO layers can also be controlled and used memristively. Resistive switching has been shown in PZO thick capacitors and is associated with the AFE to FE transition.[187] We also demonstrate resistive switching in a 26 nm PZO

epitaxial film grown on an SRO buffered STO (001) substrate, as shown in **Figure 6.3**. The PZO film is antiferroelectric, with coexisting FE phases, as inferred from writing experiments in PFM mode (**Figure 6.3a-c**) and SS-PFM on- (**Figure 6.3d**) and off-loops (**Figure 6.3e**). The film also shows resistive switching (**Figure 6.3f**) measured with Conductive AFM (C-AFM), with SRO as bottom electrode and the AFM tip as top electrode.

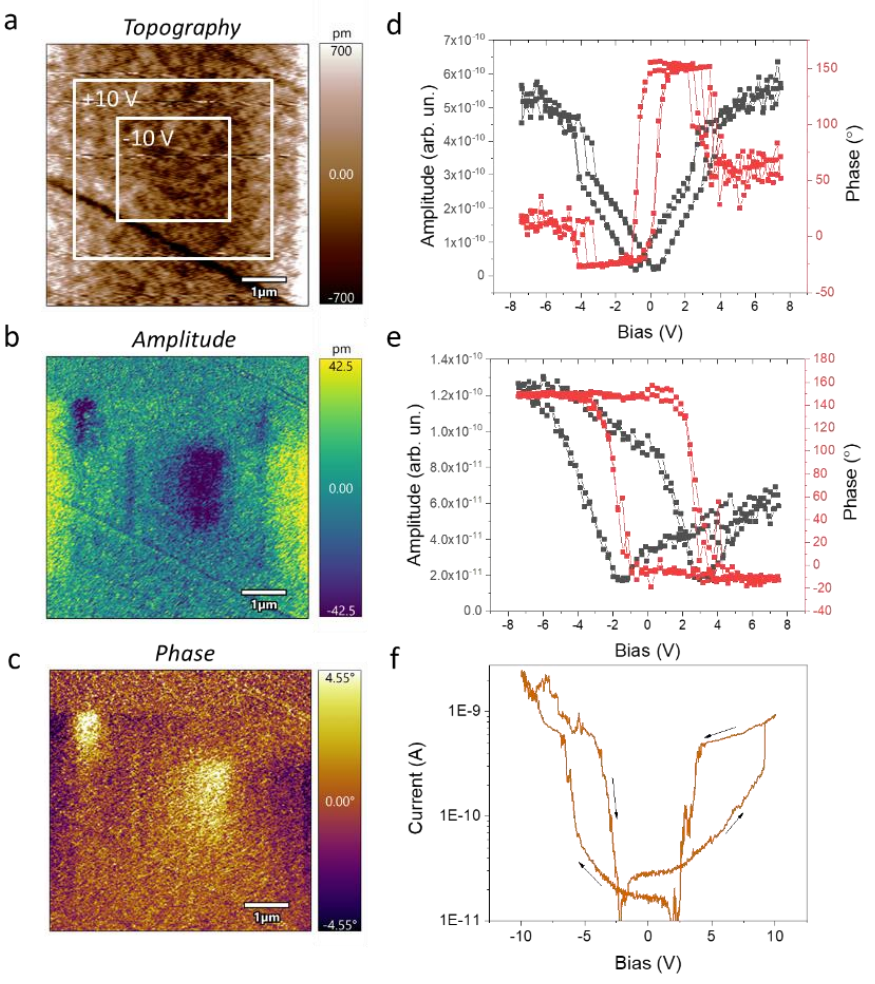


***Figure 6.3.*** *PFM of 26 nm PZO film* ***(a)*** *Topography, white square shows written regions with +10 and -10V,* ***(b)*** *Amplitude after writing,* ***(c)*** *Phase after writing,* ***(d)*** *SS-PFM On-loops,* ***(e)*** *SS-PFM Off-loops,* ***(f)*** *I-V measurement done in C-AFM.*

The switching voltages (the coercive fields) are different in the SS-PFM and C-AFM loops, probably due to the shape of the electric field loop applied: the voltage in the SS-PFM is applied as a pulsed triangular wave, whereas in C-AFM, the voltage is applied as a continuous triangular wave (**Appendix H**). This kind of resistive switching is again volatile, and PZO switches back to high resistance state once it transitions back

into the AFE phase. As for the origin of this resistive switching, there are at least two possible explanations. Either the ferroelectric phase itself is more conductive, or the domain walls of the ferroelectric phase are conducting. To try to isolate the origin, I attempt two strategies.

First, I grew an oxygen deficient film by using low oxygen pressure (50 mTorr) during growth, as well as cooling down in high vacuum environment; oxygen vacancies are known to favour pinning of the ferroelectric phase.[188] After writing domains, I performed C-AFM to measure the current maps, as shown in **Figure 6.4**.

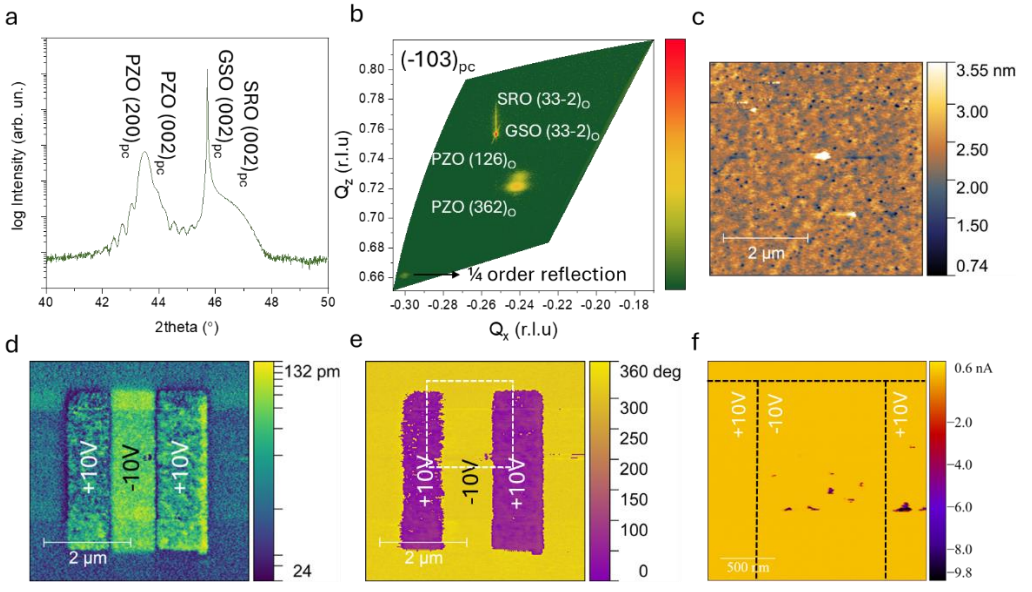


***Figure 6.4.*** *Measurements on Oxygen deficient PZO film grown on GSO (110) substrate,* ***(a)*** *theta-2theta scan,* ***(b)*** *RSM around (-103)$_{PC}$ peaks, showing ¼ order reflection of the AFE Pbam phase originating from the (120)$_O$ oriented domains,* ***(c)*** *AFM topography,* ***(d)*** *Amplitude after writing rectangular areas with +10V and -10V showing high amplitude in ferroelectric phase separated by low amplitude domain walls,* ***(e)*** *corresponding phase image,* ***(f)*** *C-AFM of the region marked as white dotted square in (e), the black lines show the written region.*

The film in this case shows high crystalline quality with the two domain orientations and the RSM around (-103)$_{PC}$ peaks show the ¼ order reflection signifying that the film is antiferroelectric despite the oxygen deficiency. After writing rectangles of +10V and -10V, we can clearly see the contrast in amplitude and phase representing the metastable ferroelectric phase. Note that the region outside the written areas show lower amplitude consistent with AFE. However, C-AFM maps show no enhanced conductivity either in the domain walls or in the domains. There can be several reasons for this observation (or the lack thereof). The ferroelectric domains might have already relaxed back by the time the C-AFM measurement is done. Moreover, the current difference in the two states might be low, since we must keep the read voltage low as

to not switch the film while reading. Finally, domain walls may not only occur just at the boundary between up and down polarized regions, but rather each written ferroelectric region has ferroelastic and ferroelectric domains, potentially making the effect more diffused and not readable.

Another strategy to try to differentiate is by growing PZO of different orientations: on STO (001) and STO (111). Since the ferroelectric phase is assumed to have a rhombohedral symmetry with polarization aligning in the $[111]_{PC}$ crystallographic direction, the field- induced ferroelectric phase on STO (001) will have ferroelastic domains (4 domain variants), while the $(111)_{PC}$ oriented PZO will have a single field-induced ferroelectric orientation and, therefore, no domain walls. Therefore, if both differently-oriented PZO capacitors show resistive switching, the origin of this switching is the ferroelectric phase itself; whereas if only $(100)_{PC}$ oriented film shows resistive switching, the ferroelastic domain walls are the likely culprit for the increase in currents. The results for our leakage current measurements on PZO membrane capacitors (PZO layer of 120 nm) initially grown on STO (001) and STO (111) substrates are shown in **Figure 6.5**.

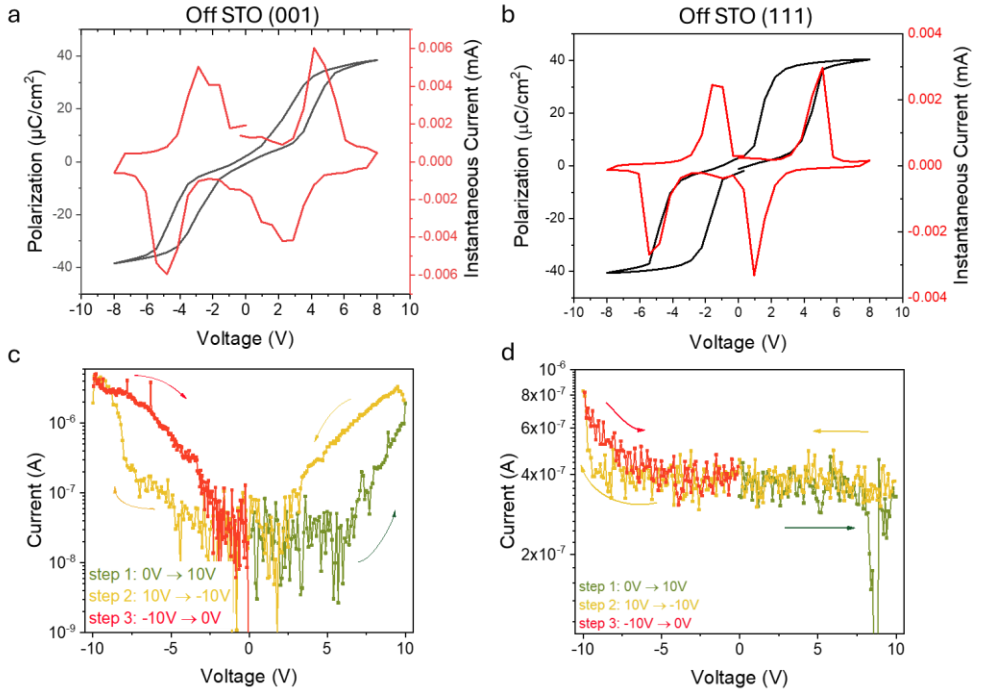


***Figure 6.5**. Measurements on 100 nm PZO membrane capacitors of different orientations, **(a, c)** SRO/PZO/SRO declamped from STO (001), **(b, d)** SRO/PZO/SRO declamped from STO (111), **(a, b)** Polarization and Switching (Instantaneous) current loops, **(c, d)** Leakage current measurements.*

Both capacitors show characteristic double hysteresis loops. The switching current peaks in $(100)_{PC}$ oriented capacitors (Off STO (001)) show a two-step switching, while the peaks in $(111)_{PC}$ oriented capacitors (Off STO (111)) are sharper. This has been previously attributed to the propensity of $(111)_{PC}$ oriented PZO to transition directly into the R3c FE phase without going through intermediate phases, contrary to the $(100)_{PC}$-oriented films.[16] Moreover, we see additional low intensity peaks (at low voltages), possibly corresponding to coexisting ferroelectric phases.[78] In the leakage current measurements, the Off STO (001) capacitor shows a clear resistive switching. This matches our C-AFM measurements on the thinner sample. Resistive switching is associated to the phase transition. On the other hand, there is almost no resistive switching in the Off STO (111) capacitor on either the positive side or the negative side. This suggests that the resistive switching might indeed be linked to ferroelastic domain walls rather than the ferroelectric phase itself.

Combining these results with the possibility of phase coexistence in PZO, it might be possible to tune the resistance of the PZO layers by small electrical pulses. These small external perturbations can locally cause PZO to transition between different phases, resulting in changes in domain wall/phase boundary density. When the writing pulses are small, the resistance changes will also be small, so a more sensitive probe to track resistivity changes is to measure the dielectric loss as a function of DC pulses.

#### *6.1.3.2. Sub-switching pulses to control dielectric loss*

Apart from the DC resistance of the antiferroelectric layers, we can also look at their AC dielectric loss, which represents the dissipation of the AC field in the material, and is proportional to the conductance of the capacitor. In PZO, ferroelectric domain wall transport has been shown to give a significant contribution to the loss,[189] further supported by our experiments, while also not having a high contribution to the permittivity. Switching loops can modify the number of domain walls and hence the loss of the capacitor. On the other hand, domain wall re-configuration may also be achieved by sub-switching pulses, since the energy difference between the AFE and FE phases is small and the energy required to modify already-existing domains (e.g. by sideways motion of their boundaries) is even smaller.[44] Based on these premises, we apply sub-switching pulses and monitor the capacitance and loss of the membrane capacitor ($(001)_{PC}$-oriented), as shown in the **Figure 6.6**.

We used our LCR meter (Agilent E4980A) to apply 5-second DC pulses of 5 V to a 300 nm PZO membrane capacitor with (001) out-of-plane orientation. The square pulses had a width of 5 seconds, with 5 s gap between them. Simultaneously, we probed the capacitance and loss with an AC voltage of 500 mV at 10 kHz. The capacitance was higher while the pulse was on (as expected, since we are driving the system closer to the high-susceptibility critical field), and decreases again as the DC

bias is removed. At zero voltage, the capacitance relaxes back to the initial value. The capacitance only adopts these two "on" and "off" values and does not change over time. However, the dielectric loss changed value after each pulse, with the "off" losses decreasing until stabilizing, mimicking a habituation behaviour. Negative voltage pulses also yield a two-value result for capacitance (albeit at somewhat higher values than for the positive voltages) and reset the dielectric loss to the pristine state. Interestingly, a single negative pulse is sufficient to reset the losses, and a subsequent train of negative pulses does not modify the loss. A second cycle shows the same trend, and if the pulse train is stopped, the dielectric loss becomes constant at the new value representing a non-volatile behaviour.

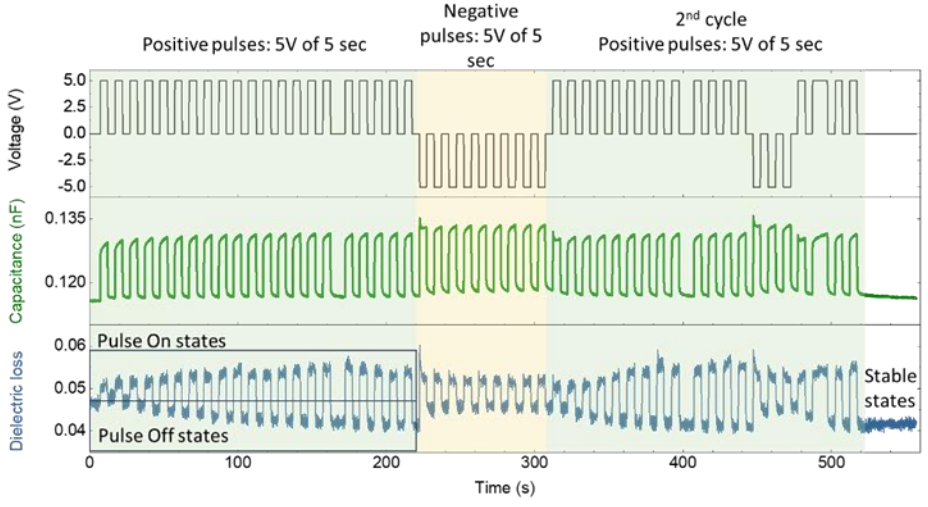


***Figure 6.6**. Influence of a train of sub-switching pulses on the capacitance and dielectric loss of a PZO capacitor.*

Our previous measurements on polarization control utilized either changing the parameters of the electric field loop or switching pulses. However, the later measurements on tuning dielectric loss show that we are also able to tune the loss by sub-switching pulses. The combination of these observations with our experiment on the origin of resistive switching indicates that sub-switching pulses can be used to change the proportion of coexisting ferroelectric phases or domains, which results in not only a multi-state change of impedance but probably also polarization. Although, a deeper investigation into the underlying mechanisms of the results observed here are required, our measurements point towards PZO, or AFEs, in general, being good candidates for novel neuromorphic-inspired memory technologies.

## 6.2. Negative Capacitance Transistors

Field effect transistors (FETs) are an integral part of many memory devices where the conductance of a channel layer (usually a semiconductor) between a source and a drain can be varied by applying a voltage to a polarizable material through a gate (**Figure 6.7a**). The equivalent circuit of an FET is shown in Figure **6.7b**. In a simplistic picture, different polarizations in the dielectric layer mean different polarity of bound charges that can attract or repel charges in the semiconductor. Hence, we can use this to modify the depletion region in the channel layer, and thus, its conductance. The most important parameter in FETs is the subthreshold switch (SS), which is defined as the gate voltage required to increase the current by one order of magnitude. For conventional transistors, the minimum SS that can be achieved is 60 mV/decade at 300 K due to the Boltzmann distribution of electrons. This limit is termed as "Boltzmann tyranny".

One possible way to improve SS below this theoretical value is to replace the gate dielectric with a "negative capacitance" (NC) dielectric, i.e. one where the gate voltage decreases as the gate charge increases.[190,191] Ferroelectrics and antiferroelectrics are excellent candidates for such applications because of their inherent switching properties. In the conventional working of a ferroelectric capacitor (**Figure 6.7c**), when a voltage greater than its coercive field is applied to the ferroelectric material, the polarization switches from up to down. There is a jump in the displacement charges associated to the switching without the system going through the negative capacitance region due to multi-charge solution of this pathway. In this case, the negative capacitance region is a forbidden region. On the other hand, if we can control the charges rather than the voltage being applied (**Figure 6.7d**), the negative capacitance region becomes accessible since there is always one solution to the equation. Therefore, controlling charge flow is a key ingredient in realizing NC, and it has been proposed that this charge control can be achieved by attaching a resistor in the circuit that controls (slows down) the charge flow, resulting in a partial switching of the FE and hence realizing a transient NC functionality.[192] The same physics apply to antiferroelectrics (**Figure 6.7e, f**), but instead of one NC region, there are two associated with the two phase transitions at either polarity of electric field ($AFE \rightarrow FE^{+/-}$).

The charge flow control of capacitance is transient, but there is another, steady-state,[191] way to obtain NC by attaching a series capacitor to the FE material. The two capacitors are electrically coupled (i.e. they have the same charges). The series dielectric capacitor has a linear response (negative gradient) as a function of voltage drop across the FE. The higher the capacitance of this dielectric, the steeper the response. Therefore, if the dielectric material is stiff (low-gradient line), we can have a situation where we obtain a single solution even in the negative capacitance region of the FE (**Figure 6.7g**), and application of a positive voltage gives a negative voltage across the FE, hence an incipient negative capacitance. The capacitance of the dielectric, therefore, should be

very low. Note that, in this case, at zero voltage, the charge is also zero, i.e. the dielectric material can also suppress ferroelectricity in a ferroelectric material in a certain temperature range. Physically, what happens is that the low dielectric constant of the material attached to the ferroelectric is unable to screen the ferroelectric depolarizing field, so the ferroelectric depolarizes itself. Mathematically, this low capacitance of the dielectric allows negative capacitance in the FE, while keeping the overall capacitance positive. In this case, there is an amplification of the voltage at the FE/dielectric interface allowing for a SS lower than the Boltzmann tyranny. In real cases, the channel layer or the interface between the gate dielectric and the channel has a capacitance that might allow for negative capacitance in the FE or AFE layers.

In AFEs, the working principle is the same, except that we need applied voltages high enough to be in the switching regime of the AFE. The advantage of AFEs, however, is that the transistor is automatically reset once the field is removed, and negative voltage pulse is not required. Due to the double hysteresis loop behaviour of AFE, there are two regions of the possible negative capacitance effect, contrary to one in FEs. Moreover, it has been shown in $ZrO_2$ that negative capacitance can occur in many different transitions such as polar to polar, non-polar to polar (and reverse) as well as structural phase transitions (non-polar to non-polar).[193] All these scenarios are present simultaneously in PZO (multi-step switching in **Chapter 3** and phase coexistence in **Chapter 4**). Finally, one of the desirable important features of NC transistors is small hysteresis, which can be achieved in PZO by disorder and phase coexistence, making PZO an interesting case study. With this in mind, I attempt to design NC transistors based on PZO.[a]

[a] This work was started with the help and planning of Pavlo Zubko (UCL, London, UK). I would like to heartily acknowledge his contributions in design and discussions. The $MoS_2$ and graphene layers were deposited by the group of Advanced electronic materials and devices, ICN2 (Prof. Jose Garrido). Special thanks to Anna Graf, Eduard Codina and Laura Gelabertó for the depositions of the channel layers and discussions.

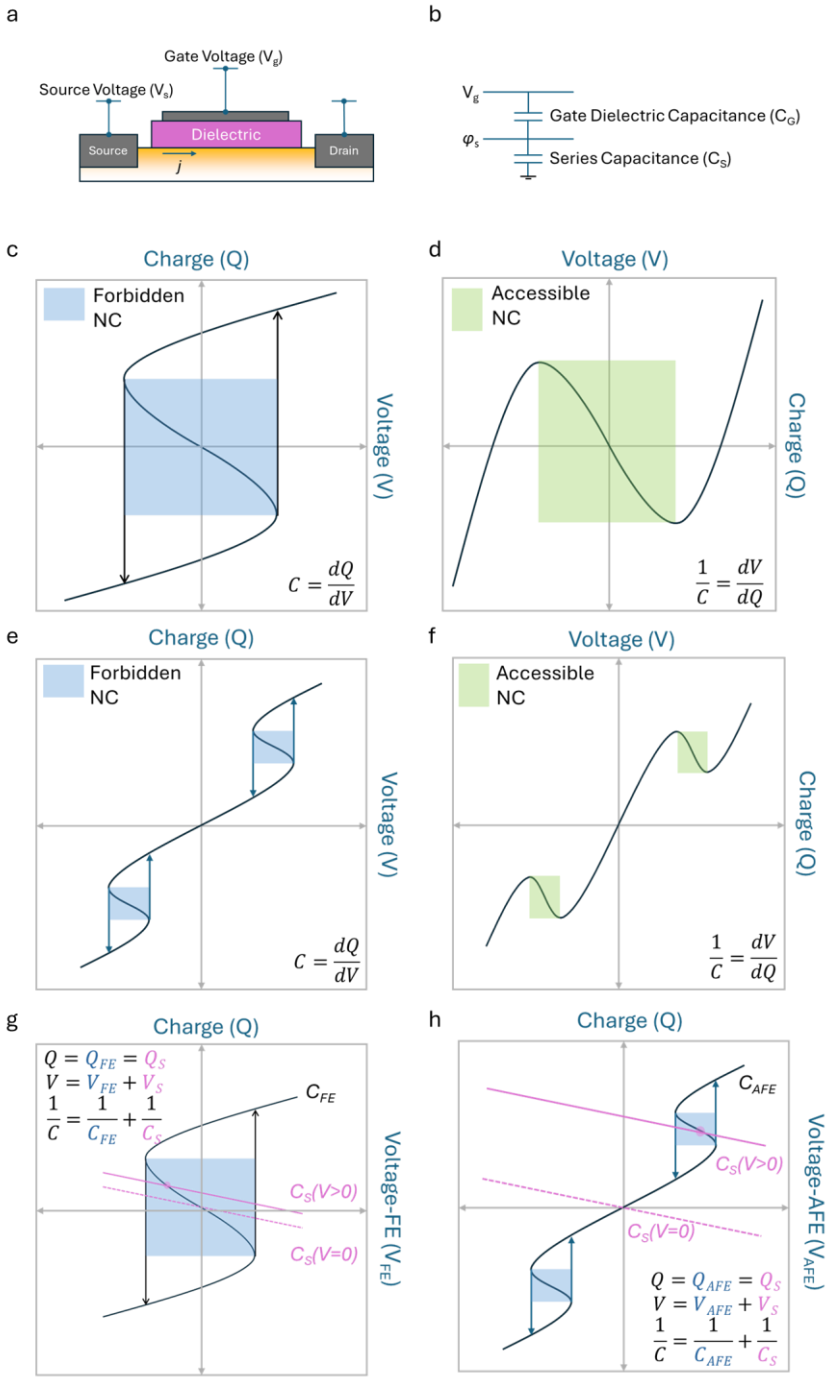


***Figure 6.7.*** ***(a)*** *Schematic of a FET,* ***(b)*** *Equivalent circuit of an FET, Voltage- Charge relations in* ***(c, d)*** *ferroelectrics and* ***(e, f)*** *antiferroelectrics when controlling* ***(c, e)*** *voltage or* ***(d, f)*** *controlling charge. Voltage across FE/AFE – Charge relationship in presence of a series dielectric capacitor with* ***(g)*** *Ferroelectric and* ***(h)*** *Antiferroelectric.*

*Strategy 1: Transistor based on PZO epitaxial film.*

Two samples of PZO/SRO films were grown on STO (001) substrates, followed by deposition of $MoS_2$ on one and Graphene on the other. Graphene and $MoS_2$ were chosen because these materials can perform excellently in transistors. While graphene has very high mobility,[194] it does not have a band gap, leading to poor ratio between On and Off state, whereas $MoS_2$ has a band gap of 1.8 eV (resulting in good On to Off ratio up to 5 orders of magnitude),[195] but with lower mobility. The channel layers were then patterned using photolithography and reactive ion etching with oxygen plasma. The third step was to pattern the sample again and deposit the source and drain electrodes (Au/Ti in this case). The schematic of the device and optical images are shown in **Figure 6.8**. In this case, I was not able to measure the devices. The device based on Graphene resulted in a poor lift-off process in the second step of patterning due to a smaller step height, while the device based on $MoS_2$ had very high leakage currents due to incomplete etching of $MoS_2$. The potential solutions to obtain proper lift is the optimization of patterning process or change in design of transistor such as using graphene or $MoS_2$ as the bottom layer and gate on top which is not an applicable strategy for epitaxial films. On the other hand, due to the slower switching dynamics of epitaxial films than membranes, the latter might be a better alternate for such devices along with the additional benefit of integrating onto Silicon and more freedom with designs strategies, so we focussed on those for the following attempts.

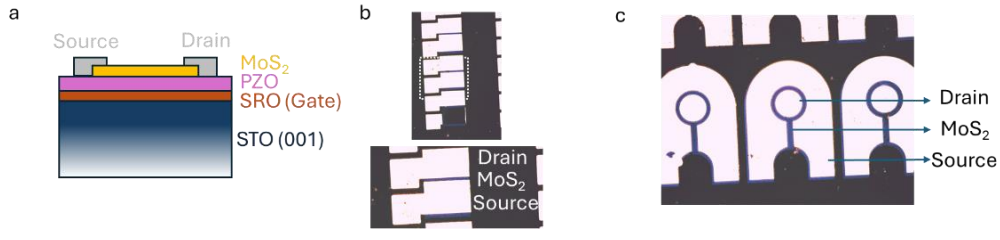


***Figure 6.8. (a)*** *Schematic of PZO/$MoS_2$ device,* ***(b, c)*** *Optical images of the fabricated devices.*

*Strategy 2: Transistor based on PZO membrane.*

The second strategy I used was to utilize PZO membrane. For this, a gate electrode was first deposited on a Silicon substrate via lift-off process, followed by transferring 120 nm PZO membrane on top. I then deposited two top electrodes to act as source and drain in regions, avoiding wrinkles and crack; the schematic is shown in **Figure 6.9a** and optical images in **6.9b-c**. In this case, the membrane does not lie flat on the gate electrode but rather is curved on top as seen in the AFM measurement (**Figure 6.9d-e**). This strategy poses two problems. First, the contact between the bottom electrode (gate) and the membrane is not perfect; second, the membrane is under strain conditions. The consequence is a broadening of the loop, as seen in **Figure 6.9f (**due to strains as well as RC effects). In this case, the capacitor has a small area (5 x 5 $\mu m^2$) to reduce leakage and therefore, the current loop also looks noisy due to the small

signal. One way of circumventing this might be to etch a pattern in the Silicon substrate first and deposit the electrode in the etched region to obtain a flat surface. Another possible way could be to transfer a full capacitor stack (SRO/PZO/SRO) onto a Pt-coated Silicon and then partially etch away some of the top SRO to expose the PZO .

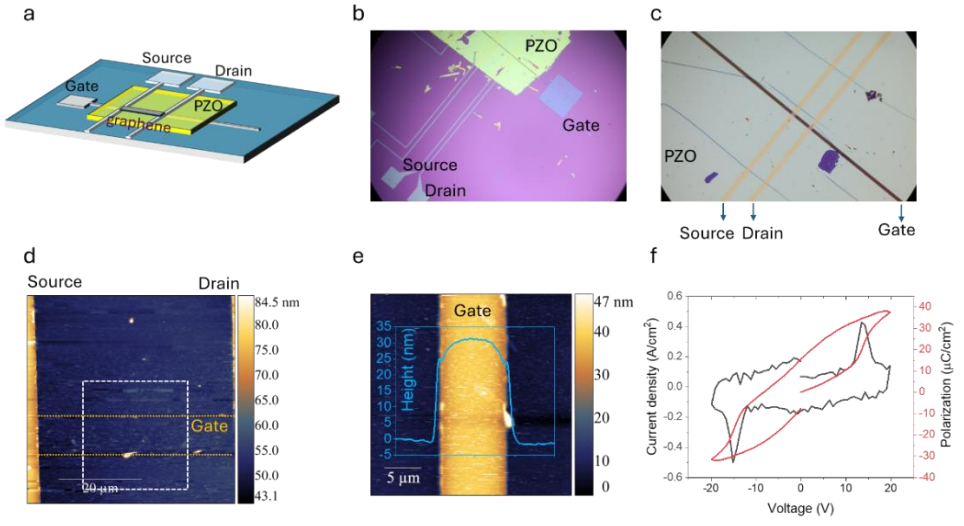


***Figure 6.9.*** ***(a)*** *Schematic of a FET based on PZO membrane,* ***(b, c)*** *Optical images of the fabricated device,* ***(d)*** *AFM of the device****, (e)*** *AFM of the region marked as white dotted box in (d), inset shows the height evolution of PZO membrane on top of the gate electrode,* ***(e)*** *Current/Polarization- Voltage loop measured on the device.*

*Strategy 3: Transistor based on SRO/PZO/SRO capacitor*

An SRO/PZO/SRO membrane capacitor was transferred to silicon substrate homogeneously coated with gold to prevent buckling of the transferred membrane and to allow a good contact between the PZO layer and the electrodes. The bottom SRO in contact with the Au acts as the gate. The top SRO is patterned to make source and drain contacts, schematic shown in **Figure 6.10a** and optical image in **6.10b**. In this case, the hysteresis loop measurements were done after transferring the membrane and after the SRO patterning process (**Figure 6.10c** and **d**). There is a change in the shape of the hysteresis loop due to the patterning process that includes multiple heating and uncontrolled cooling steps (100°C for 1 min and cooled to room temperature rapidly, followed by heating to 120°C for 2 min and cooled rapidly). To relax these stresses, the capacitor is annealed at 250°C for 20 min with heating and cooling rate of 5°C/min. Surprisingly, the loop changes again after this process as shown in **Figure 6.10e**. The change in the hysteresis loop after transfer, uncontrolled thermal processes and finally annealing might be caused by the defects (such as intercalated Hydrogen discussed in **Chapter 2**), emergence of disorder (as discussed in **Chapter 4**) or build- up of internal stresses. Hence, thermal cycling can also affect the AFE behaviour of the PZO layers (we explore this further in **Appendix G**). In any case, the capacitors still exhibit robust

antiferroelectric behaviour to be used for devices. The next steps of depositing graphene or $MoS_2$ channel layers are still under progress.

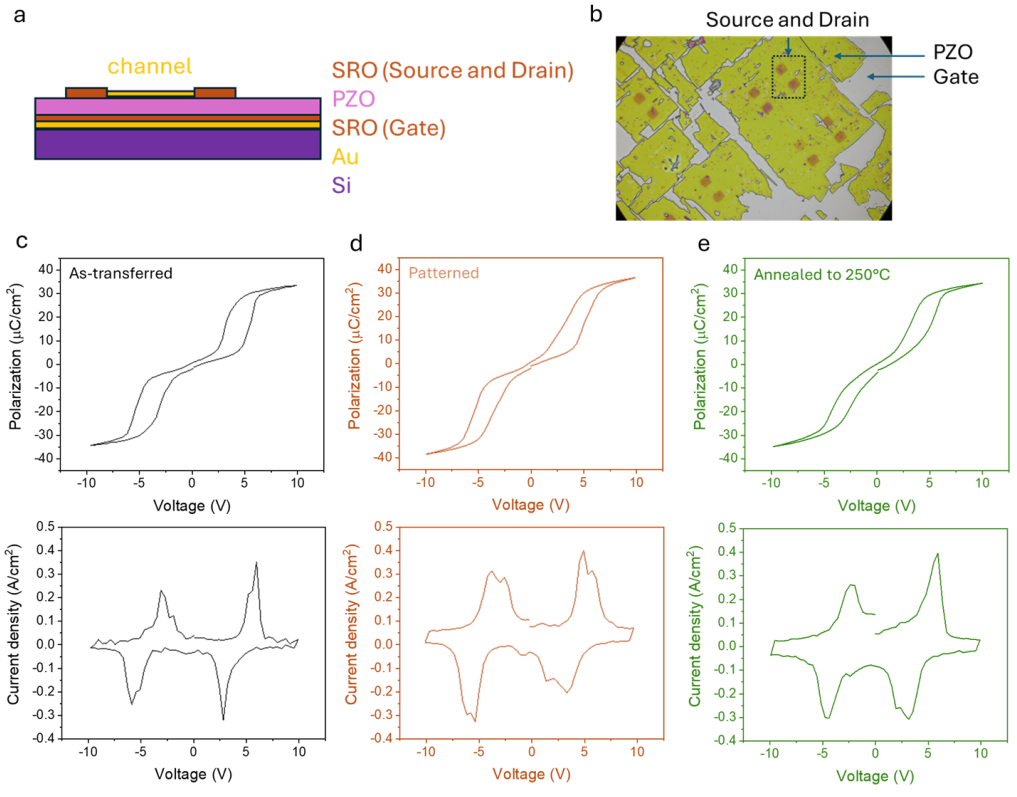


***Figure 6.10 (a)*** *Schematic of transistor based on SRO/PZO/SRO capacitor,* ***(b)*** *Optical image of the fabricated devices,* ***(c-e)*** *Polarization* ***(top panels)*** *and Displacement current density* ***(bottom panel)****-Voltage loops at different stages of the fabrication process.*

## 6.3. Outlook

When we think of antiferroelectrics or ferroelectrics, polarization is the main property that we try to use. The results that I have showed so far, as well as investigations reported in the literature, make use of the switching of the AFE to the FE phase that results in an increase in the polarization. The displacement current peak corresponding to this phase transition or the surface polarization can be used in memory devices. However, one of the most important factors driving the research in neuromorphic elements is to reduce the power consumption of computations. For FE and AFE materials, this drive translates to the decrease in the thickness of the FE/AFE layer, so the voltage required for switching decreases -but this reduced thickness means higher leakage currents. To this end, we can take advantage of the intimate phase mixture in PZO as we have discussed before. The phases in PZO are non-trivial, they have unique polarization directions and therefore, different surface polarizations. Since the energies

of these phases are very close, PZO can transition between them by small external perturbations in the form of voltage pulses. Moreover, since the amplitude of the applied voltage pulses are lower than the switching voltage, these low-voltage antiferroelectric designs are also better for power saving and minimizing leakage currents.

In polar (or antipolar) materials, resistance or conductance is a property that is usually considered a draw-back due to leakage. However, tuning the resistance of such dielectrics may allow us to fabricate multi-faceted devices. Resistive switching is one of their important properties that can be very useful. Although, the results of one of our experiments seem to suggest that the origin of this resistive switching in PZO is in the ferroelectric/ferroelastic domain walls, an extensive investigation, ideally with some form of in-situ microscopy, is still needed to substantiate this claim. In any case, our results show that using trains of pulses, we can not only control the resistance of the material but probably also the surface polarization as well (as discussed in the previous sections), allowing the tunability of two properties simultaneously. Hence, the propensity of PZO membranes to break down into multiple domains or phases can open new avenues for novel devices and applications where two properties within the same layer can be exploited simultaneously.

Finally, negative capacitance transistors are a novel application for reduction in power consumption whereby small voltages can be used to gain high conductivity changes. In this context, I have explored some design strategies to fabricate such devices in combination with 2D channel layers (graphene or $MoS_2$) to realize a functional device. While a successful device has not yet emerged, I have proposed some actions to move forward and eventually achieve (or try to achieve) negative capacitance functionalities in future work. The design proposed here, in fact, can be used for all three functionalities as discussed above.

In addition, the fabrication of membranes allows us to integrate PZO (and other perovskite oxides) on Silicon while also controlling the memory retention time (via switching dynamics) or functionality (via phase mixing). Antiferroelectrics and their manipulation in membrane form, therefore, may hold answers to some very practical issues that society is facing, ranging from energy storage to computation.

# Summary

In this thesis, I have studied different properties of antiferroelectric Lead Zirconate films. The focus was mainly on PZO free standing membranes, where the functionalities can be modified by virtue of removing epitaxial clamping. Their manipulation afterwards opens up the possibility of antiferroelectric membranes to be used in novel applications such as high energy storage capacitors and electronics.

We started with the process of fabrication of free-standing membranes using a water-based sacrificial layer etching method. We observed that the wet etching process could cause hydrogenation of the functional layers that can lead to high internal strains in the PZO membranes, as seen by Raman and XRD measurements. PFM experiments showed that these intercalated hydrogen defects caused metastability of the field-induced ferroelectric phase in PZO, which relaxed back to the AFE one over time with complete relaxation back to the AFE phase in 20 min. In contrast, membranes of STO showed no strain but exhibited a polar phonon mode in Raman linked to the hydrogenation process. The ferroelectric (or ferroelectric-like) behaviour of STO membranes was further evidenced by SS-PFM hysteresis loops. On the other hand, the post-transfer annealing of these membranes under suitable conditions was shown to mitigate the invasive hydrogenation, resulting in robust AFE loops in PZO and paraelectric STO membranes.

After optimizing the fabrication process to obtain hydrogen free membranes, we moved on to study the effect of declamping on PZO capacitors. To this end, we studied the structural and functional properties of free-standing SRO/PZO/SRO capacitors and compared them to identical epitaxial stacks. The comparison between the epitaxial and free-standing capacitors demonstrated that epitaxial clamping from the substrate hinders the motion of domain walls and phase boundaries, thereby increasing the viscosity of the switching dynamics in the system. The consequence is slower switching dynamics in epitaxial capacitors as compared to the free-standing ones, and a restricted phase growth, despite having a similar morphology and initial domain configuration. Conversely, the membranes capacitors show higher energy storage and efficiency than their epitaxial counterparts.

As we decrease the thickness of AFEs in general, they tend to become ferroelectric. Although, epitaxial clamping had been attributed as the main factor contributing to this phase transition, we observed that PZO membranes (free from substrate clamping) not only go through this size-induced AFE-FE transition, but rather the phase coexistence gets enhanced and more complex even at higher thicknesses than PZO epitaxial films reported in the literature. The results presented here, therefore, point towards surface tension being a major cause of the transition. We also observed polar disorder within our membranes that originates from decoupling of the two degrees of freedom, namely

Pb displacement and oxygen octahedral tilts. Our results expose the “plasticity” of the PZO system and its inherently complex nature.

One of the main advantages of membranes is their mechanical flexibility. Using this flexibility, we applied different levels of strains and strain gradients to the PZO system. The results of our (almost homogenous) strain study showed that the strains modify the energy barriers between the AFE and field- induced FE phases of PZO, resulting in an increase in the hysteresis under tensile strain via bending (increase in the energy barriers) and decrease under compressive strain. Furthermore, PZO/SRO rolls that are under small strains and strain gradients showed AFE behaviour. Finally, wrinkles of PZO that are subjected to larger strain gradients, exhibited signs of the FE phase, suggesting the potential of flexoelectricity for driving the AFE to FE phase transition.

There are emerging electronic device concepts where AFEs show great potential. Neuromorphic memories are one example, and they are deemed to be a viable solution for sustainability in power consumption of computing. Two important material properties that these devices make use of are polarization and resistance (or conversely, conduction), and these properties can either have long (non- volatile) or short lifetime(volatile). Our preliminary results on PZO show that the ¨remnant¨ (metastable) polarization of PZO can be tuned by controlling the strength or the time period of the electric field cycle. This polarization relaxes over time and can be further tuned by controlling the dynamics of the switching via epitaxial clamping (following our work from **Chapter 3**). Such volatile property can be used to mimic a neuron in memory devices.

In addition, we delved into the resistance of PZO layers and explored the origin of resistive switching. Our results suggested that resistive switching associated with the AFE to FE phase transition comes from the domain walls of the FE phase. Building upon our work from **Chapter 4** (phase coexistence in PZO membranes), since the FE phases are stable with the AFE phase, we applied sub-switching pulses that cause local phase transitions, allowing to modify the dielectric loss of PZO capacitors. We observed that this change in dielectric loss was a non-volatile functionality. Finally, another novel application of AFEs is negative capacitance transistors that may allow computers to overcome the Boltzmann tyranny. I attempted to fabricate proof-of-concept negative capacitance devices using PZO antiferroelectric membranes and modified the design parameters to obtain devices that showed robust antiferroelectricity. I laid out an outlook of these design optimizations and described possible future work that can be done to realize proper multi-functional devices.

# Bibliography


1. Kittel, C. Theory of antiferroelectric crystals. *Physical Review* **82**, 729 (1951).

2. Shirane, G., Sawaguchi, E. & Takagi, Y. Dielectric Properties of Lead Zirconate. *Physical Review* **84**, 476–481 (1951).

3. Kania, A. & Kwapulinski, J. $Ag_{1-x}Na_x NbO_3$ (ANN) solid solutions: from disordered antiferroelectric $AgNbO_3$ to normal antiferroelectric $NaNbO_3$. *Journal of Physics: Condensed Matter* **11**, 8933–8946 (1999).

4. Lines, M. E. & Glass, A. M. *Principles and Applications of Ferroelectrics and Related Materials*. (Oxford University Press, 2001). doi:10.1093/acprof:oso/9780198507789.001.0001.

5. Hoffman, A. Electrocaloric effect in ferroelectric ceramics with point defects. *Physical Chemistry B* 65 (1935).

6. Megaw, H. D. Crystal structure of double oxides of the perovskite type. *Proceedings of the Physical Society* **58**, 133–152 (1946).

7. ROBERTS, S. Dielectric Properties of Lead Zirconate and Barium-Lead Zirconate. *Journal of the American Ceramic Society* **33**, 63–66 (1950).

8. Sawaguchi, E., Shirane, G. & Takagi, Y. Phase Transition in Lead Zirconate. *J Physical Soc Japan* **6**, 333–339 (1951).

9. Glazer, A. M. The classification of tilted octahedra in perovskites. *Acta Crystallogr B* **28**, 3384–3392 (1972).

10. Sawaguchi, E. Ferroelectricity versus Antiferroelectricity in the Solid Solutions of $PbZrO_3$ and $PbTiO_3$. *J Physical Soc Japan* **8**, 615–629 (1953).

11. Liu, H. Origin of the intermediate phase in lead zirconate, $PbZrO_3$. *Journal of the American Ceramic Society* **101**, 5281–5286 (2018).

12. Whatmore, R. W. & Glazer, A. M. Structural phase transitions in lead zirconate. *Journal of Physics C: Solid State Physics* **12**, 1505–1519 (1979).

13. TENNERY, V. J. High-Temperature Phase Transitions in $PbZrO_3$. *Journal of the American Ceramic Society* **49**, 483–486 (1966).

14. Tan, X., Ma, C., Frederick, J., Beckman, S. & Webber, K. G. The Antiferroelectric ↔ Ferroelectric Phase Transition in Lead-Containing and Lead-Free Perovskite Ceramics. *Journal of the American Ceramic Society* **94**, 4091–4107 (2011).

15. Viehland, D. Transmission electron microscopy study of high-Zr-content lead zirconate titanate. *Phys Rev B* **52**, 778–791 (1995).

16. Si, Y. *et al.* Ideal antiferroelectricity with large digital electrostrain in $PbZrO_3$ epitaxial thin films. *Nat Commun* **16**, 4263 (2025).

17. Woodward, P. M. Octahedral Tilting in Perovskites. I. Geometrical Considerations. *Acta Crystallogr B* **53**, 32–43 (1997).

18. Woodward, P. M. Octahedral Tilting in Perovskites. II. Structure Stabilizing Forces. *Acta Crystallogr B* **53**, 44–66 (1997).

19. Zhang, H. *et al.* Finite-temperature properties of the antiferroelectric perovskite $PbZrO_3$ from a deep-learning interatomic potential. *Phys Rev B* **110**, 054109 (2024).

20. Aramberri, H., Cazorla, C., Stengel, M. & Íñiguez, J. On the possibility that $PbZrO_3$ not be antiferroelectric. *NPJ Comput Mater* **7**, 196 (2021).

21. Tagantsev, A. K. *et al.* The origin of antiferroelectricity in $PbZrO_3$. *Nat Commun* **4**, 2229 (2013).

22. Ghosez, Ph., Cockayne, E., Waghmare, U. V. & Rabe, K. M. Lattice dynamics of $BaTiO_3$, $PbTiO_3$, and $PbZrO_3$ : A comparative first-principles study. *Phys Rev B* **60**, 836–843 (1999).

23. Fujishita, H. & Katano, S. Re-Examination of the Antiferroelectric Structure of $PbZrO_3$ . *J Physical Soc Japan* **66**, 3484–3488 (1997).

24. Baker, J. S. & Bowler, D. R. First-principles soft-mode lattice dynamics of $PbZr_{0.5}Ti_{0.5}O_3$ and shortcomings of the virtual crystal approximation. *Phys Rev B* **100**, 224305 (2019).

25. Amisi, S. Ab initio investigation in $PbZrO_3$ antiferroelectric: structural and vibrational properties. *The European Physical Journal Plus* **136**, 653 (2021).

26. Baker, J. S. *et al.* A re-examination of antiferroelectric $PbZrO_3$ and $PbHfO_3$: an 80-atom Pnam structure.

27. Burkovsky, R. G. *et al.* Critical scattering and incommensurate phase transition in antiferroelectric $PbZrO_3$ under pressure. *Sci Rep* **7**, 41512 (2017).

28. Aramberri, H., Cazorla, C., Stengel, M. & Íñiguez, J. On the possibility that $PbZrO_3$ not be antiferroelectric. *NPJ Comput Mater* **7**, 196 (2021).

29. Vales-Castro, P. *et al.* Flexoelectricity in antiferroelectrics. *Appl Phys Lett* **113**, (2018).

30. Sambri, A. *et al.* Self-Formed, Conducting $LaAlO_3$ /$SrTiO_3$ Micro-Membranes. *Adv Funct Mater* **30**, (2020).

31. Lu, L. *et al.* Atomic Scale Understanding of the Epitaxy of Perovskite Oxides on Flexible Mica Substrate. *Adv Mater Interfaces* **7**, (2020).

32. Liu, J. *et al.* Mechanically Tunable Magnetic Properties of Flexible $SrRuO_3$ Epitaxial Thin Films on Mica Substrates. *Adv Electron Mater* **4**, (2018).

33. Liu, J., Liu, S. & Wu, Y. Flexible transparent conducting strontium vanadate/mica heteroepitaxial membranes with mechanically tunable transport behaviors. *J Alloys Compd* **895**, 162725 (2022).

34. Pesquera, D., Fernández, A., Khestanova, E. & Martin, L. W. Freestanding complex-oxide membranes. *Journal of Physics: Condensed Matter* **34**, 383001 (2022).

35. Lu, D. *et al.* Synthesis of freestanding single-crystal perovskite films and heterostructures by etching of sacrificial water-soluble layers. *Nat Mater* **15**, 1255–1260 (2016).

36. Pesquera, D. *et al.* Beyond substrates: strain engineering of ferroelectric membranes. *Advanced materials* **32**, 2003780 (2020).

37. Pesquera, D. *et al.* Large magnetoelectric coupling in multiferroic oxide heterostructures assembled via epitaxial lift-off. *Nat Commun* **11**, 3190 (2020).

38. Yun, S. *et al.* Strain Engineering: Perfecting Freestanding Perovskite Oxide Fabrication. *Small* **20**, (2024).

39. Mondal, P. & Jeffery, J. W. The crystal structure of tricalcium aluminate, $Ca_3Al_2O_6$. *Acta Crystallogr B* **31**, 689–697 (1975).

40. Lazic, B., Kahlenberg, V., Kaindl, R. & Kremenović, A. On the symmetry of $Ba_3Al_2O_6$ – X-ray diffraction and Raman spectroscopy studies. *Solid State Sci* **11**, 77–84 (2009).

41. Gu, K. *et al.* Simple Method to Obtain Large-Size Single-Crystalline Oxide Sheets. *Adv Funct Mater* **30**, (2020).

42. Liu, X., Li, Y., Li, Y. & Hao, X. Giant energy-storage density and thermally activated phase transition in $(Pb_{0.96}La_{0.04})(Zr_{0.99}Ti_{0.01})O_3$ antiferroelectric ceramics. *ACS Appl Energy Mater* **4**, 4897–4902 (2021).

43. Oh, S., Hwang, H. & Yoo, I. K. Ferroelectric materials for neuromorphic computing. *APL Mater* **7**, (2019).

44. Prosandeev, S. *et al.* Hidden phases with neuromorphic responses and highly enhanced piezoelectricity in an antiferroelectric prototype. *Phys Rev B* **105**, L100101 (2022).

45. Lu, D., Crossley, S., Xu, R., Hikita, Y. & Hwang, H. Y. Freestanding Oxide Ferroelectric Tunnel Junction Memories Transferred onto Silicon. *Nano Lett* **19**, 3999–4003 (2019).

46. Xu, R. *et al.* Strain-induced room-temperature ferroelectricity in $SrTiO_3$ membranes. *Nat Commun* **11**, 3141 (2020).

47. Li, Y. *et al.* Electrostatically Driven Polarization Flop and Strain-Induced Curvature in Free-Standing Ferroelectric Superlattices. *Advanced Materials* **34**, (2022).

48. Dong, G. *et al.* Super-elastic ferroelectric single-crystal membrane with continuous electric dipole rotation. *Science (1979)* **366**, 475–479 (2019).

49. Elangovan, H. *et al.* Giant Superelastic Piezoelectricity in Flexible Ferroelectric $BaTiO_3$ Membranes. *ACS Nano* **14**, 5053–5060 (2020).

50. Zhou, Y. *et al.* Tip-Induced In-Plane Ferroelectric Superstructure in Zigzag-Wrinkled $BaTiO_3$ Thin Films. *Nano Lett* **22**, 2859–2866 (2022).

51. Ganguly, S. *et al.* Photostrictive Actuators Based on Freestanding Ferroelectric Membranes. *Advanced Materials* **36**, (2024).

52. Pryds, N., Park, D.-S., Jespersen, T. S. & Yun, S. Twisted oxide membranes: A perspective. *APL Mater* **12**, (2024).

53. Catalan, G. *et al.* Polarization Vortices in a Ferromagnetic Metal via Twistronics. Preprint at https://doi.org/10.21203/rs.3.rs-6656512/v1 (2025).

54. Sánchez-Santolino, G. *et al.* A 2D ferroelectric vortex pattern in twisted $BaTiO_3$ freestanding layers. *Nature* **626**, 529–534 (2024).

55. Sha, H. *et al.* Polar vortex hidden in twisted bilayers of paraelectric $SrTiO_3$. *Nat Commun* **15**, 10915 (2024).

56. Lee, S., de Sousa, D. J. P., Jalan, B. & Low, T. Moiré polar vortex, flat bands, and Lieb lattice in twisted bilayer $BaTiO_3$. *Sci Adv* **10**, (2024).

57. Dieckmann, R. Solution and transport of water in oxides. *Materials at High Temperatures* **22**, 93–103 (2005).

58. Nedumkandathil, R. *et al.* Hydride Reduction of $BaTi_3$ − Oxyhydride Versus O Vacancy Formation. *ACS Omega* **3**, 11426–11438 (2018).

59. Kobayashi, Y. *et al.* An oxyhydride of $BaTiO_3$ exhibiting hydride exchange and electronic conductivity. *Nat Mater* **11**, 507–511 (2012).

60. Eklöf-Österberg, C. *et al.* The role of oxygen vacancies on the vibrational motions of hydride ions in the oxyhydride of barium titanate. *J Mater Chem A Mater* **8**, 6360–6371 (2020).

61. Liyanage, M., Miller, R. & Rajapakse, R. First principles study of hydrogen in lead zirconate titanate. *Smart Mater Struct* **28**, 034002 (2019).

62. Aggarwal, S. *et al.* Effect of hydrogen on Pb(Zr,Ti)$O_3$-based ferroelectric capacitors. *Appl Phys Lett* **73**, 1973–1975 (1998).

63. Li, Z. *et al.* Reversible manipulation of the magnetic state in $SrRuO_3$ through electric-field controlled proton evolution. *Nat Commun* **11**, 184 (2020).

64. Lu, Q. *et al.* Bi-directional tuning of thermal transport in $SrCoO_x$ with electrochemically induced phase transitions. *Nat Mater* **19**, 655–662 (2020).

65. Lu, N. *et al.* Electric-field control of tri-state phase transformation with a selective dual-ion switch. *Nature* **546**, 124–128 (2017).

66. Chen, H. *et al.* Protonation-Induced Colossal Chemical Expansion and Property Tuning in $NdNiO_3$ Revealed by Proton Concentration Gradient Thin Films. *Nano Lett* **22**, 8983–8990 (2022).

67. Shen, S. *et al.* Emergent Ferromagnetism with Fermi-Liquid Behavior in Proton Intercalated $CaRuO_3$. *Phys Rev X* **11**, 021018 (2021).

68. Wang, Q. *et al.* Realizing Metastable Cobaltite Perovskite via Proton-Induced Filling of Oxygen Vacancy Channels. *ACS Appl Mater Interfaces* **15**, 1574–1582 (2023).

69. Kapphan, S., Koppitz, J. & Weber, G. O-D and O-H stretching vibrations in monodomain $SrTiO_3$. *Ferroelectrics* **25**, 585–588 (1980).

70. PASTO, A. E. & CONDRATE, R. A. Raman Spectrum of $PbZrO_3$. *Journal of the American Ceramic Society* **56**, 436–438 (1973).

71. Jankowska-Sumara, I. Dielectric relaxation, electrostrictive properties and Raman light scattering in $PbZrO_3$ and $PbHfO_3$ single crystals pure and doped with small amount of $PbTiO_3$. (UPVM - Université Paul Verlaine, Metz, 1997).

72. Roleder, K. *et al.* Antiferroelectric and ferroelectric phase transitions of the displacive and order-disorder type in $PbZrO_3$ and $PbZr_{1-x}Ti_xO_3$ single crystals. *Phase Transitions* **71**, 287–306 (2000).

73. Rodriguez, B. J., Callahan, C., Kalinin, S. V & Proksch, R. Dual-frequency resonance-tracking atomic force microscopy. *Nanotechnology* **18**, 475504 (2007).

74. Jesse, S., Baddorf, A. P. & Kalinin, S. V. Switching spectroscopy piezoresponse force microscopy of ferroelectric materials. *Appl Phys Lett* **88**, (2006).

75. Lu, H. *et al.* Probing Antiferroelectric-Ferroelectric Phase Transitions in $PbZrO_3$ Capacitors by Piezoresponse Force Microscopy. *Adv Funct Mater* **30**, 2003622 (2020).

76. Ferri, A. *et al.* Evidences of the ferroelectric and antiferroelectric phases coexistence in the $(Pb_{0.96}La_{0.04})(Zr_{0.95}Ti_{0.05})_{0.99}O_3$ ceramic system by probing

nanoscale analyses via piezoresponse force microscopy. *Journal of the American Ceramic Society* **107**, 3170–3179 (2024).

77. Zhou, Z. *et al.* Ferroelectric domains and phase transition of sol-gel processed epitaxial Sm-doped $BiFeO_3$ (001) thin films. *Journal of Materiomics* **4**, 27–34 (2018).

78. Si, Y. *et al.* Phase Competition in High-Quality Epitaxial Antiferroelectric $PbZrO_3$ Thin Films. *ACS Appl Mater Interfaces* **14**, 51096–51104 (2022).

79. Pintilie, L., Boldyreva, K., Alexe, M. & Hesse, D. Coexistence of ferroelectricity and antiferroelectricity in epitaxial $PbZrO_3$ films with different orientations. *J Appl Phys* **103**, (2008).

80. Liu, Y. *et al.* Translational Boundaries as Incipient Ferrielectric Domains in Antiferroelectric $PbZrO_3$. *Phys Rev Lett* **130**, 216801 (2023).

81. Tarun, M. C. & McCluskey, M. D. Infrared absorption of hydrogen-related defects in strontium titanate. *J Appl Phys* **109**, (2011).

82. Xu, L. & Jiang, D. Understanding hydrogen in perovskites from first principles. *Comput Mater Sci* **174**, 109461 (2020).

83. Liu, X. *et al.* Nonlinear optical phonon spectroscopy revealing polaronic signatures of the $LaAlO_3/SrTiO_3$ interface. *Sci Adv* **9**, (2023).

84. Jang, H. W. *et al.* Ferroelectricity in Strain-Free $SrTiO_3$ Thin Films. *Phys Rev Lett* **104**, 197601 (2010).

85. Fang, X. *et al.* Hydrogen response to high-density dislocations in bulk perovskite oxide $SrTiO_3$. *ArXiv* (2025).

86. Marrocchelli, D., Sun, L. & Yildiz, B. Dislocations in $SrTiO_3$ : Easy To Reduce but Not so Fast for Oxygen Transport. *J Am Chem Soc* **137**, 4735–4748 (2015).

87. Bjørheim, T. S. *et al.* A combined conductivity and DFT study of protons in $PbZrO_3$ and alkaline earth zirconate perovskites. *Solid State Ion* **181**, 130–137 (2010).

88. Pauling, L. THE NATURE OF THE CHEMICAL BOND. IV. THE ENERGY OF SINGLE BONDS AND THE RELATIVE ELECTRONEGATIVITY OF ATOMS. *J Am Chem Soc* **54**, 3570–3582 (1932).

89. Varley, J. B., Janotti, A. & Van de Walle, C. G. Hydrogenated vacancies and hidden hydrogen in $SrTiO_3$. *Phys Rev B* **89**, 075202 (2014).

90. Yukawa, H., Nakatsuka, K. & Morinaga, M. Electronic structures of hydrogen in perovskite-type oxide, $SrTiO_3$. *Solid State Ion* **116**, 89–98 (1999).

91. Wakim, F. G. Hydrogen and Deuterium in $SrTiO_3$ Single Crystals. *J Chem Phys* **49**, 3738–3739 (1968).

92. Pryds, N., Park, D.-S., Jespersen, T. S. & Yun, S. Twisted oxide membranes: A perspective. *APL Mater* **12**, (2024).

93. Sánchez-Santolino, G. *et al.* A 2D ferroelectric vortex pattern in twisted $BaTiO_3$ freestanding layers. *Nature* **626**, 529–534 (2024).

94. Wang, H., Harbola, V., Wu, Y., van Aken, P. A. & Mannhart, J. Interface Design beyond Epitaxy: Oxide Heterostructures Comprising Symmetry-Forbidden Interfaces. *Advanced Materials* **36**, (2024).

95. Chen, C. *et al.* Defect and Strain Engineering Coenhanced Nanoscale Ferroelectricity in $SrTiO_3$ Thin Films. *ACS Nano* **19**, 13479–13488 (2025).

96. Van Truong, D., Quang, T. T., Linh, N. H., Van Hoi, N. & Van Thanh, V. Enhancement of Polarization Properties of Bulk $PbTiO_3$ by Engineering Strain. *Integrated Ferroelectrics* **232**, 186–196 (2023).

97. Han, L. *et al.* Giant Uniaxial Strain Ferroelectric Domain Tuning in Freestanding $PbTiO_3$ Films. *Adv Mater Interfaces* **7**, (2020).

98. Zhang, L. *et al.* Controllable Ferromagnetism in Super-tetragonal $PbTiO_3$ through Strain Engineering. *Nano Lett* **20**, 881–886 (2020).

99. Hoffman, J. *et al.* Ferroelectric Field Effect Transistors for Memory Applications. *Advanced Materials* **22**, 2957–2961 (2010).

100. Yoong, H. Y. *et al.* Epitaxial Ferroelectric $Hf_{0.5}Zr_{0.5}O_2$ Thin Films and Their Implementations in Memristors for Brain-Inspired Computing. *Adv Funct Mater* **28**, (2018).

101. Zeng, T. *et al.* Approaching the Ideal Linearity in Epitaxial Crystalline-Type Memristor by Controlling Filament Growth. *Advanced Materials* **36**, (2024).

102. Gruverman, A. *et al.* Tunneling Electroresistance Effect in Ferroelectric Tunnel Junctions at the Nanoscale. *Nano Lett* **9**, 3539–3543 (2009).

103. Chanthbouala, A. *et al.* Solid-state memories based on ferroelectric tunnel junctions. *Nat Nanotechnol* **7**, 101–104 (2012).

104. Garcia, V. & Bibes, M. Ferroelectric tunnel junctions for information storage and processing. *Nat Commun* **5**, 4289 (2014).

105. Tian, Z., Kim, J., Fernandez, A., Huang, X. & Martin, L. W. Effect of substrate clamping on evolution of properties in homovalent and heterovalent relaxor thin films. *Phys Rev B* **105**, 094107 (2022).

106. Setter, N. *et al.* Ferroelectric thin films: Review of materials, properties, and applications. *J Appl Phys* **100**, (2006).

107. Pan, H. *et al.* Clamping enables enhanced electromechanical responses in antiferroelectric thin films. *Nat Mater* **23**, 944–950 (2024).

108. Jiang, R.-J. *et al.* A Roadmap for Ferroelectric–Antiferroelectric Phase Transition. *Nano Lett* **24**, 11714–11721 (2024).

109. Catalan, G., Noheda, B., McAneney, J., Sinnamon, L. J. & Gregg, J. M. Strain gradients in epitaxial ferroelectrics. *Phys Rev B* **72**, 020102 (2005).

110. Langford, J. I. & Wilson, A. J. C. Scherrer after sixty years: A survey and some new results in the determination of crystallite size. *J Appl Crystallogr* **11**, 102–113 (1978).

111. Corker, D. L., Glazer, A. M., Dec, J., Roleder, K. & Whatmore, R. W. A Re-investigation of the Crystal Structure of the Perovskite $PbZrO_3$ by X-ray and Neutron Diffraction. *Acta Crystallogr B* **53**, 135–142 (1997).

112. Banerjee, A. & Bar, T. Finite-dimensional signature of spinodal instability in an athermal hysteretic transition. *Phys Rev B* **107**, 24103 (2023).

113. Bar, T., Ghosh, A. & Banerjee, A. Suppression of spinodal instability by disorder in an athermal system. *Phys Rev B* **104**, 144102 (2021).

114. Zhu, Q. *et al.* Frequency dependence of antiferroelectric ferroelectric phase transition of PLZST ceramic. *Journal of the American Ceramic Society* **105**, 2634–2645 (2022).

115. Ge, J. *et al.* Dynamic hysteresis and scaling behavior in epitaxial antiferroelectric film. *Thin Solid Films* **584**, 108–111 (2015).

116. Kim, Y.-H. & Kim, J.-J. Scaling behavior of an antiferroelectric hysteresis loop. *Phys Rev B* **55**, R11933–R11936 (1997).

117. Ishibashi, Y. & Orihara, H. A theory of DE hysteresis loop. *Integrated Ferroelectrics* **9**, 57–61 (1995).

118. Song, T., Sánchez, F. & Fina, I. Impact of non-ferroelectric phases on switching dynamics in epitaxial ferroelectric $Hf_{0.5}Zr_{0.5}O_2$ films. *APL Mater* **10**, 31108 (2022).

119. Yang, S. M. *et al.* ac dynamics of ferroelectric domains from an investigation of the frequency dependence of hysteresis loops. *Phys Rev B* **82**, 174125 (2010).

120. Yang, S. M. *et al.* Ac dynamics of ferroelectric domains from an investigation of the frequency dependence of hysteresis loops. *Phys Rev B* **82**, 174125 (2010).

121. Hashimoto, S., Orihara, H. & Ishibashi, Y. Study on D-E hysteresis loop of TGS based on the Avrami-type model. *J Physical Soc Japan* **63**, 1601–1610 (1994).

122. Sawaguchi, E. & Kittaka, T. Antiferroelectricity and Ferroelectricity in Lead Zirconate. *J Physical Soc Japan* **7**, 336–337 (1952).

123. Damjanovic, D. & Demartin, M. The Rayleigh law in piezoelectric ceramics. *J Phys D Appl Phys* **29**, 2057–2060 (1996).

124. Rayleigh, Lord. XXV. Notes on electricity and magnetism.—III. On the behaviour of iron and steel under the operation of feeble magnetic forces. *The London, Edinburgh, and Dublin Philosophical Magazine and Journal of Science* **23**, 225–245 (1887).

125. Borderon, C., Renoud, R. & Gundel, H. W. Description of the nonlinear dielectric properties of ferroelectrics under a weak AC-field. in *2010 IEEE International Symposium on the Applications of Ferroelectrics (ISAF)* 1–4 (IEEE, 2010). doi:10.1109/ISAF.2010.5712233.

126. Phillips, J. C. Stretched exponential relaxation in molecular and electronic glasses. *Reports on Progress in Physics* **59**, 1133–1207 (1996).

127. Ding, X. *et al.* Dynamically strained ferroelastics: Statistical behavior in elastic and plastic regimes. *Phys Rev B* **87**, 094109 (2013).

128. Pesquera, D., Carpenter, M. A. & Salje, E. K. H. Glasslike Dynamics of Polar Domain Walls in Cryogenic $SrTiO_3$. *Phys Rev Lett* **121**, 235701 (2018).

129. Chen, S.-W. *et al.* Jamming Behavior of Domains in a Spiral Antiferromagnetic System. *Phys Rev Lett* **110**, 217201 (2013).

130. Yu, Z. *et al.* Room-temperature stabilizing strongly competing ferrielectric and antiferroelectric phases in $PbZrO_3$ by strain-mediated phase separation. *Nat Commun* **15**, 3438 (2024).

131. Liu, Y. *et al.* Coexistence of ferroelectric and ferrielectric phases in ultrathin antiferroelectric $PbZrO_3$ thin films. *Microstructures* **4**, (2024).

132. Ma, T. *et al.* Uncompensated Polarization in Incommensurate Modulations of Perovskite Antiferroelectrics. *Phys Rev Lett* **123**, 217602 (2019).

133. Zhang, W. *et al.* Phase Coexistence Induced Giant Dielectric Tunability and Electromechanical Response in $PbZrO_3$ Epitaxial Thin Films. *Small* **21**, (2025).

134. Maity, N. *et al.* Ferroelectricity at the extreme thickness limit in the archetypal antiferroelectric $PbZrO_3$. *NPJ Comput Mater* **11**, 48 (2025).

135. Kondovych, S. *et al.* Surface-Tension-Induced Phase Transitions in Freestanding Ferroelectric Thin Films. *Nano Lett* https://doi.org/10.1021/acs.nanolett.5c03216 (2025).

136. de la Peña, F. *et al.* HyperSpy: Multi-dimensional data analysis tool. Preprint at https://doi.org/10.5281/zenodo.1469364 (2018).

137. Nord, M., Vullum, P. E., MacLaren, I., Tybell, T. & Holmestad, R. Atomap: a new software tool for the automated analysis of atomic resolution images using two-dimensional Gaussian fitting. *Adv Struct Chem Imaging* **3**, 9 (2017).

138. Knudsen, J., Woodward, D. I. & Reaney, I. M. Domain variance and superstructure across the antiferroelectric/ferroelectric phase boundary in $Pb_{1-1.5\,x}La_x(Zr_{0.9}TiM_{0.1})O_3$. *J Mater Res* **18**, 262–271 (2003).

139. Liu, Y. *et al.* Vortices and antivortices in antiferroelectric $PbZrO_3$. *Nat Mater* https://doi.org/10.1038/s41563-025-02245-3 (2025)

140. Glazer, A. M., Thomas, P. A., Baba-Kishi, K. Z., Pang, G. K. H. & Tai, C. W. Influence of short-range and long-range order on the evolution of the morphotropic phase boundary in $Pb(Zr_{1-x}Ti_x)O_3$. *Phys Rev B* **70**, 184123 (2004).

141. Welberry, T. R., Goossens, D. J., Withers, R. L. & Baba-Kishi, K. Z. Monte Carlo Simulation Study of Diffuse Scattering in PZT, $Pb(Zr,Ti)O_3$. *Metallurgical and Materials Transactions A* **41**, 1110–1118 (2010).

142. Noheda, B., Wu, L. & Zhu, Y. Low-temperature superlattice in monoclinic $PbZr_{0.52}Ti_{0.48}O_3$. *Phys Rev B* **66**, 060103 (2002).

143. Noheda, B. *et al.* Tetragonal-to-monoclinic phase transition in a ferroelectric perovskite: The structure of $PbZr_{0.52}Ti_{0.48}O_3$. *Phys Rev B* **61**, 8687–8695 (2000).

144. Liu, S. Z. *et al.* Atomic-scale insight into antiferroelectric–ferroelectric transition in low-Ti-doped $PbZr_{1-x}Ti_xO_3$. *Acta Mater* **298**, 121395 (2025).

145. Fu, Z. *et al.* Atomic reconfiguration among tri-state transition at ferroelectric/antiferroelectric phase boundaries in $Pb(Zr,Ti)O_3$. *Nat Commun* **13**, 1390 (2022).

146. Han, M. J. *et al.* Coexistence of rhombohedral and orthorhombic phases in ultrathin $BiFeO_3$ films driven by interfacial oxygen octahedral coupling. *Acta Mater* **145**, 220–226 (2018).

147. Íñiguez, J., Stengel, M., Prosandeev, S. & Bellaiche, L. First-principles study of the multimode antiferroelectric transition in $PbZrO_3$. *Phys Rev B* **90**, 220103 (2014).

148. Xu, R. *et al.* Size-Induced Ferroelectricity in Antiferroelectric Oxide Membranes. *Advanced Materials* **35**, (2023).

149. Chaudhuri, A. R. *et al.* Epitaxial strain stabilization of a ferroelectric phase in $PbZrO_3$ thin films. *Phys Rev B* **84**, 54112 (2011).

150. Mirzamohammadi, N., Pesquera, D., De Luca, G., Cordero-Edwards, K. & Catalan, G. Molecular electrodes enable faster switching in ferroelectric thin films. *Appl Phys Lett* **127**, (2025).

151. Liu, S. Z. *et al.* Atomic-scale insight into antiferroelectric–ferroelectric transition in low-Ti-doped $PbZr_{1-x}Ti_xO_3$. *Acta Mater* **298**, 121395 (2025).

152. Zhang, N. *et al.* A neutron diffuse scattering study of $PbZrO_3$ and Zr-rich $PbZr_{1-x}Ti_xO_3$. *J Appl Crystallogr* **48**, 1637–1644 (2015).

153. Pan, H. *et al.* Highly Tunable Relaxors Developed from Antiferroelectrics. *Advanced Materials* **37**, (2025).

154. Huang, X. *et al.* Modulation of the relaxor antiferroelectric behavior in the lead-free Gd-modified $NaNbO_3$-$MnO_2$ ceramics via phase engineering. *Ceram Int* https://doi.org/10.1016/j.ceramint.2025.06.461 (2025).

155. Kang, X. *et al.* Excellent dielectric energy storage properties of Pb-based antiferroelectric ceramics via phase structure regulation and grain engineering. *Chemical Engineering Journal* **521**, 166739 (2025).

156. Sun, Z. & Wang, R. Emerging nanomaterials for energy storage: A critical review of metrics, hotspots, and future directions. *Renewable and Sustainable Energy Reviews* **224**, 116093 (2025).

157. Haeni, J. H. *et al.* Room-temperature ferroelectricity in strained $SrTiO_3$. *Nature* **430**, 758–761 (2004).

158. Choi, K. J. *et al.* Enhancement of Ferroelectricity in Strained $BaTiO_3$ Thin Films. *Science (1979)* **306**, 1005–1009 (2004).

159. Damodaran, A. R. *et al.* New modalities of strain-control of ferroelectric thin films. *Journal of Physics: Condensed Matter* **28**, 263001 (2016).

160. Parmar, K. *et al.* Establishing a pure antiferroelectric $PbZrO_3$ phase through tensile epitaxial strain. *Nat Commun* **16**, 6536 (2025).

161. Guo, Y. *et al.* Remarkable flexibility in freestanding single-crystalline antiferroelectric $PbZrO_3$ membranes. *Nat Commun* **15**, 4414 (2024).

162. Dong, G. *et al.* Periodic Wrinkle-Patterned Single-Crystalline Ferroelectric Oxide Membranes with Enhanced Piezoelectricity. *Advanced Materials* **32**, (2020).

163. Puchberger, S., Soprunyuk, V., Majchrowski, A., Roleder, K. & Schranz, W. Domain wall motion and precursor dynamics in $PbZrO_3$. *Phys Rev B* **94**, 214101 (2016).

164. Pesquera, D. *et al.* Hierarchical domain structures in buckled ferroelectric free sheets. *Acta Mater* **293**, 121080 (2025).

165. Huang, S. *et al.* Ferroelectric Order Evolution in Freestanding $PbTiO_3$ Films Monitored by Optical Second Harmonic Generation. *Advanced Science* **11**, (2024).

166. Taklo, M. M. V, Storås, P., Schjølberg-Henriksen, K., Hasting, H. K. & Jakobsen, H. Strong, high-yield and low-temperature thermocompression

silicon wafer-level bonding with gold. *Journal of Micromechanics and Microengineering* **14**, 884–890 (2004).

167. Zhang, G. G., Ang, X. F., Chen, Z., Wong, C. C. & Wei, J. Critical temperatures in thermocompression gold stud bonding. *J Appl Phys* **102**, (2007).

168. Mao, L., Meng, Q., Ahmad, A. & Wei, Z. Mechanical Analyses and Structural Design Requirements for Flexible Energy Storage Devices. *Adv Energy Mater* **7**, (2017).

169. Rashid, M., Mahmood, Q., Babar, F., Ramay, S. M. & Mahmood, A. Study of mechanical, electronic and optical properties of $PbZrO_3$ and $PbHfO_3$ ; DFT approach. *Mater Res Express* **6**, 066311 (2019).

170. Yamanaka, S. *et al.* Thermophysical properties of $SrHfO_3$ and $SrRuO_3$. *J Solid State Chem* **177**, 3484–3489 (2004).

171. Espinosa, H. D., Prorok, B. C. & Fischer, M. A methodology for determining mechanical properties of freestanding thin films and MEMS materials. *J Mech Phys Solids* **51**, 47–67 (2003).

172. Dufour, P. Structural and physical properties of antiferroic oxide thin films. (Université Paris-Saclay, 2023).

173. Wakabayashi, Y. K., Kaneta-Takada, S., Krockenberger, Y., Taniyasu, Y. & Yamamoto, H. Wide-Range Epitaxial Strain Control of Electrical and Magnetic Properties in High-Quality $SrRuO_3$ Films. *ACS Appl Electron Mater* **3**, 2712–2719 (2021).

174. Segantini, G. *et al.* Curvature-Controlled Polarization in Adaptive Ferroelectric Membranes. *Small* https://doi.org/10.1002/smll.202506338 (2025).

175. Goldstine, H. H. *The Computer from Pascal to von Neumann*. (Princeton University Press, 2008). doi:10.1515/9781400820139.

176. von Neumann, J. First draft of a report on the EDVAC. *IEEE Annals of the History of Computing* **15**, 27–75 (1993).

177. Samsi, S. *et al.* From Words to Watts: Benchmarking the Energy Costs of Large Language Model Inference. in *2023 IEEE High Performance Extreme Computing Conference (HPEC)* 1–9 (IEEE, 2023). doi:10.1109/HPEC58863.2023.10363447.

178. Krestinskaya, O. *et al.* Neural architecture search for in-memory computing-based deep learning accelerators. *Nature Reviews Electrical Engineering* **1**, 374–390 (2024).

179. Syed, G. S., Le Gallo, M. & Sebastian, A. Phase-Change Memory for In-Memory Computing. *Chem Rev* **125**, 5163–5194 (2025).

180. Lee, S.-T. & Lee, J.-H. Review of neuromorphic computing based on NAND flash memory. *Nanoscale Horiz* **9**, 1475–1492 (2024).

181. Gerstner, W., Kistler, W. M., Naud, R. & Paninski, L. *Neuronal Dynamics*. (Cambridge University Press, 2014). doi:10.1017/CBO9781107447615.

182. Indiveri, G. & Liu, S.-C. Memory and Information Processing in Neuromorphic Systems. *Proceedings of the IEEE* **103**, 1379–1397 (2015).

183. Mikolajick, T., Park, M. H., Begon-Lours, L. & Slesazeck, S. From Ferroelectric Material Optimization to Neuromorphic Devices. *Advanced Materials* **35**, (2023).

184. Kim, I. & Lee, J. Ferroelectric Transistors for Memory and Neuromorphic Device Applications. *Advanced Materials* **35**, (2023).

185. Lee, D. H. *et al.* Neuromorphic devices based on fluorite-structured ferroelectrics. *InfoMat* **4**, (2022).

186. Xu, K. *et al.* Fluorite-structured antiferroelectric hafnium-zirconium oxide for emerging nonvolatile memory and neuromorphic-computing applications. *Appl Phys Rev* **11**, (2024).

187. Lv, Z. *et al.* Tunable Volatile to Non-Volatile Resistive Switching in $PbZrO_3$ Antiferroelectric Thin Film for Neuromorphic Computing. *Adv Mater Interfaces* **9**, (2022).

188. Pan, H. *et al.* Defect-Induced, Ferroelectric-Like Switching and Adjustable Dielectric Tunability in Antiferroelectrics. *Advanced Materials* **35**, (2023).

189. Coulibaly, M. D., Borderon, C., Renoud, R. & Gundel, H. W. Effect of ferroelectric domain walls on the dielectric properties of $PbZrO_3$ thin films. *Appl Phys Lett* **117**, (2020).

190. Alam, M. A., Si, M. & Ye, P. D. A critical review of recent progress on negative capacitance field-effect transistors. *Appl Phys Lett* **114**, (2019).

191. Íñiguez, J., Zubko, P., Luk'yanchuk, I. & Cano, A. Ferroelectric negative capacitance. *Nat Rev Mater* **4**, 243–256 (2019).

192. Khan, A. I. *et al.* Negative capacitance in a ferroelectric capacitor. *Nat Mater* **14**, 182–186 (2015).

193. Hoffmann, M. *et al.* Antiferroelectric negative capacitance from a structural phase transition in zirconia. *Nat Commun* **13**, 1228 (2022).

194. Banszerus, L. *et al.* Ultrahigh-mobility graphene devices from chemical vapor deposition on reusable copper. *Sci Adv* **1**, (2015).

195. Wu, W. *et al.* High mobility and high on/off ratio field-effect transistors based on chemical vapor deposited single-crystal $MoS_2$ grains. *Appl Phys Lett* **102**, (2013).

196. Xu, B., Hellman, O. & Bellaiche, L. Order-disorder transition in the prototypical antiferroelectric $PbZrO_3$. *Phys Rev B* **100**, 020102 (2019).

197. Fu, Z. *et al.* Unveiling the ferrielectric nature of $PbZrO_3$-based antiferroelectric materials. *Nat Commun* **11**, 3809 (2020).

# Appendices

Appendix A

# *PZO growth on STO (001) substrates*

## A1. PZO epitaxial films on SRO buffered STO (001) substrates

### A1.1. High temperature growth: Case for interdiffusion between SRO and PZO

PZO was grown on either SAO or SRO buffered STO (001) substrates using PLD (KrF excimer laser (248 nm, COMPex 201, Lambda Physik) to fabricate membranes and epitaxial films respectively.

The initial conditions used for epitaxial film growths are as follows:

| Material | Fluence ($J/cm^2$) | Temperature (°C) | Frequency (Hz) | $O_2$ partial pressure (mTorr) |
|---|---|---|---|---|
| $SrRuO_3$ | 1.25 | 700 | 1 | 80 |
| $PbZrO_3$ | 1.5 | 550 | 3 | 100 |

PZO films of different thicknesses were grown ranging from 26 nm to 1.5 nm. X-Ray diffraction was used to characterize the films as shown in figure.

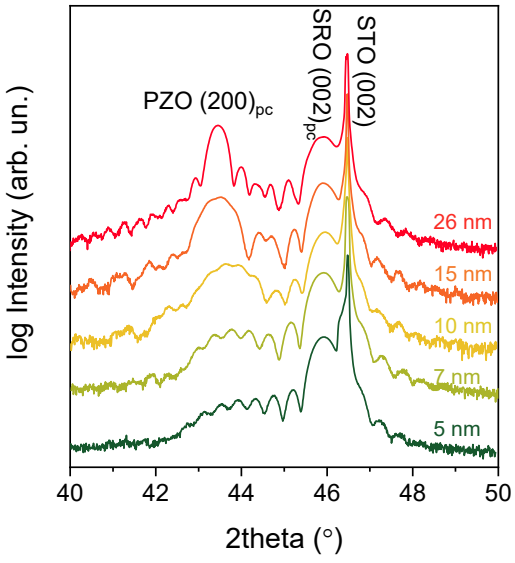


***Figure A1:*** *Theta- 2theta scans of PZO films of different thicknesses on SRO buffered STO (001) substrates.*

Both the SRO (35 nm in all cases) and PZO layers grow coherently with the substrates with high crystalline quality as evident from the Lau fringes (**Figure A1**). However, as the film thickness decreases, the PZO peak moves towards higher angles marking a decrease in the out-of-plane lattice parameter. This has been previously attributed to the presence of misfit dislocations that apply strain to the film. We further measure the in-plane lattice parameters by using reciprocal space mapping around $(-103)_{PC}$ peaks of the PZO/SRO//STO stack for PZO thicknesses of 15, 10 and 7 nm and grazing incidence XRD around $(200)_{PC}$ and $(110)_{PC}$ for 5, 2.5 and 1.5 nm films, shown in **Figure A2**.

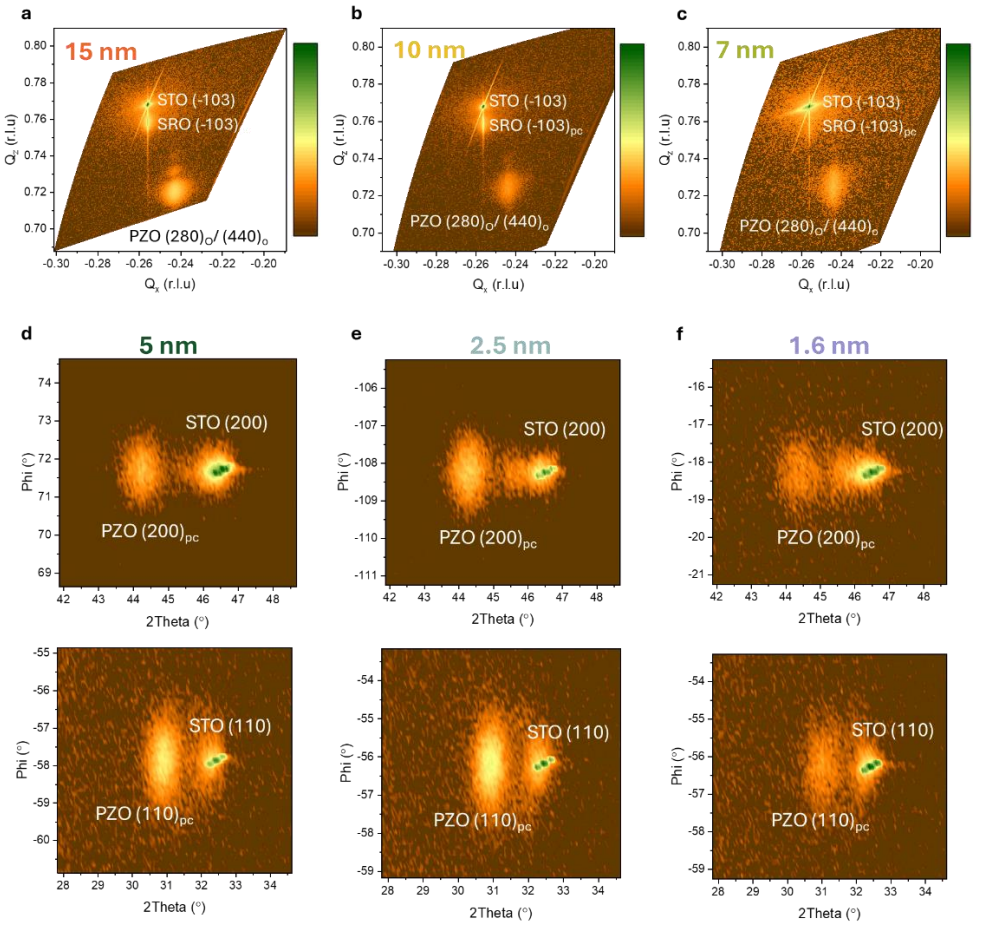


***Figure A2:*** *RSMs around (-103)$_{pc}$ peaks for* ***(a)*** *15 nm,* ***(b)*** *10 nm,* ***(c)*** *7 nm PZO films on SRO buffered STO (001) substrates; GIXRD around* ***(002)$_{pc}$ (top panels)*** *and* ***(110)$_{pc}$ (bottom panels)*** *for* ***(d)*** *5 nm,* ***(e)*** *2.5 nm, and* ***(f)*** *1.6 nm PZO films.*

The summary of IP and OOP lattice parameters is shown in the **Figure A3**. Our results show that both the IP and OOP lattice parameters decrease as the thickness of the PZO layer decreases. As film thickness decreases, the IP lattice parameters decrease because of incomplete relaxation of misfit strain. However, we would expect that the OOP lattice parameters would increase accordingly (by Poisson´s ratio), but this is not what we observe. Instead, there is a decrease in both lattice parameters marking a decrease in the volume of the unit cell. In fact, we can fit the theta-2theta scans of the thicker films to get the unit cell by unit cell lattice parameter evolution as shown in the **Figure A3b-d** below (fitting was done using InteractiveXRDFit: Lichtensteiger, C. *Applied Crystallography* 51.6 (2018): 1745-1751). The fitting shows that even in the thicker films, the initial layers show a smaller OOP lattice parameters followed by a relaxation of the top layers towards the bulk parameter. This is not consistent with the strain fields caused by misfit dislocations but rather interdiffusion between the SRO and PZO layers.

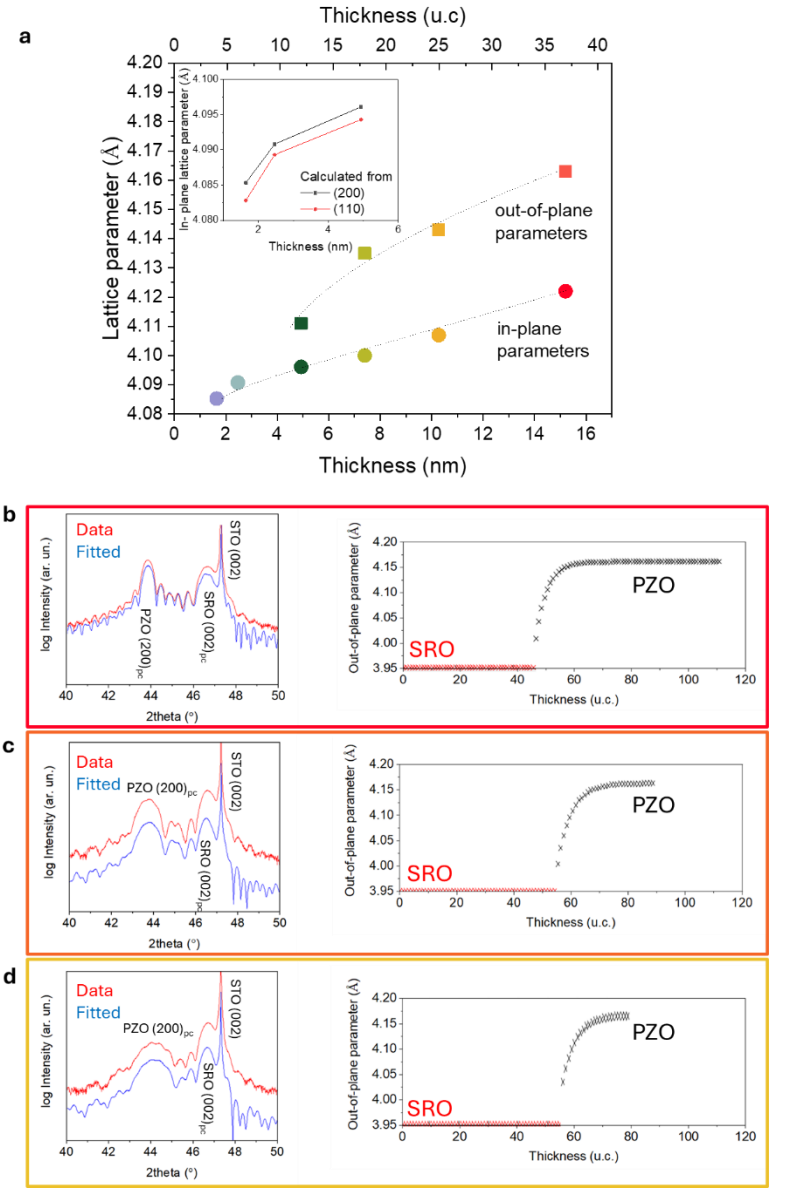


***Figure A3: (a)*** *Summary of IP and OOP lattice parameters of PZO films of different thicknesses measured from RSMs and GIXRD measurements; Fittings of theta- 2theta scans for* ***(b)*** *26 nm,* ***(c)*** *15 nm and* ***(d)*** *10 nm PZO films.*

To substantiate this, we then did a cross section of the 1.6 nm PZO film on SRO buffered STO (001) substrate and use integrated Differential Phase contrast (iDPC) to obtain atomic resolution images (**Figure A4**). We can make two important observations.

1. The surface of the film seems to be very rough from the iDPC images, but the topography image on the same film shows a very smooth surface. The roughness as seen in the iDPC is on an atomic scale and is not captured by the

AFM due to limitation in its lateral resolution. Moreover, we can see that the thickness of PZO varies very much along the surface. This means that the growth of PZO or SRO is inhomogeneous on the substrate.

2. There is no sharp interface between the PZO and SRO (inferred from the intensity of the cation columns), instead there is a gradient of intensity from low intensity SRO layer to high intensity PZO layer, evidence for interdiffusion between the layers.

We can also see the mixture of cubic and tetragonal- like ferroelectric phases in the PZO layer, but these phases cannot be accurately assigned to intrinsic properties of PZO due to interdiffusion.

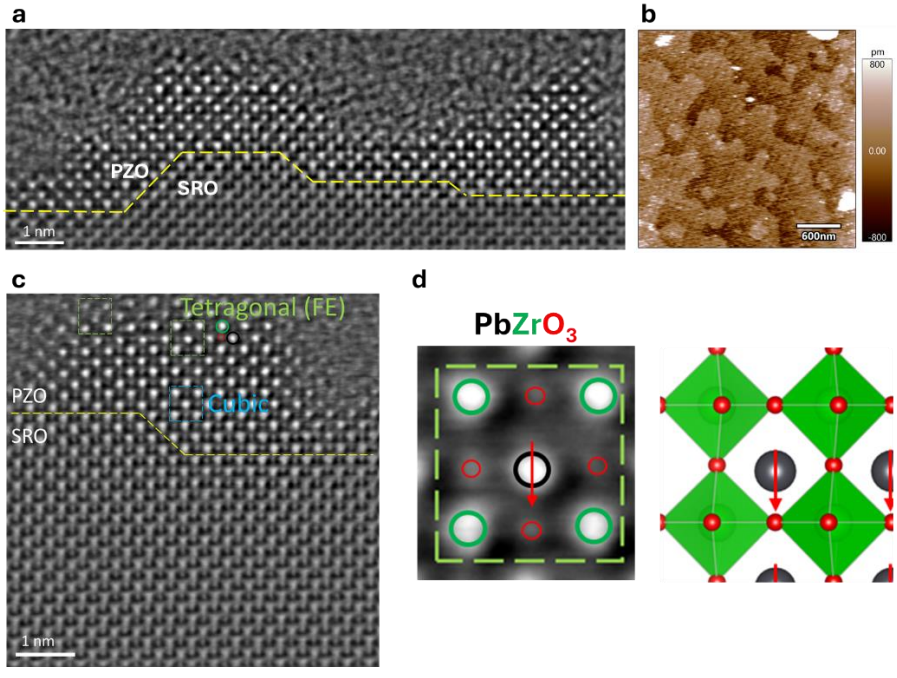


***Figure A4:*** ***(a)*** *iDPC image of a cross section of 1.6 nm PZO film of SRO buffered STO (001) substrate,* ***(b)*** *AFM topography image of the 1.6 nm PZO film,* ***(c)*** *iDPC image of another region showing a mixture of cubic and tetragonal ferroelectric regions,* ***(d)*** *Magnified region of a tetragonal unit cell showing displaced Pb atom* ***(left panel)*** *and the model of the tetragonal FE phase of PZO* ***(right panel).***

This interdiffusion can be caused by 1. high growth temperatures, 2. a strain release mechanism to accommodate the high misfit. The next step is, therefore, to optimize the PZO growth at a lower temperature to reduce the chances of interdiffusion. Following section discusses the optimization procedure of the PZO growth on SRO buffered STO substrates.

## A1.2. Optimization at lower temperature and substrate treatment

Due to aforementioned analysis, I optimized the growth of PZO on SRO (of thickness 10 nm) buffered STO (100) substrates again, this time at lower temperatures. The processes (substrate treatment) and growth conditions are listed below along with the topography of the substrate, the grown stacks and corresponding XRD. (Not all the steps in the growth optimization are shown but rather where the major differences are seen.)

| **Growth 1** | **Substrate treatment** | None | | |
|---|---|---|---|---|
| | **Fluence ($J/cm^2$)** | **Temperature (°C)** | **Frequency (Hz)** | **$O_2$ partial pressure (mTorr)** |
| **$PbZrO_3$** | 1.5 | 500 | 3 | 100 |

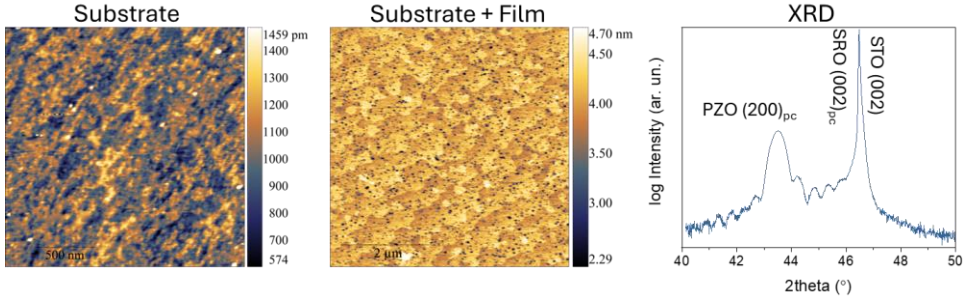


**Observations:** Flat film growth with good crystalline quality, however, with a lot of pits. The pits can be caused by inhomogeneous growth of SRO on STO substrate due to preferential growth on $TiO_2$ termination. The pits were not visible at higher temperature growths due to higher diffusion.

---

| **Growth 2** | **Substrate treatment** | Annealed at 1000°C for 4 hours | | |
|---|---|---|---|---|
| | **Fluence ($J/cm^2$)** | **Temperature (°C)** | **Frequency (Hz)** | **$O_2$ partial pressure (mTorr)** |
| **$PbZrO_3$** | 1.5 | 500 | 3 | 100 |

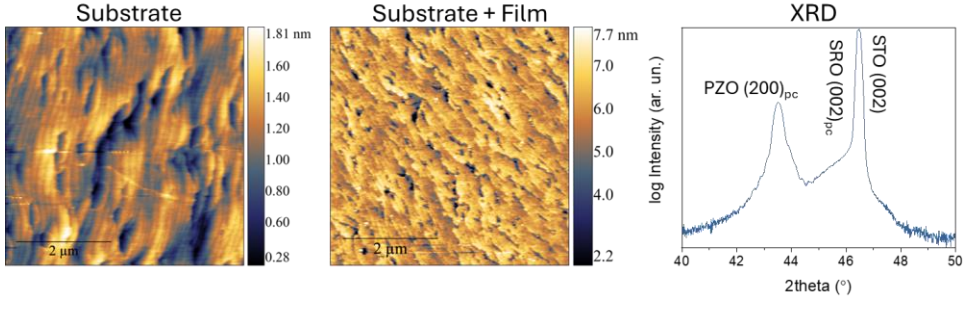

**Observations:** Incomplete surface reconstruction of STO substrate, effecting the film growth as well.

---

| **Growth 3** | **Substrate treatment** | Annealed at 1250°C for 8 hours | | |
|---|---|---|---|---|
| | **Fluence ($J/cm^2$)** | **Temperature (°C)** | **Frequency (Hz)** | **$O_2$ partial pressure (mTorr)** |
| **$PbZrO_3$** | 1.5 | 500 | 3 | 100 |

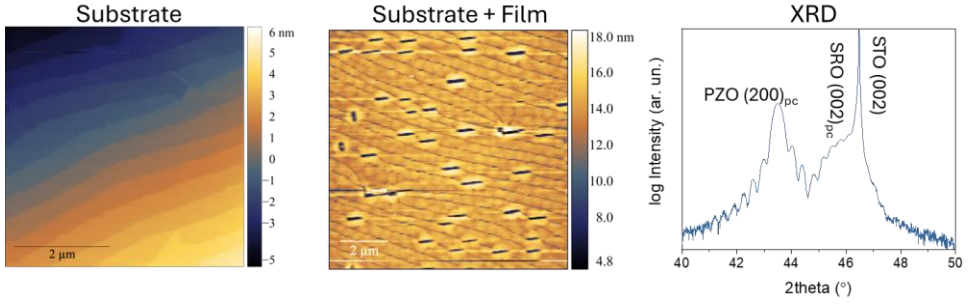


**Observations:** The surface of STO substrate reconstructs properly at higher annealing temperatures and time. We still see inhomogeneous growth: the growth lacks at the terrace edges where the secondary termination (SrO) accumulates.

---

| **Growth 4** | **Substrate treatment** | Annealed at 1250°C for 8 hours | | |
|---|---|---|---|---|
| | **Fluence ($J/cm^2$)** | **Temperature (°C)** | **Frequency (Hz)** | **$O_2$ partial pressure (mTorr)** |
| **$PbZrO_3$** | 1.5 | 450 | 3 | 100 |

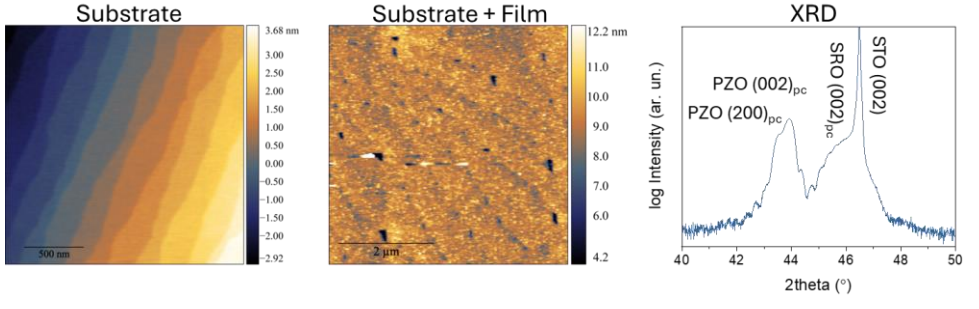


**Observations:** I decrease the temperature to 450°C. The film gets rougher and PZO has both domain orientations present.

---

| **Growth 5** | **Substrate treatment** | Annealed at 1250°C for 8 hours (note: the substrate for this growth and the previous one is the same, just cut into two pieces) | | |
|---|---|---|---|---|
| | **Fluence (J/cm²)** | **Temperature (°C)** | **Frequency (Hz)** | **$O_2$ partial pressure (mTorr)** |
| **$PbZrO_3$** | 1.25 | 450 | 2 | 100 |

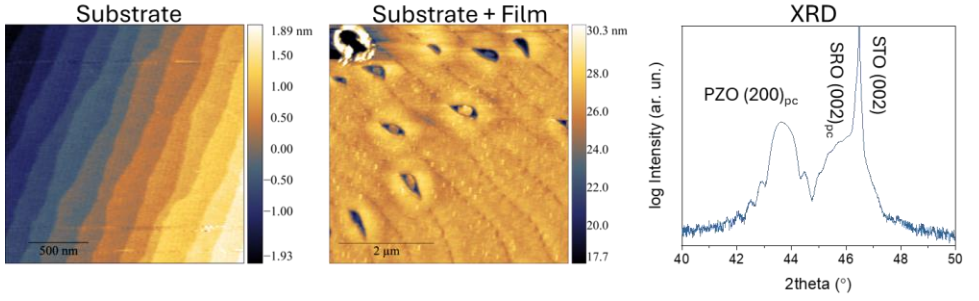


**Observations:** I decrease the fluence to 1.25 J/cm² and frequency to 2 Hz, the grown film has a lower roughness. XRD reveals a crystalline growth (evident from the Laue fringes).

---

For the following growths, I try to treat the substrate with buffered Hydrogen fluoride (BHF) to obtain single termination.

| **Growth 6** | **Substrate treatment** | Etched in BHF for 5 min, followed by annealing at 1250°C for 8 hours. | | |
|---|---|---|---|---|
| | **Fluence (J/cm²)** | **Temperature (°C)** | **Frequency (Hz)** | **$O_2$ partial pressure (mTorr)** |
| **$PbZrO_3$** | 1.25 | 450 | 2 | 100 |

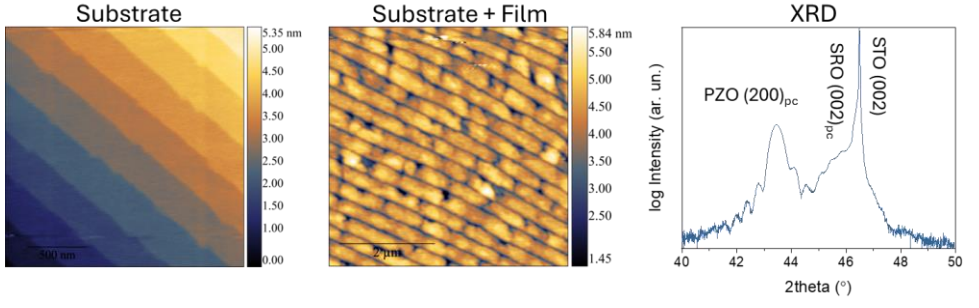


**Observations:** The roughness of the film decreases further, and the inhomogeneity of the growth also reduces. The etching seems to be incomplete in this case.

---

| **Growth 7** | **Substrate treatment** | Etched in BHF for 20 min, followed by annealing at 1250°C for 8 hours. | | |
|---|---|---|---|---|
| | **Fluence ($J/cm^2$)** | **Temperature(°C)** | **Frequency (Hz)** | **$O_2$ partial pressure (mTorr)** |
| **$PbZrO_3$** | 1.25 | 450 | 2 | 100 |

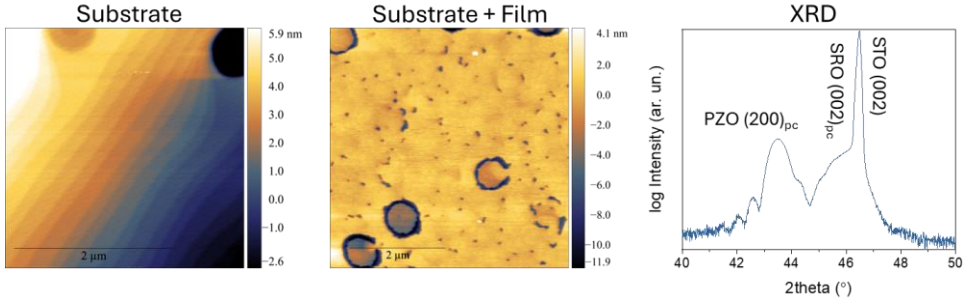


**Observations:** The substrate is over etched, resulting in deep cavities after annealing. However, the films grow smoothly on the substrate with fewer pits. I speculate that the annealing step after the etching process results in some SrO termination to reemerge resulting in the smaller pits shown.

---

| **Growth 8** | **Substrate treatment** | Annealing at 1250°C for 8 hours, followed by immersing the substrate in water at 60°C for 1 hour, and then etching in BHF for 10 min. This was followed by second annealing step with temperature of 1000°C for 2 hours. The substrate was immediately used for AFM and followed by growth. | | |
|---|---|---|---|---|
| | **Fluence ($J/cm^2$)** | **Temperature (°C)** | **Frequency (Hz)** | **$O_2$ partial pressure (mTorr)** |
| **$PbZrO_3$** | 1.25 | 450 | 2 | 100 |

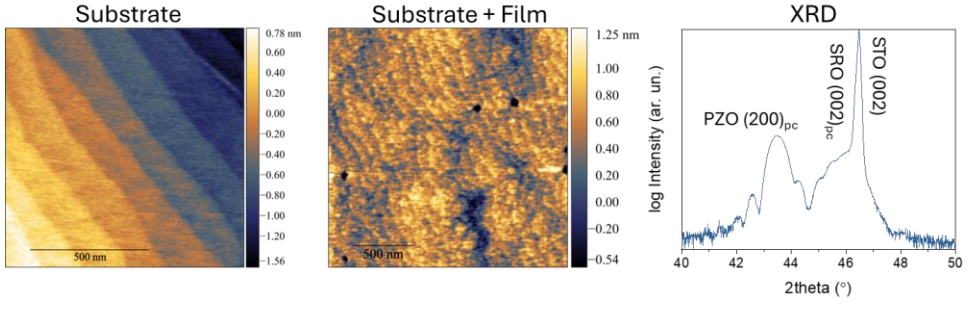


**Observations:** The film growth is very smooth (the terraces are visible). Some pits are still visible. This might be due to the exposure of substrate to ambient atmosphere during the AFM measurements (the treated substrates are to be stored in vacuum). The

XRD shows a high crystalline growth. At low temperature growths, there is always a mixture of the two domain orientations.

## A2. PZO epitaxial films on SAO buffered STO (001) substrates

Growth of SAO on STO (001) substrates do not have any preference for the termination, therefore no additional substrate treatment is required. After optimization process (not shown here), I do the growths on SAO with the following growth conditions:

| Material | Fluence ($J/cm^2$) | Temperature (°C) | Frequency (Hz) | $O_2$ partial pressure (mTorr) |
|---|---|---|---|---|
| $Sr_3Al_2O_6$ | 1.83 | 750 | 1 | 1 |
| $PbZrO_3$ | 1.25 | 450 | 2 | 100 |

The XRDs (theta-2theta scans) of the epitaxial films and membranes around $(002)_{PC}$ peaks are shown in **Figure A5a** and **b**. Moreover, RSMs around $(-103)_{PC}$ reflections on PZO membranes are also shown in **Figure A5c**. In epitaxial film form, all PZO layers excluding 75 nm, shows a single domain orientation. However, after transferring and annealing the membranes (as discussed in **Chapter 2**), membranes of 75 nm to 36 nm show some reorientation resulting in the two domain orientations (the schematics of the two domain orientations are discussed in the next section: **A3**). Thinner membranes, on the other hand, exhibit broad peaks due to size induced broadening and different domain orientations cannot be distinguished. All membranes show lattice parameters close to the bulk value. We could not perform the XRD measurements of 5 and 2.5 nm membranes because of the low thickness, hence very low intensity of the peaks.

As a comparison, I also show a 5 nm PZO film on SAO buffered STO (001) substrate at a higher frequency, fluence and temperature (3 Hz, 1.5 J $cm^{-2}$ and 550°C), the conditions that lead to interdiffusion between SRO and PZO (as described in the previous section). In this case, XRD measurements (**Figure A6**) show the out-of-plane lattice parameters remain the same, but the peak for strained PZO disappears and the PZO film seems to be completely relaxed, hinting at interdiffusion in this case as well.

Note: there is an additional peak in the 50 nm PZO epitaxial stack appearing exactly between the STO (002) and PZO $(200)_{PC}$ peaks. This peak arises from double diffraction (i.e. combination of two reciprocal vectors: substrate plus film). This peak is, however, very sensitive to Bragg conditions, so it can be avoided by minutely changing the phi angle.

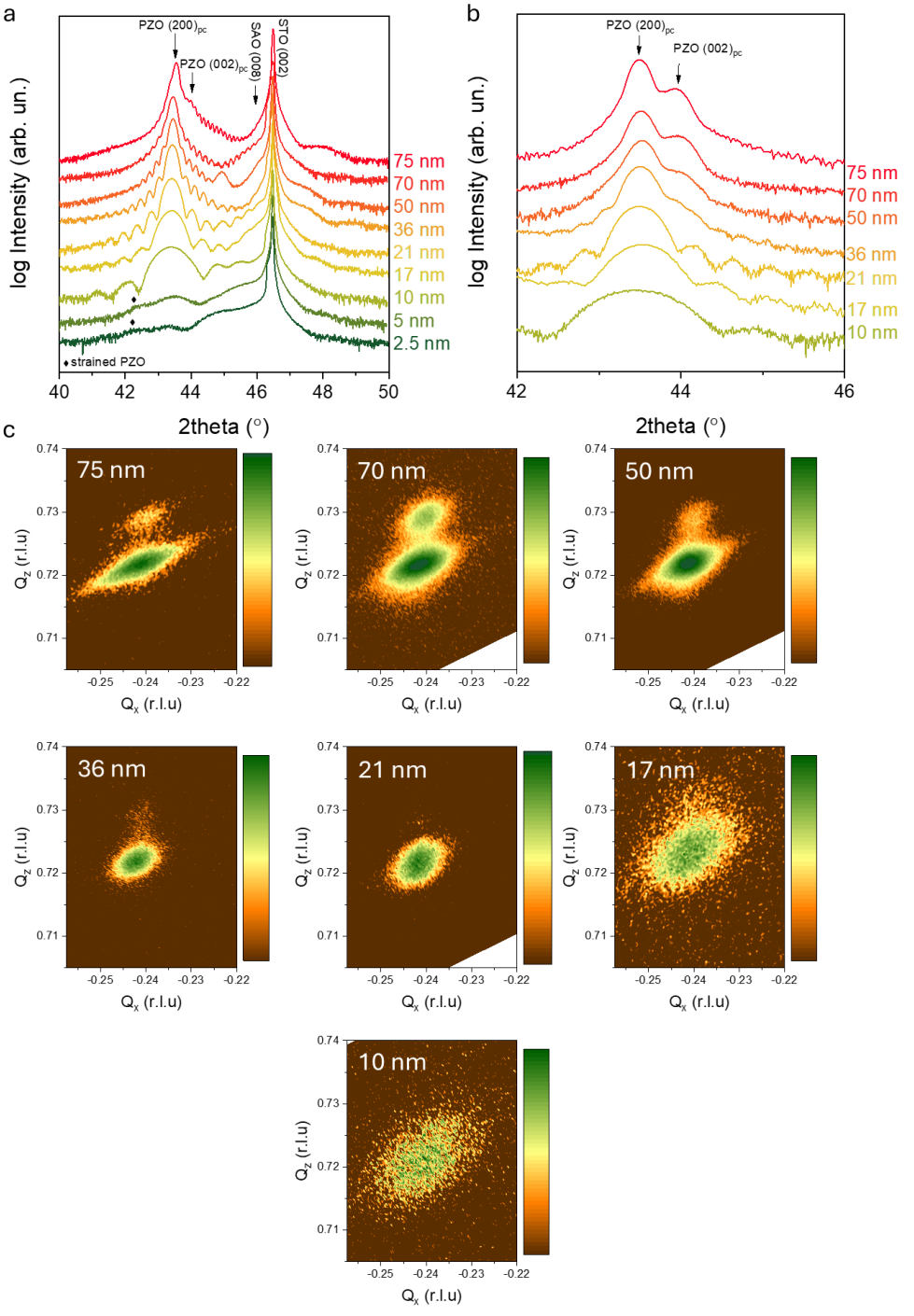


***Figure A5***. *Theta- 2theta scans around* ***(a)*** *PZO on SAO buffered STO (001) substrate before release,* ***(b)*** *PZO membranes after transfer and annealing,* ***(c)*** *RSMs around (-103)$_{PC}$ of PZO for 75 to 10 nm membranes.*

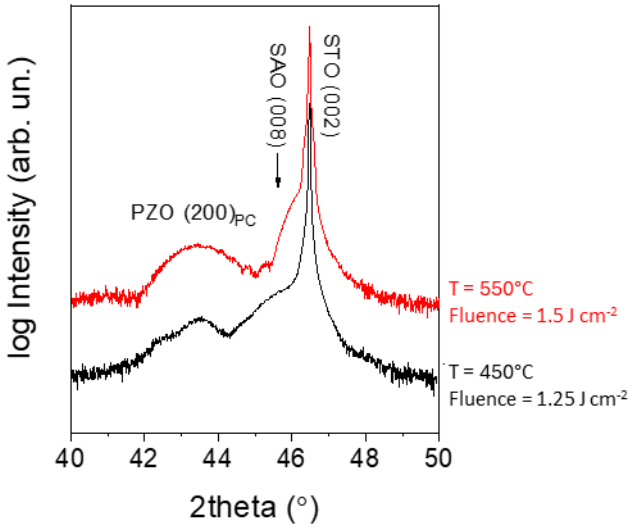


***Figure A6**. XRD (theta- 2theta scans) comparison of PZO grown on SAO buffered STO (001) substrates with two different growth conditions.*

## A3. Two domain orientations in PZO grown on STO (001) substrates

PZO films grown on STO (001) substrates are also (001) oriented. However, the films are grown at temperatures higher than the Curie temperature of PZO, and when the films are cooled down, they transition into the AFE phase. In AFE phase, films can adopt two different symmetrically non-equivalent structures: one where the $[001]_{PC}||[001]_{O}$ directions point out of plane, or $[100]_{PC}||[120]_{O}$ directions point of plane. Since the antipolar direction is $[110]_{PC}$, the antipolar directions can be either in plane in the former domain or have both in-plane and out of plane component in the latter. Additionally, since $[100]_{PC}$ axis (~4.16 Å) is larger than $[001]_{PC}$ axis (~4.11 Å), we can have a peak splitting in diffractograms, both in-plane and out of-plane. The schematic of the different domains is shown in **Figure A7**.

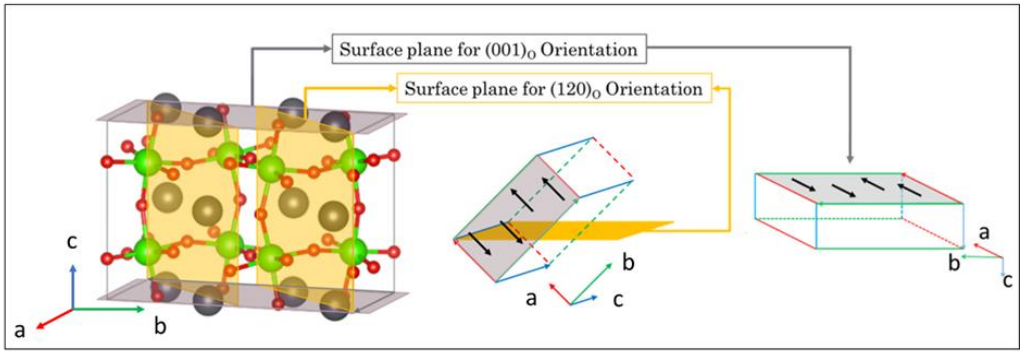


***Figure A7.** Schematic of the two different domain structures present in PZO films, axes in the compass given in orthorhombic directions.*

# Appendix B

## *Transfer methods for membranes*

The transfer process I used throughout this work utilizes the support polymer method, Polydimethylsiloxane (PDMS). The process starts with cleaning the glass slide with acetone using ultra-sonication and then treated with UV light (Ozone cleaning) to remove any adsorbates from the surface. This allows the PDMS to adhere strongly to the glass slide for the later steps. From here onwards, we have the possibility of using only PDMS or with other buffer polymer layers depending on the conditions. I will briefly describe some of these methods and the scenarios where they might be useful.

### B1. Simple PDMS transfer

We attach the PDMS to a glass slide, followed by the epitaxial stack (functional film is brought into contact with the PDMS). The assembly is then placed in water, where the sacrificial layer SAO etches away, and the substrate can be removed. The PDMS with the functional film attached is brought into contact with a secondary substrate, heated and the PDMS slowly peeled away leaving the membrane on the recipient substrate. A simple schematic is shown in **Figure B1**.

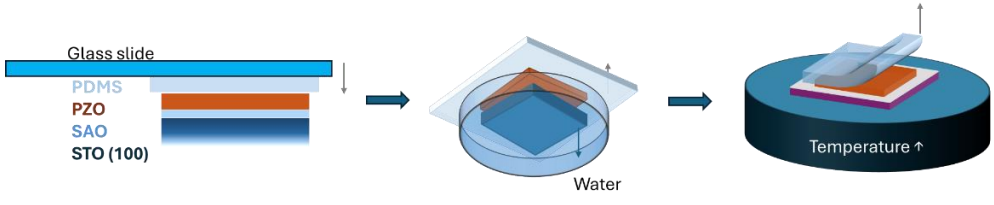


***Figure B1**: Schematic of simple PDMS transfer method*

The temperature at which the transfer is done can vary between room temperature and 100°C, but higher the temperature, higher the polymer contaminants on the surface. This transfer method is the simplest method and uses only PDMS. One advantage of this method is that we can tune the stiffness of the polymer by changing the ratio of the epoxy and hardener. Stiffer PDMS (high hardener content) results in less contaminants but the transfer yield is lowered. Another advantage is the simplicity and no additional preparation of the PDMS and works very well for transfers where the secondary substrate has a very low roughness such as Silicon substrates. However, this transfer method results in contaminants on the surface which makes the samples less suitable for planar view TEM and AFM. PDMS contaminants are also very stable due to silicon atoms in the polymer chain and are very difficult to remove.

## B2. TPD as buffer layer

The chemical name for TPD is Poly[N,N'-bis(4-butylphenyl)-N,N'-bisphenylbenzidine] ($(C_{22}H_{21}N)_n$) and is a semiconducting polymer that is widely used in perovskite solar cell technologies. However, here, we do not use it for its semiconducting properties but rather as a buffer layer between the PDMS and our epitaxial stack. TPD can be deposited on PDMS and our epitaxial stack via thermal evaporation, followed by bringing the stack and PDMS in contact and immersing in water, schematic shown in **Figure B2**.

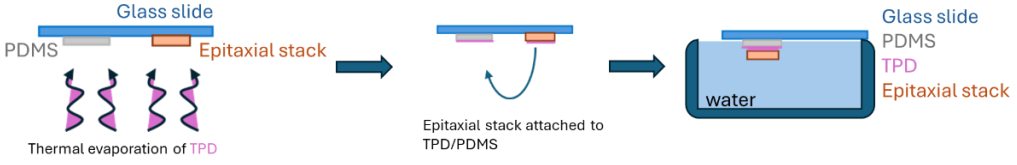


***Figure B2**: Schematic of TPD transfer method.*

TPD allows for a softer contact between the membrane and the secondary substrate. Moreover, in later stages during transfer, the secondary substrate is heated to 60°C or above (higher than the glass transition temperature of TPD) allowing for a higher yield transfer. Hence, TPD transfer method is very suitable for high thickness films being transferred onto rough substrates where the contact surface area is lower between the membrane and the substrate. Using this method, we can also obtain membranes with low crack densities which is very useful where large area membranes are needed such as to make devices. TPD buffer layer also helps in preventing the contaminants from PDMS to remain on the sample, whereas TPD contaminants can be cleaned by either immersing the sample in acetone overnight, or by annealing at 100°C in vacuum conditions.

## B3. Spin coated Polypropylene carbonate (PPC)

PPC is another polymer that is used as a buffer layer. PPC can be deposited on PDMS via spin coating. First, 10 % (mass percentage) PPC solution is made by dissolving it in anisole. PDMS is treated by ultra-sonicating it in isopropanol and then by activating it using oxygen plasma cleaning to ensure good adhesion between PPC and PDMS. A few drops of PPC solution are then put on the PDMS and spin coated to obtain a homogeneous coating. The spin coated PDMS is then heated to 40°C for 10 minutes to evaporate the anisole leaving the PPC layer on the PDMS. The rest of the transfer process is the same as before, process shown in **Figure B3**.

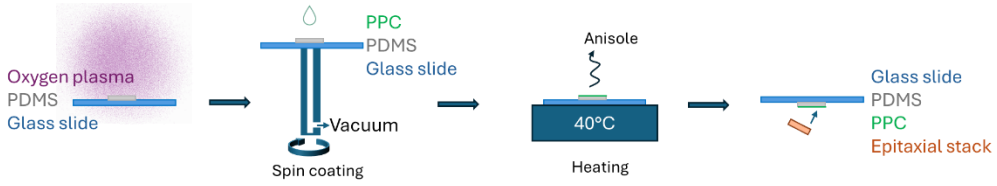


***Figure B3**: Schematic of spin coated PPC transfer method.*

The preparation for this method has multiple steps which adds to the complexity of the process. However, PPC allows for a softer contact between the membrane and the secondary substrate and prevents PDMS contaminants. PPC itself can be cleaned by acetone as well as annealing in oxygen environments at 260°C. Since PPC is a soft polymer, it is specifically useful for obtaining wrinkles on membranes for strain and strain gradient investigations.

## B4. Tape-held PPC and PC (polycarbonate) method

Another buffer polymer that I have used is PC. The method I describe below can be used for both PPC and PC. The process starts with making PPC solution (in anisole) or PC solution (in chloroform). A few drops of this solution are put on a glass slide, and then another glass slide is pressed on top of it and slid towards one side, leaving a thin layer of solution on both slides. The glass slides are then heated to 40°C to evaporate the solvent leaving a thin layer of polymer on the slides. The concentration of the solutions determines the thickness of this layer. Some of the polymer is then scratched off from the slide, leaving a polymer island. A piece of scotch tape with a window is brought into contact with this island and picked up. The tape/polymer stack is then attached to PDMS/ glass slide assembly, hence, a thin layer of PPC or PC is placed on top of PDMS held by the tape (**Figure B4**). This stack is then heated to 40°C in case of PPC and 100°C in case of PC, and the polymer is allowed to relax on the PDMS surface and become smooth. The epitaxial film is attached to the polymer/PDMS and heated to 40°C to have a good contact between the polymer and the epitaxial film. The assembly is then placed in water and SAO is etched, followed by the transfer to a secondary substrate.

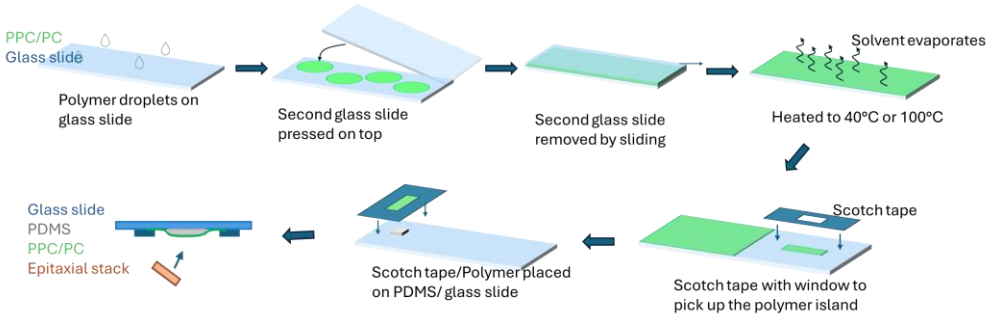


***Figure B4**: Schematic of tape-held PPC/PC transfer method.*

This method involves a long process and is complex. However, the advantage of this method is that the buffer layer polymer is not adhered strongly to the PDMS. During transfer, the secondary substrate can be heated to 100°C, and the buffer polymer becomes very soft, such that it breaks from the areas where it is suspended at the edges of the PDMS. The polymer and the membrane then fall on the secondary substrate completely. The polymer can then be cleaned using acetone/chloroform, annealing in oxygen or reactive ion etching in oxygen environment. Although, the preparation and post-cleaning for this process are complex, this method is very suitable for very rough substrates or thicker membranes where the contact between the membrane and substrate is not sufficient. This process is also especially useful for transferring membranes on to perforated substrates (i.e. holes) where there is no contact of the membrane at all to allow for successful peeling of the PDMS.

## B5. PDMS drop method for small area membranes

We can also pick up the membranes once they are transferred to a secondary substrate to transfer to a third recipient substrate. In most of these cases, the idea is to transfer small area membranes (on TEM grids for example). In this case, we pour some uncured PDMS onto a clean glass slide, and then using a sharp needle or a toothpick, put some small droplets of PDMS on the PDMS layer. After curing, we either put a PPC layer on these droplets by the spin coating method as described in **B3** or use them without any buffer layer. We bring the small PDMS semi-sphere in contact with our membrane, heat the membrane/PDMS assembly to 60°C and cool down to room temperature while still in contact. The PDMS is then raised rapidly (with a sudden jerk) to break the membrane and pick a part of it up. This small membrane can then be transferred to the next substrate as described in previous sections, as shown in **Figure B5**. The idea here is to reuse a membrane different times to ensure as much as possible the homogeneity of the samples for different experiments.

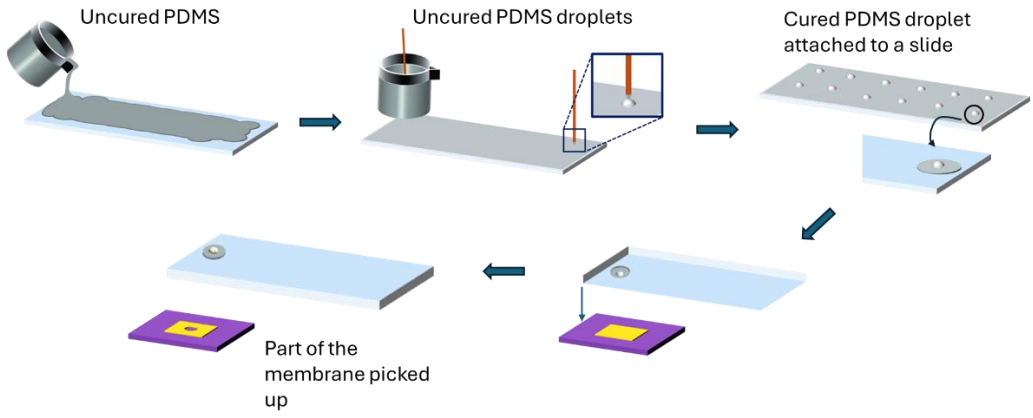


***Figure B5**: Schematic of PDMS drop pickup method*

There are other considerations to be made while doing the transfer.

1. I have observed that the yield of the transfer is higher when the membrane is still wet when it is brought into contact with the secondary substrate. This might be due to the capillary action of water: as the water evaporates, it applies a lot of pressure between the membrane and the secondary substrate allowing for a better contact between the two surfaces and stronger adhesion.
2. In order to avoid contamination from the polymers, it is also advisable to attempt the transfer at lower temperatures and only use higher temperatures when the transfer yield is not sufficient or not successful at all.
3. The membrane and the secondary substrate should be as parallel as possible to avoid additional pressure on one side of the membrane while bringing the other edge into contact. This is a crucial step while transferring the membranes to TEM grids or other substrates that are mechanically weak (such as perforated suspended $SiN_x$ membranes).
4. The secondary substrates are cleaned before the transfer which is done to remove any dust particles or other contaminants. They can also be cleaned by UV exposure to remove adsorbates to have a better adhesion with the membrane.

Other than the transfer or membrane fabrication methods described above, I have used other ways to transfer membranes for specific measurements such as bending the membranes on flexible substrates or to make rolls. These methods are described in the main chapters.

# Appendix C

## *Addendum Chapter 2: Fabrication of chemically pure free-standing membranes: hidden hydrogenation due to sacrificial layer etching*

### C1. RSMs around $(-103)_{PC}$ peaks for 75 nm PZO film on SAO buffered STO (001) substrate

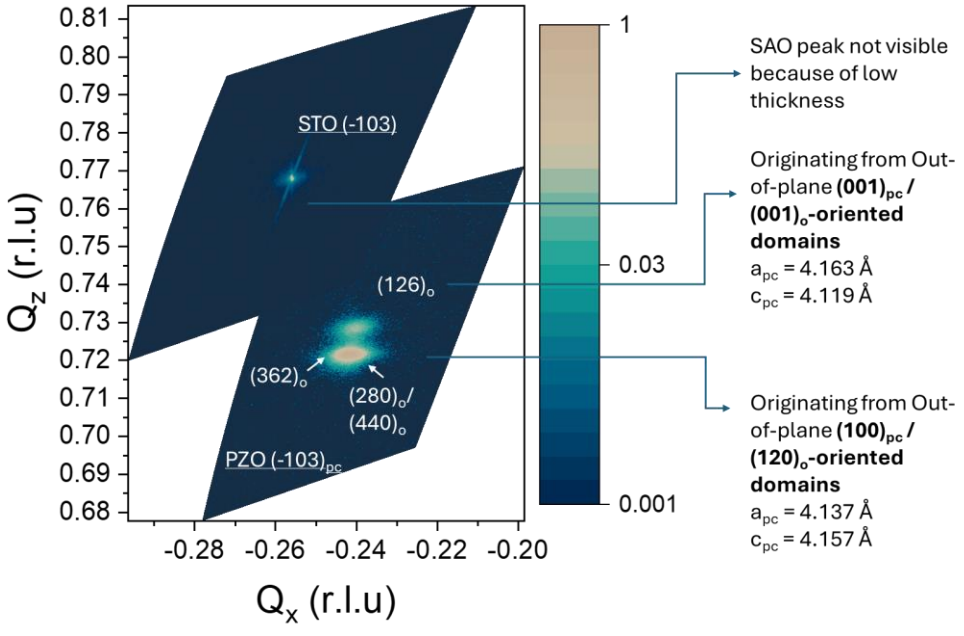


***Figure C1**. RSM of the 75 nm PZO film grown on SAO buffered STO (001) substrate around $(-103)_{PC}$ peak.*

The RSM around $(-103)_{PC}$ peaks of STO and PZO show a fully relaxed PZO film as expected due to high mismatch. PZO shows a multiple domain state consistent with the theta-2theta scan. The lattice parameters, obtained from the $(280)_O/(440)_O$ peak, are 4.135 Å in-plane and 4.156 Å out-of-plane, (the in-plane lattice parameters measured here is the average of the two ferroelastic domains that have $(120)_O$ in-plane or $(001)_O$ in-plane), whereas the $(126)_O$ peak shows lattice parameters of 4.159Å in-plane and 4.112Å out-of-plane, closely matching the bulk value.

## C2. SS-PFM loops in the written region of the As-transferred PZO membrane of thickness 75 nm

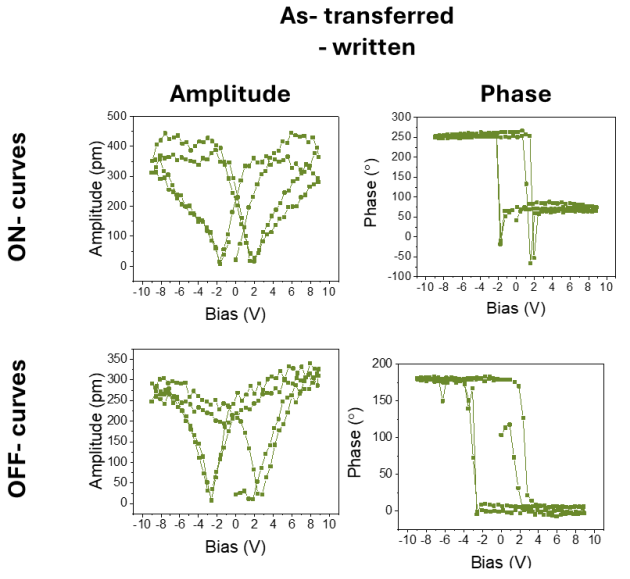


***Figure C2**. SS-PFM loops for 75 nm as-transferred PZO membrane inside a written region.*

SS-PFM loops on the written region in the as-transferred membrane show typical FE like loops. In this case, the amplitude and coercive fields in the on- and off- loops are more similar signifying an increased stability of the FE domains with low back switching.

## C3. Structural characterization of 36 nm as-transferred and annealed PZO membrane

XRD of the 36 nm membrane in **Figure C3** shows the same trend as the 75 nm membrane, the rocking curve has a higher FWHM for the as-transferred membrane but decreases after annealing. In this case, the in-plane lattice parameter is 4.21 Å for the as-transferred membrane (1.2% tensile strain), which is higher than the 75 nm membrane. After annealing, the lattice parameters approach those of the bulk.

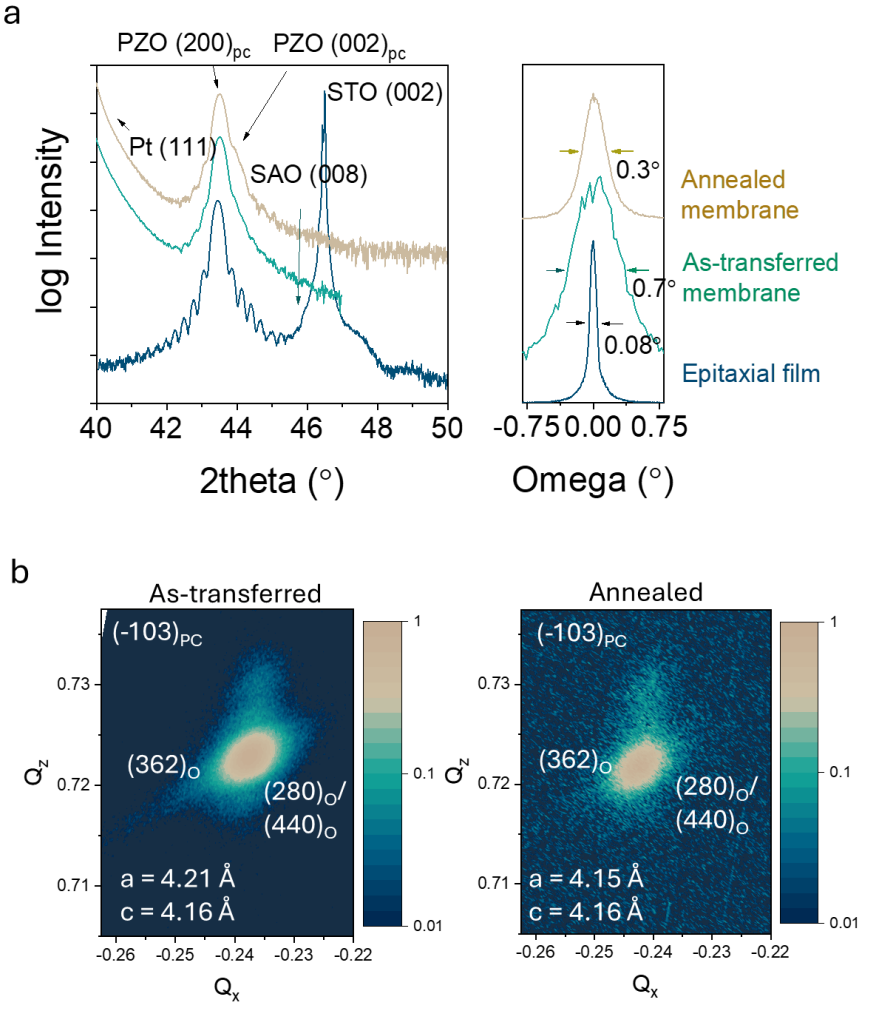


***Figure C3**. **(a)** Theta-2theta scans and rocking curves for PZO of 36 nm membrane at different stages of processing. **(b)** RSMs around (-103)$_{PC}$ peak of PZO; the as-transferred membrane shows tensile strain of 1.2% in the in-plane direction, while the annealed membrane has bulk-like lattice parameters.*

## C4. PFM results for the 36 nm as-transferred and annealed PZO membrane

PFM and SS-PFM measurements done on 36 nm as-transferred PZO membranes show that the field induced ferroelectric phase is metastable, while the annealed PZO membrane shows an AFE response with co-existing FE phase.

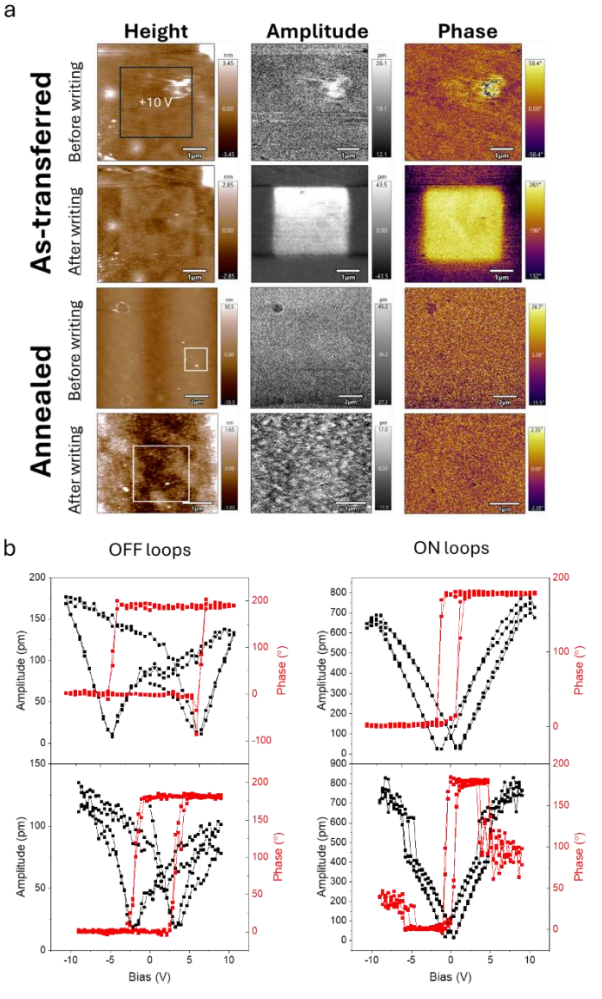


***Figure C4***. ***(a)*** *Writing experiment on the 36 nm PZO membrane for as-transferred and annealed membrane. The as-transferred was poled with +10V and the subsequent scan shows contrast in amplitude and phase, whereas the same procedure does not result in a stable ferroelectric phase in the annealed membrane,* ***(b)*** *SS-PFM loops for the as-transferred (**top**) and annealed (**bottom**) membrane shows FE-like behaviour and AFE-like behaviour respectively.*

## C5. Structural characterization of 17 nm as-transferred and annealed PZO membrane

**(a)** Theta-2theta scans and rocking curves for PZO of 17 nm membrane at different stages of processing.

**(b)** RSMs around $(-103)_{PC}$ peak of PZO; the as-transferred membrane shows tensile strain of 1.2% in the in-plane direction, while the annealed membrane has bulk-like lattice parameters.

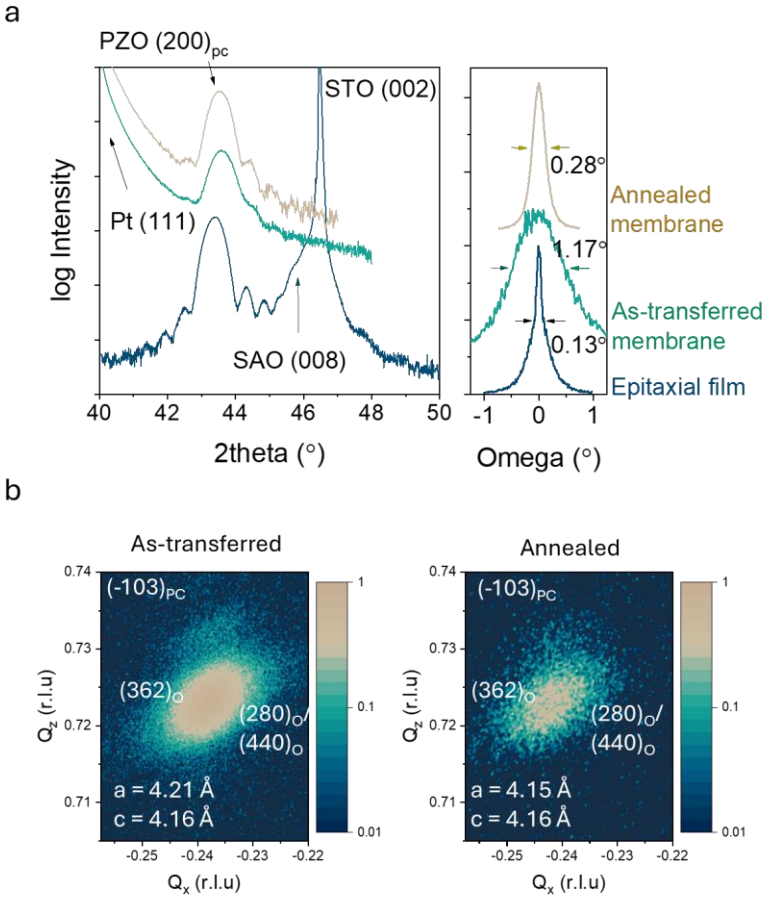


***Figure C5. (a)*** *Theta-2theta scans and rocking curves for PZO of 36 nm membrane at different stages of processing,* ***(b)****RSMs around* $(-103)_{PC}$ *peak of PZO; the as-transferred membrane shows tensile strain of 1.2% in the in-plane direction, while the annealed membrane has bulk-like lattice parameters.*

Appendix D

# *Addendum Chapter 3: Switching dynamics of antiferroelectric capacitors: Effect of mechanical clamping due to substrate*

## D1. Supporting data for investigation of On GSO and Off GSO capacitors

### D1.1. STEM of columnar boundary in "off GSO" membrane.

The images show STEM observation of a region where the two columns intersect. We see $(100)_{pc}$ planes of one the columns are not parallel to the surface plane. The GPA of this region shows dislocations where the two columns meet, and the resulting strain in the locale. The GPA does not show a strain pattern as in **Figure 3.2** of the main text, as this region does not contain the right variation of the $(120)_o$ orientation. These dislocations and changes in strain state between two columns might act as pinning points for phase boundaries during electric field induced AFE to FE transition, that affects the dynamics of the transition. This might also contribute to the values of the fitting parameters of KAI model used in the main text, and lead to high values of β exponent.

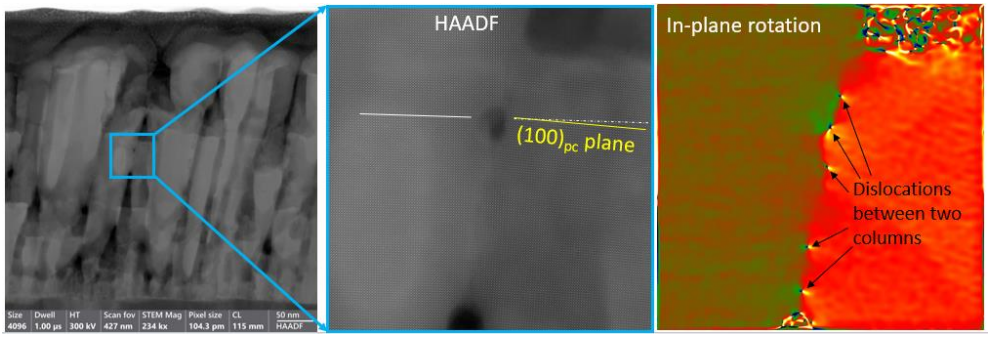


***Figure D1.1***. *STEM imaging of a boundary between two columns in Off GSO membrane: low magnification HAADF image (left panel), zoom in of the region marked as blue square (middle panel) and in-plane rotation (right panel).*

## D1.2. RSMs around PZO (-103)$_{PC}$ and PZO (-303)$_{PC}$ peaks for ¨On GSO¨ and ¨Off GSO¨.

The RSMs of ¨On GSO¨ and ¨Off GSO¨ capacitors were done around PZO(-103)$_{pc}$ and PZO(-303)$_{pc}$ peaks, to calculate the strain states. Each of the peaks are identified in orthorhombic notations and show splitting due to different domains. The summary of lattice parameters obtained are shown in the table below.

| | **Reflection** | **Peak** | **In-plane PC lattice parameter (Å)** | **Out of plane PC lattice parameter (Å)** |
|---|---|---|---|---|
| **On GSO** | (-103)$_{PC}$ | (001)$_O$ orientation | 4.155 | 4.118 |
| | | (120)$_O$ orientation | 4.153 | 4.155 |
| | (-303)$_{PC}$ | (001)$_O$ orientation | 4.157 | 4.115 |
| | | (120)$_O$ orientation/ [001]$_{PC}$ IP | 4.114 | 4.153 |
| | | (120)$_O$ orientation/ [100]$_{PC}$ IP | 4.162 | 4.153 |
| **Off GSO** | (-103)$_{PC}$ | (001)$_O$ orientation | 4.154 | 4.119 |
| | | (120)$_O$ orientation | 4.111 | 4.160 |
| | (-303)$_{PC}$ | (001)$_O$ orientation | 4.156 | 4.123 |
| | | (120)$_O$ orientation/ [001]$_{PC}$ IP | 4.117 | 4.159 |
| | | (120)$_O$ orientation/ [100]$_{PC}$ IP | 4.156 | 4.164 |

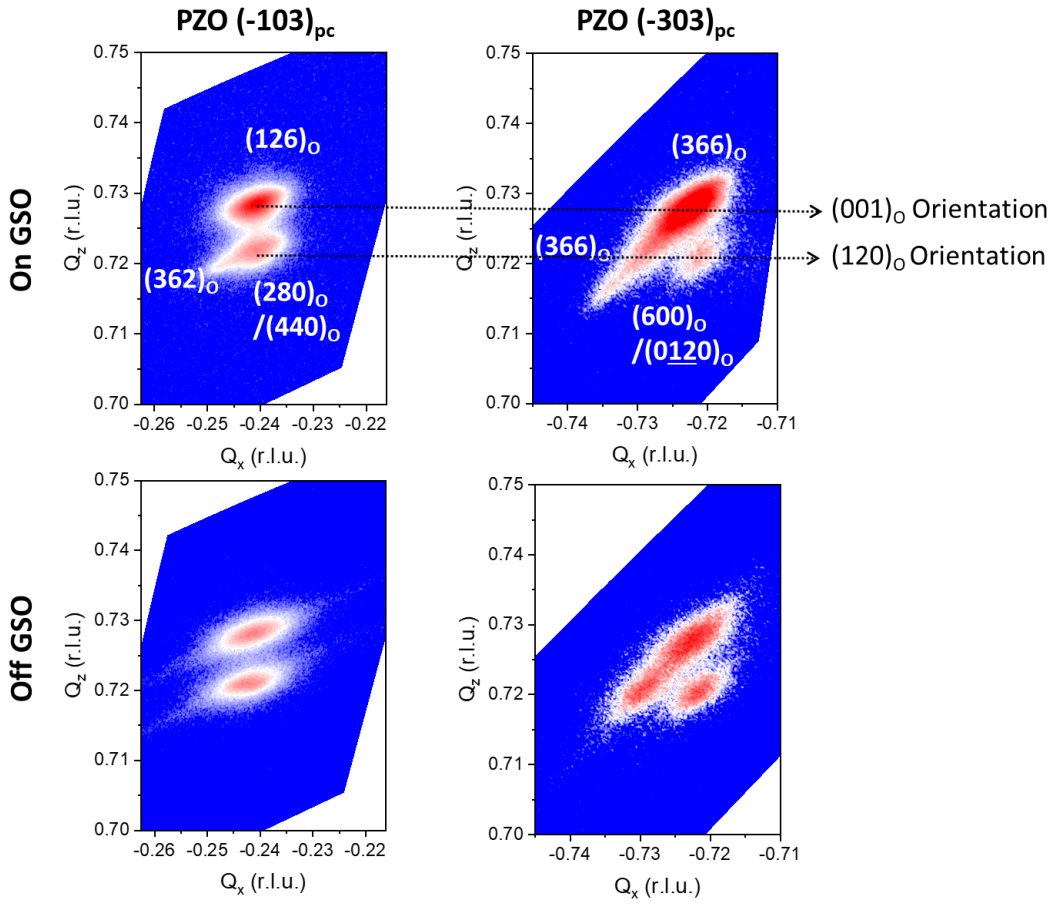


***Figure D1.2**. RSMs for On GSO (top row) and Off GSO (bottom row) capacitors around the (-103)$_{PC}$ (left column) and (-303)$_{PC}$ (right column) peaks of PZO.*

## D1.3. Hysteresis loops comparison of "On GSO" and "Off GSO" at different frequencies.

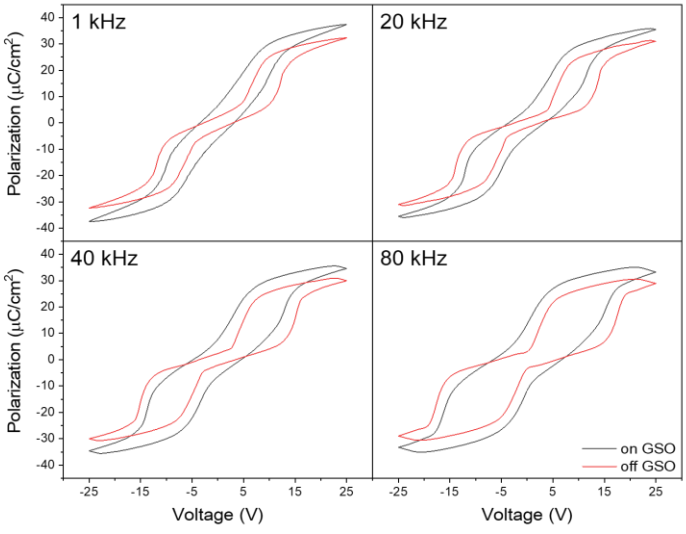


***Figure D1.3.*** *P-E loops for On GSO and Off GSO capacitors at different frequencies, these loops are calculated by integrating the current loops in the main text with respect to time.*

## D1.4. Resistance- Capacitance (RC) time constants in PZO capacitors.

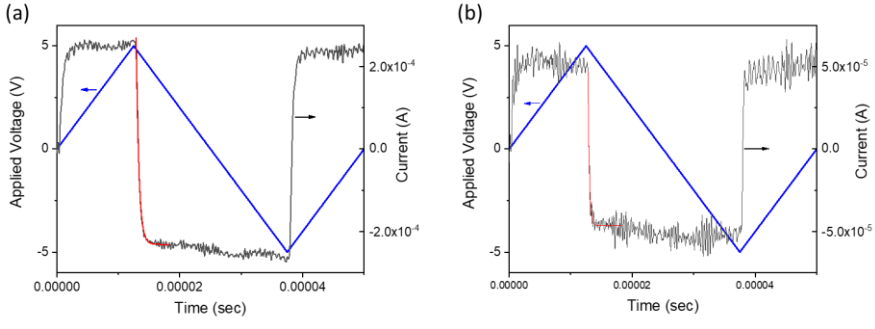


***Figure D1.4****. Resistance- Capacitance (RC) time constant measured for* ***(a)*** *On GSO capacitor, and* ***(b)*** *Off GSO capacitor, the red lines show the fitting.*

RC effects in samples can affect the shift of the characteristic switching electric fields with change in frequency. Therefore, it is important to know the RC time constants of each sample. To measure the RC time constants, the epitaxial film "on GSO" and the

membrane "off GSO" were tested by applying a 5V AC loop, at 20 kHz. 5V is chosen as the amplitude because at this voltage, no switching of the sample occurs. The frequency is chosen in a way that the preset current range is the same as the range at which the frequency dependent loops were measured at 1 mA, since this range can also affect the impedance and the change in the switching electric fields with frequency.
The drop in current with voltage is fitted with the equation (red line in the **Figure D1.4**):

$$I = I_0 . exp^{-\frac{t}{\tau}}$$

Tau ($\tau$) is the RC time constant and is calculated to be 453 ns in ¨on GSO¨ sample and 225 ns in ¨off GSO¨ sample. This difference in tau is due to the bottom electrodes i.e., SRO in the ¨on GSO¨ sample has higher RC effects than gold in ¨off GSO¨ samples. However, even at the highest frequency of 80 kHz, the voltage cycle has a time-period of 12 µs which is much higher than the RC time constants and hence, the shift in switching electrode fields depending on frequency can be said to have been not affected by the RC effects.

## D1.5. Component in the current peaks for On GSO and Off GSO.

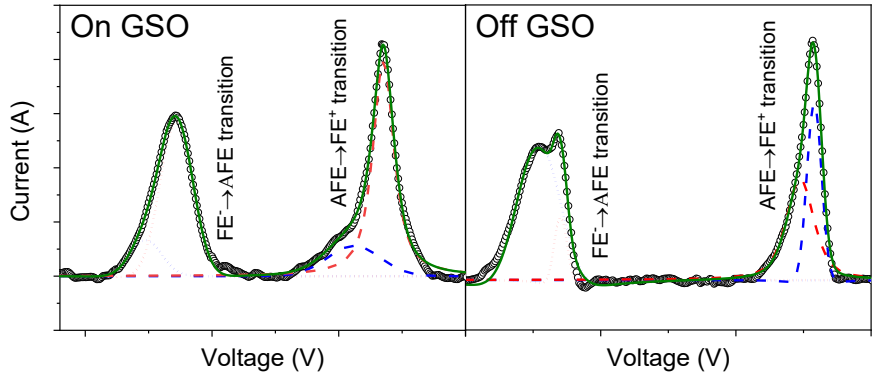


***Figure D1.5.*** *Fittings of the switching current peaks with two component peaks for On GSO (left panel) and Off GSO capacitors.*

## D1.6. KAI model fittings for the smaller fitted peak in FE to AFE switching in Off GSO membrane.

The current peaks for the FE to AFE transition were fitted with two components for each frequency and then their behaviour as a function of frequency was fitted with the KAI model. The results show that the two peaks also have different frequency dispersions, however, they both have a lower dispersion as compared to the epitaxial films.

Similar analysis was not done for other switching events since the two component peaks as shown in **Figure D1.6** are very close and convoluted that might result in a higher error.

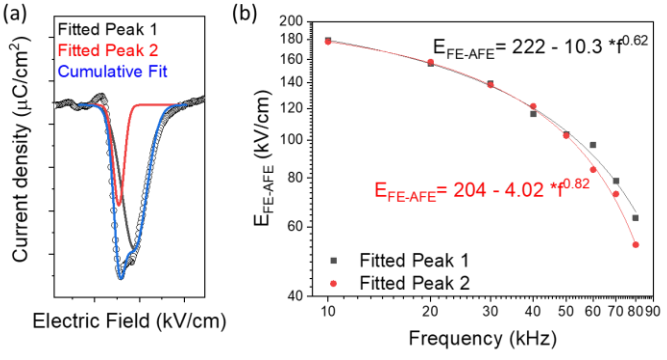


***Figure D1.6. (a)*** *Peak fitting for the displacement current peak associated to the FE to AFE transition at 50 kHz,* ***(b)*** *KAI model fittings on the two component peaks.*

## D1.7. Temperature dependant PE loops for Off GSO membrane and modified Curie Weiss law for the two capacitors.

**(a)** PE loops for Off GSO membrane as a function of temperature, the loops move towards the y-axis (E=0 kV/cm) as the temperature increases, ultimately showing a leaky non-linear dielectric behaviour above the Curie temperature.

**(b)** Fitting of permittivity as a function of temperature above the Curie temperature with the modified Curie Weiss law: $\frac{1}{\varepsilon r} - \frac{1}{\varepsilon_r^m} = \frac{(T-Tm)^\gamma}{C}$, where $\varepsilon_r{}^m$ is the maximum permittivity obtained, $T_m$ is the temperature of maximum permittivity, $\gamma$ is the modified Curie- Weiss exponent and $C$ is the modified Curie constant. The value of $\gamma$ represents the diffusiveness of the transition and equals 1 for regular ferroelectrics and 2 for relaxor ferroelectrics. The deviation from value of 1 also mean that there are polar

nano-regions above the Curie temperature. In our case, the value of this exponent is very similar for both On GSO and Off GSO capacitors and deviate slightly from 1.

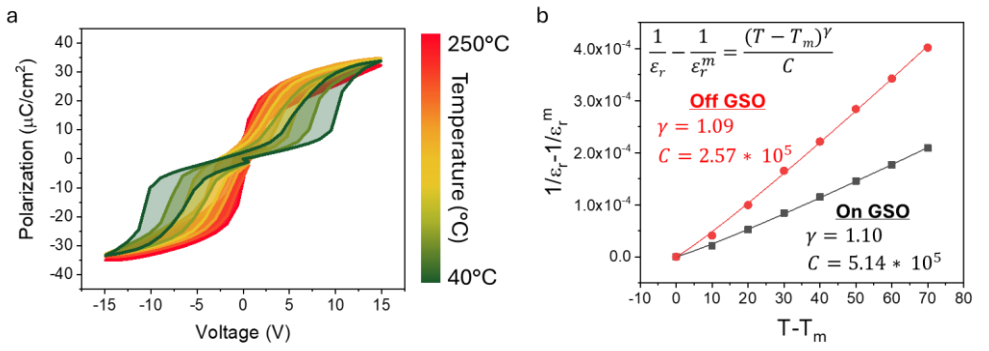


***Figure D1.7.*** *Temperature dependent measurements done on PZO capacitors,* ***(a)*** *PE loops as a function of temperature for the Off GSO capacitor,* ***(b)*** *dielectric constant as a function of temperature above the Curie temperature, and modified Curie Weiss law fitting.*

## D2. Investigation of capacitors grown on (001)-oriented $SrTiO_3$ (STO) substrates: Epitaxial film (On STO) vs membrane (Off STO).

We also studied epitaxial films grown on STO (001) substrate, and membrane capacitors removed from STO (001) substrate. The comparison between the epitaxial film and the membrane capacitors (On STO and Off STO) show similar trends, therefore, the analysis done in **Chapter 3** is applicable to these capacitors as well.

### D2.1. XRD (Θ-2Θ scans) for epitaxial film and membrane capacitor

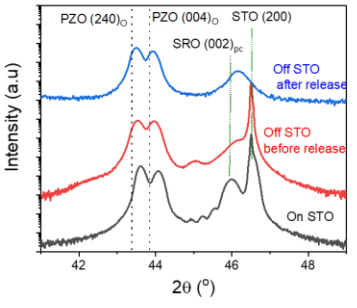


| | Peak | Volume fraction | Lattice parameter (Å) | Strain (%) |
|---|---|---|---|---|
| On STO | $(002)_{pc} = (004)_o$ | 0.58 | 4.105 | -0.509 |
| | $(200)_{pc} = (240)_o$ | 0.42 | 4.147 | -0.503 |
| Off STO | $(002)_{pc} = (004)_o$ | 0.60 | 4.119 | -0.169 |
| | $(200)_{pc} = (240)_o$ | 0.42 | 4.156 | -0.288 |

***Figure D2.1.*** *HRXRD measurements (theta-2theta scans) for SRO/PZO/SRO capacitors grown directly on STO (001) substrate or on SAO buffered STO (001) substrate.*

The strains in these samples are also very low but higher than the samples grown on GSO. Since the PZO layers grow almost relaxed, this strain may arise from dislocations at the interface of

bottom SRO and PZO, as well as dislocations between columns of PZO. However, the difference in the strains of the two PZO layers is minimal.

## D2.2. Functional properties of On STO and Off STO capacitors.

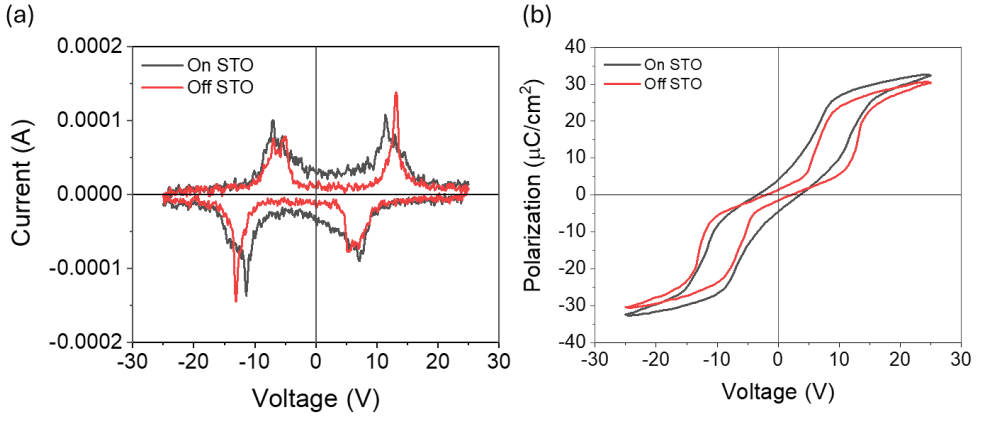


***Figure D2.2**. **(a)** I-V loops and **(b)** P-E loops on On STO and Off STO capacitors at 10 kHz.*

## D2.3. Frequency dependence of switching fields and KAI model fittings.

I-V loops of On STO **(a)** and Off STO **(b)** capacitor as a function of loop frequency and KAI-model fittings **(c-d)**.

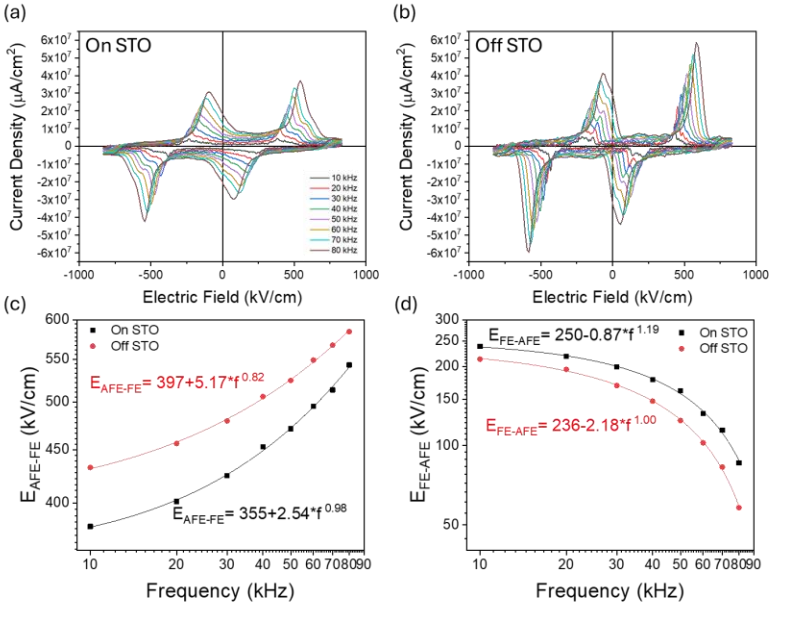


***Figure D2.3**. Current density – Electric field curves of, **(a)** On STO film, **(b)** Off STO membrane, and KAI model fittings for **(c)** AFE- FE switching fields and, **(d)** FE- AFE switching fields.*

## D2.4. Components in switching current peaks in On STO and Off STO capacitor.

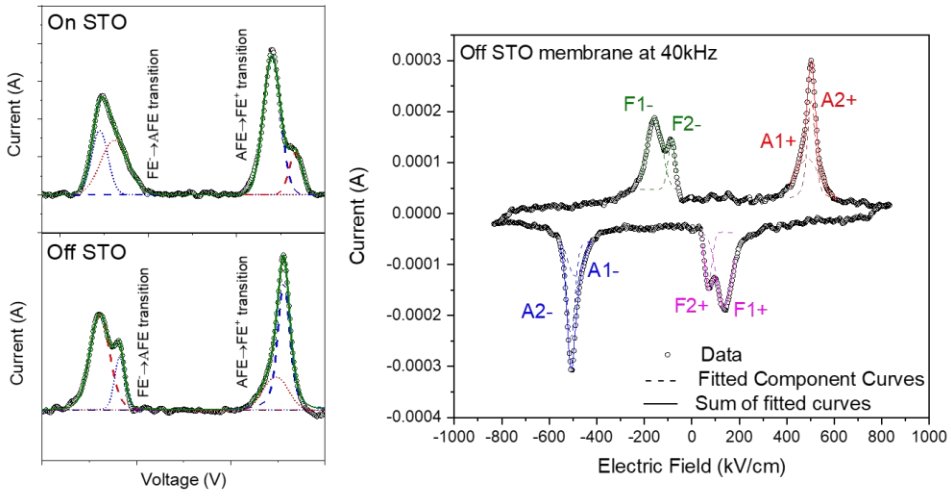


***Figure D2.4.*** *Fittings of the displacement current peaks with multiple peaks representing different switching events for On STO and Off STO capacitors.*

# Appendix E

## *Addendum Chapter 4: Dimensionality-driven Phase transitions in PZO membranes*

### E1. Ferroelectric phases of PZO: Monoclinic (Pc) and Tetragonal (I4cm)

**Figure E1** shows the crystal models of two of the novel ferroelectric phases of PZO: Monoclinic Pc phase and tetragonal I4cm phase.

In the Monoclinic Pc phase, the major Pb displacement is in the [111] direction (marked by red arrows), and a small tilt towards the c axis (marked by dark blue arrows). Moreover, there is an additional small antiparallel modulation in the a-b plane (marked as dotted, double-headed light blue arrows). This displacement direction is termed as [*uuv**]. From this model, the tilt pattern appears to be $a^-a^-c^+$.

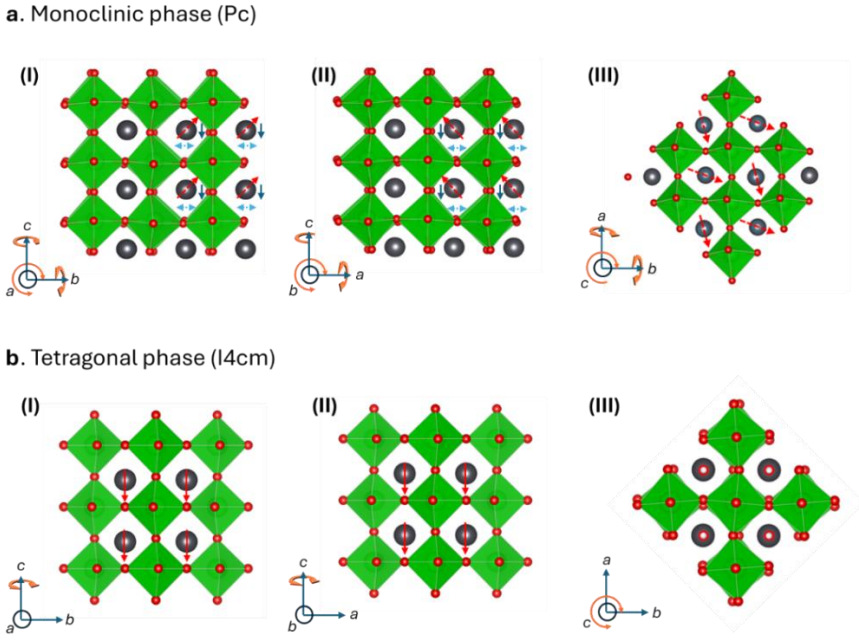


***Figure E1****: Crystal models of two of the ferroelectric phases of PZO,* ***(a)*** *Monoclinic Pc phase,* ***(b)*** *Tetragonal (I4cm) phase viewed from different zone axes:* $a_{PC}$ ***(i)***, $b_{PC}$ ***(ii)*** *and* $c_{PC}$ ***(iii)****. The orange arrows in in the compass show tilt axes. Red colour represents major Pb displacement, dark blue shows minor Pb displacement contribution, whereas the light blue shows an overlapping antiparallel modulation. Solid arrows represent complete in-plane displacement, dotted arrows represent an out-of-plane component of the displacement, and the circles show a complete out-of-plane displacement. The magnitudes of the displacements represented by arrows are exaggerated for better visualization.*

## E2. Crystal lattice of Pnam phase of PZO

The phase observed in 17 nm PZO membrane (corresponding to the ¼(100)$_{PC}$ super lattice reflections) is an antiferroelectric phase. The Pnam phase is marked by a complex tilting pattern of oxygen octahedra and Pb displacement. The crystal structure is drawn in **Figure E2.**

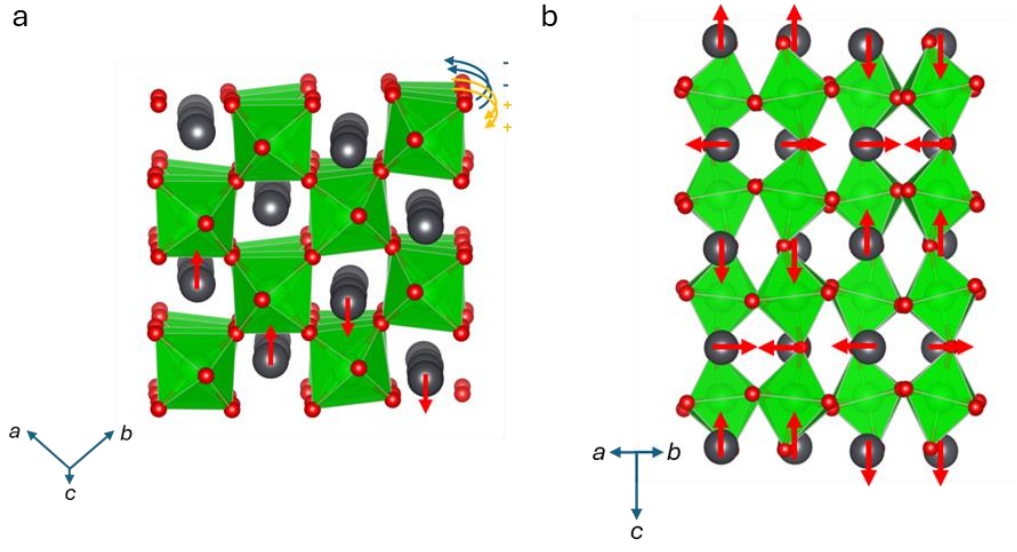


***Figure E2.*** *Crystal structure of the AFE PZO in the Pnam phase from two directions. The compasses show the directions in the pseudocubic notations; in* ***a****, the blue and orange arrows represent the tilt directions of the oxygen octahedral.*

## E3. Note on the interpretation of phases

The PZO membranes that we have studied usually contain a coexistence of multiple phases. The best way to determine the phases present is electron diffraction that probes the whole volume of the membrane and gives information about the presence of antiparallel modulation and the tilt systems. We have used electron diffraction to determine the phases and is the primary method of the determination. The tilt system present in the monoclinic phase is also determined using the diffraction experiments plus rotating the samples. However, in some cases, diffraction cannot be used to distinguish certain phases such as Pbam, R3c, and I4cm since the patterns coming from the tilting are similar, if not identical. In this case, we also use high resolution STEM to observe different phases and ascertain if certain phases are present, not observable via diffraction. It is important to note that such high-resolution imaging gives information about the surface of the membranes.

We combine different observations from our ABF imaging to interpret the phases present. From the ABF images, we can obtain Pb displacements (from the geometric

centre of the surrounding Zr atoms) and O displacements from the surrounding cations (Pb and Zr). Since in PZO, the Zr atoms are not displaced from their cubic positions, the Pb displacement vectors do not need further processing. However, the procedure to calculate O displacements include Pb atoms as reference points, so they are influenced by the Pb displacements as well. In such cases, we have to also consider how the displacements of Pb atoms can shift the geometric centre of the cations that add extra apparent displacement to the oxygen atoms. Therefore, while the oxygen displacements show how the tilt system might be changing, the actual tilt system (and hence, the phase) cannot be interpreted from the displacements. However, we can infer the oxygen chain linearity (that run along <110> directions) from the displacement vectors and compare them to how these chains appear in different phases. When taking this holistic picture, we can speculate on the phases present. Electron diffraction patterns can then provide further credence to our interpretation.

**Rhombohedral R3c phase:** Polar direction: $[111]_{PC}$, tilt: $a^-a^-a^-$

In regions of R3c phase, we expect to see Pb displacements along $<110>_{PC}$ directions (projection of [111]), and non-linear oxygen chains. In Oxygen displacement mapping, this appears as zig zag displacements of Oxygen atoms. This will be true for all domain variants of the R3c phase.

**Monoclinic Pc phase:** Polar direction: $[uuv^*]_{PC}$

For Pc phase, two zone axis are symmetrically equivalent (*a* and *b*), and the third one is not. For the former, the Pb displacement will be in a direction between <110> and <001> with oxygen chains linear in one direction and zig zag in the other. This can be inferred from the displacement vectors of oxygen atoms. An example of these domains is **Figure 4.5f** of the main text (ABF imaging of 5 nm PZO membrane).

For the other variant where the zone axis is *c*, the antiparallel modulation is in-plane and hence can be visualized. In this case, the Pb atoms seem to be displaced in a zig zag pattern, and this is the most straight forward observation. The corresponding oxygen chains alternate between linear (the two dipoles point towards this chain) and zig zag (dipoles point away from this chain). However, because of the changing Pb displacement, the geometric centre moves as well. In this case, the corresponding oxygen displacements will be different. All oxygens show major displacement towards <110> direction, but with a <001> component as well, with alternating magnitudes of <001> component. The two examples are the regions of monoclinic phase in 36 nm PZO membrane (**Figure 4.2b** in the main text) and **Figure E4** below.

**Tetragonal I4cm phase:** Polar direction: $[001]_{PC}$, tilt: $a^0a^0c^-$

I4cm phase can also show two variants. In both cases, oxygen chains are completely linear. If the axis of tilt is in-plane, we will see minimum displacements of the oxygen atoms, since the Pb displacement is very regular. If the tilt axis is out-of-plane, the Pb displacements will also be out-of-plane and hence not visualized. In this case, although there is an anti-phase tilt, the oxygen columns will not show displacements since the oxygen atom is considered to be the centre of the fitted 2D gaussian. Although, we can look how elliptical the oxygen columns look in these regions, but without the relevant information regarding Pb displacement, we cannot be sure of the phase.

## E4. Drumheads of 17 nm membrane with stress relief pattern

Some drumheads of 17 nm membrane as shown in Figure **E3a-c**, show different structures in the presence of a star-shaped wrinkle pattern due to stress relief. There are additional fringes along the edges of the drumhead, marked as yellow arrows in **Figure E3a** resulting from composite bending. It can be observed in the EDP obtained from $[001]_{PC}$ zone axis that the ¼ $(110)_{PC}$ reflections are replaced by diffuse streaks suggesting a formation of a continuum of equally favourable modulations along the $<hh0>^*_{PC}$ directions. This observation is consistent with the flatness of the energy landscape and the known propensity of the system to develop long period modulations and incommensurations.[28,196,197] A low-magnification HR-TEM image of one of these arms (**Figure E3c**) shows fringes that are unevenly spaced and the FFT of the regions exhibits diffused streaks corresponding to these incommensurate phases (IC), consistent with the theoretical prediction that stress may allow PZO to adopt IC phases.[27]

Moreover, near the centre of the drumhead (**Figure E3d**), we can see fringes along two orthogonal directions marked as orange arrows and the FFT of this region shown in **Figure E3e** shows the diffused streaks corresponding to these fringes.

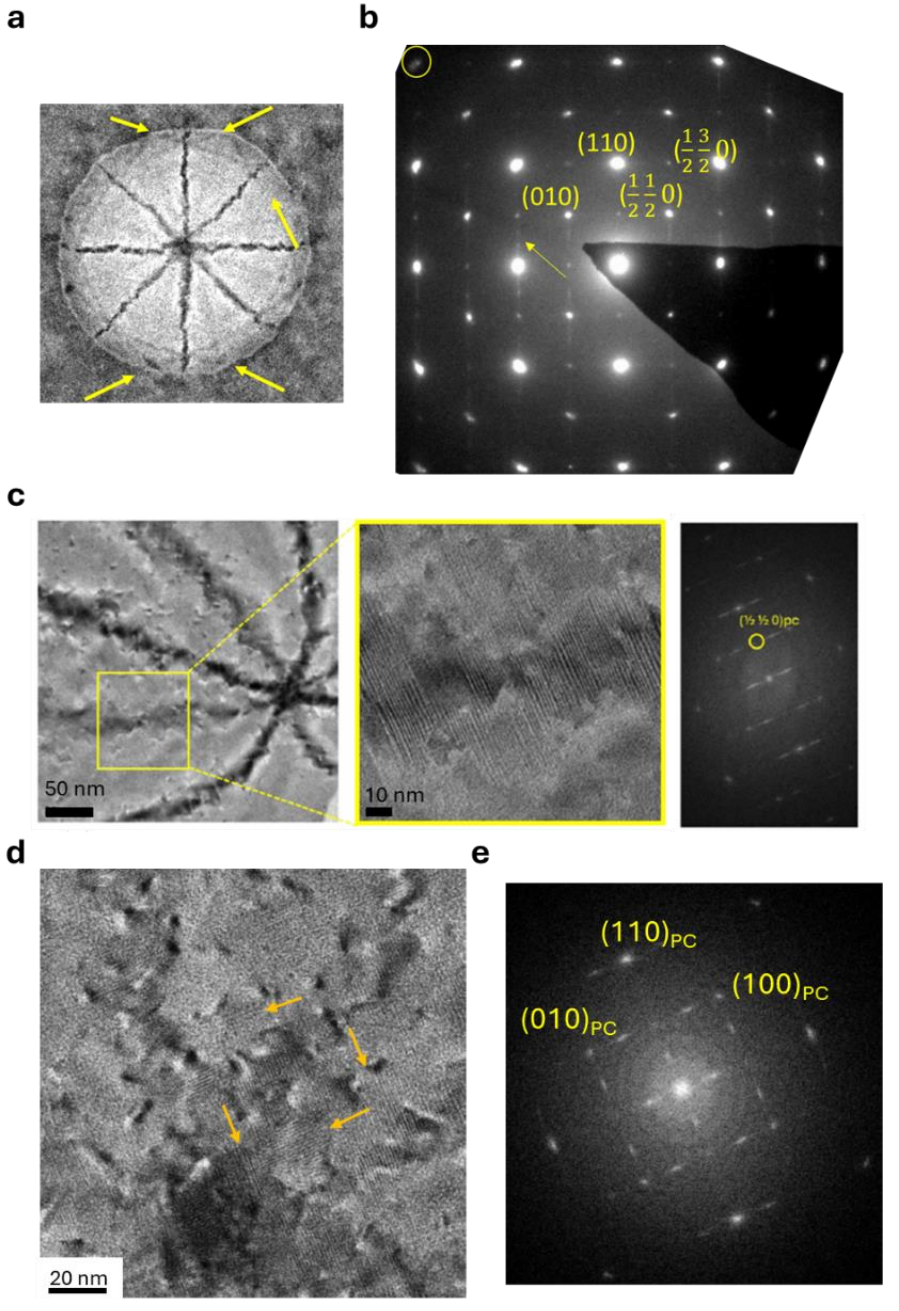


***Figure E3***. ***(a)*** *Suspended membrane of 17 nm PZO showing the stress relief pattern,* ***(b)*** *$[001]_{PC}$ zone axis EDP pattern showing diffused streaks in the $<110>_{PC}$ directions,* ***(c)*** *Low magnification HRTEM image of the drumhead, while the middle panel shows a magnified region of one of the arms, right panel shows the FFT on the zoomed in region,* ***(d)*** *Low magnification HRTEM image near the centre of the pattern,* ***(e)*** *FFT of the image in (d).*

## E5. Additional images for 36 nm membrane.

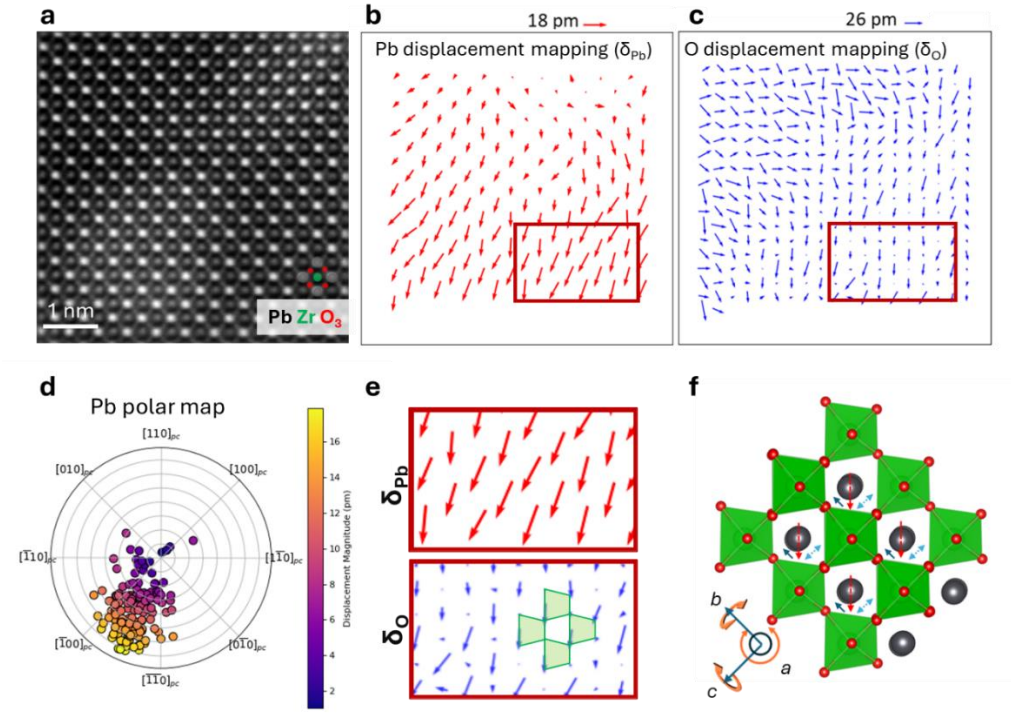


***Figure E4***. *ABF imaging on 36 nm membrane,* ***(a)*** *ABF image (contrast inverted),* ***(b)*** *Pb displacement mapping,* ***(c)*** *Oxygen displacement mapping,* ***(d)*** *Pb displacement polar map,* ***(e)*** *magnified Pb and O displacements from b and c,* ***(f)*** *Structure model of Pc phase matching the observed domain variant.*

# E6. Additional images for 5 nm PZO membrane.

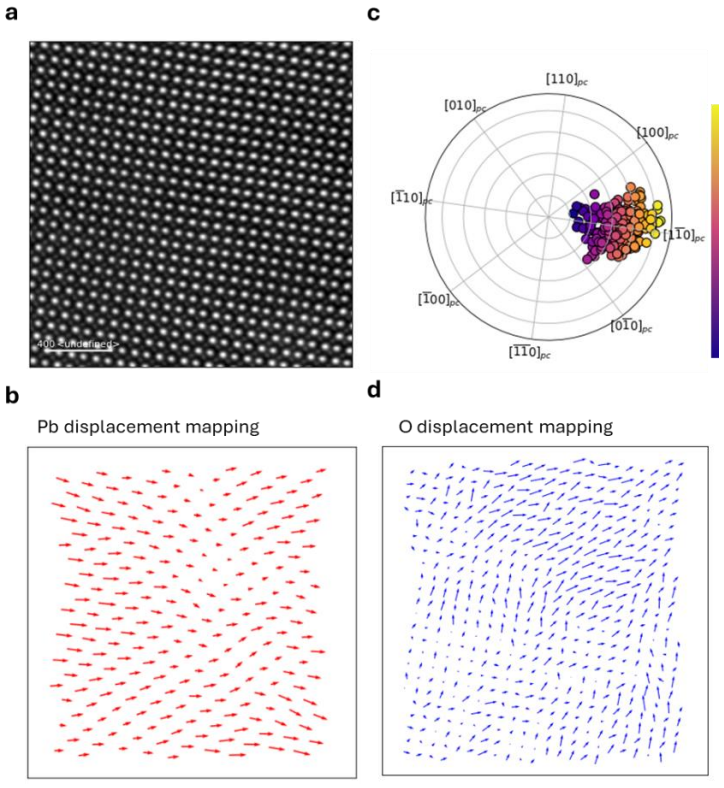


***Figure E5**. ABF imaging on 5 nm membrane, **(a)** ABF image (contrast inverted), **(b)** Pb displacement mapping, **(c)** Pb displacement polar map, **(d)** Oxygen displacement mapping. The polar map also represents the compass for the ABF image, note that the image is not taken from a raw file and therefore has undefined scale.*

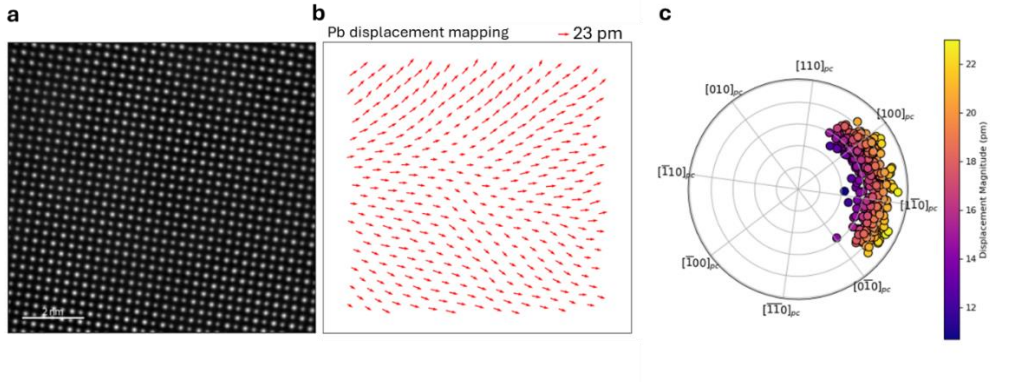


***Figure E6**. HAADF image of 5 nm PZO membrane **(a)** HAADF image, **(b)** Pb displacement mapping, **(c)** Pb displacement polar map, the polar map also represents the compass for the HAADF image.*

## E7. GPA rotation map of the region shown in Figure 4.4d.

GPA rotation maps of the region in Figure 4.4d shows high strains in the dark regions, while minimal strain in the rest of the membrane.

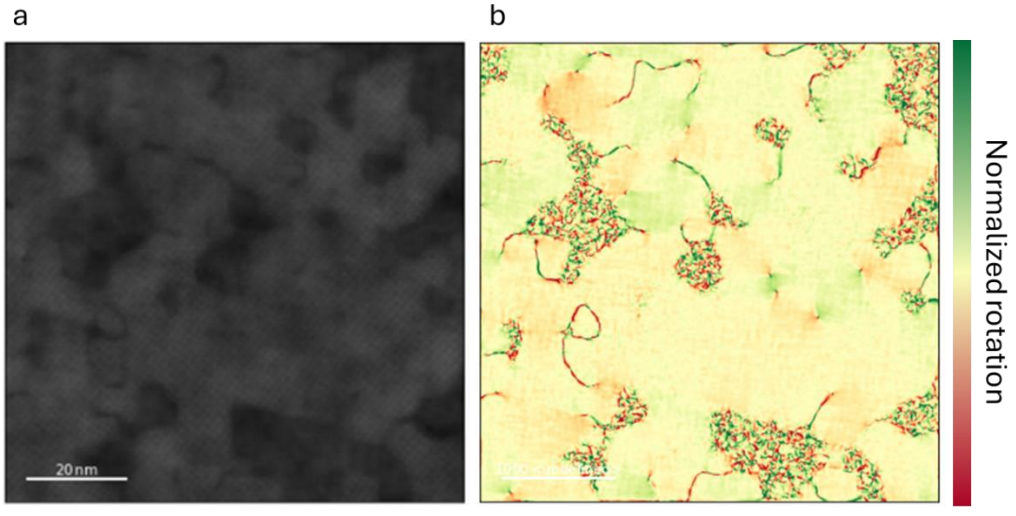


***Figure E7. (a)*** *Reprinted* ***Figure 4.4d****,* ***(b)*** *GPA rotation of the same region showing high dislocation density in the strained regions. Dislocations in relaxed regions are also visible.*

# Appendix F

## *Addendum Chapter 5: Strain effects in PZO membranes*

### F1. XRD peak fittings for the bent SRO/PZO/SRO capacitors with bending radius 5 mm.

In order to calculate the relative populations of the two domain variants in the bent PZO layer, and since, the peaks might be convoluted with the additional peaks from the copper stage and gold, the theta-2theta scan was fitted with multiple pseudo-voigt peaks as shown in **Figure F1**. The relative domain populations can now be calculated using the relative intensities of the two peaks and the ratio of $(120)_O$ : $(100)_O$ equals 1 : 0.6.

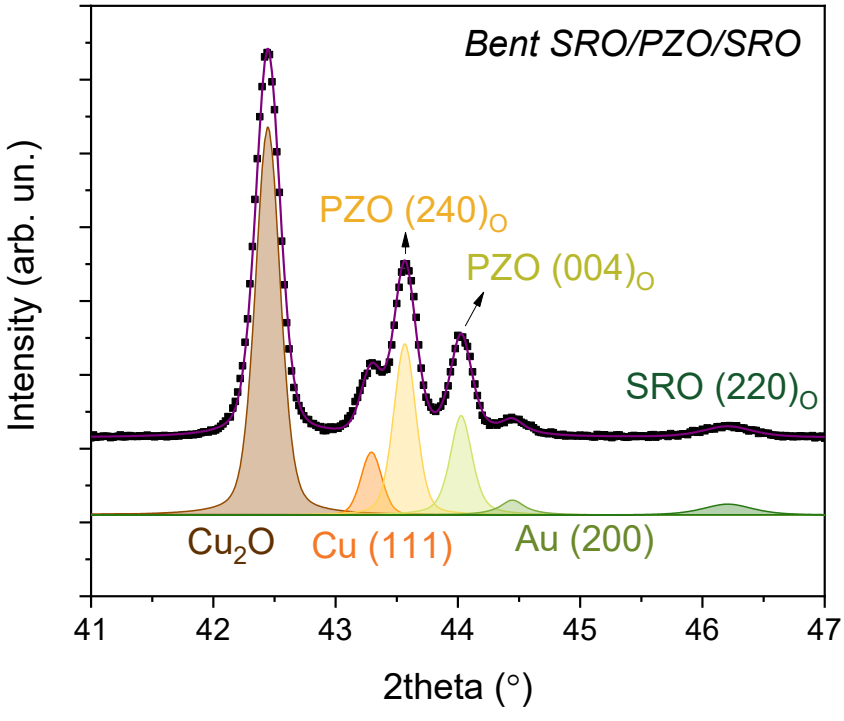


***Figure F1**. Peak fittings for the theta-2theta scan of the SRO/PZO/SRO membrane bent with a radius of 5 mm.*

## F2. Raman spectroscopy of PZO/SRO rolls transferred onto fused Silica substrates

To gain insights into the phase of the PZO in rolled form, we use Raman and compare it to a similar thickness flat PZO membrane transferred to Pt coated Silicon shown in **Figure F2a-b**. The main difference that can be seen from the two spectra are the change in intensity of the peaks at ~400 $cm^{-1}$ and 532 $cm^{-1}$ marked as arrows. These peaks correspond to the LO and TO mode and originate from Zr-O tension and $ZrO_3$ stretching. However, these peaks are present in both the AFE, FE phases of PZO- based materials as well as paraelectric phase; and their intensities are also similar in the different phases so they cannot be used to distinguish between phases. We can see this in **Figure F2c** where the temperature of the membrane is increased by increasing the laser power. Although most of the peaks change, the peak at 532 $cm^{-1}$ stays intense. The inconsistency between the flat and rolled membrane in this case comes from the fact that the rolled membrane has an SRO layer and is transferred to a fused Silica substrate that also contribute to the Raman. Hence, here, we will not take into account their relative intensities but rather their position since fitting the peaks has some uncertainties involved specially in case of thin films, in addition to some signals that might be coming from the SRO as well as the fused Silica substrate. Considering all this, it seems that the rolled membrane still has the AFE phase and rolling does not induce a phase change.

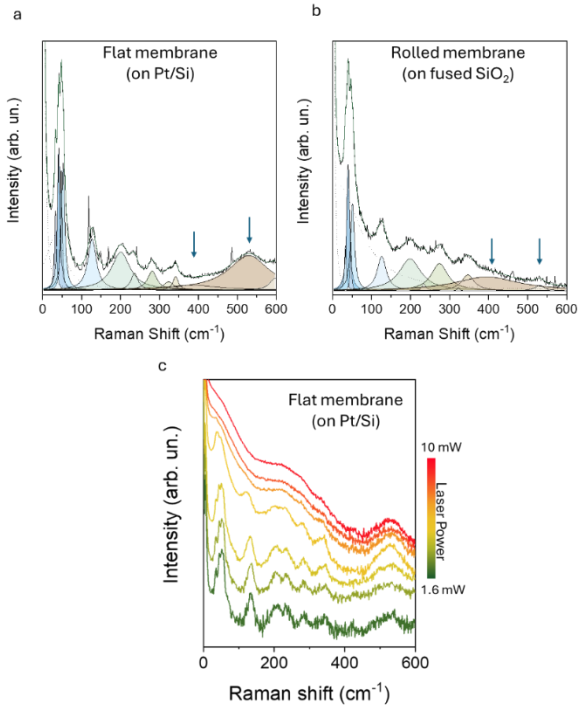


***Figure F2.*** *Raman spectra of* ***(a)*** *PZO membrane of 75 nm on Pt coated Silicon substrate for reference,* ***(b)*** *PZO/SRO rolls on fused Silica,* ***(c)*** *Raman spectra of flat 75 nm membrane as a function of laser power.*

## F3. Second Harmonic Generation (SHG) in wrinkles on 17 nm PZO membrane

SHG mapping was done on a 17 nm PZO membrane with wrinkles on a Pt- coated Silicon substrate, results shown in **Figure F3**. The mapping was done in reflection mode with a normal incidence (i.e. we are sensitive to polarization perpendicular to the beam direction). SHG mapping reveals three regions, (i) bare substrate where the SHG intensity is almost zero, (ii) flat regions of the PZO membrane that has non-zero but lower intensity, and (iii) wrinkles of PZO that show much higher intensity. The results show that the flat PZO membranes have in-plane polarization consistent with our TEM investigations in **Chapter 4**. Moreover, the flexoelectricity due to strain gradients polarize the PZO wrinkles, but this higher intensity might arise from either a ferroelectric phase (the PZO is completely ferroelectric at the wrinkles) or a biased AFE phase with unequal sublattices. In any case, strain gradients drive the PZO layer to a higher polarization state.

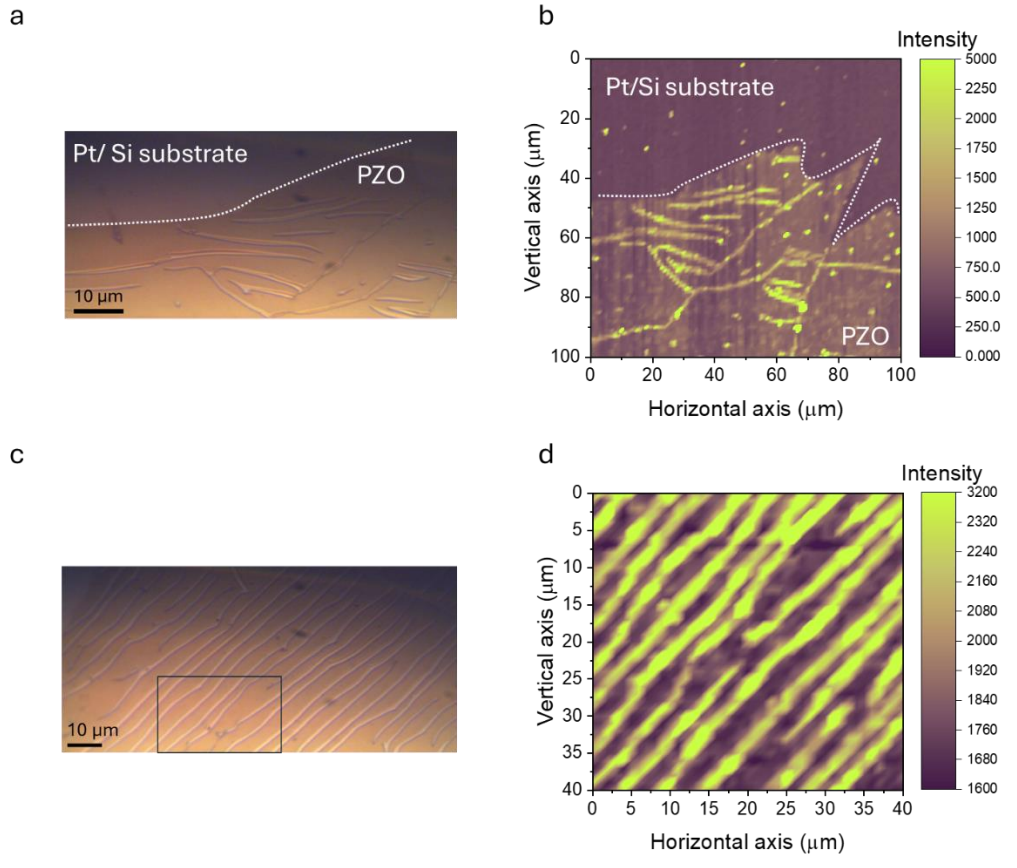


***Figure F3**. SHG in PZO wrinkles on 17 nm membrane **(a, c)** optical images, **(b, d)** SHG mapping, note that the optical images match partially to the SHG mapping area, the white dotted lines show the boundary of the PZO membrane.*

# Appendix G

## *Effect of thermal treatments on double hysteresis loop of PZO capacitors*

SRO/PZO/SRO capacitors (PZO layer of 300 nm) that were pre-annealed to remove hydrogen, were subjected to different thermal treatments to investigate how their hysteresis loops change due to the treatments. The loops of three different treatments were compared: one capacitor immediately after annealing, second was heated to above Curie temperature and cooled in air (Air quenching) and last was heated to above Curie temperature and cooled via water (Water quenching). The results are shown in **Figure G1**.

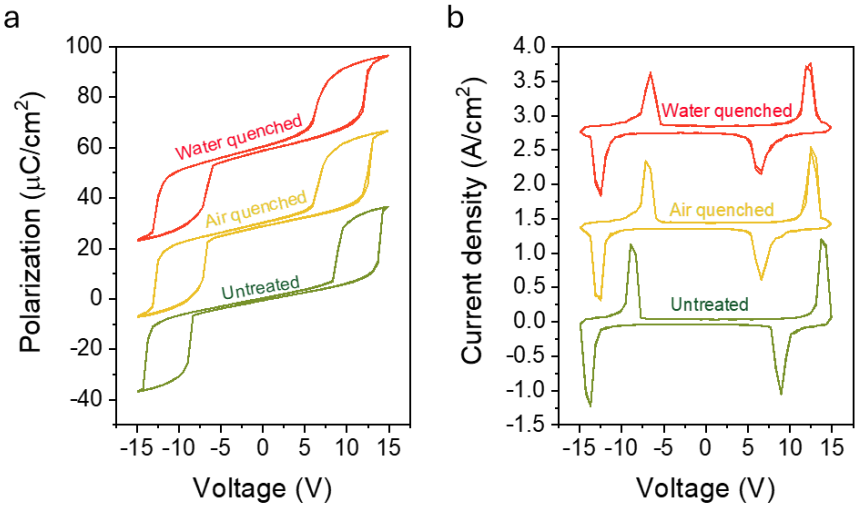


***Figure G1. (a)*** *Polarization-Voltage loops,* ***(b)*** *Switching current- Voltage loops for PZO capacitors subjected to three different thermal treatments, loops are manually offset for better visualization.*

The capacitors show robust antiferroelectric behaviour in each case (double hysteresis and four switching current peaks with low remnant polarizations). Due to quenching, the switching fields for both AFE to FE and FE to AFE decrease, signifying a higher stability of FE phase compared to the untreated sample. The difference is lower between air quenching and water quenching samples, but the trend is consistent. Quenching generally induces high stresses (usually compressive in nature) that reduces the free energy of the ferroelectric phase. However, the shape of the loops does not change significantly as compared to the thinner PZO capacitors shown in **Chapter 6**, signifying the role of hydrogen in the functional behaviour, and effect of thickness.

Another heat treatment that can be done is field cooling where I heated the capacitor above the Curie temperature, applied a DC voltage of 15 V and cooled the sample in

the presence of the field. The cooling rate is similar to the air quenching sample, and has to be kept high, since the amount of time of DC poling has to be minimized to prevent breakdown of the capacitor. The results of field cooling are shown in **Figure G2**.

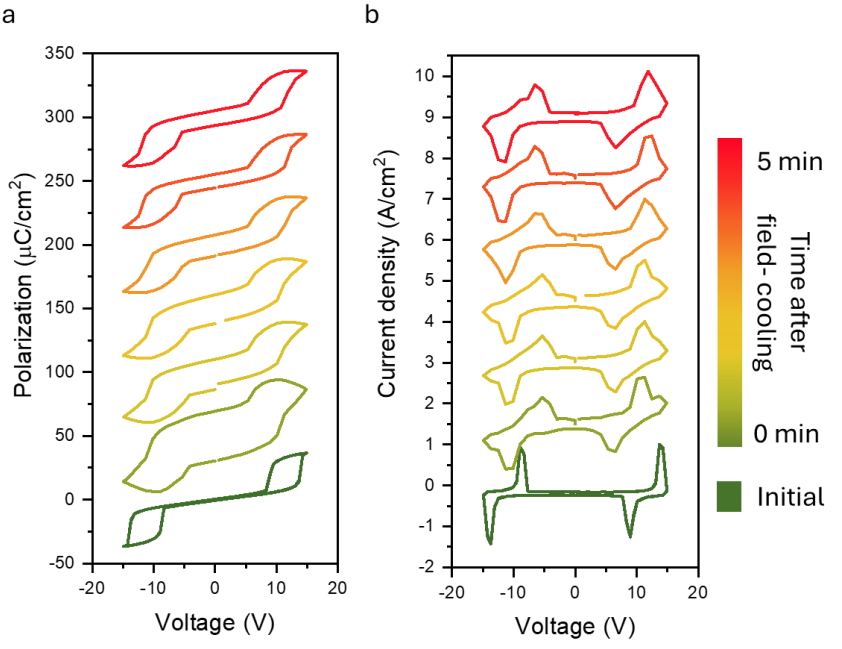


***Figure G2**. **(a)** Polarization-Voltage loops, **(b)** Switching current density- Voltage loops for PZO capacitor subjected to field cooling taken over time, loops are manually offset for better visualization.*

The loops were taken every minute after field cooling the capacitor. All loops show double hysteresis and four switching current peaks. However, the first loop after field cooling shows a high remnant polarization as well as leakage current. Subsequent peaks show less influence of the leakage currents while maintaining the high remnant polarization, showing how the field cooling can stabilize ferroelectric phase. Surprisingly, the switching corresponding to the AFE phase happens at the same fields as the air quenched sample; therefore, although, there is a larger proportion of the ferroelectric phase, the remaining antiferroelectric phase has the same switching behaviour as the air quenched one. Moreover, the increase in leakage current due to field cooling that relaxes over time (or due to the repeated cycles) may be due to the creation of charged defects, or high domain wall density.

The heat treatments, therefore, also provide another way to control phase coexistence and energy landscape of PZO system.

# Appendix H

## *Electric field loops used for different measurements*

The types of loops used to measure different properties are shown below. **Figure H1a** shows a triangular pulse used to measure PE loops and leakage current loops. In **Figure H1b**, the loop is a stepped triangular function used for SS-PFM with an on- and off stage. The values of amplitude and phase are taken at the end of each on- and off- stage to allow for relaxation at the new value.

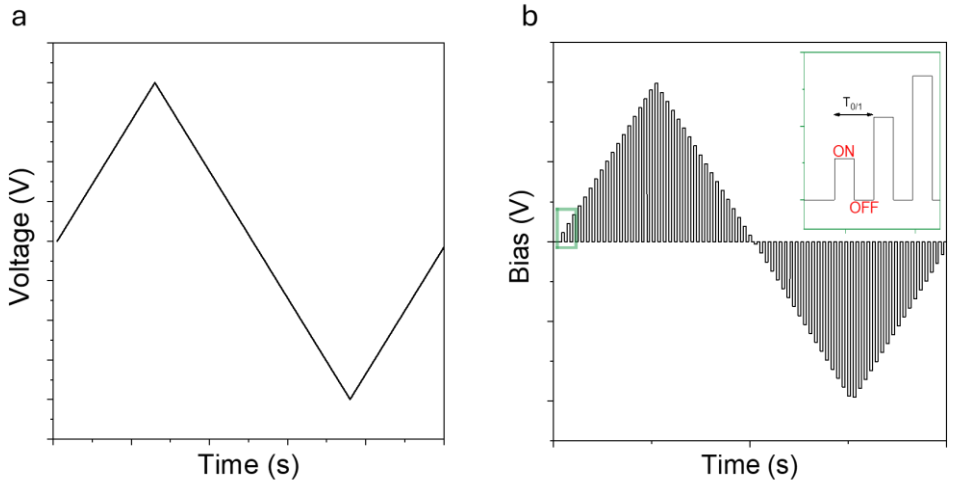


***Figure H1**: Electric field loops for different measurements, **(a)** PE loops on capacitor and leakage current measurements, **(b)** SS-PFM loop.*